



UNIVERSIDADE ESTADUAL DE CAMPINAS
Faculdade de Engenharia Mecânica
e Instituto de Geociências

MARCOS ROBERTO MENDES PENTEADO

**THEORETICAL, EXPERIMENTAL AND NUMERICAL
STUDY OF GAS-LIQUID FLOW IN AN
ELECTRIC SUBMERSIBLE PUMP IMPELLER**

**ESTUDO TEÓRICO, EXPERIMENTAL E NUMÉRICO
DO ESCOAMENTO GÁS-LÍQUIDO EM ROTOR DE
BOMBAS CENTRÍFUGAS SUBMERSAS**

CAMPINAS
2020

MARCOS ROBERTO MENDES PENTEADO

**THEORETICAL, EXPERIMENTAL AND NUMERICAL
STUDY OF GAS-LIQUID FLOW IN AN
ELECTRIC SUBMERSIBLE PUMP IMPELLER**

**ESTUDO TEÓRICO, EXPERIMENTAL E NUMÉRICO
DO ESCOAMENTO GÁS-LÍQUIDO EM ROTOR DE
BOMBAS CENTRÍFUGAS SUBMERSAS**

Thesis presented to the School of Mechanical Engineering and to the Institute of Geosciences of the University of Campinas in partial fulfillment of the requirements for the degree of Doctor of Sciences and Oil Engineering, in the area of Exploitation.

Tese de Doutorado apresentada à Faculdade de Engenharia Mecânica e Instituto de Geociências da Universidade Estadual de Campinas como parte dos requisitos exigidos para obtenção do título de Doutor em Ciências e Engenharia de Petróleo, na Área de Exploração.

Orientador: Prof. Dr. Marcelo Souza De Castro
Coorientador: Prof. Dr. Antonio Carlos Bannwart

Este exemplar corresponde a versão final da tese defendida pelo aluno Marcos Roberto Mendes Penteado, e orientado pelo Prof. Dr. Marcelo Souza de Castro e pelo Prof. Dr. Antonio Carlos Bannwart.

.....
Assinatura do Orientador

**CAMPINAS
2020**

Ficha catalográfica
Universidade Estadual de Campinas
Biblioteca da Área de Engenharia e Arquitetura
Luciana Pietrosanto Milla - CRB 8/8129

P387t Penteadó, Marcos Roberto Mendes, 1985-
Theoretical, experimental and numerical study of gas-liquid flow in an electric submersible pump impeller / Marcos Roberto Mendes Penteadó. – Campinas, SP : [s.n.], 2020.

Orientador: Marcelo Souza De Castro.
Coorientador: Antonio Carlos Bannwart.
Tese (doutorado) – Universidade Estadual de Campinas, Faculdade de Engenharia Mecânica.

1. Bomba centrífuga submersa. 2. Escoamento bifásico. I. Castro, Marcelo Souza De, 1986-. II. Bannwart, Antonio Carlos, 1955-. III. Universidade Estadual de Campinas. Faculdade de Engenharia Mecânica. IV. Título.

Informações para Biblioteca Digital

Título em outro idioma: Estudo teórico, experimental e numérico do escoamento gás-líquido em rotor de bombas centrífugas submersas

Palavras-chave em inglês:

Electric submersible pump

Two-phase flow

Área de concentração: Exploração

Titulação: Doutor em Ciências e Engenharia de Petróleo

Banca examinadora:

Marcelo Souza De Castro [Orientador]

Valdir Estevam

Geraldo Afonso Spinelli Martins Ribeiro

Rigoberto Eleazar Melgarejo Morales

Oscar Mauricio Hernandez Rodriguez

Data de defesa: 28-02-2020

Programa de Pós-Graduação: Ciências e Engenharia de Petróleo

Identificação e informações acadêmicas do(a) aluno(a)

- ORCID do autor: <https://orcid.org/0000-0002-0634-5064>

- Currículo Lattes do autor: <http://lattes.cnpq.br/8803280068315437>

**UNIVERSIDADE ESTADUAL DE CAMPINAS
FACULDADE DE ENGENHARIA MECÂNICA
E INSTITUTO DE GEOCIÊNCIAS**

TESE DE DOUTORADO ACADÊMICO

**THEORETICAL, EXPERIMENTAL AND NUMERICAL
STUDY OF GAS-LIQUID FLOW IN AN
ELECTRIC SUBMERSIBLE PUMP IMPELLER**

**ESTUDO TEÓRICO, EXPERIMENTAL E NUMÉRICO
DO ESCOAMENTO GÁS-LÍQUIDO EM ROTOR DE
BOMBAS CENTRÍFUGAS SUBMERSAS**

Autor: Marcos Roberto Mendes Penteadó

Orientador: Prof. Dr. Marcelo Souza de Castro

Coorientador: Prof. Dr. Antonio Carlos Bannwart

A Banca Examinadora composta pelos membros abaixo aprovou esta Tese:

Prof. Dr. Marcelo Souza De Castro, Presidente
DE/FEM/UNICAMP

Dr. Valdir Estevam
DE/FEM/UNICAMP

Dr. Geraldo Afonso Spinelli Martins Ribeiro
Petrobras S.A.

Prof. Dr. Rigoberto Eleazar Melgarejo Morales
UTFPR

Prof. Dr. Oscar Mauricio Hernandez Rodriguez
EESC-USP

A Ata de Defesa com as respectivas assinaturas dos membros encontra-se no SIGA/Sistema de Fluxo de Dissertação/Tese e na Secretaria do Programa da Unidade

Campinas, 28 de fevereiro de 2020.

Dedication

I dedicate this work to my parents, Claudio and Ines, who always encouraged me to grow. All my deepest gratitude in especial to my mother. I also dedicate to my brothers Rodrigo and Karin, who always accompanies me in the stages of life.

Acknowledgments

In the first place, I am very grateful to God, sovereign of all the learning that I am having. Thank you for my health and to provide the necessary tools for my development.

I would like to thank my parents, Inês and Claudio, for their support along this doctorate, for understanding the moments that I was absent, where I was dedicated to studies and, for always receiving affection and comprehension. Also, I would like to thank my brothers, Rodrigo and Karin, for providing support and excellent moments. My family grows, so thanks to my blessed nephews, Giovanna, Arthur and Manuela.

My thanks go out to Prof. Dr. Marcelo Souza de Castro for his guidance, patience, comprehension, and the friendship built throughout this Thesis. At the beginning he was my co-advisor, and along the path, he became my advisor.

Thanks to Prof. Dr. Antonio Carlos Bannwart for being my co-advisor and for his confidence in assigning me a job of this magnitude.

My sincere gratitude to M.Sc Saon Crispim Vieira for his collaboration. Thank you for your patience and for your numerous enlightening remarks. The discussions on the results were of great value. Thank you very much for sharing your knowledge.

I am also grateful to my friends for the richness of our coexistence, of the spent moments; for sure, every moment with each one were of great value. Gratitude for having you in my life, my appreciation is enormous because of it.

Many thanks to the professors of the School of Mechanical Engineering at UNI-CAMP, for their teachings. Also, I am grateful for the Oil Engineering division for the opportunity. Thanks to my colleagues of CEPETRO and ALFA Research group, for their support, friendship, and the great living environment.

I wish to thank UTFPR, Prof. Dr. Rigoberto E. M. Morales and the entire team of NUEM (Nucleus for Multiphase Flow). You were very receptive and helped me in the guidance through the numerical simulations.

I would like to acknowledge the support of PRH-ANP and Petrobras for the financial assistance.

*The important thing is to not stop
questioning. Curiosity has its own
reason for existing.*

Albert Einstein

RESUMO

O presente trabalho estudou características do escoamento bifásico ar-água no interior do rotor de uma bomba centrífuga submersa (BCS). Esse equipamento destina-se ao bombeio de líquidos e é instalado no interior de poços de petróleo, porém dificilmente o escoamento na sucção da bomba é monofásico de líquido. Com capacidade de produzir elevadas vazões, esse dispositivo pode apresentar instabilidades operacionais devido à presença de gás livre. Isso faz com que a BCS sofra uma degradação em termos de pressão e eficiência. Para o desenvolvimento do trabalho e melhor entendimento dessa fronteira instável, conhecida como “surging”, o protótipo de visualização projetado por Monte Verde (2017) foi usado nos experimentos com algumas melhorias quanto à iluminação e tratamento das imagens para capturar maiores detalhes do escoamento dentro do rotor. A iluminação foi melhorada com o objetivo de reduzir as sombras, uma vez que o ar e a água possuem uma aparência similar, o que dificulta sua visualização. Os experimentos foram realizados com vazão mássica de ar constante, variando a vazão de água. As imagens foram processadas em um código computacional desenvolvido pelo autor para capturar as principais características das bolhas de ar, como diâmetro e velocidade. As simulações numéricas dos escoamentos monofásico de água e bifásico ar-água no interior do rotor foram realizadas usando o software da ANSYS®. Elas foram comparadas com dados experimentais de diâmetros das bolhas e o valor do diferencial de pressão também foi correlacionado. Um modelo de fluxo de deslizamento bidimensional foi desenvolvido para o escoamento gás-líquido no rotor, analisando entre outros termos o fator de atrito da mistura gás-líquido e sua variação com o escoamento. Além disso, foram analisadas as forças interfaciais. Com isso foi possível calcular o coeficiente de arrasto da partícula com resultados comparáveis aos apresentados na literatura. Os dados experimentais foram utilizados para fechamento do modelo de fluxo de deslizamento proposto. A partir da modelagem e do balanço de forças nas bolhas foi possível criar um critério quantitativo para o início das condições de “surging” e “gas locking”.

Palavras-chave: Bombeio centrífugo submerso (BCS); Escoamento gás-líquido; CFD; Modelo de fluxo de deslizamento; critério de transição; surging; gas locking.

ABSTRACT

The present work studied air-water two-phase flow characteristics inside an electrical submersible pump impeller (ESP). This equipment is intended for the pumping of liquids and is installed inside oil wells. However the flow in the suction of the pump rarely is single-phase liquid. Having the capacity to produce high flow rates, this device can present operational instabilities due to the presence of free gas. This causes the ESP to suffer degradation in terms of pressure and efficiency. For the development of the work and a better understanding of this unstable phenomenon, known as “surging”, the visualization prototype designed by Monte Verde (2017) was used in the experiments with some improvements on the lighting and treatment of the images to capture greater details of the flow inside the impeller. The lighting was improved in order to reduce shadows, since the water / air interface has a very close coloring, which is difficult to detect. The experiments were carried out with constant air mass flow, varying the water flow. The images were processed by a computational code developed by the author to capture the main characteristics of air bubbles, such as diameter and velocity. The numerical simulations of the single and two-phase air-water flows inside the impeller were performed using the ANSYS® software. The numerical results were compared with experimental data on bubble diameters and the value of the experimental pressure drop was correlated. A two-dimensional drift-flux model was developed for the air-water flow in the impeller, analyzing, among other terms, the friction factor of the gas-liquid mixture and its variation with the flow. In addition, the interfacial forces as well. With this it was possible to calculate the particle drag coefficient with results comparable to those presented in the literature. The experimental data were used to give closure to the proposed drift-flux model. From the modeling and the balance of forces in the bubbles, it was possible to create a quantitative criterion for the starting point of the conditions of "surging" and "gas locking".

Keywords: Electric Submersible pump (ESP); Gas-liquid flow; CFD; Drift-Flux model; transition criterion; surging; gas locking.

List of Figures

1.1	Two main components of centrifugal pumps: impeller and diffuser (adapted from GÜLICH, 2008).	23
1.2	Impeller view. (adapted from VERDE <i>et al.</i> , 2017)	24
1.3	Onshore ESP installation: power cables, motor, seal protector and the ESP. (BARRIOS, 2007)	25
2.1	Schematic pump performance curves - Takacs (2009)	31
2.2	Velocity Triangle - White (2003)	33
2.3	Entrance vector	34
2.4	Flow patterns (Adapted from SHOHAM, 2005).	38
2.5	Slippage and liquid holdup - Adapted from Shoham (2005).	40
2.6	Dimensionless graph (SOLANO, 2009).	43
2.7	Two-phase flow with constant gas flow rate (BIAZUSSI, 2014)	45
2.8	(a) Bubbles in impeller, 1000 rpm (b) Side view (ESTEVAM, 2002)	47
2.9	Impeller patterns at 600 rpm: (a) Isolated Bubbles (b) Bubble Flow (c) Gas Pocket (d) Segregated Gas. (GAMBOA, 2009)	48
2.10	Impeller patterns: (a) Bubble Flow (b) Agglomerated Bubble Flow (c) Gas Pocket Flow (d) Segregated Flow. (MONTE VERDE, 2016)	50
2.11	Pump flow rate as a function of rotation speed in (a) and as a function of inlet gas volume fraction in (b) (SCHÄFER <i>et al.</i> , 2015)	51
2.12	Experimental data (ED) and numeric data (ND) from Amaral (2007) and Segala (2010).	53
2.13	Pump H-Q curve and its derivations according to Takacs (2009)	54
2.14	Schematic of LNG cryogenic submerged pump(HOU <i>et al.</i> , 2016)	56
2.15	Different fluid viscosities at 3500 rpm showing pressure head versus normalized flow rates (OFUCHI <i>et al.</i> , 2017)	57
2.16	H-Q curve for different viscosities (CHENG <i>et al.</i> , 2019).	58
2.17	Bubble forces (BIAZUSSI, 2014)	60
3.1	(a) Frame and ROI - (b) Cropped image.	64
3.2	Visualization Prototype - Adapted from Monte Verde (2016)	65
3.3	Experimental Apparatus Scheme	66
3.4	Graphical Interface of the Data Acquisition and Control Software	70

3.5	Experimental Apparatus during experiments: (a) Light + Camera - (b) Light source - (c) Camera	71
3.6	Example of a captured image of the impeller: (a) ROI - (b) Cropped image.	74
3.7	Image with: (a) No equalization - (b) Equalization	75
3.8	Morphological operations: (a) Centroids of the image - (b) Subtraction applied	76
3.9	(a) Original Image - (b) Laplacian lp_4 - (c) Laplacian lp_8	77
3.10	Constrast Improvement: (a) Original Image - (b) Laplacian filter applied.	78
3.11	Binarized image with values 0 (black) and 1 (white).	79
3.12	Bubble analysis: (a) Bubbles centroids (b) Bubbles' velocity vectors. . .	81
4.1	Impeller domain	83
4.2	Profile geometry - 1: Leading edge; 2: Max. thickness; 3: Camber; 4: Pressure side; 5: Trailing edge; 6: Camber mean-line; 7: Suction side. .	85
4.3	Blade characterization using trailing and leading edge	85
4.4	Impeller channel: (a) control volume - (b) dimensionless form	87
4.5	Blade coordinates	87
4.6	Non-inertial (x,y,z) and inertial (X,Y,Z) reference frame	90
4.7	Particle P along the impeller	92
4.8	Velocity vectors at the discharge	94
4.9	Velocity vectors at the discharge	94
4.10	Impeller domain	96
4.11	Impeller domain	101
4.12	Impeller channel approximation	106
4.13	C_H x C_Q	109
4.14	Moody diagram.	110
4.15	Friction factor: model x S.Vieira (2014)	111
4.16	$Fr_{TP,s}$ x Fr_m	118
4.17	$Fr_{TP,s}$ x Fr_m x α	119
5.1	Experiment images: (a) IM1 - (b) IM3 - (c) IM5 - (d) IM7 - (e) IM9 - (f) IM11.	123
5.2	Histograms of the experiments - 900 rpm and 0.025 kg/h gas mass flow rate.	125
5.3	Bubble trajectories in the impeller channel.	126

5.4	Following one bubble with 0.5 mm diameter through the impeller. . . .	127
5.5	Evolution of the measured gas void fraction α in the impeller channel with time.	128
5.6	Experimental point IM11.	132
5.7	Drag Coefficient, C_D x Reynolds Number, Re - Adapted from Haberman and Morton (1953).	135
5.8	Shape regimes for bubbles using: Eötvös Number E_o , Reynolds Number, Re and Morton number M (CLIFT <i>et al.</i> , 2005)	136
5.9	Force balance on a bubble inside the impeller channel.	139
5.10	Transition criteria	140
5.11	Transition criteria - Condition 1 (red line) and Condition 2 (blue line) . .	142
A.1	Prototype Components: (a) Solid components (CAD) (b) Simulation Domains.	160
A.2	Two-phase flow experimental data, which will be used to validate numerical simulations.	162
A.3	Control-volume definition. (ANSYS, 2017)	165
A.4	Diffuser: (a) Diffuser entrance; (b) Diffuser entrance mesh.	166
A.5	Subdivisions of the near-wall region (ANSYS, 2017).	169
A.6	Comparison between numerical and experimental (MONTE VERDE, 2016) using 600 to 1500 rpm - Pressure increment.	173
A.7	Comparison between numerical and experimental (MONTE VERDE, 2016) using 600 to 1500 rpm - Head H^* versus flow rate Q^*	174
A.8	Part-load condition single-phase simulations: velocity vector	175
A.9	Comparison of Experimental and simulated Pressure increment for two-phase air-water flow (900 rpm and $m_G = 0.012 \text{ kg/h}$).	183
A.10	Pressure and water velocity fields (900 rpm, IM6, $m_L = 3.428 \text{ m}^3/\text{h}$ e $m_G = 0.025 \text{ kg/h}$).	185
A.11	Bubble size and profile velocity (900 rpm, IM6, $m_L = 3.428 \text{ m}^3/\text{h}$ e $m_G = 0.025 \text{ kg/h}$).	185

A.12 Numerically data of 900 rpm, indicating circumferential and radial velocity from: (a) Water (b) Air(900 rpm, IM6, $m_L = 3.428 m^3/h$ e $m_G = 0.025 kg/h$).	186
A.13 Experimental and numerical data for IM1 in (a) and (b), and for IM3 in (c) and (d).	188
A.14 Experimental and numerical data for IM5 in (a) and (b), and for IM7 in (c) and (d).	190
A.15 Numerical x Experimental velocity - (a) Radial (b) Circumferential	191
E.1 Rectangle shape of the impeller channel.	239
F.1 256 points with Vogel's method.	243
F.2 Equal thickness versus equal areas concentric rings.	244
F.3 Effect of the angle step parameter, on 256 points.	245
F.4 Matlab code projection for LED's	246
F.5 (a) Front view - (b) Rear view	246
G.1 Impeller mesh.	247
G.2 Pressure increment x flow rate.	248
G.3 (a) Domain view - (b) Configuration of cyclic boundary condition with GGI.	249
G.4 GGI conection problem.	250

List of Tables

2.1	Dimensionless variables determined by the Buckingham π theorem for single phase flow, newtonian fluid with constant properties	35
2.2	Dimensionless variables. (SOLANO, 2009)	43
3.1	Geometrical specifications of ESP	63
3.2	Equipment used in the experimental apparatus	67
3.3	Measured variables	68
3.4	Instrumentation	69
5.1	Experimental data flow rate of gas Q_g and water Q_l	121
5.2	Impeller rotation ω , mass gas flow rate \dot{m} , diameter d , pressure increment ΔP , radial velocity v_r , circumferential velocity v_θ , standard deviation of radial velocity δv_r , standard deviation of δv_θ and gas void fraction α	129
5.3	Impeller rotation ω , mass gas flow rate \dot{m} , pressure increment ΔP , mixture volumetric flux in \hat{s} direction j_{ms} , bubble velocity v_2 and gas void fraction α	131
A.1	Dimensions of Prototype's Impeller and Diffusers	161
A.2	Numerical Simulation test matrix for single-phase water flow.	161
A.3	Numerical simulation test matrix for two-phase air-water flow.	163
A.4	Mesh, Number of elements ($Q_{BEP} = 3.2112 \text{ m}^3/h$)	171
A.5	Mesh sensitivity for ET and DE.	171
A.6	Timestep per blade passage	172
A.7	Numerical Simulation Results for Single-Phase Water Flow.	173
A.8	Pressure increment for single phase flow - 600 rpm.	177
A.9	Pressure increment for single phase flow - 900 rpm.	177
A.10	Pressure increment for single phase flow - 1200 rpm.	178
A.11	Pressure increment for single phase flow - 1500 rpm.	179
A.12	Summary of bubble force correlations	180
A.13	Groups of Diameters used in MUSIG.	181
A.14	Timestep per blade passage: part-load condition, IM7 - $m_2 = 3.088 \text{ m}^3/h$	182

A.15	mass gas flow rate \dot{m} , experimental pressure increment ΔP_{exp} , numerical pressure increment ΔP_{num} , Difference between pressure increment, radial velocity v_r , circumferential velocity v_θ , flow rate ratio Q/Q_{BEP} .	184
A.16	Pressure increment for two phase flow - $m_g = 0.025 \text{ kg/h}$	187
A.17	Pressure increment for two phase flow - $m_g = 0.0125 \text{ kg/h}$	187
A.18	Gas void fraction.	189
A.19	mass gas flow rate \dot{m} , experimental radial velocity $v_{r,exp}$, experimental circumferential velocity $v_{\theta,exp}$, standard deviation of radial velocity δv_r , standard deviation of δv_θ , numerical radial velocity $v_{r,num}$, numerical circumferential velocity $v_{\theta,num}$ Deviation v_r , Deviation Δv_θ	191
A.20	Impeller rotation ω , mass gas flow rate \dot{m} , experimental diameter d_{exp} , numerical diameter d_{num} , experimental and numerical difference in value and in %, flow rate ratio Q/Q_{BEP}	191
D.1	Impeller rotation ω , mass gas flow rate \dot{m} , rotational Reynolds Re_ω , two-phase mixture Reynolds Re , particle Reynolds Re_P	236
D.2	Pressure increment	238

List of Symbols

Lattin Letters

B_b	-	Bubble volume
C_B	-	Basset coefficient
C_D	-	Drag coefficient
C_V	-	Virtual mass coefficient for bubbles
d	-	diameter
\vec{F}	-	Sum of the force acting on the bubbles
\vec{F}_B	-	Basset force
\vec{F}_D	-	Drag force
\vec{F}_P	-	Pressure force
\vec{F}_V	-	Added mass force
\vec{g}	-	Gravitational acceleration
H	-	Head
H^*	-	Dimensionless Head
I	-	Impeller rotation between frames
\dot{m}_1	-	Liquid mass flow rate
\dot{m}_2	-	Gas mass flow rate
P	-	Pressure
ΔP	-	Pump pressure increment
Q_{BEP}	-	Liquid flow rates at the best efficiency point
Q	-	Flow rate
Q^*	-	Dimensionless Flow rate
r_i	-	Impeller channel intake radius
r_o	-	Impeller channel exit radius
r_b	-	Bubble radius
\vec{V}	-	Velocity vector in absolute frame of reference
\vec{v}	-	Relative velocity vector
W_{Euler}	-	Ideal power or Euler power

Greek Letters

- α - Actual gas void fraction
- β - Angle between relative flow velocity and circumferential direction
- θ - Tangential coordinate
- λ - Non-slip gas void fraction
- ρ - Density
- σ - Interfacial or surface tension.
- τ - Surface tension
- μ - Viscosity
- Ω - Rotational vector
- ω - Angular velocity
- $\Delta\rho$ - Density difference between phases

Acronyms

- BEP - Best Efficiency Point
- CCD - Charge-Coupled Device
- CEPETRO - Center for Petroleum Studies (Unicamp)
- CFD - Computational Fluid Dynamics
- DNS - Direct Numerical Simulation
- ESP - Electrical Submersible Pump
- FEM - Faculty of Mechanical Engineering
- IM - Data measured
- LED - Light-Emitting Diode
- NS - Navier-Stokes
- PIV - Particle Image Velocimetry
- RANS - Reynolds-Averaged Navier-Stokes equations
- ROI - Region Of Interest
- SST - Shear Stress Transport
- UNICAMP - University of Campinas

Subscripts

- 1 - Liquid phase
- 2 - Gas phase
- b - Bubble
- m - Mixture
- i* - Intake
- o* - Exit
- r,θ* - Polar coordinate system components
- s,n* - Blade coordinate system components
- BEP* - Best efficiency point
- exp* - Experimental
- num* - Numerical

Other Notations

- $\langle \rangle$ - Average

Contents

1	INTRODUCTION	23
1.1	Motivation	26
1.2	Objectives	27
1.3	Thesis' Outline	28
2	LITERATURE REVIEW	31
2.1	Basic concepts of pumps	31
2.1.1	Euler Equation for ESP	32
2.1.2	Dimensionless analysis for single phase flow	35
2.1.3	Two-phase Flow	37
2.2	Modeling studies of two-phase flow	40
2.3	Visualization studies	46
2.4	CFD studies	51
2.5	Force balance on bubble	57
3	EXPERIMENTAL DEVELOPMENT	63
3.1	ESP Prototype	63
3.1.1	Instrumentation	66
3.1.2	Visualization Equipment	68
3.1.3	Experimental Setup Validation	70
3.1.4	Experimental Procedure - Two-Phase Flow	70
3.1.5	Test Matrix - Two Phase Flow	72
3.2	Image Processing Software	72
3.2.1	Code development	73
3.2.2	Bubble Velocity, Displacement and Diameter Analysis	80
4	MODELING	83
4.1	Geometric Notation	83
4.1.1	Non-Inertial and Inertial Frames of Reference	90
4.1.2	Kinematics for Rotor Dynamics	93
4.2	Modeling Gas-Liquid Flow - Drift-Flux Model	95

4.2.1	Continuity Equation:	97
4.2.2	Momentum Equation:	103
4.2.3	Viscous Stress Tensor Modeling	105
4.2.4	Momentum Transfer Between Phases:	112
5	RESULTS	121
5.1	Experimental Results	121
5.1.1	Flow visualization	121
5.1.2	Bubbles Diameter	124
5.1.3	Bubbles' Trajectories and Velocities	125
5.1.4	Gas Void Fraction	127
5.2	Experimental and Modeling Comparison	129
5.3	Modeling Results	132
5.3.1	Distribution Parameter - C_0	132
5.3.2	Analysis of forces acting on bubbles	134
5.4	Transition Criteria for Surging and Gas Locking	137
5.4.1	Criteria Conditions	138
	Condition 1	139
	Condition 2	141
6	CONCLUSIONS AND RECOMMENDATIONS FOR FUTURE WORK	143
6.1	Conclusions	143
6.2	Recommendations for Future Work	145
	REFERENCES	148
	APPENDICES	159
A	– NUMERICAL SIMULATION	159
A.1	Computational Procedure	159
A.1.1	Test Matrix - Single-Phase Water Flow	160
A.1.2	Test Matrix - Two-Phase Air-Water Flow	161
A.2	CFD Simulations	162
A.2.1	Creating the mesh	163

A.2.2	Numerical Discretization	164
A.2.3	Domains and Interfaces	165
A.2.4	Boundary Conditions	167
A.3	Single-phase Water Flow CFD Simulation	167
A.3.1	Governing Equations	167
	Conservation of mass	168
	Conservation of momentum	168
	Source terms	168
A.3.2	Turbulence Model	169
A.3.3	Mesh Sensitivity Test	170
A.3.4	Time step study	172
A.3.5	Simulation Results for Single-Phase Flow	172
A.3.6	Mean results for single-phase flow	176
A.4	Two-Phase Flow CFD Simulation	176
A.4.1	Governing equations - Two-phase air-water flow	178
	Conservation of mass	179
	Conservation of momentum	179
	Interphase momentum terms	180
	Boundary conditions	181
A.4.2	Time step study	182
A.4.3	Simulation Results for Two-Phase Flow	182
A.4.4	Mean results for two-phase gas-liquid flow	186
A.4.5	Gas void fraction results	188
B	– Bubble force correlations	192
B.1	Interphase Drag	192
B.2	Virtual Mass Force	193
B.3	Lift Force	194
B.4	Wall lubrication Force	195
B.5	Turbulent Dispersion Force	195
C	– Math extension	197
C.1	Radial Pressure Gradient	197

C.2	Viscous Stress Tensor Modeling	200
C.3	Radial and viscous term	205
C.4	Momentum Transfer Between Phases	207
C.4.1	Development of Interfacial Terms	213
C.5	Development of Bubble Forces	218
C.5.1	Drag force	218
C.5.2	Basset and Virtual/Added Mass Force	219
C.5.3	Centripetal and Coriolis Forces	221
C.5.4	Buoyancy Force	223
C.6	Development of Transition Criteria	227
C.6.1	Condition 1	228
C.6.2	Condition 2	231
D	– Dimensionless Groups and Diffuser Pressure Gradient Analysis	234
D.1	Dimensionless Groups	234
D.1.1	Scaling	235
D.2	Diffuser Pressure Gradient	237
E	– Friction Factor Comparison	239
E.1	Reynolds number	240
E.2	Friction factor for circular, straight and stationary tubes	240
E.3	Effects in friction factor	240
E.3.1	Friction factor due to rectangular cross-section	240
E.3.2	Friction factor due to channel curvature	241
E.3.3	Friction factor due to pump rotation	242
E.4	Friction factor for the ESP impeller channel	242
F	– Spreading Illumination Efficiently	243
G	– OpenFOAM Numerical Simulations	247

1 INTRODUCTION

Artificial lift systems are required by the oil industry when the bottom-hole pressure is not sufficient to bring the fluids to the surface. One reliable artificial lift method used in many cases is the Electric Submersible Pumps (ESP), which is capable of producing higher flow rates comparing to other artificial lift options. The ESPs adds energy to the fluid in the wellbores so it can be brought to the surface. The performance of ESPs gives good efficiency as it works pumping higher flow rates, preferentially in wellbores that has low gas/oil ratio. Besides, these pumps are capable of working with heavy viscosity fluids (higher API - *American Petroleum Institute*).

Centrifugal pumps have two main components which are: the impeller and the diffuser. The impellers are rotating components where the fluids join in the central part flowing towards the periphery. In this process, it undergoes an increase in kinetic energy. The flow reaches the diffuser with an increased initial velocity, which is converted into pressure energy. ESPs have multiple stages, thus many sequences of impellers/diffusers are presented. The two main components are shown in Figure 1.1.

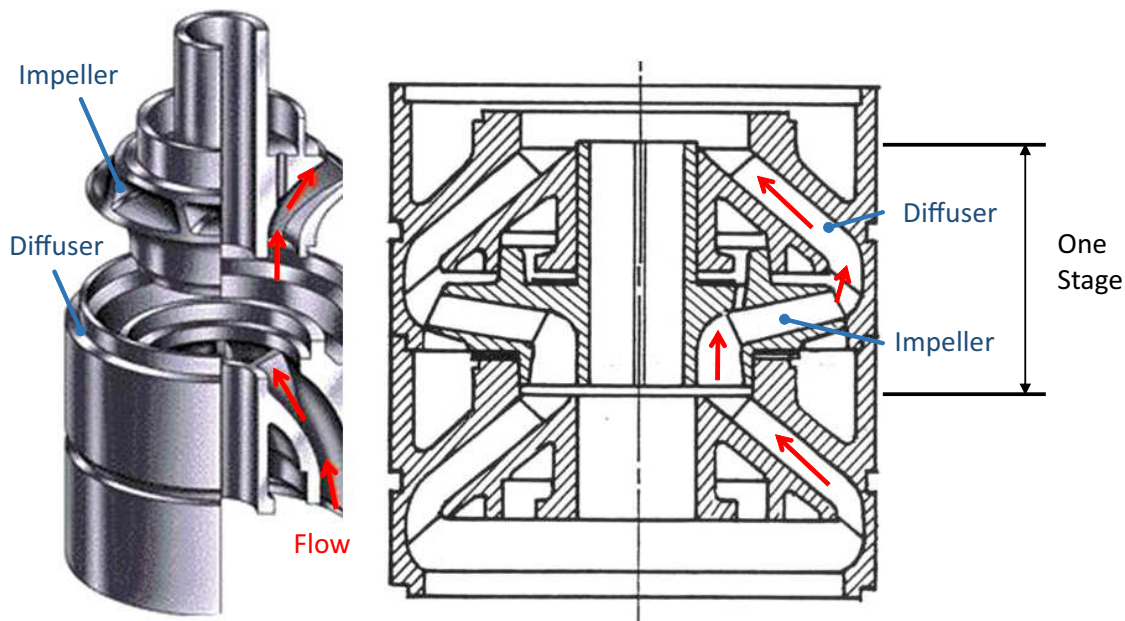


Figure 1.1: Two main components of centrifugal pumps: impeller and diffuser (adapted from GÜLICH, 2008).

A view of an impeller is shown in Fig. 1.2. This figure shows the impeller chan-

nels, impeller blades, blade pressure side, and blade suction side.

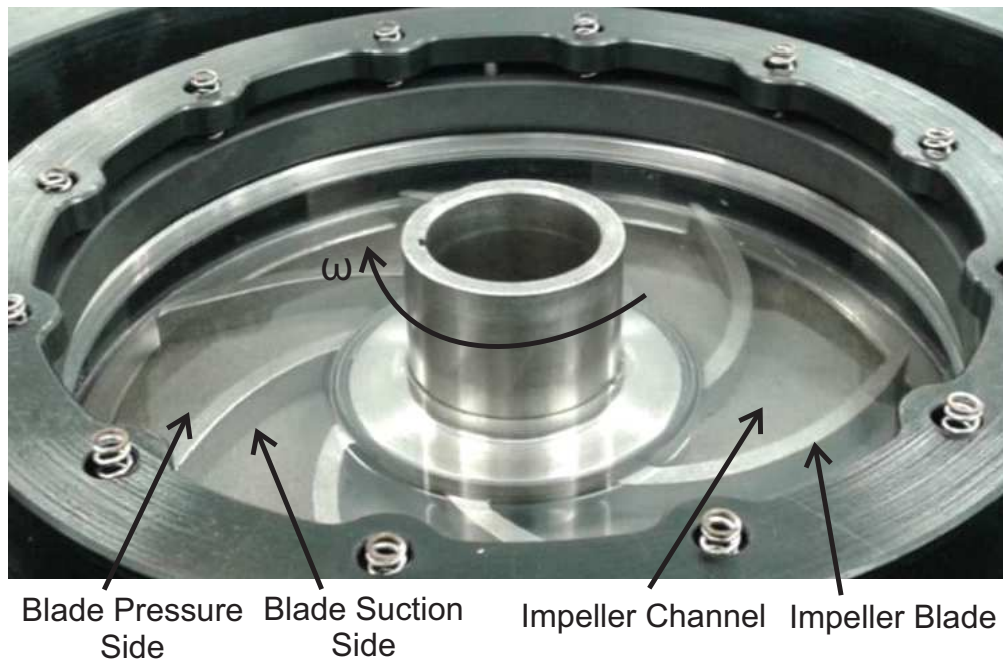


Figure 1.2: Impeller view. (adapted from VERDE *et al.*, 2017)

Figure 1.3 shows an overview of an ESP installed in an onshore oil well. The ESP is driven by an electric motor, installed in the well served by power cables. The rotational speed is controlled by a variable frequency driver (VFD). The motor is connected to the protective seal. For cooling reasons, the engine works immersed in the produced fluid.

The performance of an ESP operating with a single-phase liquid depends, among other factors, on the geometry and surface roughness of its internal walls, fluid properties (density and viscosity) and operating conditions (rotation and flow rate). However, in an actual oil production scenario these pumps rarely work with single-phase flow only. If the pressure at any point of the flow is less than the bubble point of the fluid, free gas is present. In oil well production, for instance, the pressure decreases continuously as the fluid flows upwards along the wellbore. At some point, the pressure reaches the bubble point pressure. So, it is common that free gas is pumped with liquid in this kind of operation.

Under two-phase flow conditions, the pump loses its capacity to generate the same amount of head increment, as occurs for single-phase flow, losing performance. Thus it is known as head degradation. The multiphase flow not only causes problems in pump-

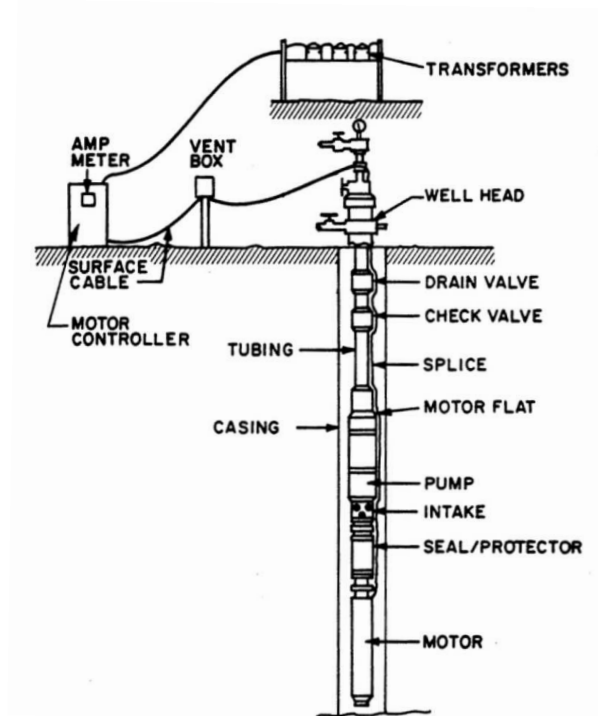


Figure 1.3: Onshore ESP installation: power cables, motor, seal protector and the ESP. (BARRIOS, 2007)

ing applications in the oil production scenario, but also in nuclear reactors, chemical industry applications, among others. The pump performance curves show a change in the sign of the derivative of the head with respect to the flow rate, reducing at a certain point of operation. This change is an unstable behavior of the system, and it is referred to as a surging condition. As more gas accumulates in the system, particularly inside the pump, it tends to result in the gas locking process, a condition in which the pump loses all its head capacity.

The first attempts to design an ESP to operate with gas-liquid flow relied on the assumption that the pump curves can be determined from the single-phase liquid performance, only replacing the liquid flow rate and liquid density by the multiphase mixture flow rate and mixture density, respectively. This kind of approach is the homogeneous model. This model did not account for head degradation, and only small gas fractions and high liquid flow rates (GAMBOA, 2009).

Therefore, there is a requirement for the development of adequate tools capable

of correctly predicting the two-phase flow performance of ESPs, and also the surging and the gas locking events.

1.1 Motivation

Centrifugal pumps are equipment used in wastewater treatment, food production, agriculture, heating installations in the oil industry, among others. This kind of pump has important advantages, such as high operational efficiency and reliability. They are commonly designed for single-phase flow only. However, in some situations, gas is pumped together with the liquid, thus decreasing its efficiency. Moreover, this mixture might damage the pump. The varying mixture density may cause vibrations that lead fatigue in bearings or other components. Thus, it is important for engineers to understand the mechanisms that induce damage.

For multiphase fluids in pipelines or in centrifugal pumps, different flow patterns were established (ESTEVAM, 2002, GAMBOA, 2009, VERDE *et al.*, 2017). Several researchers claim that the surging point and discontinuities in the performance curves of the pumps are associated with changes in the flow pattern and the accumulation of gas in the impeller channels. At liquid flow rates near surging conditions there are fluctuations in the pressure signals, followed by fluctuations on the shaft torque, and the electric motor current. These instabilities reduce the average time until equipment failure, which causes production losses and increases costs as interventions need to be made.

The techniques used experimentally to investigate this phenomenon usually need investment, which is realized under pump operations conditions, so this can be costly. It happens because this equipment operates under high pressure, and gaining access to understand the flow inside an impeller is not an easy task. Thus can be the reason to explain that only a small amount of experimental data exists so far to describe the phenomenon. However, Computational Fluid Dynamics (CFD) techniques can be used to reproduce the pump operation. For single-phase flow this process is easier than for two-phase flow. Two-phase flow simulations are still difficult due to the complexity of the flow (BARRIOS, 2007, FENG *et al.*, 2010, STEL *et al.*, 2015), and again, the lack of suitable validated data and benchmark experiments.

The data obtained by experimental and numerical analysis should be enough to improve the current models in the literature. Mechanistic modeling considers that each

flow regime corresponds to a set of specific governing equations for flow characteristics, such as bubble size (r_b), in-situ gas void fraction (α), and slippage velocity (v_s) between gas and liquid phases. Considering the flow pattern prevailing inside the impeller channel, the governing equations based on mass and momentum conservations can be simplified, although empirical correlations are much easier to implement compared to mechanistic models.

The correct understanding of flow phenomena inside an impeller is very important and can lead to increased production, improved efficiency, and greater safety. Nowadays, many studies have dealt with the idea of increasing the efficiency of this equipment, and also, many works are devoted to understanding surging and gas lock events.

This work is meant to analyze the air-water two-phase flow inside the impeller of an ESP through visualization experiments and numerical CFD simulations. Then, the drift-flux model and an analysis on the force balances in bubbles will be used to predict surging and gas locking points.

1.2 Objectives

The main objective of this work is the development of a drift-flux model for the air-water two-phase flow inside the impeller of an ESP. The basic concept of the drift-flux model is to consider the mixture as a whole, rather than as two phases separately. The drift-flux model considers the slippage between phases, and its formulation is simpler than the two-fluid model, which can make it very useful in many engineering applications, such as ESP. However, some closure relations, as bubble velocities and pressure fields, are necessary for the model.

The objective of a predictive method is to determine, for a specific set of operational conditions, how the pump would work under a two-phase flow condition. To achieve the objective, a set of tools will be used, such as image treatment and computational fluid dynamics (CFD).

The numerical approach begins with single-phase data from Verde *et al.* (2017). After that, tests with gas-liquid flow were performed in order to get more details on the fluids behavior inside the ESP's impeller, especially when the gas flow rate increase which may provoke instabilities in the pump operation, such as surging and gas locking. In summary, the specific objectives of this work are:

- Experimentally determine the bubble velocity inside the impeller under different operational conditions;
- replicate the experimental data from Verde *et al.* (2017) using CFD and also replicate data collected for two-phase flow;
- develop a drift-flux model for a log spiral radial impeller channel;
- develop a transition criterion for the two-phase flow inside the impeller which might be used for the ESP operation analysis.

1.3 Thesis' Outline

This work comprehends the following chapters:

- Chapter 2 presents the a literature review on the basic concepts of the pumps, the modeling studies for two-phase flow, visualization studies in centrifugal pumps, followed by CFD studies, and then is concluded with works related to the forces acting on bubbles.
- Chapter 3 presents a description of the experimental facility, the prototype used to visualize the flow as well as the test matrix. After that, the post-processing of the images is done, and the experimental results are shown.
- Chapter 4 presents the modeling, the blade coordinate system, the slip velocity, interfacial moments, and discussion of bubble dynamics. Dimensionless coefficients and the drift flux model are presented in this chapter.
- Chapter 5 presents the results of the image post-processing in the chapter 3 and a discussion about the drift-flux model. Moreover the variables acquired by the model were discussed comparing with the literature, such as the distribution parameter.
- Chapter 6 presents the conclusion and recommendations for future works.
- Reference list.
- The appendices have a detailed description of numerical simulations. The computational procedure, the creation of the mesh, domains, boundary conditions, single and two-phase simulations are topics discussed in appendix. Besides, dimensionless groups, and details about friction factors are also presented. Also, the

spreading of efficient illumination is explained and, finally, a brief description of the OpenFOAM simulations is given.

2 LITERATURE REVIEW

This literature review is separated into five sections. The first part describes the basic concepts of pumps. The next three sections review experiments, numerical and modeling aspects of two-phase flow in pumps. Finally, there is a section for force balance on bubbles. Some works presented here have both approaches, experimental and numerical, but they were separated by a subjective criterion made by the author.

2.1 Basic concepts of pumps

The centrifugal pump's energy efficiency can be calculated from the brake horsepower required to drive the pump and the hydraulic power spent on liquid transfer, by dividing the useful (hydraulic) power by the brake horsepower. Plotting in function of the liquid rate, the pump efficiency curve follows the shape of the hydraulic power, as shown in Fig. 2.1.

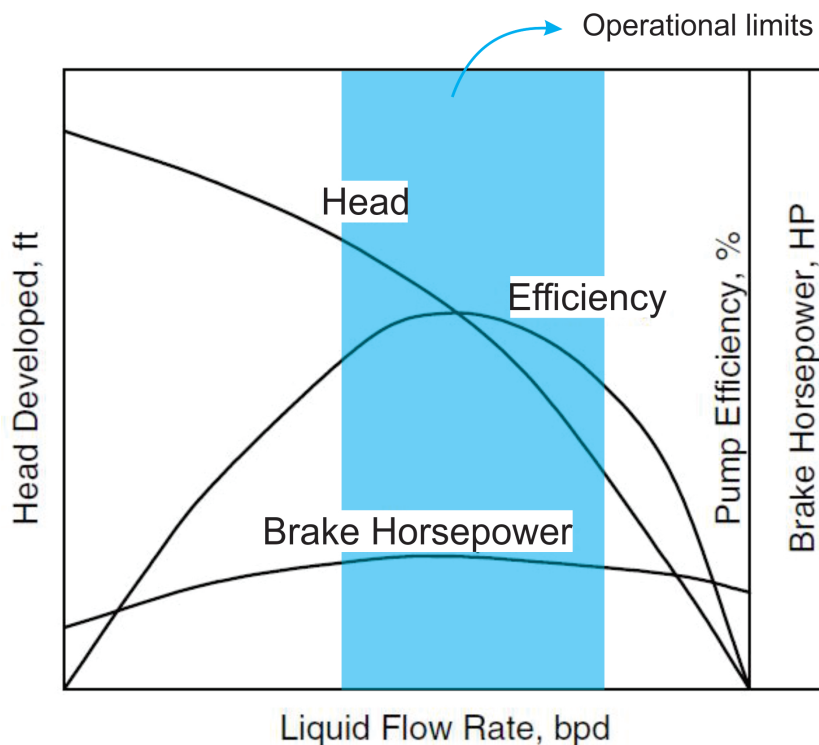


Figure 2.1: Schematic pump performance curves - Takacs (2009)

The ESPs are tested by running them with water at constant rotational speed while varying the pumping rate by throttling the flow at the pump discharge. The following parameters are measured during the tests: flow rate, suction and discharge pressures and, the brake horsepower required to drive the pump. Usually, the pump performance curves are supplied by manufacturers of submersible equipment. They provide the curves following the recommendation of RP 11S2 of the American Petroleum Institute (API, 1997). The catalog curves show the following notable points of operation:

- Shut-in: The flow rate is zero and the pressure increment is maximum.
- Best Efficiency Point (BEP): This is the point of best efficiency of the pump, as implied in the name.
- Open-flow: The pump head is zero. If the flow rate is higher than the point "open-flow" it means that hydraulic energy is lost.

Flow rates excessively below or above the pump's operational limits, which was indicated by the region in blue in Fig. 2.1, may cause cases of down-thrust or up-thrust. These conditions are associated with unstable axial forces at the impellers and might cause exaggerated friction between moving and stationary parts of the pump.

2.1.1 Euler Equation for ESP

In order to describe the movement of the fluids inside the impeller channels a velocity triangle is used. It can be used at any point of the flow passing through the impeller. However in the present work, the focus are on the triangles at the inlet and outlet of the channel (STEPANOFF, 1957).

Figure 2.2 shows the velocity triangles for turbomachinery. The triangles at the impeller inlet and outlet are the bases to formulate a relation known as "Euler equations" which calculates the head and flow rates of the pump. These equations do not consider losses during the energy transfer between the impeller and flow. The expressions correspond to *Navier-Stokes* equations when the dissipative terms are neglected

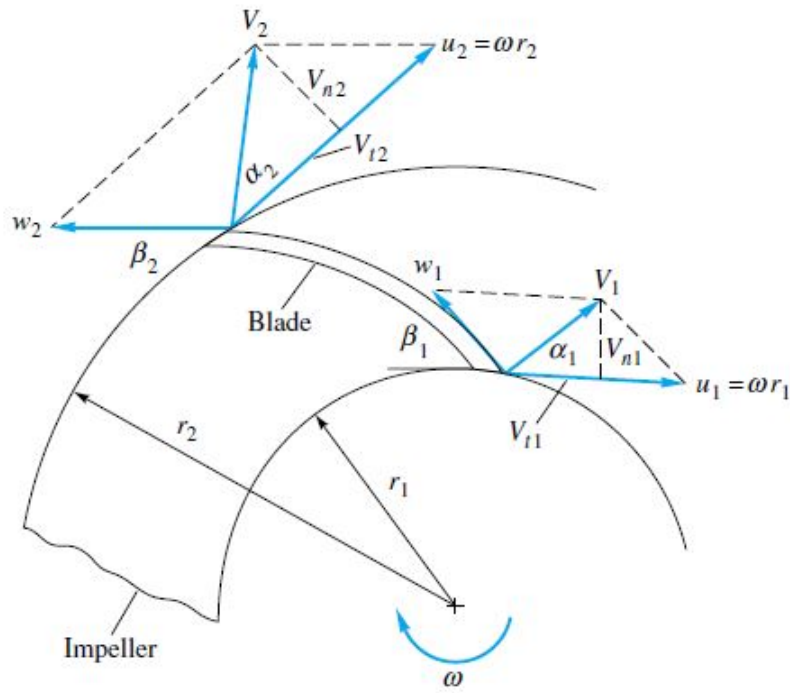


Figure 2.2: Velocity Triangle - White (2003)

and the convective terms remains.

$$W_{Euler} = \omega T = \rho Q(u_2 V_{t2} - u_1 V_{t1}) \quad (2.1)$$

$$H = \frac{P}{\rho g Q} = \frac{1}{g}(u_2 V_{t2} - u_1 V_{t1}) \quad (2.2)$$

The Euler turbomachine equations (Eqs. 2.1 and 2.2) neglect the viscous effects, showing that torque, T , power delivered to the fluid, W_{Euler} , and ideal head, H , are only functions of the tangential velocities u_1 and u_2 . Where in the Fig. 2.2, w ω is the rotational speed, and V is the absolute velocity, where the subscript t represents the tangential component of this vector and the subscript n is the normal component, as represented in Fig 2.2. The variable P indicates the static pressure in Equation 2.2.

Supposing steady state, following a streamline, without heat transfer and considering frictionless and incompressible flow, Bernoulli equations were obtained for turbo-

machinery (White (2003), Fox *et al.* (1998)).

$$\frac{P}{\rho g} + z + \frac{w^2}{2g} - \frac{r^2\omega^2}{2g} = \text{const} \quad (2.3)$$

For a centrifugal pump, the power delivered to the fluid can be related to the radial velocity $V_n = V_t \tan \alpha$, so:

$$W_{Euler} = \rho Q (u_2 V_{n2} \cot \alpha_2 - u_1 V_{n1} \cot \alpha_1) \quad (2.4)$$

V_{n2} and V_{n1} are given by:

$$V_{n2} = \frac{Q}{2\pi r_2 b_2} \quad V_{n1} = \frac{Q}{2\pi r_1 b_1} \quad (2.5)$$

where b_1 and b_2 represent the blade width at the inlet and outlet, respectively. The flow rate Q is estimated assuming that it enters in the normal direction of the impeller entrance surface, which means:

$$\alpha_1 = 90^\circ \quad V_{n1} = V_1 \quad (2.6)$$

Figure 2.3 relates to the direction of the velocity vector at the impeller entrance surface. The best condition for the flow direction arriving at the impeller entrance is without pre-whirl, pointing to the middle of the impeller channel, so minimizing the shock losses.

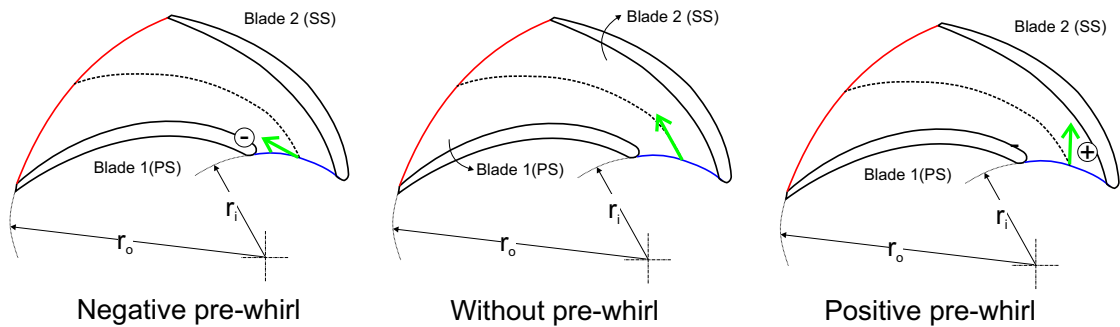


Figure 2.3: Entrance vector

2.1.2 Dimensionless analysis for single phase flow

The independent variables that represents the centrifugal pumping, for a single phase flow of a newtonian fluid with constant properties are: H , the pump head, W_{shaft} , the brake horsepower, Q , the flow rate, D , the pump diameter, μ , the fluid viscosity, ω , the pump rotation, ρ , the density of the fluid and ϵ , the surface roughness (WHITE, 2003). There is a certain freedom to choose the independent variables, for example, to represent the effective gain of the pump one can choose the pressure increment ΔP instead of H . Applying the Buckingham π theorem for centrifugal pumping with single phase flow, using D , ω and ρ as the primary variables, the following dimensionless groups were obtained and are presented in Table 2.1 (Eq. 2.7 to 2.11):

Table 2.1: Dimensionless variables determined by the Buckingham π theorem for single phase flow, newtonian fluid with constant properties

Dimensionless	Equation
Head Coefficient, C_H	$\Pi_1 = C_H = \frac{gH}{\omega^2 D^2}$ (2.7)
Flow Coefficient, C_Q	$\Pi_2 = C_Q = \frac{Q}{\omega D^3} \left(\frac{3600}{\omega} \right)$ (2.8)
Viscosity Coefficient, χ	$\Pi_3 = \chi = \frac{\mu}{\rho \omega D^2}$ (2.9)
Relative roughness	$\Pi_4 = \frac{\epsilon}{D}$ (2.10)
Power Coefficient, C_P	$\Pi_5 = C_P = \frac{W_{shaft}}{\rho \omega^3 D^5}$ (2.11)

The dimensionless coefficients are the base of similarity analysis in centrifugal pumping. Considering applications where viscous effects are negligible, the flow coefficient is treated like an independent parameter. On the other hand, the pump and power coefficients are like dependent parameters (BIAZUSSI, 2014). So $C_H = f(C_Q)$ and

$C_P = f(C_Q)$. Under this hypothesis, the following equalities can be obtained:

$$C_{Q1} = C_{Q2} \rightarrow \left(\frac{Q}{\omega D^3} \right)_1 = \left(\frac{Q}{\omega D^3} \right)_2 \quad (2.12)$$

$$C_{H1} = C_{H2} \rightarrow \left(\frac{g H}{\omega^2 D^2} \right)_1 = \left(\frac{g H}{\omega^2 D^2} \right)_2 \quad (2.13)$$

$$C_{P1} = C_{P2} \rightarrow \left(\frac{W_{shaft}}{\rho \omega^3 D^5} \right)_1 = \left(\frac{W_{shaft}}{\rho \omega^3 D^5} \right)_2 \quad (2.14)$$

Eqs. 2.12 to 2.14 are useful to test a project with models and then transpose the results to another scale. Generally, the Reynolds number express the rate between inertial and viscous forces. The inverse dimensionless number represented by χ is the viscosity coefficient which corresponds to the inverse of the centrifugal Reynolds number (Eq. 2.9). The hydraulic efficiency is defined as:

$$\eta = \frac{W_{hydr}}{W_{shaft}} = \frac{\rho Q g H}{W_{shaft}} = \frac{\rho (C_Q \omega D^3)(C_H \omega^2 D^2)}{\rho C_P \omega^3 D^5} = \frac{C_Q C_H}{C_P} \quad (2.15)$$

The classification of pumps follows that developed by Stepanoff (1957), that uses the specific speed, a non dimensional parameter which classifies taking into account pump type and size. The specific speed, η_s , is calculated at the best efficiency point, as:

$$\eta_s = \frac{Q_{BEP}^{0.5} \omega}{H_{BEP}^{0.75} g^{0.75}} \quad (2.16)$$

where ω is the rotational speed (in rad/s), Q_{BEP} is the pump capacity at the best efficiency pump in m^3/s , g is the acceleration of the the gravity in m^2/s and H_{BEP} is the pump head at the best efficiency point in m . However, another simplified equation for the specific speed, N_s , is also used by ESP manufacturers, even it not been dimensionless, which was defined as:

$$N_s = \frac{\omega Q_{BEP}^{0.5}}{H_{BEP}^{0.75}} \quad (2.17)$$

where the rotational speed ω is in rpm, the pump capacity at the best efficiency point, q_{BEP} , is in gpm , and the pump head at the best efficiency point, H_{BEP} , is expressed in ft . The specific speed ins a parameter characteristic of the impeller geometry. Relating

these coefficients in Eq. 2.17, the specific velocity becomes:

$$N_s = \frac{C_Q^{0.5}}{C_H^{0.75}} = \frac{\omega Q_{BEP}^{0.5}}{(g H_{BEP})^{0.75}} \quad (2.18)$$

The specific velocity is an important parameter in the study of centrifugal pumps. This variable is defined at the point of best efficiency (BEP) and it is useful in the selection and use of the equipment. Radial impellers have lesser values than axial impellers and, intermediate impellers present values between these two conditions.

Further, the selection is aided using another dimensionless variable, which is related to the pump rotation, flow rate and head, but not the diameter. This is achieved by eliminating the diameter of the ratio between head and flow rate, as showed by Eq. 2.18. Physically, the specific velocity is interpreted as the necessary rotation to produce a certain pump head at a certain flow rate at the BEP.

2.1.3 Two-phase Flow

In two-phase flow, the mixture of fluids can be distributed in several spatial configurations called flow patterns. In this work, the focus will be the bubbly flow in an ESP impeller channel. Figure 2.4 shows the bubbly flow patterns present in vertical and horizontal pipes (SHOHAM, 2005). Typical characteristics of this gas-liquid flow are deformable interfaces of bubbles and complex interactions between the interfaces.

The flow patterns in an ESP will be discussed in section 2.3. The terminology used for two-phase flow was proposed by Shoham (2005) and is presented next.

- a. Mixture Mass Flow Rate (\dot{m}_m): is defined as the sum of mass flow rate of the phases, expressed as:

$$\dot{m}_m = \dot{m}_l + \dot{m}_g \quad (2.19)$$

where \dot{m}_l and \dot{m}_g are the mass flow rates of liquid and gas, respectively. Volumetric flow rates can be related to the mass flow rates using the density of each phase using the expressions:

$$q_l = \frac{\dot{m}_l}{\rho_l} \quad \text{and} \quad q_g = \frac{\dot{m}_g}{\rho_g} \quad (2.20)$$

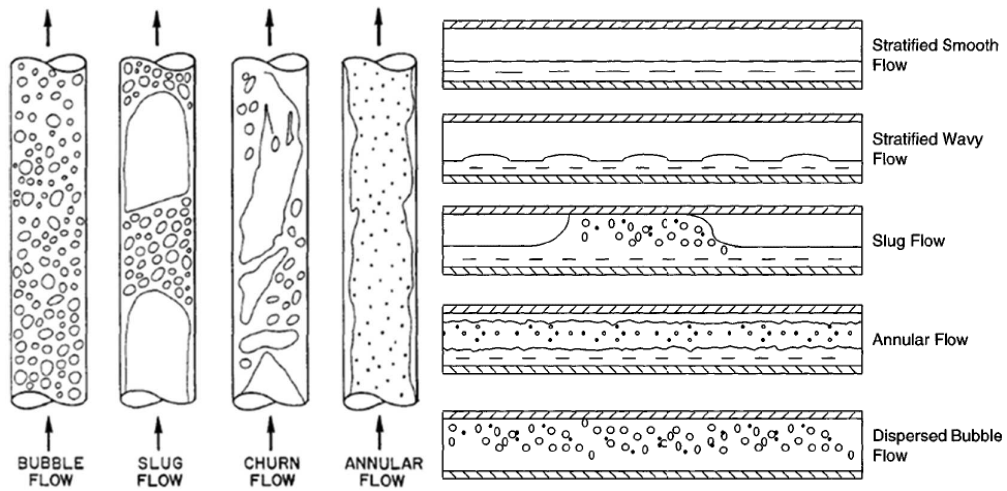


Figure 2.4: Flow patterns (Adapted from SHOHAM, 2005).

where q_l and q_g are the volumetric flow rate for liquid and gas, respectively, and ρ_l and ρ_g are the specific mass for liquid and gas. The subscripts l and g can also be represented by numbers: 1 for liquid and 2 for gas.

- b. Superficial Velocities (j_l and j_g): They are defined as the volumetric flux of the phase, representing the volumetric flow rate divided by the cross-sectional area, A_P . These are the velocities of the phases if a phase flows alone in the pipe/channel.

$$j_l = \frac{q_l}{A_P} \quad \text{and} \quad j_g = \frac{q_g}{A_P} \quad (2.21)$$

- c. Mixture Velocity (j_m): It is the sum of the superficial velocities of both phases divided by the cross-sectional area, and it is given by:

$$j_m = \frac{q_l + q_g}{A_P} = j_l + j_g \quad (2.22)$$

- d. Gas Void Fraction (α): It is a local quantity of the gas volume fraction, i.e., it is the fraction of the volume element occupied by the gas-phase. This variable is a statistical property of the flow and continuously changes with time. The gas void fraction is a local quantity determined from the local velocity of the phase.

$$\alpha = \alpha_g = \frac{A_g}{A_P} \quad (2.23)$$

where A_g is the area occupied by the gas. Similarly, for the liquid it becomes:

$$\alpha_l = \frac{A_l}{A_P} \quad (2.24)$$

Considering a two-phase flow of liquid and gas, the sum of both void fractions must be equal to 1.

$$1 = \alpha_l + \alpha_g \quad \rightarrow \quad \alpha_g = 1 - \alpha_l \quad (2.25)$$

The velocities can be written as a function of the gas void fraction:

$$v_l = \frac{j_l}{\alpha_l} \quad \text{and} \quad v_g = \frac{j_g}{\alpha_g} \quad (2.26)$$

These velocities v_k are higher than the superficial velocities j_k of the phases.

- e. Liquid Holdup (H_L): Similarly to the gas void fraction, the liquid holdup is the fraction of a volume element in a two-phase flow field occupied by the liquid-phase.
- f. Phase Slip (v_s) or relative velocity: This is the difference between local phases velocities.

$$v_s = v_g - v_l \quad (2.27)$$

where v_g and v_l are the local velocities of the gas and of the water, respectively. A schematic description of the slippage is shown in Fig. 2.5 (for illustration purposes only). The concept of the liquid holdup is introduced here, where it represents the slippage as being equal to zero, meaning that the gas phase travels at the same velocity as the liquid phase ($v_g = v_l$). However, in real situations, the gas and the liquid phases do not travel at the same velocity. Under this condition, Fig. 2.5 shows that the gas phase moves faster than the liquid phase due to buoyancy and lower frictional forces. Considering continuity, Fig. 2.5 (b) shows that the gas phase is faster than the liquid phase and the cross-sectional area of the gas phase reduces while the cross-sectional area of the liquid phase increases.

The result is an accumulation of liquid in the pipe and the in-situ liquid holdup becoming larger than the no-slip liquid holdup. This phenomenon does not happen in the entry region, contrary to what might have been implied from Fig. 2.5(b). Another example of this condition is the flow in vertical pipes. Under this

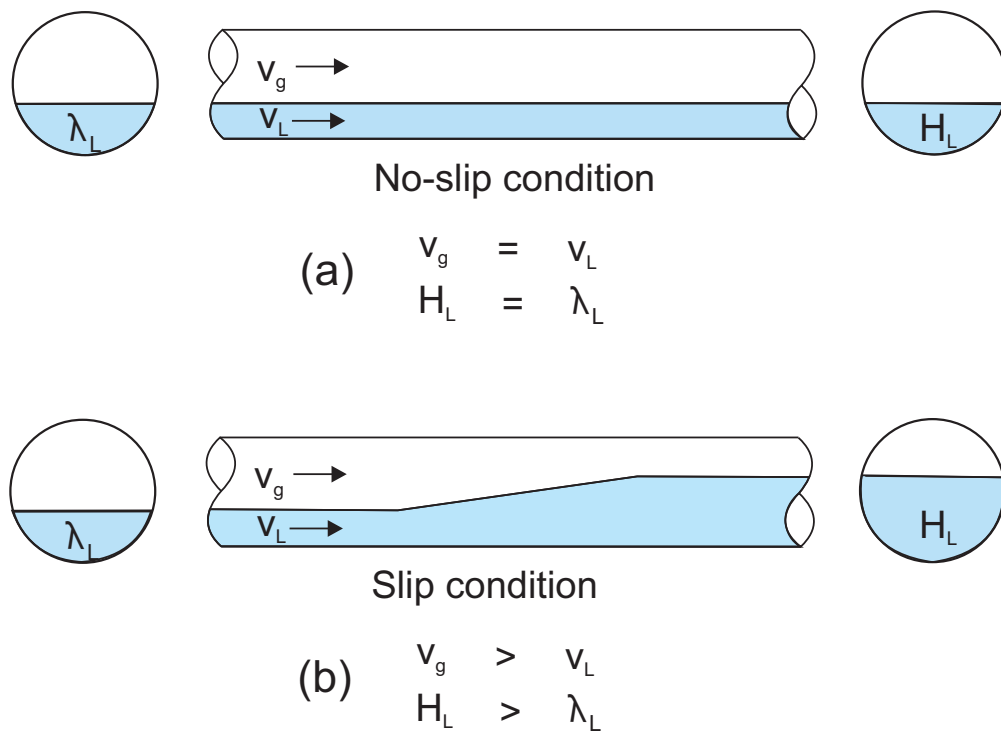


Figure 2.5: Slippage and liquid holdup - Adapted from Shoham (2005).

situation, because of buoyancy, the gas phase moves faster than the liquid phase, resulting again in a higher liquid holdup than no-slip liquid holdup (SHOHAM, 2005).

- g. Volumetric Gas Fraction (λ): This is the ratio between the gas flow rate and the total flow rate. This variable is associated with the no-slip gas void fraction, which considers that v_s equals to zero.

$$\lambda = \frac{q_g}{q_g + q_l} \quad (2.28)$$

2.2 Modeling studies of two-phase flow

The first modeling studies developed for two-phase flow in centrifugal pumps were developed by Murakami and Minemura (1974a) and Murakami and Minemura (1974b). They investigated the equipment performance operating with gas. After this, the first dimensional models were proposed, assuming dispersed bubbly flow

through all the impeller channel, that did not explain the surging phenomenon satisfactorily.

Some analytical models are available in the literature for the prediction of head degradation from low to high void fractions for the nuclear industry, such as Mikielwicz *et al.* (1978) and Wilson *et al.* (1979). These models used a semi-empirical approach, obtaining correlations from single-phase and two-phase flows from experimental data.

Mikielwicz *et al.* (1978) used the simple theory of idealized pump operation and incorporated experimental data from single-phase and two-phase flow. In order to express the change of work done by the fluid, Mikielwicz *et al.* (1978) used Euler Equations, which combines Newton's second law and the first law of thermodynamics, thus obtaining an equation where the ratio of the two phase flow losses to those in single phase flow is a function of: void fraction (α), liquid flow rates at the BEP (q_{BEP}), mixture flow rate (q_M) and the pump geometry. Wilson *et al.* (1979) used the same principles developed by Mikielwicz *et al.* (1978), which means that the simple theory of idealized pump operation was used and incorporates experimental data for single and two-phase flow in order to obtain correlations.

The literature has other models based on the streamline approach, basically one-dimensional two-phase flow models, such as Furuya (1985), Zhou and Sachdeva (2010), Minemura *et al.* (1998), and Sun and Prado (2003). From these authors, only the Sachdeva and Sun were models directly applicable to the pumps used by the petroleum industry.

Barrios (2007) developed a model based on bubble diameter in order to determine surging conditions. Two approaches were proposed, one of them was based on a mechanistic model, one-dimensional, based on the balance of the forces acting on bubbles, which are: centrifugal, drag and pressure. This model depends on two important variables. Firstly the bubble diameter which may causes its own stagnation in the impeller channels and the second is the drag coefficient. The model assumes that for a bubble diameter smaller than a critical value, drag forces pushes them into the diffuser. Larger bubbles stayed stationary at admission and coalesced with other bubbles having the same or larger diameters, accumulating, thus causing surging. In some cases, this model showed good agreement with experimental data.

Fluid viscosity has received attention in centrifugal pump performance. The variation of pump performance curves with liquid viscosity is a fact well-known

(STEPANOFF, 1957). If the flow was frictionless when pumped, performance curves would be straight lines. Manufacturers usually conduct viscosity tests at the best efficiency point and at one rotational speed. The losses were affected by a host of design and manufacturing parameters, such as gap width, blade angle, etc. It is a difficult task determining pump performance by theoretical methods. Therefore, performance curves of commercial centrifugal pumps are always established using water as a conventional test liquid. Since pump performance curves are based on water tests, adjustment to work with viscous fluids is required. The adjustments are obtained from tests, which allow the determination of viscosity correction factors valid for the tested rotational speed. Correction factors for flow rate are denoted by C_Q and for head were denoted by C_H .

A visualization prototype was built by Trevisan (2009) with two-phase flow. Two types of combinations were used: water/air and oil/air. Five flow patterns were identified in the study and they were compared with the increment pressure measured in the ESP. The air injection was controlled which allowed a reduction in the bubble diameter, improving pump performance. Besides this, a model was proposed in order to predict the bubble diameter at the impeller's outlet.

In this context, Solano (2009) realized experiments allowing the determination of viscosity correction factors. The procedure established involves the use of Affinity Laws. The "Affinity Laws" are similitude relations for inviscid flow. They state that for low viscosity, a fluid's pump capacity is directly proportional to rotational speed and the head performance is directly proportional to the square of the rotational speed. Dimensionless numbers usually chosen are the specific head Ψ and the specific capacity Φ . Table 2.2 shows the dimensionless variables, where $H_{w,60\text{ Hz}}^{shut-in}$ and $Q_{w,60\text{ Hz}}^{shut-in}$ are the shut-in pump head and the open flow capacity for water at 60 Hz, respectively. The difference for this new case presented by Solano, which means the difference between Table 2.1 and 2.2, refers to geometric terms not neglected and normalized.

According to Solano (2009), only two dimensionless parameters, which are Reynolds number Re and the specific speed N_s , are necessary and sufficient for the determination of the dimensionless performance curve for the pump. Consequently, if a graph like that presented in Fig. 2.6 is available for any single pump, it is possible to obtain the typical non-dimensionless performance curves knowing two dimensionless numbers. The average error of this process is 3% and 10% for the total pump head and single stage head, respectively.

Table 2.2: Dimensionless variables. (SOLANO, 2009)

Dimensionless	Equation
Specific head	$\Psi = \frac{H}{H_{w,60 Hz}^{shut-in}} \left(\frac{3600}{\omega} \right)^2$ (2.29)
Specific capacity	$\Phi = \frac{Q}{Q_{w,60 Hz}^{shut-in}} \left(\frac{3600}{\omega} \right)$ (2.30)
Specific viscosity	$\chi = \frac{\mu_1}{\rho_1} \left(\frac{3600}{\omega} \right)$ (2.31)
Specific speed	$N_s = 0.1707825 \frac{Q^{0.5} \omega}{H^{3/4}}$ (2.32)

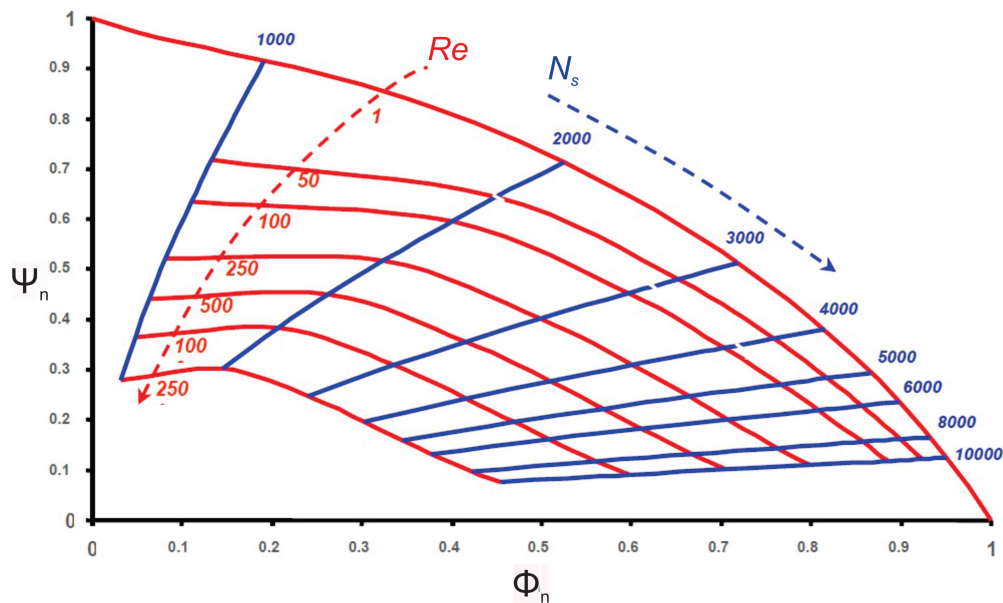


Figure 2.6: Dimensionless graph (SOLANO, 2009).

The applicability of what was proposed by Solano (2009) was tested by Paternost *et al.* (2015), showing that the dimensionless groups were capable of reproducing the effect of rotation and viscosity, besides showing that the Stepanoff (1957) correlation is valid beyond the best efficiency point. Paternost *et al.* used an experimental bench capable of visualizing the flow at the entrance. They showed that the presence of laminar

flow at the pump inlet leads to the coalescence of bubbles in the center of the pipe, increasing the bubble diameter. So, this causes severe degradation in pump performance and may cease the operation, i.e., the gas locking condition.

Considering the viscosity and the same void fraction, Paternost *et al.* concluded that higher viscosity of the liquid phase results in less turbulence in the flow, decreasing the bubble breakage with consequently higher bubble diameter, impacting the pump head negatively. Besides, with the data acquired was possible to calculate the maximum viscosity in function of the void fraction that results in the pump head equals to zero.

Biazussi (2014) realized an experimental study in order to analyze the influence of three main characteristics related to pump performance: the rotational effects, the gas mass flow and the suction pressure. Three pumps model were tested, all of them having three stages.

The rotational effect varied between 1800 to 3500 rpm. These changes have effects on the pump performance and in transition patterns. Increasing the angular velocity of the impeller also increases the centripetal force acting on the bubble. The flow rate rises together with this. So, two forces are rising together in this situation, the buoyancy force proportioned by the increase of the flow rate and the centripetal force rising due to changes in angular velocity. The rise in the flow rate can not overcome growth in the centripetal field, which makes the bubble velocity fall in comparison to the previous situation.

The tests realized with constant gas mass flow rate and varying the liquid flow rate are shown in Fig. 2.7. The results performed in terms of C_H , which is dimensionless for head performance denoted by $C_H = gH/(\omega^2 D^2)$, where ω is the rotational speed and D is the impeller diameter. It is possible to notice performance degradation increasing when gas increases, as a result of decreasing the liquid flow.

The suction pressure tests vary between 100 to 500 kPa. For higher pressure, the pump operation has better performance due to a reduction in the bubble size and an increase of its population at a given gas void fraction. Besides, the changes in the suction pressure provoke shifts the flow pattern transition to the right, considering a chart $\Delta P \times Q$.

Longhi (2016) studied the performance of a Helico axial gas handler (HGH) and an ESP performing different types of tests: each equipment operating isotely and the two operating together. The experiments were done with single and two-phase flow, using

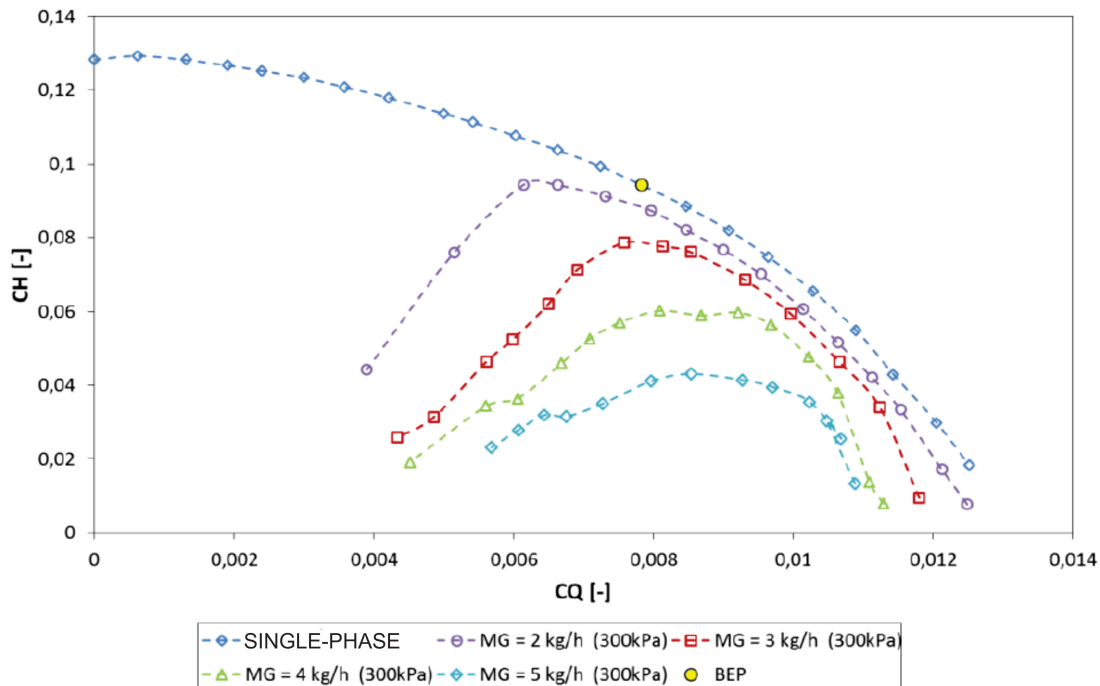


Figure 2.7: Two-phase flow with constant gas flow rate (BIAZUSSI, 2014)

water and air. Also, a model was developed for both types of flow for pressure increment and torque, adjusting the coefficients for the ESP and the HGH. The two-phase model can calculate the pressure increment for each equipment separately and also working together. The two-phase model predicts the existence of the points known as *open-flow*, BEP and *surging* for the performance tests. In addition to this, a reduction in two-phase efficiency and mixture flow rate occurs when the volumetric gas fraction λ increases.

The two-phase flow model originally proposed by Biazussi (2014) assumes that the only effect of the gas phase in centrifugal pumping consists of changes in its mixture density. It is explained by changes in the proportion of gas in the mixture, consequently changing the density of local fluid. The distortions in the velocity fields or even the losses provoked by the increase in pressure increment were not considered, nor the brake horsepower. Mathematically, this approximation does not allow that model to represent a reduction of the mixture flow rate at *open-flow* nor the two-phase efficiency degradation associated with the increase of volumetric gas fraction λ . The phenomena was able to be represented by allowing the coefficients of the two-phase model (increment pressure and brake horsepower) varying with parameters λ , ρ_2/ρ_1 and ω , improving the

adjustment of the model proposed by Longhi (2016).

However, better adjustment should be made in order to improve the interactions between both fluids. The models do not consider losses due to slippage between phases, and they assume that these losses could be contemplated in single phase model, by just being corrected on losses coefficients of the single phase model. Eventually, the conceptual inconsistencies of the single phase model propagated the two-phase model.

2.3 Visualization studies

The first works using visualization to improve the knowledge of two-phase flow phenomenon were applied to the nuclear industry. However, the first study investigating the influence of gas bubbles in a centrifugal pump was performed by Murakami and Minemura (1974a). In order to allow visualization of the flow, a transparent shell was built, allowing the visualization of the flow patterns, bubble displacement and diameters in the impeller channel. They reported that the pressure increment changes as a consequence on many hydraulic factors, such as pump geometry, fluid properties and multi-phase flow conditions.

Considering two-phase flow, the increment of the gas fraction results in an oscillation in the pump pressure. It was verified that the gas fills part of the impeller channel, as the ratio of gas increases, it begins to accumulate. When the concentration of gas bubbles increases in the impeller channels, the consequence is the reduction of the liquid passage area, increasing the liquid velocity and reducing pump performance. As the gas fraction keeps rising, the gas accumulation extends from the entire impeller channel, while in this process, the pump gradually loses its capacity. However, this decline in the pressure increment reduces the gas void fraction, which makes the pump returns to its normal operation. This cycle is continuous (MURAKAMI AND MINEMURA, 1974b). From this instability to the normal operation, a new increase in gas flow rate results in a fast growth of the void fraction, which provokes gas locking making the pump stops its functionality. Besides the behavior described, the following details were observed:

- The gas quantity increases with the rotation of the pump. Associated with this fact is the bubble break up due to the high velocity of the impeller.

- The bubble diameter at the entrance of the impeller is directly proportional to the gas injected.

The work of Estevam (2002) is directly applicable to the petroleum industry using visualization techniques. The impeller and diffuser were produced in transparent acrylic, enabling the visualization of the flow inside the pump. The tests were performed with water and air, varying the flow rate of both fluids and the rotation of the pump. The author observed that when the void fraction is high enough, bubbles begin to form clusters at the entrance of the impeller. These begin to cluster and coalesce and the pump increment pressure decreases inversely with the increase in size of the bubble. Fig. 2.8(a) shows the image captured in the experiment of Estevam (2002), at 1000 rpm. It is possible to note the bubble being agglomerated at the impeller inlet.

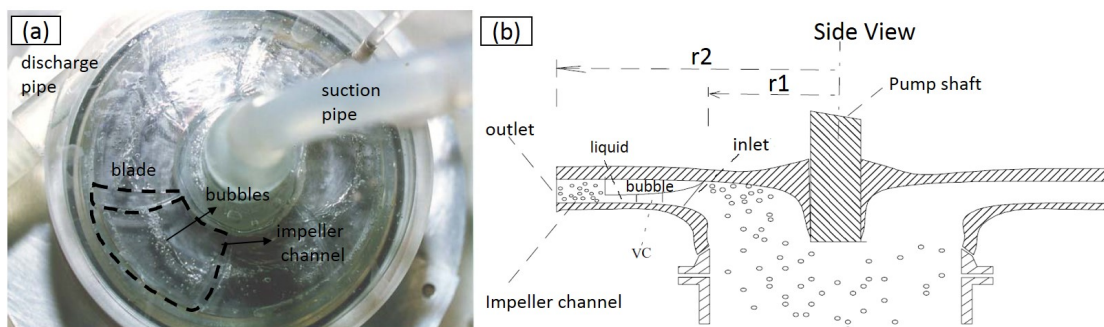


Figure 2.8: (a) Bubbles in impeller, 1000 rpm (b) Side view (ESTEVAM, 2002)

Figure 2.8(b) is a side view and indicates schematically what appears in the Fig. 2.8(a). The process where the bubbles stay stationary in the channel is called surging, which means that only a part of the channel is active, in terms of the energy transfer to the fluid. Gas locking occurs when the gas void fraction continues growing until the process of pumping ceases.

One of the objectives of Barrios (2007) was to determine surging conditions. First, the flow patterns were acquired and then the behavior of bubbles was studied as the instabilities happened in the pump operation. An experimental program was conducted by Barrios and techniques of visualization were used to study the dynamics of the flow and measure the bubble diameter. The second approach proposed the use of CFD, as

an extension of the visualization study. For single phase flow the vortices were analyzed and their influence on the gas bubbles was compared experimentally. Two-phase simulations were made for a similar purpose, the correlation for drag coefficient found experimentally being compared with ones found numerically. The CFD results showed that no recirculation was observed at the impeller outlet and, a good agreement with experimental data was not reached. However, comparison between the predicted pressure increment from the CFD simulation and experimental data correlated fairly well.

Gamboa (2009) investigated the two-phase flow in ESP experimentally. The impeller was adapted to visualize the flow inside. The shroud was removed and replaced by transparent acrylic, exposing the blades and the channels, allowing the visualization of the fluid behavior into the impeller channels. His tests were performed with rotation varying between 600 and 1000 rpm, suction pressure of 2 psig and gas void fraction of 10%. Fig. 2.9 shows the flow patterns observed in these conditions. In the tests, the gas flow rate is gradually increased, keeping the liquid flow rate constant. Four patterns were observed: (a) Isolated Bubbles, (b) Bubble Flow, (c) Gas Pocket and (d) Segregated Gas, which are described below.

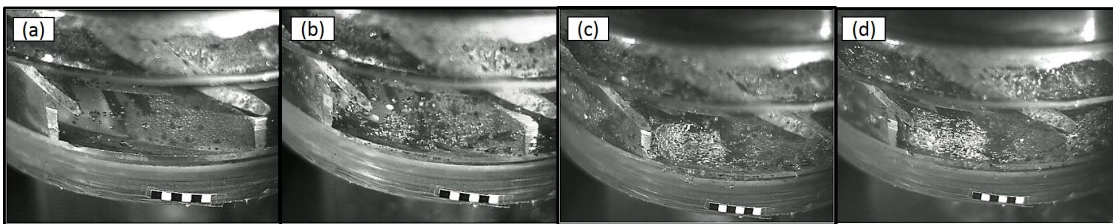


Figure 2.9: Impeller patterns at 600 rpm: (a) Isolated Bubbles (b) Bubble Flow (c) Gas Pocket (d) Segregated Gas. (GAMBOA, 2009)

- (a) Isolated Bubbles: the pump presents the same pressure increment as working with one phase. The term "isolated" refers to the distance between bubbles which is sufficient to not allow interaction between them.
- (b) Bubble Flow: as the gas void fraction is increased, this pattern is reached. Due to the increased population of bubbles, the interaction between them grows, with bubble clusters appearing. The small bubbles continue to be carried by the liquid flow with the larger bubbles recirculating in the impeller channels.

- (c) Gas Pocket: in this pattern, the gas begins to form a continuous phase, forming a bubble that is larger enough to extend from the entrance to the middle of the channel. The energy transfer to the liquid is severely impaired when this pattern is observed.
- (d) Segregated Gas: as the void gas fraction is still increased, the stationary bubble grows until it extends to the entire channel. The bubble pattern can be verified at the entrance of the impeller.

Sabino (2015) performed experiments to identify the most important parameters for bubble behavior. According to Sabino these parameters include the rotation speed of the pump and the bubble diameter. He observed that the bubble flows mainly on the blade suction side. However, in most cases analyzed, the bubble flows along the impeller channel. It gradually moves away from the blade suction side, in some cases, reaching the blade pressure side. In the cases where the bubbles tended to move to the pressure side, their velocities decreased until they ceased. This is the moment that bubbles tended to return to the inlet of the impeller channel, so the author concluded that the pressure gradient is the dominant force. Besides, the suction side showed higher velocity but smaller pressure when compared to the pressure side.

Monte Verde (2016) designed an experimental bench for an electric submersible pump with a single stage. In their experiments, a high-speed camera was used. His test matrix contemplated two kinds of liquid fluids: viscous and non-viscous. For the viscous fluids, oil was used, varying viscosity between 1 to 161 cP. Water was used as a non-viscous. Both combinations used air as the other phase. Four patterns were identified in both combinations, water-air and oil-air, and are shown in Fig. 2.10, which are: (a) Bubble Flow, (b) Agglomerated Bubble Flow, (c) Gas Pocket Flow and (d) Segregated Flow.

As expected, the combined effects of viscosity and two-phase flow promoted a severe degradation on pump performance. The effects of both are added. The presence of gas promoted degradation by itself and the increase in viscosity as well. The viscosity of the fluid acts directly in the drag of the bubbles, increasing the drag force which is responsible for carrying the bubbles through the impeller, as observed by Monte Verde.

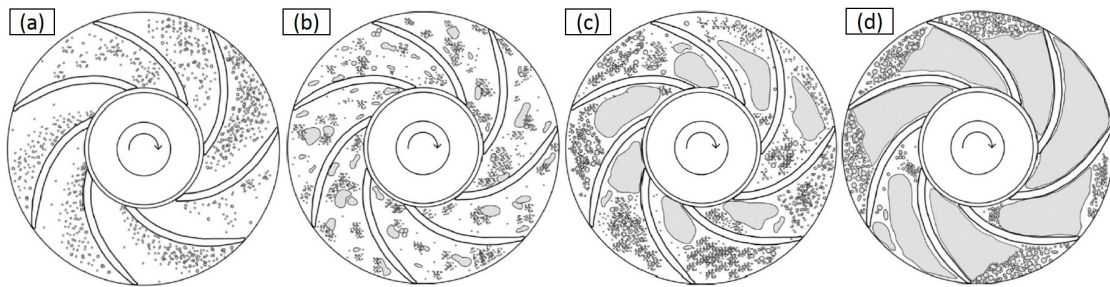


Figure 2.10: Impeller patterns: (a) Bubble Flow (b) Agglomerated Bubble Flow (c) Gas Pocket Flow (d) Segregated Flow. (MONTE VERDE, 2016)

However, the increase in drag force was not enough to overcome the degradation caused by viscosity dissipation. The increase in viscosity of the fluid also increases the diameter of bubbles, promoting coalescence.

Monte Verde observed that the reduction of surface tension shifts the surging point to the left in the performance curve (pressure increment \times liquid flow rate), indicating that the maximum pressure increment point occurs for a higher gas fraction. For operational conditions through the right of the surging point, the study not found any significant result that indicates changes in the pump performance considering the reduction in surface tension. This reduction difficult the coalescence, delaying the flow pattern transition.

A study of the inlet flow conditions has been performed by Schäfer *et al.* (2015). In his work, the high-resolution gamma-ray computed tomography scanner (HireCT) was used. In Fig. 2.11(a) it is possible to see a discontinuity in certain rotation and gas void fraction. Also indicated in Fig. 2.11(b) is a critical gas void fraction.

This physical phenomenon is not fully understood. The author reported that it occurs above a threshold value of the void fraction (corresponding to 3% in his work), which corresponds to a change in flow pattern followed by a change in axial thrust. This interrupts the gas recirculation at the inlet of the channel. Besides, the pump geometry contribution, deeper studies in this area are recommended.

Cubas *et al.* (2017) realized a study with the gas-liquid mixture in a radial impeller using a high-speed camera. The images obtained were associated with the instabilities observed in the performance degradation in two-phase flow operation under surging conditions. Four flow pattern were observed, as suggested by Gamboa (2009)

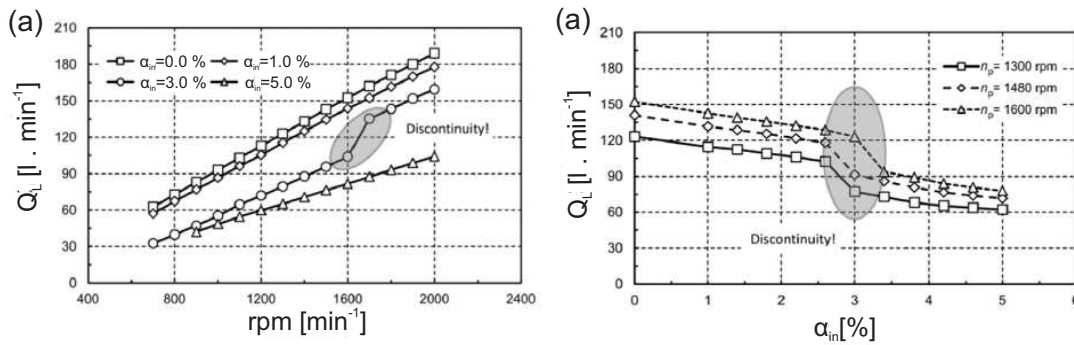


Figure 2.11: Pump flow rate as a function of rotation speed in (a) and as a function of inlet gas volume fraction in (b) (SCHÄFER *et al.*, 2015)

and Monte Verde (2016). The gas void fraction was measured using a wire mesh sensor installed at the intake of the pump. The results of the void fraction shown discrepancy when comparing to the homogeneous model. Cubas *et al.* concluded that this difference occurs because the homogeneous model does not consider the slip velocity. In cases where the gas void fraction was higher than BEP, the bubbles have a tendency to flow at the suction blade side. However, considering the majority of the cases, in the middle of their way or near the impeller outlet the bubbles change their direction going directly through the pressure suction side.

Visualization experiments can help reveal gas-liquid flow behaviors. However, the experimental facility needs special designs associated with necessary modifications of pump geometries, such as the removal of the impeller hub in order to be replaced by a material able to support the pressure and allowing visualization.

2.4 CFD studies

The acquisition of flow characteristics inside the pump is not an easy job due to the high pressures that this equipment is submitted to. However improvements in pump operation can bring considerable benefits to the industry, as the extraction of petroleum offers profitability. Computational fluid dynamics, known as CFD, is a generalized numeric simulation of all physical and/or chemical processes and can offer a representation of what is happening inside the pump. Nowadays, some technologies such as the technique of PIV (Particle Image Velocity), are very expensive. Facing this market, compu-

tational tools are an option to study flow behavior in some equipment, in our case, the ESP (Amaral (2007), Estevam (2002)).

The numerical tools may provide a wide range of variables to understand the physics inside the ESP better. Some variables are challenging to acquire in an experimental facility, such as the friction factor, turbulent energy, among others. The single-phase simulation is an initial step to understand the process as a whole. For example, viscosity is an essential variable in the performance and it can be studied separately from the two-phase flow. Some models were proposed in the literature to predict the pump performance relating to viscous flow, such as Gamboa (2009) and Biazussi (2014). Considering more than one phase, complexity increases. The interactions between phases should be considered and it is more difficult in a rotating structure. Besides, the void gas fraction is present now and it is an important variable to understand the velocity field (FENG *et al.*, 2009a, BARRIOS, 2007).

In this context, Segala (2010) used the software Ansys CFX for simulations. The flow considered was in transient regime, Newtonian fluid, single phase, incompressible and with constant properties. The geometry of the first stage was constructed in SolidWorks and the results of the pump head, power and efficiency were acquired and compared with the experimental data realized in LabPetro/Unicamp by Amaral (2007). The transient model present in the software considered the interaction between the blades of the impeller and the vanes of the diffuser. The others were denominated as Stage and Frozen-Rotor. These models are steady state models, where the impeller assumes a fixed position in relation to the diffuser. Figure 2.12 shows the results obtained experimentally and numerically, where E.D. means experimental data and N.D. numerical data.

Many studies related to losses in the pump, such as Stepanoff (1957), Nelik (1999) and S.Vieira (2014). The actual head developed by the pump is always less than the theoretical one. Takacs (2009) divided the pump losses into three types:

- Hydraulic losses occurring due to fluid friction in the impeller as well as diffusion losses. These increase progressively with liquid flow rate.
- Shock losses are negligible at the best efficient point (BEP). Beyond that point they increase. This type of loss occurs at the entrance and the exit of the impeller,

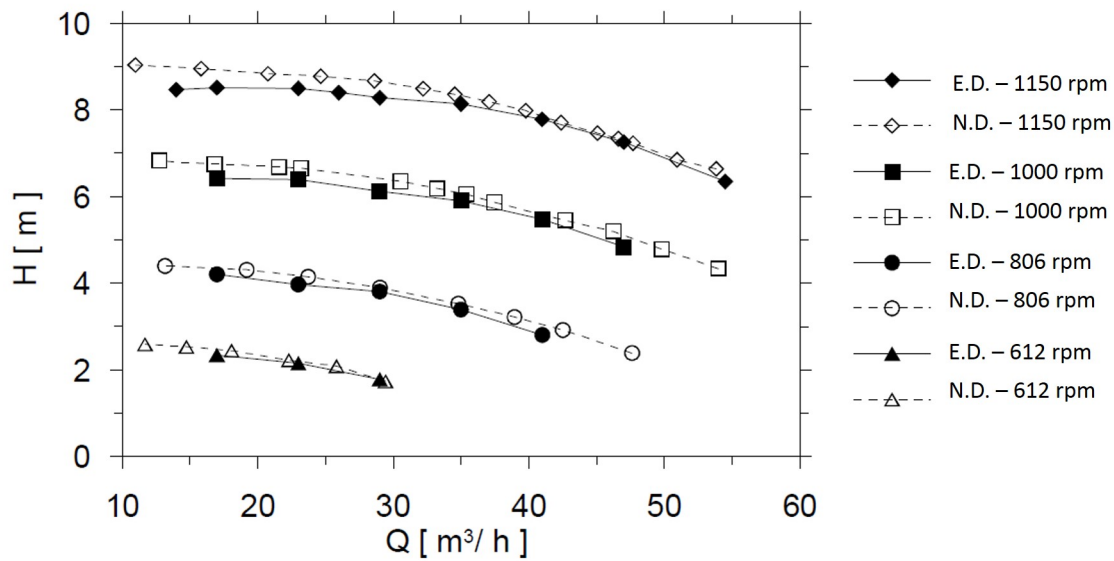


Figure 2.12: Experimental data (ED) and numeric data (ND) from Amaral (2007) and Segala (2010).

caused by sudden changes in the direction of flow.

- Leakage losses are a kind of loss that reduces the produced head at any liquid rate. It represents the loss of liquid rate through the clearances between the rotating and stationary parts of the pump stage. Leakage losses diminish with increased liquid rates, as shown in Fig. 2.13.

After considering all of the head losses described above, the performance of real centrifugal pump stages are represented by the H–Q curve schematically presented in Fig. 2.13. The head pump curve suffers the influence of the pressure losses that occur in an impeller. Due to shocks, flow turbulence increases and, the slippage between the phases and the friction provoke a non-uniformity in their velocities, which affects the pump curve. Many authors claim that the most significant losses occur mainly to shocks and turbulence at lower and higher flow rates. In higher flow rates, friction losses are crucial, even though this effect coexist at lower flows. Information on losses may indicate how to reduce them, so many studies have been devoted to this, like Sun *et al.* (2006), Amaral (2007), among others.

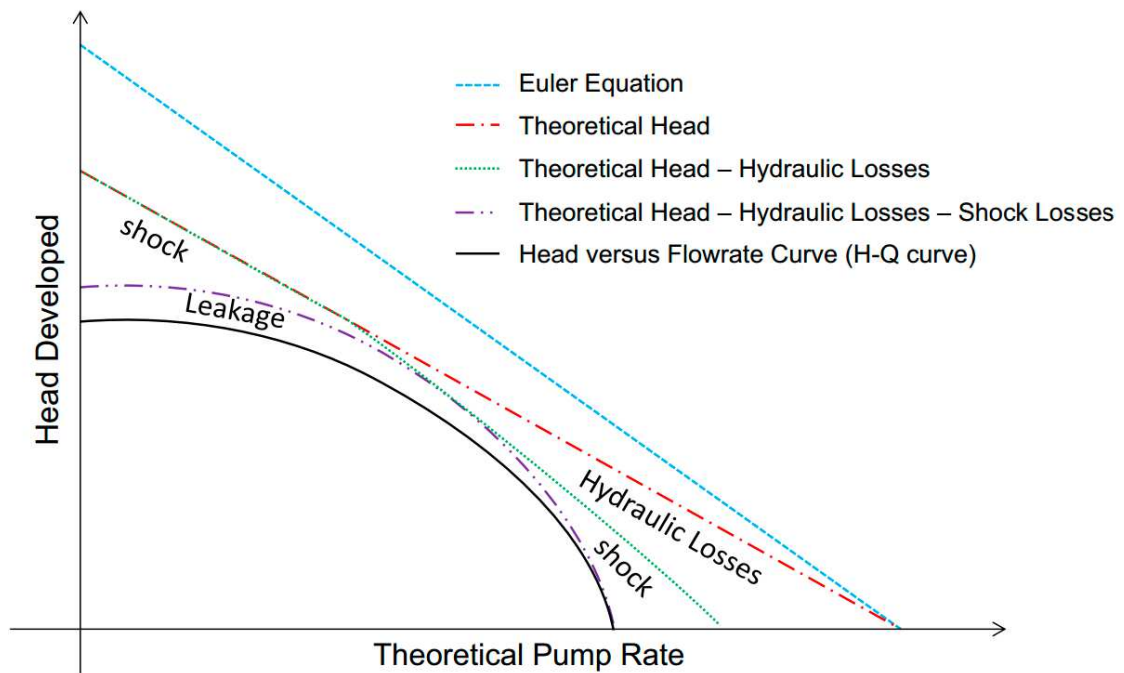


Figure 2.13: Pump H-Q curve and its derivations according to Takacs (2009)

Sirino (2013) used the experimental data of Amaral (2007) with the objective of analyzing performance degradation of the ESP as a function of fluid viscosity, pump rotational speed and the range of flow rate operation. Some discrepancies were observed when the pump worked with water, their results suggesting that working with water, the pump was more susceptible to numerical errors. Besides, the vortex and turbulence levels generated with water as the working fluid showed more intensity comparing with viscous flow. Numeric simulations using water fluid add more complexity than viscous flows due to instabilities that provokes more discrepancy compared with experimental data.

S.Vieira (2014) performed a simulation in order to study the pump losses. The velocity fields showed the presence of vortices in the channels of the impeller at partial flow rates, with more intensity in the case of less viscous fluids. Around the BEP, the vortices were negligible or absent. The largest discrepancies in the numeric modeling were observed at flow rates distancing from BEP and at the lowest flow rates, particularly with pumps working with water. Another discrepancy concluded by the works refers to the friction factor. Comparing this variable for water, their values were a little

bit higher than those that were calculated numerically, especially for high flow rates. However, for viscous fluids, the friction factor was the opposite, their values being less as those calculated numerically. This fluctuation in numeric values and experimental values impacts on the results, as showed by Fig. 2.12.

The data acquired from Amaral (2007) was used in a numerical study by Stel *et al.* (2015). The numerical modeling was described using the software Ansys® CFX®. Single-phase, isothermal and incompressible flow of water was assumed and mass and momentum equations were commonly referred to as Unsteady Reynolds-Averaged Navier-Stokes (U-RANS), which can be represented in a general form as (ANSYS, 2017):

$$\rho \left[\frac{\partial \phi}{\partial t} + \nabla \cdot (\vec{V} \phi) \right] = \nabla \cdot (\Gamma \nabla \phi) + S \quad (2.33)$$

where ρ is the fluid density and \vec{V} represents the Reynolds-Average velocity vector relative to the frame of reference being considered. The continuity equation assumes $\phi = 1$ and $\Gamma = S = 0$. For the momentum equations, $\phi = \vec{V}$, $\Gamma = \mu + \mu_t$ and $S = -\nabla P + S_{Cor} + S_{c.f.g}$, where μ is the fluid dynamic viscosity, μ_t is the turbulent or eddy viscosity resulted from Reynolds-averaging together with the Boussinesq hypothesis, and ∇P is the pressure gradient. The terms S_{Cor} and $S_{c.f.g}$ represent the Coriolis and centrifugal effects. If the frame of reference is considered static, $S_{Cor} = S_{c.f.g} = 0$.

Some turbulence models were tested, such as $k - \epsilon$ (WILCOX *et al.*, 1998), $k - \omega$ (MENTER, 1994) and SST (Shear Stress Transport). The models chosen were based on the models available in the commercial CFD software. Differences were too small to be conclusive in favor of any model, and any of those models tested gave a fair estimation of performance values. However, $k - \epsilon$ based models may not represent flow separation which occur at part-load operation. Stel *et al.* (2015) evaluate the performance parameters for simulations testing different turbulent models in a single stage of the ESP and found no significant differences in favor of any of them.

Hou *et al.* (2016) studied liquefied natural gas (LNG) cryogenic submerged pumps using a numerical approach. This equipment is considered as one type of low specific speed centrifugal pump with low efficiency and bad cavitation performance. The main components of this pump are shown in Fig. 2.14.

Their objective was to improve performance and, decrease the losses. The irre-

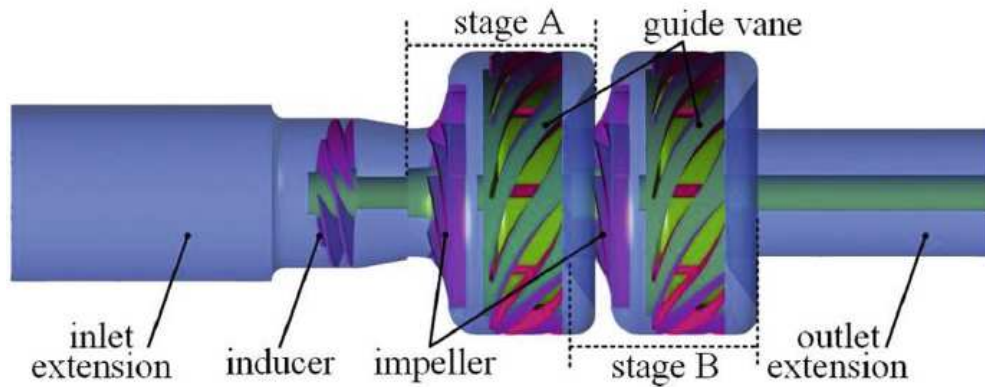


Figure 2.14: Schematic of LNG cryogenic submerged pump(HOU *et al.*, 2016)

versible energy loss based on entropy production theory was investigated. Turbulent dissipation and wall friction were considered as primary sources, where turbulent entropy corresponds to a generation of 75% losses, and wall friction to $\sim 23\%$. The overall losses increase at the second stage of the pump. The entropy production theory can help to quantify irreversible energy loss in order to optimize pump performance.

Ofuchi *et al.* (2017) studied the effects of pump performance degradation due to oil viscosity in ESPs using numerical tools. The author conducted a wide range of fluid viscosity, flow rates, and rotational speeds. The performance deteriorated continuously with viscosity as a consequence of the increase in friction losses in the hydraulic channel. Besides this best efficiency point shifted to lower flow rates when the viscosity increases, as shown in Fig. 2.15.

The pump simulated had three stages, and the interaction between the diffuser and the impeller was evaluated. It shows that the recirculation from the diffuser can influence downstream into the following impeller, as well as turbulence generated inside the impeller can be spread downstream to the diffuser. This fact contributes to a significant difference in the performance of the pump.

The flow inside a multistage ESP model is highly influenced by stage-to-stage transition, impeller-diffuser interaction and part-load operation. Several other factors, such as turbulence, highly-viscous liquid pumping and two-phase flow inside an ESP deserve detailed studies on their own, since all of them are responsible for key influences on the pump performance.

Cheng *et al.* (2019) conducted an unsteady flow field simulation inside the pump

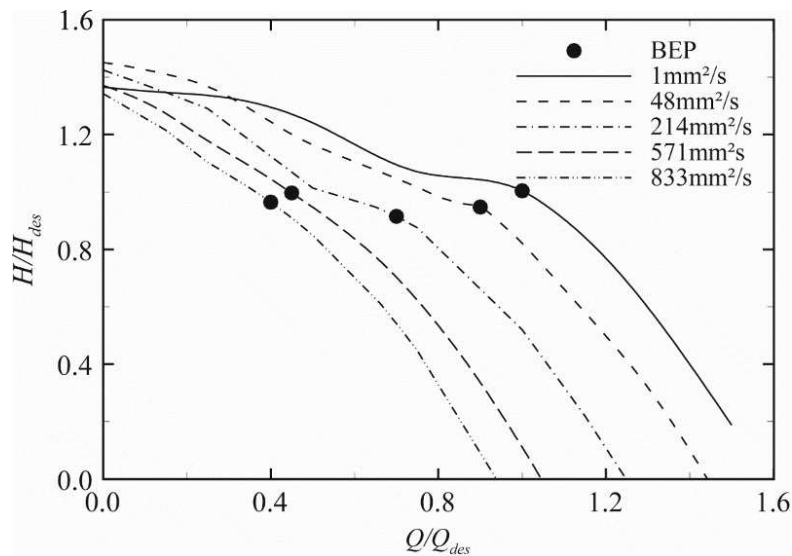


Figure 2.15: Different fluid viscosities at 3500 rpm showing pressure head versus normalized flow rates (OFUCHI *et al.*, 2017)

for molten salt conveying mediums with different viscosities. Water was selected to model the molten salt, as it is difficult to test because the temperature of the molten salt needs to be high. The model established a similarity theory by analyzing dimensionless characteristics of the pump. He found that interaction between the blades and the vanes affects the velocity distribution in the volute significantly.

Besides, when the molten salt pump delivers a low-viscosity medium ($\sim 0.003 Pa.s$), the maximum value in H-Q curve appeared easily to form a hump curve. This is opposite when a high-viscosity medium was delivered. The impact of losses under small flow rate conditions was smaller than with a low-viscosity medium, and the H-Q performance curve was not prone to humps. This is represented in Fig. 2.16. The viscosities above 0.08 Pa.s clearly not shown the tendency in H-Q curve to form a hump.

2.5 Force balance on bubble

Murakami and Minemura (1974a) studied the bubble size in centrifugal pumps. They took photographs with the aid of stroboscopic light, measuring the diameter of the bubbles at the inlet region of the impeller in different rotation conditions. When

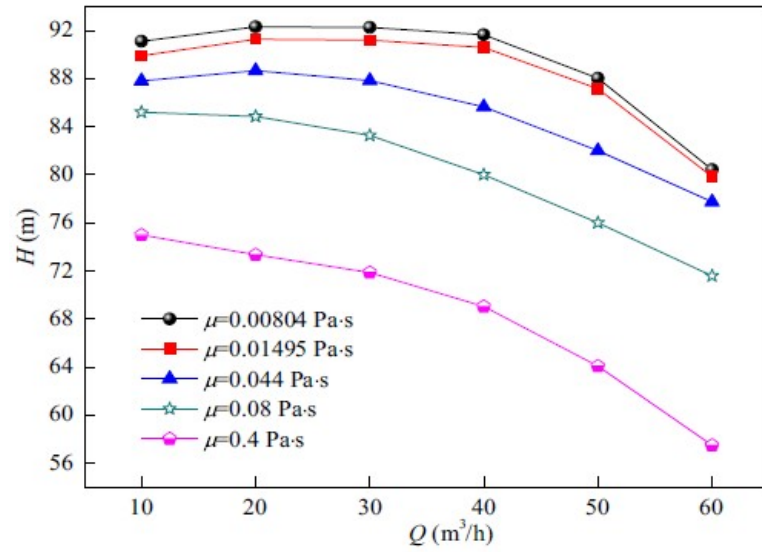


Figure 2.16: H-Q curve for different viscosities (CHENG *et al.*, 2019).

the volumetric gas fraction increased, the Sauter Mean Diameter (SMD) increased too. Equation 2.34 for the bubble size is given by:

$$\frac{d_{32}}{d_{\lambda=0.1}} = 2.3\lambda + 0.75 \quad (2.34)$$

where $d_{\lambda=0.1}$ is the bubble diameter at a volumetric gas fraction of 0.1 which needs to be directly determined by experimental data. The rotation speed is implicit in $d_{\lambda=0.1}$. The authors mentioned that bubbles at the intake of the impeller were broken into finer bubbles in that region. The equation provided to calculate the bubble diameter may not have had the rotational speed equal to zero; this may have caused an inconsistency in the model. Besides, the correlation of Murakami and Minemura (1974a) only works for a specific type of pump, and its universality is questionable. The bubble size diameter in centrifugal pumps can be predicted using Hinze's maximum bubble diameter equation, which is given by:

$$d_{max} = 1.17 \left(\frac{\tau}{\rho_1} \right)^{0.6} \left(\frac{2f_{\beta,\omega}}{D_h} v_M^3 \right) \quad (2.35)$$

According to this equation, the maximum stable bubble diameter size, d_{max} , is a function of fluid properties, mixture velocity (v_M), hydraulic diameter (D_h), and modi-

fied friction factor ($f_{\beta,\omega}$), where it is a function of rotational speed and pump geometry (ESTEVAM, 2002). This equation showed that bubble diameter is not a function of pressure and gas density since their effects were not represented in Eq. 2.35. Barrios (2007) also assumed that Hinze's (HINZE, 1955) equation for the maximum stable bubble size was valid for the centrifugal pump case.

Furthermore, Estevam (2002) found that the drag coefficient calculated through the correlations for an infinite medium were not applicable for a bubble inside the ESP impeller. Using the conventional drag correlations, he demonstrated that the drag coefficient was over-predicted. It constitutes the first evidence that the drag coefficient in pumps is different from that obtained for pipes. This was found by Barrios (2007) who proposed a new drag coefficient based on Ihme *et al.* (1972) correlation, given by:

$$C_D = \frac{24}{Re_p Y} (1 + f(Re_p, Y)) \quad (2.36)$$

where C_D is the drag coefficient, Re_p is the particle Reynolds number and $f(Re_p, Y)$ is given by Eq. 2.37:

$$f(Re_p, Y) = \frac{5.48}{24} (Re_p, Y)^{0.427} + \frac{0.36}{24} (Re_p, Y) \quad (2.37)$$

and Y is expressed by:

$$Y = 0.00983 + 389.9 \frac{Re_p}{\omega^2} \quad (2.38)$$

The Ihme *et al.* (1972) equation does not give a drag coefficient for rotation condition, indicating that rotational speed reduces the drag for a certain range of particle Reynolds numbers (BARRIOS, 2007). Van Nierop *et al.* (2007) showed that the drag coefficient could be predicted as proposed by Legendre and Magnaudet (1998) using Strouhal number.

$$C_{D,Sr} = C_{D,0}(1 + 0.55Sr^2) \quad (2.39)$$

$$Sr = \frac{d_b \omega}{v_2 - v_1} \quad (2.40)$$

where Sr is the Strouhal number, d_b is the bubble size, v_2 is the particle velocity, v_1

is the fluid velocity and ω is the angular velocity. His experimental results strongly support the hypothesis proposed by Estevam (2002) and Barrios (2007) that a specific drag coefficient is required for the flow inside pumps.

Another force present on the bubbles is the Lift force. This type of force is of a lesser order of magnitude than the drag force. Thus, in many studies of the centrifugal pump, this force is neglected.

Virtual mass and the Basset force are common in studies regarding two-phase flow in centrifugal pumps. If the bubble is displacing underwater, the virtual mass force is related to the inertia of water being accelerating or decelerating due to the passage of the bubble through the water. Basset force may be described as the force which has the historical effect of the flow pattern around the bubble. Thus, it may become important as the volumetric gas fraction is increased (ZUBER, 1964).

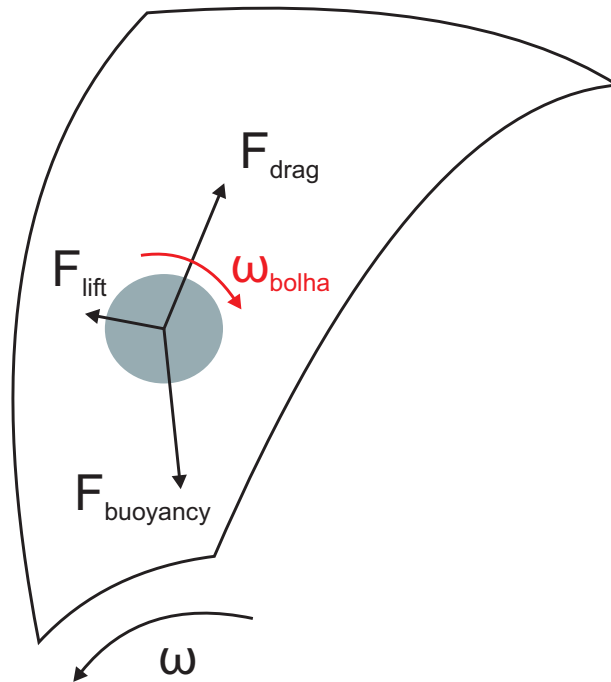


Figure 2.17: Bubble forces (BIAZUSSI, 2014)

Figure 2.17 shows an hypothetical model of the forces acting on the bubble. The drag generated by the flow passing through the bubble pushes it to the exit of the impeller. The bubble was hit by a distorted velocity field, which generates a lateral lift force, as represented in the Figure. In contrast to the drag force, a force generated by

the centripetal field was called buoyancy, oriented to the center of the impeller. The slip between the phases occurs by the difference of drag and buoyancy forces. The growth of rotation increases the flow rate and the centripetal field.

In a pump with a low flow rate, as the pump P23 tested, the drag force promoted by the increase of flow rate can be insufficient to compensate for the buoyancy force promoted by the growth of the centripetal field. When this occurs, the growth of rotation decreases the pump performance. However, in larger pumps, as P47 and P100, the growth of rotation generates the inverse process, i.e. the buoyancy force is much less than the drag force. Consequently, the pump performance is better (BIAZUSSI, 2014).

Stel *et al.* (2019) studied the gas-phase behavior numerically and experimentally. The main components were replaced by transparent components that allow the use of the high-speed camera. The numerical capability was explored to evaluate the bubble trajectory, comparing how it is affected by some variables, such as bubble diameter and liquid flow rate. A Lagrangian solution was used to calculate the motion of individual bubbles inside the pump, considering drag, virtual mass, pressure gradient and rotational forces. In his tests, the lift force showed a negligible effect in comparison to other forces, so it was not considered. In conclusion, bubble trajectories were sensitive to the bubble diameter. Besides, the virtual mass can be reasonably high in regions of high-velocity gradients.

The phenomenon of gas-liquid flow in pumps needs deeper studies in order to design better pumping systems. For example, the mechanisms of coalescence need to be better understood, which may lead to a reduction of losses inside the pump. The motion of bubbles can be the key to more efficient pumps for gas-liquid flow applications.

3 EXPERIMENTAL DEVELOPMENT

This chapter presents the experimental procedure to obtain data for single and two-phase flow characteristics inside the ESP impeller channel. This chapter is divided into three sections. The first section details the pump prototype used, the instrumentation, the experimental procedure and the test matrix. The second explains the scripts developed for image analysis and data analysis. The results of the scripts are shown in chapter 5.

3.1 ESP Prototype

In order to get access to the flow inside the pump, a prototype of an electric submersible pump (ESP) was used. It allows the visualization of the flow in the impeller channel. The prototype construction was based on a pump P23 model, manufactured by *Centrilift*, used in oil production and described in details by Biazussi (2014). This model was chosen because it was already constructed in the facilities of CEPETRO. Besides, the impeller geometry was radial and channel depth (h) was constant. Operating at its designed point (BEP) at 3500 rpm , the pump flow rate was $15.2 \text{ m}^3/\text{h}$ and the head equal to 17 m . Geometrical specifications of the impeller are shown in Fig. 3.1 and summarized in Table 3.1.

Table 3.1: Geometrical specifications of ESP

Parameter	Values
Inner radius, R1	22.05 mm
Outer radius, R2	55.69 mm
Blade number	7
Blade thickness (inner / outer)	3,1 / 2.2 mm
Channel depth, h	6 mm

The impeller of the BCS P23 is of a closed type, therefore, to visualize the flow inside it was necessary remove the steel shroud and replace it with one produced with acrylic, keeping the channels sealed. Also, the diffuser was modified for a kind of volute, allowing the impeller channel to be exposed. Before the entrance of the impeller channel, the intake remains the same, without modifications that could change the characteristics of the flow. Figure 3.2 shows the prototype, and a detailed description of it can be seen in Monte Verde (2016).

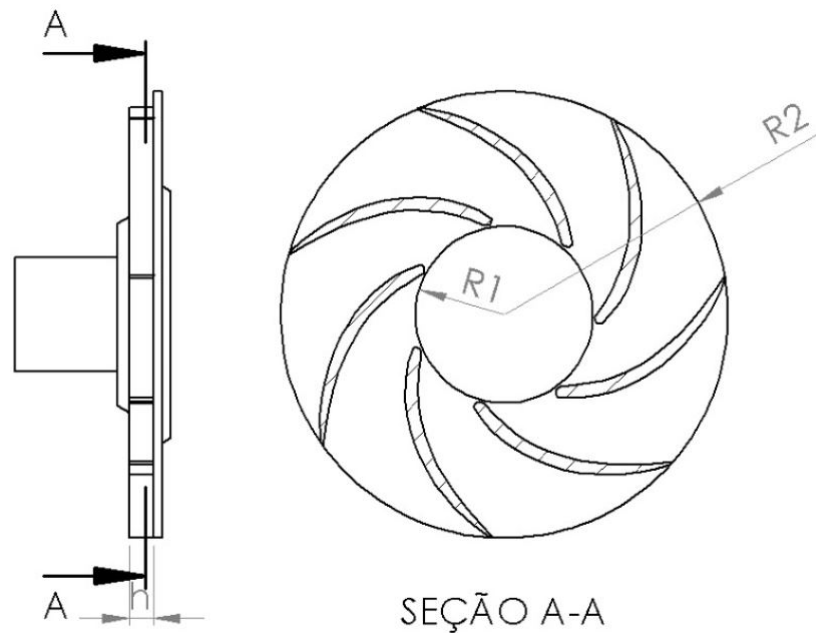


Figure 3.1: (a) Frame and ROI - (b) Cropped image.

The experimental apparatus is presented in Fig. 3.3. It consisted of two tanks, a booster pump, a heat exchanger, a heat pump, the necessary instrumentation, piping and camera. As presented in Fig. 3.2 the booster pump displaced the water from the tank to the test line (green lines), overcoming losses along pipes and accessories. It had an important function of controlling the inlet pressure in the prototype pump through rotational speed control via a variable speed drive (VSD) installed in the booster pump motor. Then, the pumped water flowed through a shell-and-tube heat exchanger. It could work by heating or cooling the fluid temperature between 5 and 56°C. Before the fluid reached the prototype inlet, its mass flow rate was measured through a Coriolis type flow meter. Compressed air was provided through a compressor and its flow rate measured through laminar flux flow meters. After the flow meter air was injected into the prototype (blue lines).

Finally, closing the loop, the water-air mixture was pumped by the ESP prototype returning to the tank where the phases were separated by gravity. The mixture flow rate was controlled by a globe valve, installed on the discharge, while the air mass flow rate was controlled through a precision manual needle valve. The mixture of phases was made in the suction tube before the prototype. The compressed air was injected into

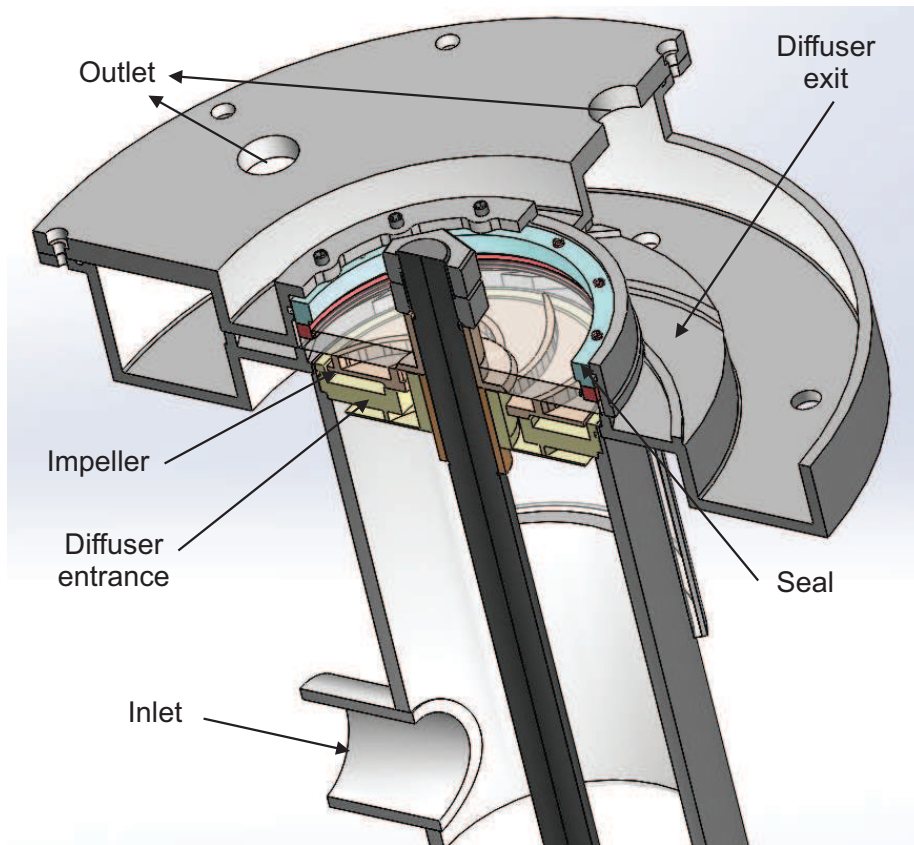


Figure 3.2: Visualization Prototype - Adapted from Monte Verde (2016)

the liquid stream through holes of 0.5 mm diameter. The mixture was fed directly to the entrance to avoid phase development and segregation. In this way, the gas was suctioned into the pump as bubbles.

The ESP prototype was driven by a three-phase induction motor, 380 V , 5 HP , controlled by VSD from which the pump prototype rotation could be varied. In addition, two angular contact bearings were installed between the motor and the ESP prototype. They were responsible for supporting axial forces generated by the pump prototype. A tachometer was used to measure rotation. Table 3.2 shows the main equipment in the experimental apparatus.

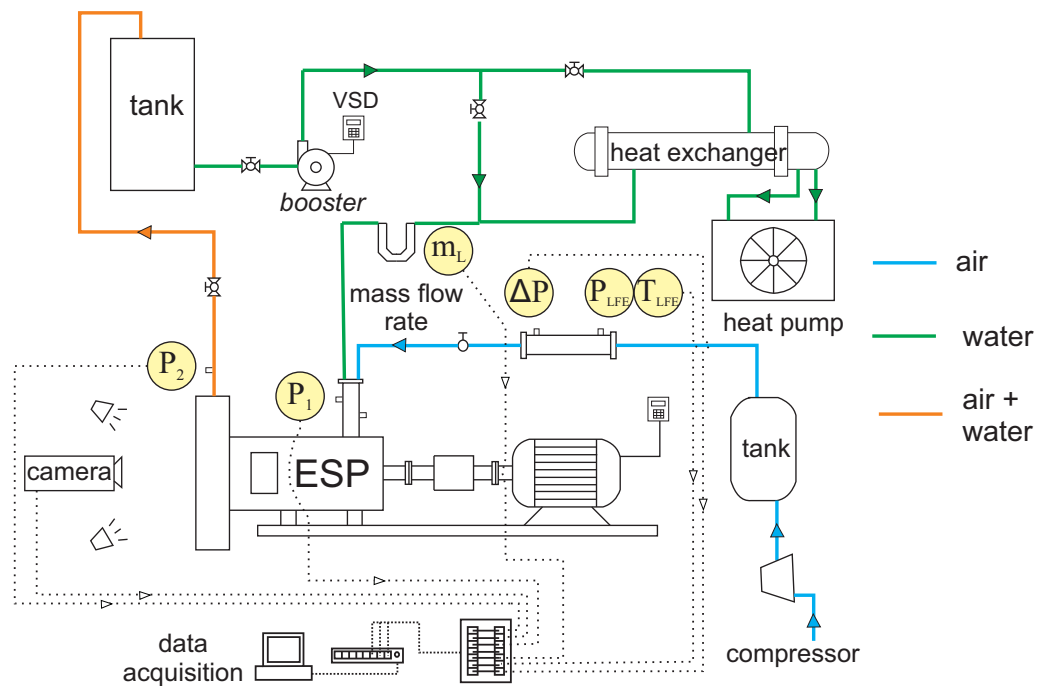


Figure 3.3: Experimental Apparatus Scheme

3.1.1 Instrumentation

The pressure gain of the fluid was measured through gauge pressure transducers, installed at the ESP prototype entrance and exit. At the entrance, the pressure transducer was fixed in the suction pipe, after the gas injection. In the exit, the pressure was measured using a piezometric ring, connecting radially and equalizing the six exit points on the diffuser. At the entrance of the ESP prototype, temperature was measured using a PT100 sensor. The rotation was measured using a tachometer directly on the drive shaft of the prototype.

The liquid mass flow rate was measured using a Coriolis-type flow meter, installed in the suction line, before the injection point. The gas volumetric flow rate was measured using the laminar flux, installed after the tank, as represented in Fig. 3.3. This device provided the flow rate indirectly, measuring the pressure, temperature and pressure difference generated by the flow while it passed through the equipment. The gas volumetric flow rate measured by the laminar flux is given by Eq. 3.1.

Table 3.2: Equipment used in the experimental apparatus

Equipment	Manufacturer/Model	Specifications
Electric motor of ESP prototype	WEG	Three-phase 220/380 V, 13/7.53 A, 60 Hz, 3.7 HP , 3485 rpm
Electric motor of booster pump	WEG	Three-phase 220/380/440V, 13.8/7, 99/6.90 A, 60 Hz, 3.7 HP, 1730 rpm
Booster pump	KSB Meganorm Bloc, 40-250F	Single stage, rotor de 238 mm, flow rate $25 \text{ m}^3/h$ and head 24 m, on BEP
Variable speed driver (VSD)	WEG GFW-08	Three-phase 200-240V 3-19A, 60 Hz, micro processed with digital display
Termochiller	Carrier AQUASNAP 30RH20	Cooler capacity 61.4 kW, heating 62.5kW, working fluid temperature between 5 to 56°C
Tank	-	Tank made with polypropylene, 0.5 m^3 of capacity
Heat exchanger	Shell-and-tube	Own manufacture
Tachometer	MDT 2238A	Measure range: 2.4 to 99999 rpm
Globe valve	-	Manual liquid flow control
Micrometric valve	Festo GRP-10-PK-3	Gas flow control

$$q_{G,LFE} = 1.4296311 \cdot 10^{-2} \Delta P_{LFE} - 4.5950282 \cdot 10^{-5} \Delta P_{LFE}^2 \quad (3.1)$$

where $q_{G,LFE}$ is the gas volumetric flow rate in CFM and ΔP_{LFE}^2 is the pressure difference in H_2O . The mass flow rate of the gas phase can be obtained trough volumetric flow rate, absolut pressure and temperature:

$$\dot{m}_{G,LFE} = \rho_{LFE} q_{G,LFE} = 1.699011 \frac{P_{LFE}}{R_G T_{LFE}} q_{G,LFE} \quad (3.2)$$

where $\dot{m}_{G,LFE}$ is the mass flow rate in kg/h , P_{LFE} is the absolute pressure in the laminar

flux in kPa , T_{LFE} is the absolute temperature of the gas in Kelvin and R_G is the gas constant in kJ/kgK . Table 3.3 shows all the variables measured in the experiments while Table 3.4 shows a description of the instruments.

Table 3.3: Measured variables

Variable	Definition	Unit
P_1	Suction pressure	kPa
P_2	Discharge pressure	kPa
P_{LFE}	Pressure in the element of laminar flux	kPa
ΔP_{LFE}	Pressure difference in the element of laminar flux	inH_2O
T_{LFE}	Discharge temperature	$^{\circ}C$
\dot{m}_L	Liquid mass flow rate	kg/h
ω	Rotation speed	rpm

The data acquisition system was composed of a computer, signal acquisition modules and a program to process the signals. Two data acquisition modules were used according to the exit signals of the instrument, which were electrical current (4 - 20 mA) or voltage (± 10 volts). In the modules, analog signals were received and digitized. Through the LabVIEW® based software, the data acquired were monitored and displayed in a graphical interface. The signals coming from the instruments were showed in a real time scheme during the tests, and they were also processed and showed to the user as a mean or in charts, and then they were saved as text files for post-processing. The graphical interface of the software is shown in Fig. 3.4.

3.1.2 Visualization Equipment

High-speed cameras have been widely used in multiphase flow experiments, such as liquid-liquid, gas-liquid, liquid-solid, among others (Ofuchi (2011), Penteado and Franklin (2016)). This method is precise and non-intrusive. However, its limitation is related to the fact that an optical access to the phenomena is necessary and this rarely happens in turbo-machinery, because the fluids are, frequently, under high pressure. A high-speed camera, model Phantom VEO 640S, capable of 4 megapixel with a reso-

Table 3.4: Instrumentation

Instrument	Variable	Manufacturer / Model	Characteristics
Pressure transducers	P_1, P_2	Emerson Rosemount 2088	Gauge pressure instrument, exit 4-20 mA, calibration 0-20 bar.
Mass flow rate for liquid	\dot{m}_L	Emerson Micro Motion F100	Coriolis measurement, exit 4-20 mA, operating between 0-32650 kg/h .
Tachometer	ω	Minipa MDT 2238A	Digital, remote control or contact, operating between 2.5 - 99999 rpm
Temperature transducer		ECIL APAQ LR	Thermoresistance, exit 4-20 mA.
Data acquisition module		National Instruments NI 9203	08 analog input channels between 4-20 mA.
Chassis acquisition module		National Instruments NI cDAQ 9178	Chassis with 08 slots for acquisition modules, with USB connection

lution of $2560 px \times 1600 px$ at 1.400 frames per second (fps) is used on the tests. A resolution of $512 px \times 512 px$ can be used to acquire 14.000 fps. The camera has 72GB RAM and can record 8.5 seconds at maximum resolution. A computer is used to control the frequencies and exposure times of the high-speed camera and to store the acquired images in .cine format, and then convert to .avi in proprietary camera software for post-processing.

Due to high acquisition frequencies high-speed cameras demand an efficient illumination. This means that the object should not have shadows when being captured. In the experiments, the illumination was constant and provided by three sources containing 24 LED (Light-Emitting Diode) lamps each. They were of 84 Watts, delivering 7.700 lumens of brightness each. For the tests, the number of acquired images was around 7.400 and 15.000 frames, depending on the prototype rotational speed, with resolution of $1536 px \times 1536 px$, and a Canon® lens f/1.4 of 50 mm focal length was used.

For the tests, the image acquisition frequency was of 1000 Hz (or 1000 fps) for 600

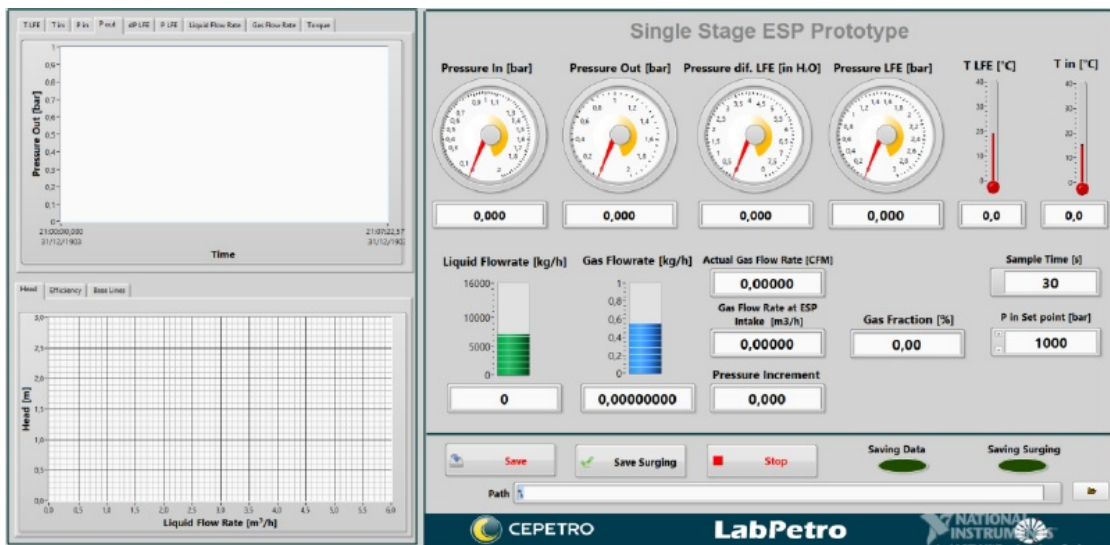


Figure 3.4: Graphical Interface of the Data Acquisition and Control Software

rpm of the pump and 1500 Hz for 900 rpm. In other words, in both rotations the impeller moves 3.6° degrees from one picture being captured to another. Figure 3.5 shows the light source, the camera and their positions in the experimental apparatus.

3.1.3 Experimental Setup Validation

The author performed experiments with water single-phase flow in the same experimental setup as Perissinotto *et al.* (2017) and Monte Verde (2016). The experiments gave the same performance curves as the ones presented by Monte Verde (2016). So, the experimental setup was considered validated for this study as well. The single-phase flow experimental data was used for comparison with numerical simulation. Details of validation and experimental data can be found in Perissinotto *et al.* (2017) and Monte Verde (2016).

3.1.4 Experimental Procedure - Two-Phase Flow

The following experimental procedure refers to the prototype operating with two-phase air-water flows, where the gas mass flow rate was kept constant during the

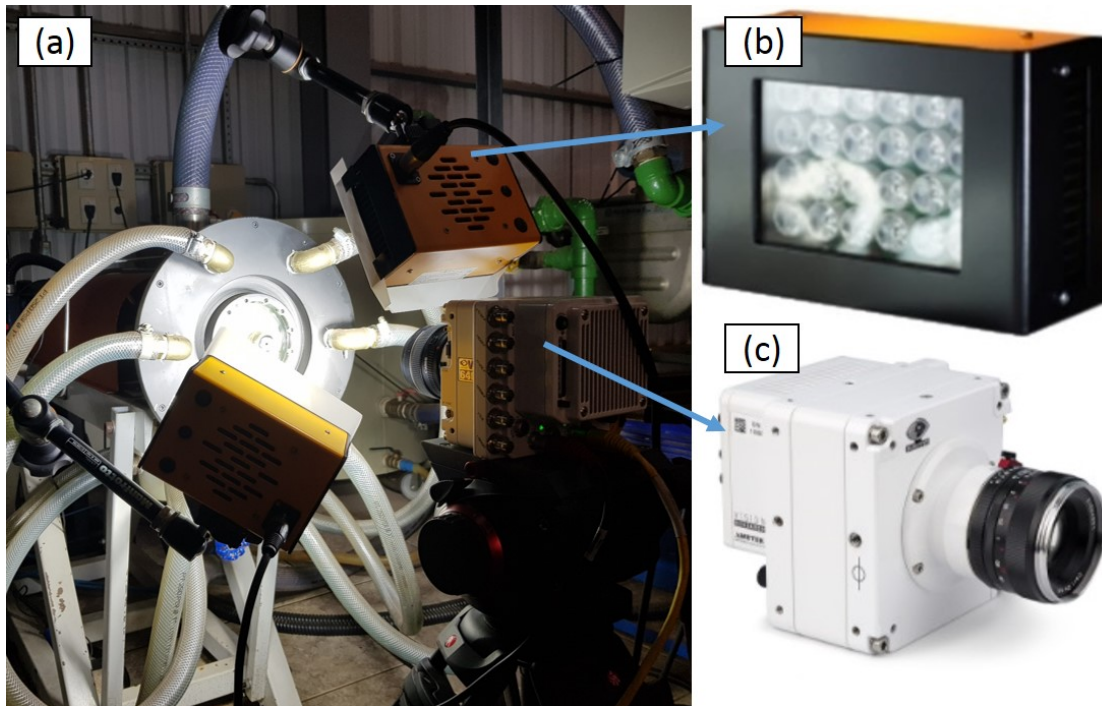


Figure 3.5: Experimental Apparatus during experiments: (a) Light + Camera - (b) Light source - (c) Camera

tests. The experimental procedure consisted of the following steps:

1. The illumination system is turned on, aligning the three light sources in order to get the fewest shadows as possible in the visualization window.
2. The camera is positioned on a tripod and then the desired lens inserted. The software of the camera is executed and set to real time exhibition. The images are inspected through the monitor, adjustments are made in camera position and focus if demanded. If necessary, changes are made to the alignment of the light sources.
3. Instruments are turned on for the experiment. Verification of the connection between them and the computer is made. The camera software to monitor the data acquisition is then executed.
4. The booster pump is turned on and then the ESP prototype, certifying that valves are open. The rotation of the pump is adjusted using the VSD and the tachometer. Rotation stays constant during the experiments.

5. The heat pump is turned on. The liquid temperature is kept constant during the tests, at around 25 ° C.
6. Adjustments are made to both the rotation of the booster pump using its VSP and the globe valve in the discharge of the prototype in order to obtain the desired liquid flow rate, and keep the suction pressure constant.
7. Gas injection is initiated until the desired mass flow rate is reached, which is constant during the tests.
8. A delay of three minutes is needed until the operational condition stabilizes.
9. The data are acquired and saved on the computer. The images are also saved.
10. The next operational condition is established, changing the rotation in booster pump and opening/closing the globe valve at the discharge line.

The procedures 8, 9 and 10 were repeated until the lowest liquid flow rate in which the variables of interest could still be controlled.

3.1.5 Test Matrix - Two Phase Flow

The tests with water and air were performed with constant air mass flow rate. They were performed using the rotation of 600 *rpm* and 900 *rpm*. Above 900 *rpm*, such as 1200 and 1500 *rpm*, the bubbles appeared as a cloud of bubbles. In order to capture the displacement of bubbles at such speed, the illumination and some other aspects should be improved, and they will be discussed in suggestions for future works. The suction pressure was kept at 150 kPa and mass gas flow rate at 0.0250 and 0.0125 *kg/h*.

3.2 Image Processing Software

The next section describe the code made in Matlab® by the author. The code aims to capture the displacements and size of the bubbles.

3.2.1 Code development

A numerical code was developed in order to determine the displacements and velocities of air bubbles in an Eulerian framework from the high-speed movies.. The post-processing of the images comprised two main steps. First, the code identified the regions where bubbles were moving. In the second stage of the code, the displacements of the bubbles identified by the code were acquired. The steps of the first part of the code are:

- | | |
|---------------------------|--------------------------|
| 1. Image rotation. | 7. Laplacian filter. |
| 2. Definition of the ROI. | 8. Binarization. |
| 3. Adaptive histogram. | 9. Median filter. |
| 4. Strel filter. | 10. Eccentricity filter. |
| 5. Image subtraction. | 11. Pairing |
| 6. Wiener filter. | 12. Cell formation. |

The scripts created needed to rotate the image in order to capture only the displacement of the bubble meaning that the camera remains frozen when capturing the images. The frequency represents how much the impeller rotates from one frame to another. In possession of this information, the image needs to be rotated by:

$$I = \frac{\omega}{60} \frac{360}{fr} \quad (3.3)$$

where ω is the rotation of the impeller in *rpm* and fr is the acquisition frequency of the camera in *Hz*. The result of I in Eq. 3.3 corresponds to 3.6° degrees of rotation from the first image captured to the following one. For all the tests the acquisition frequency is adjusted in order for the camera to take a shot every 0.24 seconds. This is the sampling interval. The next step was the creation of a Region of Interest (ROI).

Figure 3.6(a) represents the image acquired from the tests, and the border in blue separates the unnecessary pixels. In image post-processing this represents the mask (OPPENHEIM AND SCHAFER, 2014). With the mask representing the region of interest (ROI) the pixels outside it are replaced by the value 0, which means that it appears as black. The cropped image is shown in Figure 3.6(b).

The creation of the ROI is an essential process because the scripts applied in

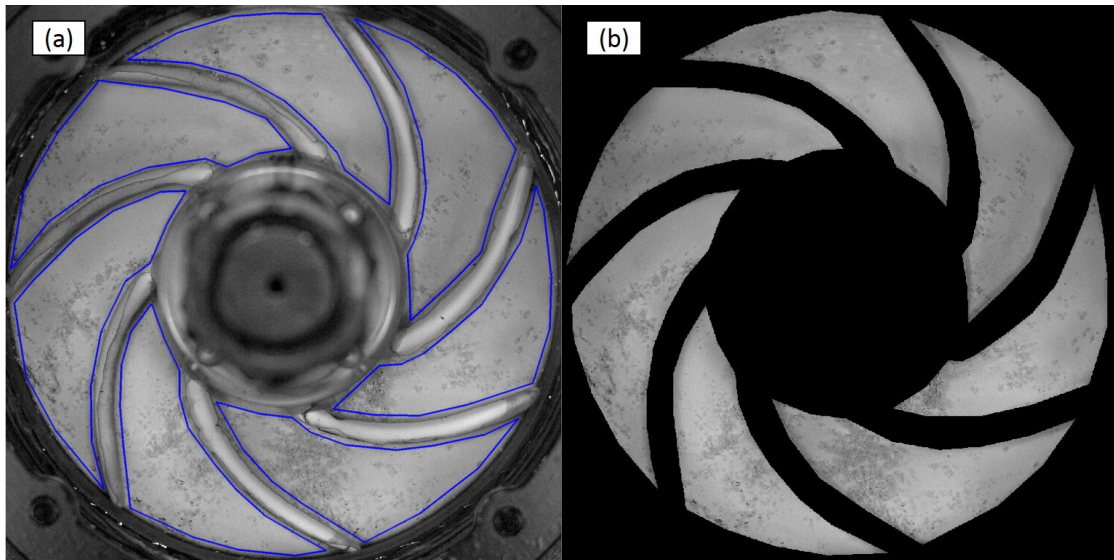


Figure 3.6: Example of a captured image of the impeller: (a) ROI - (b) Cropped image.

the sequence have the guarantee that displacements of bubbles receive the next filters without the noise of unnecessary pixels.

The next scripts counts with techniques used in spatial processing. The intensities of a pixel can be changed according to the neighboring pixels' intensities through a technique called spatial filtering. An image is a two-dimensional function, $f(x, y)$ where x and y are spatial coordinates and the amplitude of f at any pair of coordinates (x, y) is called the intensity of the image at that point. In our case, the output (processed) image is $g(x, y)$, and T is an operator on f defined over a specified neighborhood of point (x, y) . The spatial domain processes are denoted by Eq. 3.4:

$$g(x, y) = T[f(x, y)] \quad (3.4)$$

The original image $f(x, y)$ receives the treatment of an operator, $T[\cdot]$, such as the median filter. After that, the new image is $g(x, y)$. The operator is described by the scripts created. The intensity values acquired in gray-scale corresponds to values between 0 (black) or 255 (white). In signal processing, noise is characterized as any information that blurs the object, an undesirable aspect such as small changes in illumination that may occur in our case. The script uses adaptive histogram equalization (AHE) to improve the contrast in images (GONZALEZ AND WOODS, 2008). Its function redis-

tributes the lightness values of the image. Therefore it improves edge definitions in each region of an image.

Seven channels are noted in Fig. 3.6(b). The external observation, which can be done by the operator who is making the code, have more quality in the analysis if the image window is amplified. This means that reduced windows improve the details of images, working as a zoom or amplification lens. Figure 3.7 explains better to the reader what this means. Figure 3.7(a) shows the image after cropping and its respective histogram on the right side. The adaptive histogram redistributes the pixel intensity on the images (GONZALEZ AND WOODS, 2008). The result of this process is shown in 3.7(b) and its respective histogram.

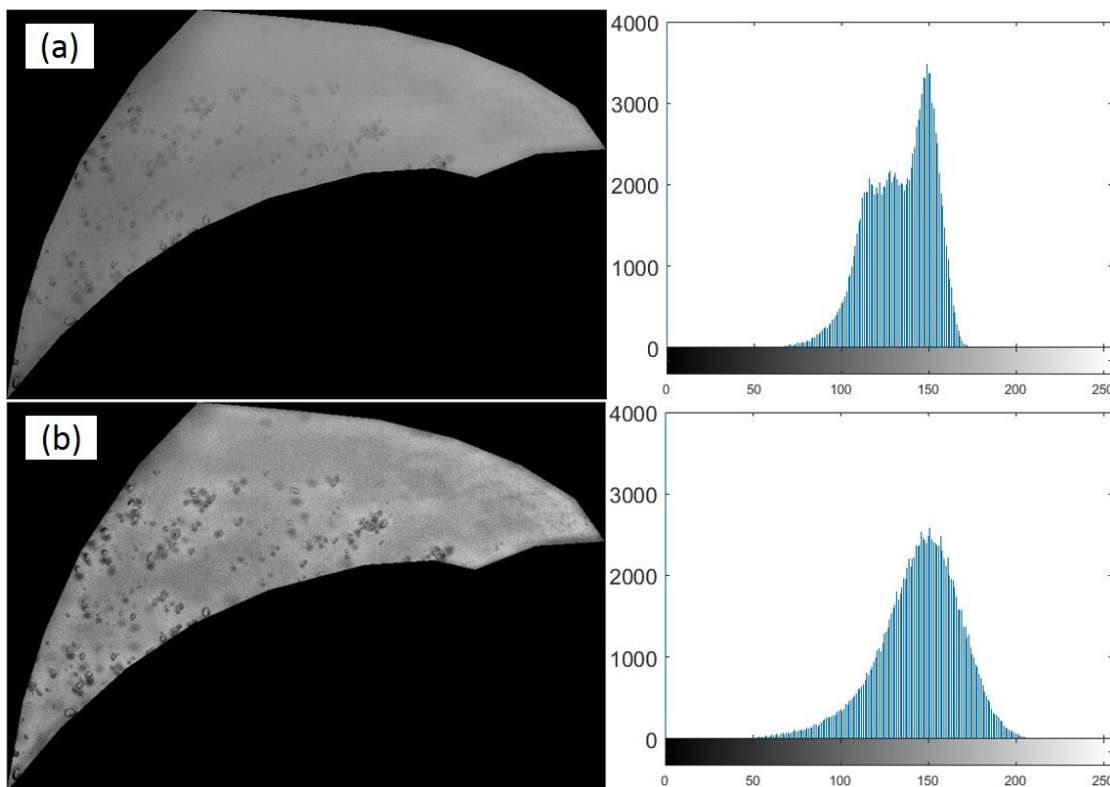


Figure 3.7: Image with: (a) No equalization - (b) Equalization

Morphological operations as dilation and erosion were executed in Matlab. The strel filter is a morphological operation that uses a disk-shaped structuring element in the present work. Typically, the structured element selected should be the most similar to bubble shape and have the nearest size to improve the effectiveness of this operation.

The next operation was the image subtraction, a similar process to that made by Penteado and Franklin (2016). Two consecutive images were necessary to execute this script, which indicated the possible displacements that occurred. This script goes a little further in the code steps, so it executes the Wiener, Laplacian and binarization process to then return the values acquired. After these processes, the centroids were captured and they are shown in Fig. 3.8. The red circle indicates the current frame, the blue square, the next frame, and the green marking indicates the location of possible displacement as a result of the script.

Thus Fig. 3.8(a) shows the process without the use of image subtraction. The centroids had already been calculated in two consecutive images and plotted. Fig. 3.8(b) shows the filter acting and removing some centroids where no displacement occurring. For example, consider a green mark in the Figure. The code searches possible displacements in a radius of 5 mm in the current and next frame. If some point is not founded, it is considered that no movement occurs in that region, so it is removed. The centroids removed are shown by a blue arrow in Fig. 3.8(a).

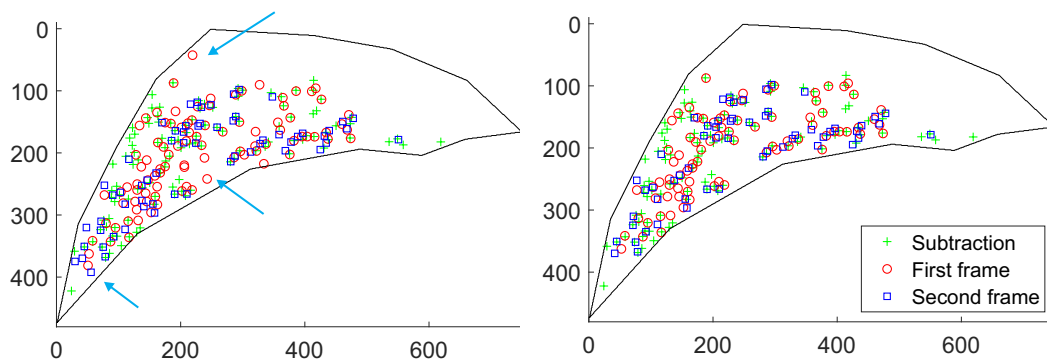


Figure 3.8: Morphological operations: (a) Centroids of the image - (b) Subtraction applied

The pump's axis makes some shadow in the impeller channel, and even with the best effort made to try better positioning for illumination, a small portion of this still appeared. The Wiener deconvolution is a process to deblur the images, it reduces a portion of the noise. This is one of the filters used to decrease the shadows, and improve the results of the code.

The Laplacian filter was employed after the Wiener deconvolution. It is a linear

spatial filter used to emphasize image contrast. It allows the enhancement of bubble contours. Considering this situation, two types of spatial masks to enhance edges were tested. They are shown in Eq. 3.5 and are named as lp_4 and lp_8 . Both enhanced the contour, and are shown in Fig. 3.9. The spatial mask used is lp_8 , which has contours more prominent than lp_4 .

$$lp_4 = \begin{bmatrix} 0 & 1 & 0 \\ 1 & -4 & 1 \\ 0 & 1 & 0 \end{bmatrix} \quad lp_8 = \begin{bmatrix} 1 & 1 & 1 \\ 1 & -8 & 1 \\ 1 & 1 & 1 \end{bmatrix} \quad (3.5)$$

As already mentioned in Fig. 3.6(b), seven channels were treated. Fig. 3.9 shows a channel that is chosen in order to present an enhanced visualization to the reader. Fig. 3.9(a) represents the original image, Fig. 3.9(b) 3.9(c) represent the image treated using lp_4 and lp_8 , respectively.

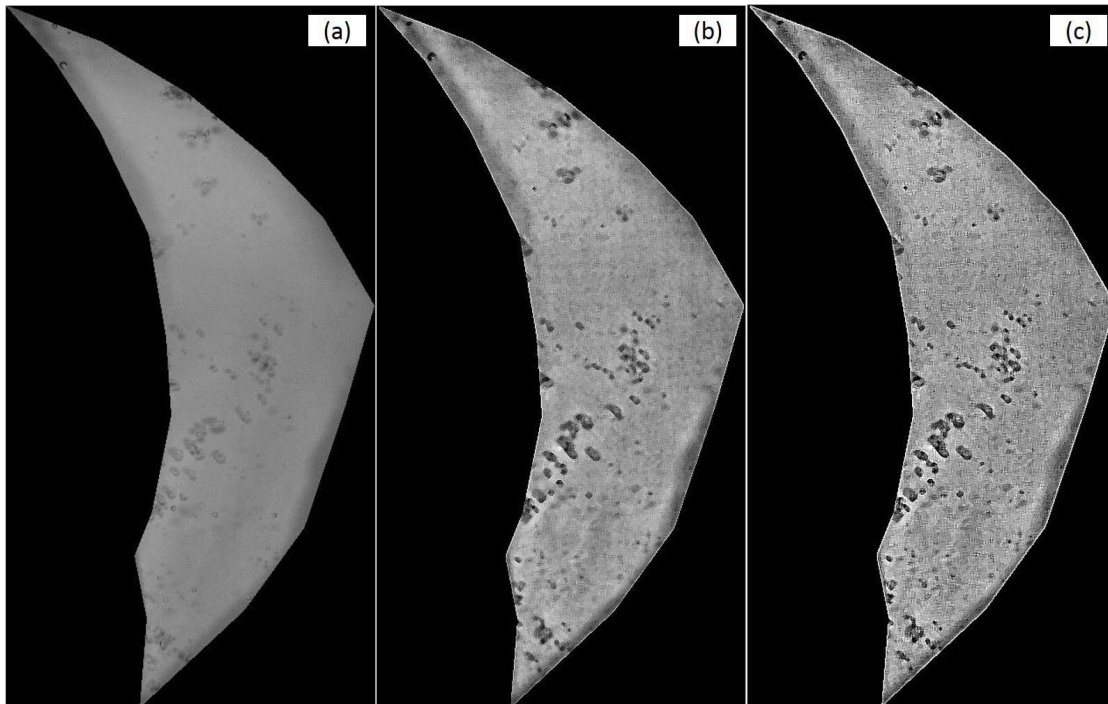


Figure 3.9: (a) Original Image - (b) Laplacian lp_4 - (c) Laplacian lp_8 .

Equation 3.6 defines the Laplacian operation, where the input image is given by $f(x,y)$ and the Laplacian is denoted as $\nabla^2 f(x,y)$. This expression was implemented

at all points in the image, convolving using the spatial mask that takes into account diagonal elements.

$$g(x,y) = f(x,y) + c [\nabla^2 f(x,y)] \quad (3.6)$$

The enhanced image is given by $g(x,y)$, and c is 1 if the center coefficient of the mass is positive, or -1 if it is negative (GONZALEZ AND WOODS, 2008). Figure 3.10(a) and (b) show the comparison between an original image and the enhanced one. In order to apply this filter, the image class was changed, allowing intensity numbers in the range of 0 to 1, which corresponds to 255. Values near 0 were considered black.

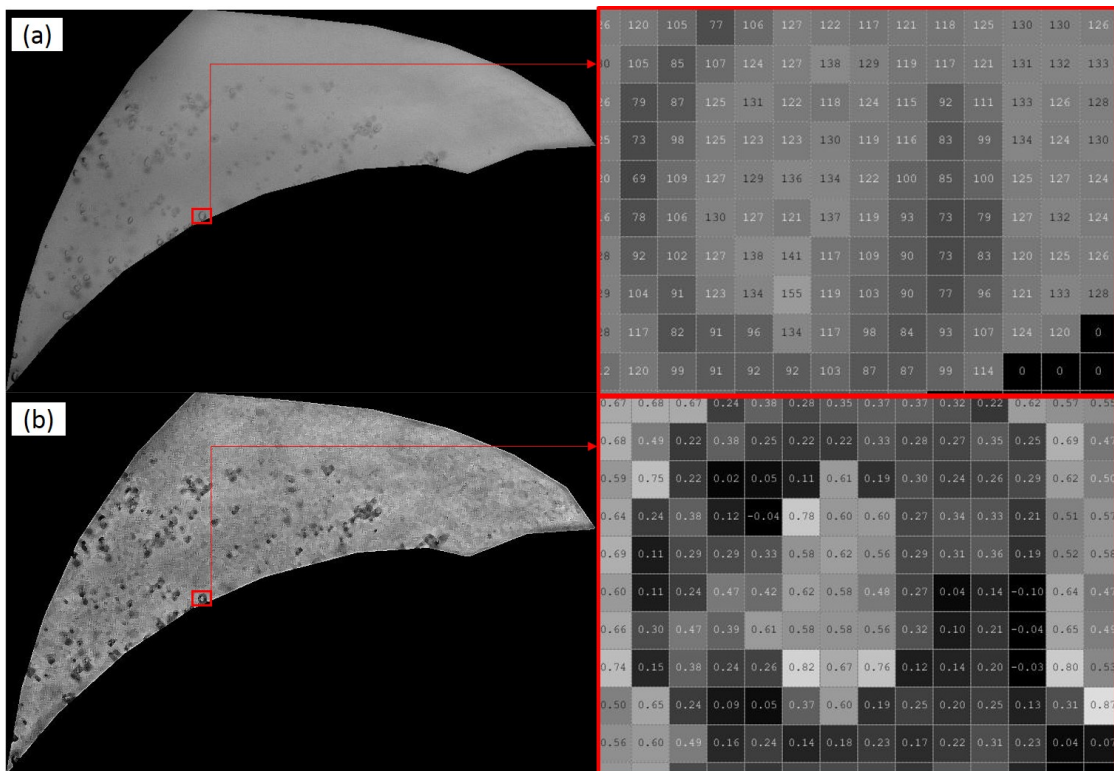


Figure 3.10: Contrast Improvement: (a) Original Image - (b) Laplacian filter applied.

The borders of bubbles in Figure 3.10 were prominent in the comparison, thus increasing the efficiency when binarizing the frames. The binarization process has a threshold value between 0 and 255, changing the color of divided pixels into black, 0 or white, 1 (SONKA *et al.*, 2014). The threshold value is chosen and checked visually. After that, a median filter was applied, reducing noise. Each output pixel contains the median value in a 3-by-3 neighborhood around the corresponding pixel in the input

image, symmetrically extending the image at the boundaries.

The resulting matrix contains values of pixel intensities of 0 and 1. The black values inside the mask indicate the bubbles, where the values corresponding to 1 are white. This matrix is submitted to a filter called "area filter", inside the same script. It consists of removing regions with an area smaller than a threshold value ($5 px^2$ in our experiments), i.e., values smaller than this were changed from 0 to 1 inside the binarized matrix. This value is chosen because comparing visually to real images it was shown not to be a bubble.

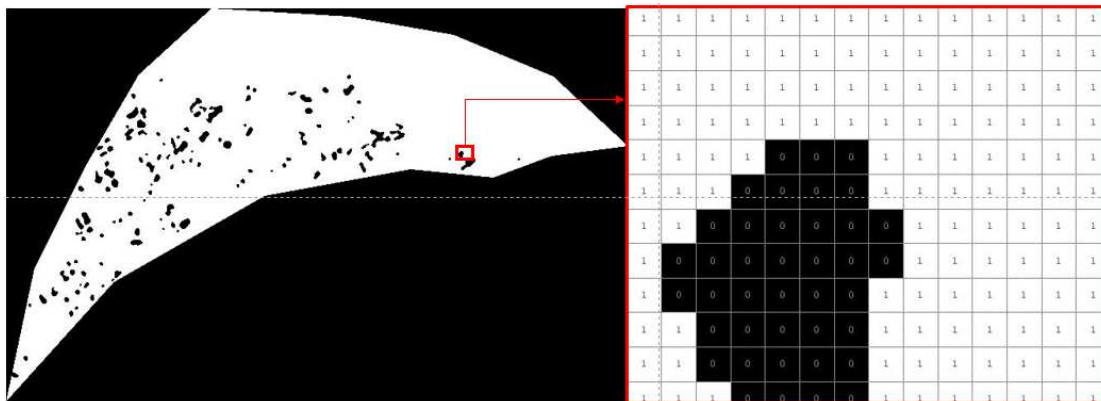


Figure 3.11: Binarized image with values 0 (black) and 1 (white).

Some parameters may be acquired from the bubbles, such as area, perimeter, hydraulic diameter, eccentricity, and some others. For the eccentricity information, a filter called "eccentricity filter" was used in order to remove some elements with higher eccentricity. This parameter is useful to compare with the bubble's circumferential shape. High values were not expected, so they were excluded from the analysis. The threshold of .95 was arbitrarily chosen after a comparison with real images, so values above this one were removed.

Finally, the information acquired from the first part of the code was saved in a cell array inside Matlab. Each cell may contain any kind of data, such as text, numbers, among others. In our case, four variables were saved: diameters, bubble position, size of the matrix and the sum of the bubble's areas in the impeller channel.

3.2.2 Bubble Velocity, Displacement and Diameter Analysis

The second part of the code starts opening the data matrices acquired in the first part. The cell array is opened, and the raw data needs to be placed in a manner that every bubble position should be certified to be placed in the same address of the next, and the next one, and so on successively in the matrices. This is achieved by writing a script that enables the code to follow a bubble as it passes through the impeller channel. If this is not adequately applied, the bubble's velocity is not computed correctly. The matrices changed their size because that bubble being followed leaves the impeller channel or a new bubble enters, or even both situations.

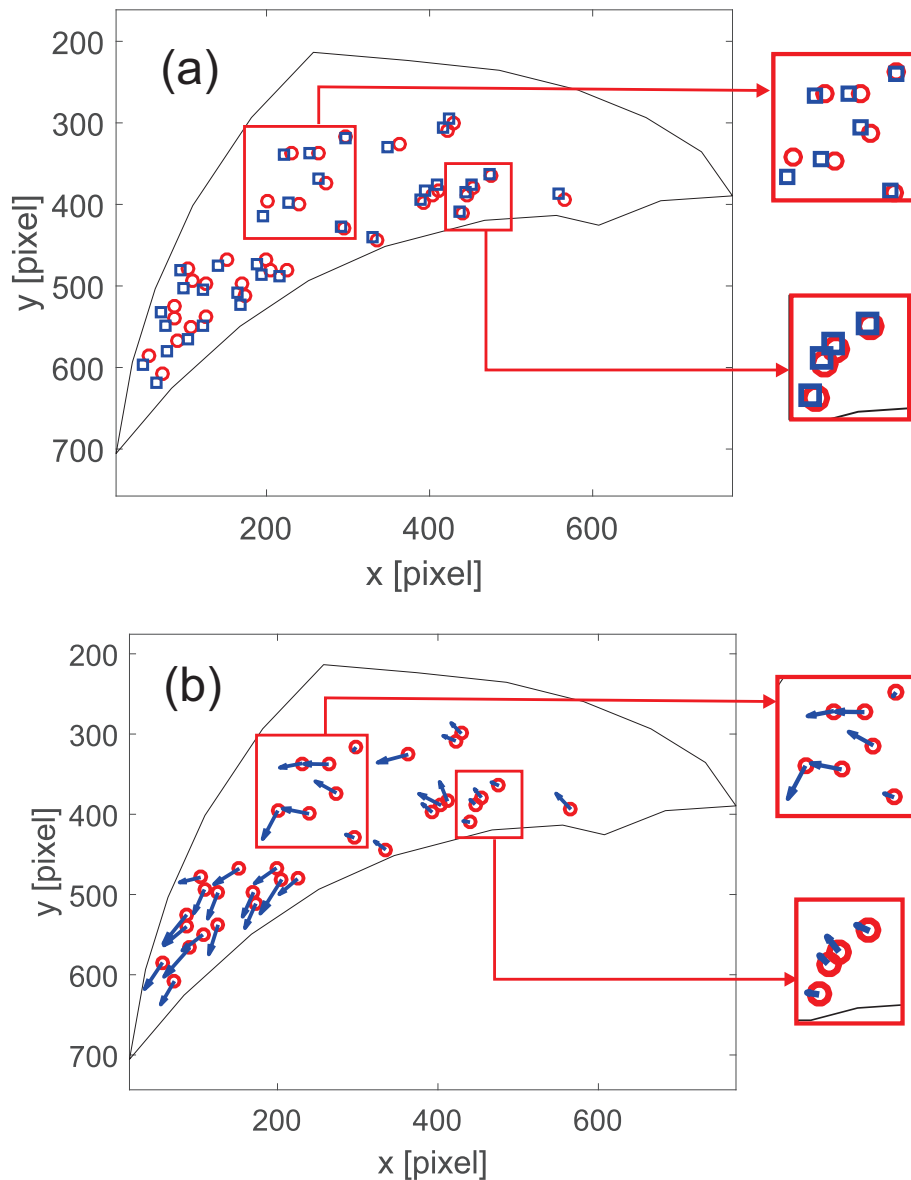


Figure 3.12: Bubble analysis: (a) Bubbles centroids (b) Bubbles' velocity vectors.

The pairing process demands a comparison between sequential matrices. The possible pairs were only accepted after passing through a filter, which is related to the position expected from that bubble. In a pair of frames, the bubble position denoted by S_{b2} should be near the position of the same bubble in the first frame analyzed, denoted by S_{b1} .

The filter is based on the Kalman filters found in the literature (WELCH

et al., 1995), which is a well-known technique in space and military industries. The principle of this filter is prediction, and this is used here. The script follows the displacements of the same bubble in time, computing those that are nearest the first one. In some cases, more than one result may be found, so the diameter is used as a tiebreaker. However, if the diameter criterion is insufficient, the proximity criterion is used. So, the one that is nearest the first bubble is chosen.

After passing through this filter, the pair is accepted. This is done repeatedly for all pairs of frames. The difference between the matrices is obtained, and the displacements are acquired. Figure 3.12(a) shows the centroids of bubbles, red circles in the first frame (t_1) and blue squares in the second frame (t_2).

Finally, by multiplying the displacements by the frequency acquired, the velocities were obtained. Figure 3.12(b) shows the velocity vectors of air bubbles. The code also computes bubbles' areas in the impeller, allowing the possibility to calculate both the diameter and an approximation for the gas void fraction. The results of the code are shown in chapter 5.

4 MODELING

This chapter presents the two-dimensional drift-flux model for the gas-liquid flow within the ESP impeller. Initially, the geometric notation used is discussed and the blade coordinate system is presented here with the non-inertial frame of reference. Besides, the Navier-Stokes equations are shown and also the closure relationship, such as the interfacial terms used.

4.1 Geometric Notation

The geometry of a rotodynamic machines consists of a set of rotor blades attached to a hub and operating within a static casing. In the case studied the gap between the case and the blade is neglected which means that looking at a cross-section view through the axis of the pump impeller, the blade perfectly match the space between hub and shroud. The angle $\beta(r)$ is related to the blade angle in relation of $\hat{\theta}$ -direction showed in Fig. 4.1. The velocity represented by the letter v is the velocity of a flow particle \mathbf{P} in non-inertial frame of reference. A detailed description of the kinematics of the movement is in section 4.1.2. The angle φ is the angle of velocity \vec{v} in relation of $\hat{\theta}$ -direction. The inner/entrance and outer/exit radius are defined as r_i and r_o , respectively, and the subscript b refers to the blade.

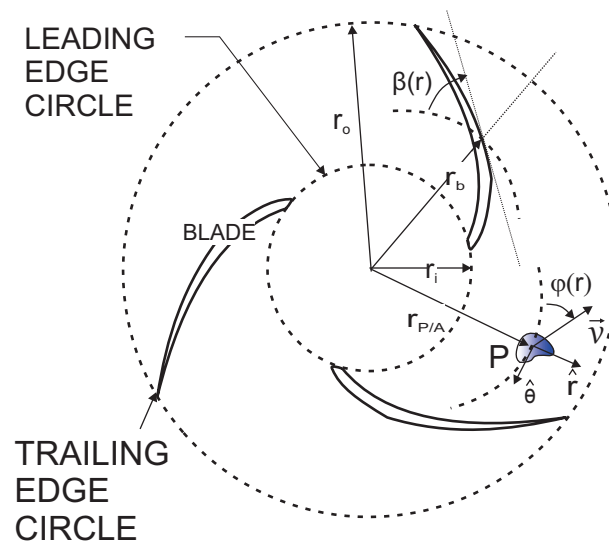


Figure 4.1: Impeller domain

The geometry of the pump in radial cascade is sketched in Fig. 4.1. Cascade is a concept that exists for axial and radial pumps. Considering a purely axial flow machine, the development of a cylindrical surface within the machine produces a linear cascade. In a centrifugal machine which the flow is purely radial, a cross-section of the flow is shown by Fig. 4.1 which means an array known as radial cascade (BRENNEN, 1994). Radial pumps can be approximated as a channel that have a variable cross-section, which means that the cross-sectional area at entrance is different from the exit. Besides, the channel has a curvature and its structure is axisymmetric, allowing periodic condition in the simulations. To represent that, the cross-section area is a function of radius and subscripts i and o are used to denote the areas for entrance and exit, respectively. The transversal area varies between the entrance radius r_i and the exit radius r_o , and it is represented by Eq. 4.1 as a function of the radius.

$$A(r) = \frac{2\pi h}{Z_b} r \quad (4.1)$$

where h is related to the channel height and Z_b is the number of blades.

The analysis of the hydrofoil and the impeller channels begins in a two-dimensional perspective. The terminology used to define foil section geometry is described in Fig. 4.2, where:

- 1: Leading edge;
- 2: Maximum thickness;
- 3: Camber;
- 4: Pressure side;
- 5: Trailing edge;
- 6: Camber mean-line;
- 7: Suction side.

The cord length was represented by letter c . The camber mean-line of the hydrofoil is a parametric curve in polar coordinates which can be represented by logarithmic spiral described by Eqs. 4.2. The angle θ can be related as a function of radius, $\theta = f(r)$ and with this, the blade profile is described in polar coordinates. The blade parametric curve which describes the camber mean-line is given by:

$$r_b = ae^{b\theta_b} \quad \text{or} \quad \theta_b = \frac{\ln r_b/a}{b} \quad (4.2)$$

where r is the distance from the origin, θ is the angle from the x-axis, and a and b

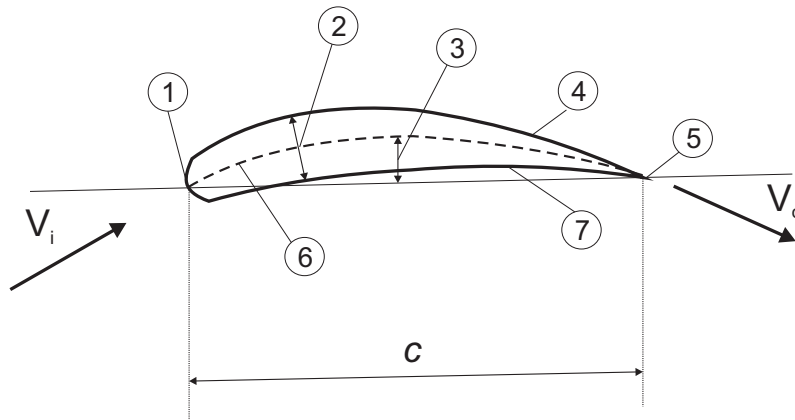


Figure 4.2: Profile geometry - 1: Leading edge; 2: Max. thickness; 3: Camber; 4: Pressure side; 5: Trailing edge; 6: Camber mean-line; 7: Suction side.

are arbitrary constants. The logarithmic spiral is also known as the growth spiral or equiangular spiral. The system coordinates are related in Eq. 4.3:

$$\begin{aligned} x &= r \cos(\theta) = a e^{b\theta} \cos(\theta) \\ y &= r \sin(\theta) = a e^{b\theta} \sin(\theta) \end{aligned} \quad (4.3)$$

The camber mean-line profile can be characterized using the coordinates of trailing and leading edge, as indicated in Fig. 4.3. The coordinates of r_{bL} and r_{bT} are given by Eq. 4.4.

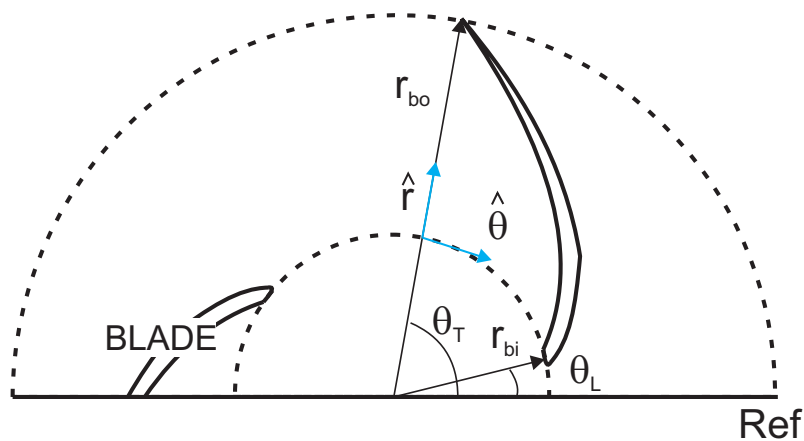


Figure 4.3: Blade characterization using trailing and leading edge

$$\begin{aligned} r_{bL} = \{r_{bi}, \theta_L\} &\rightarrow r_i = ae^{b\theta_L} \\ r_{bT} = \{r_{bo}, \theta_T\} &\rightarrow r_o = ae^{b\theta_T} \end{aligned} \quad (4.4)$$

The constants a and b can be calculated using Eq. 4.2 for two points $\{r_i, \theta_L\}$ and $\{r_o, \theta_T\}$, so b becomes:

$$\frac{r_i}{r_o} = \frac{ae^{b\theta_L}}{ae^{b\theta_T}} = e^{b(\theta_L - \theta_T)}$$

$$\boxed{b = \ln\left(\frac{r_i}{r_o}\right) / (\theta_L - \theta_T)} \quad (4.5)$$

The constant a is:

$$a = \frac{r_i}{(e^b)^{\theta_L}} = \frac{r_i}{[e^{\ln(r_i/r_o)}]^{\theta_L/(\theta_L - \theta_T)}} = \frac{r_i}{(r_i/r_o)^{\theta_L/(\theta_L - \theta_T)}}$$

$$\boxed{a = \frac{r_o^{\theta_L/(\theta_L - \theta_T)}}{r_i^{\theta_T/(\theta_L - \theta_T)}}} \quad (4.6)$$

The radius and the azimuth of trailing and leading edge with Eqs. 4.5 and 4.6 were used to acquire the constants a and b , which represents the camber mean-line of the hydrofoil used experimentally. The constant parameters a and b were estimated using the points in the blade profile. Those constants were acquired using a code in the Matlab platform, so they are 105.61 and -0.550, respectively. Thus, those constants defines the logarithmic spiral.

In posses of those constants the log-polar coordinates were used followed by a transformation in order to acquire dimensionless form of radius and theta:

$$r = ae^{b\theta} \rightarrow \rho = \ln r = b\theta + \ln a \rightarrow \theta = \frac{\rho - \ln a}{b}$$

$$\tilde{\rho} = \frac{\rho - \rho_i}{\rho_o - \rho_i} = \frac{\ln r - \ln r_i}{\ln r_o - \ln r_i} = \frac{\ln(r/r_i)}{\ln(r_o/r_i)} \rightarrow \boxed{\tilde{\rho} \in [0,1]} \quad (4.7)$$

$$\tilde{\theta} = \frac{\theta - (\rho - \ln a)/b}{\theta_c} = \frac{b\theta - \rho + \ln a}{b\theta_c} \quad \text{where } \theta_c = 2\pi/Z_b \rightarrow \boxed{\tilde{\theta} \in [0,1]} \quad (4.8)$$

Using Eqs. 4.7 and 4.8 it is possible to transform the volume control presented in Fig. 4.4(a) in a dimensionless form, as showed in Fig. 4.4(b).

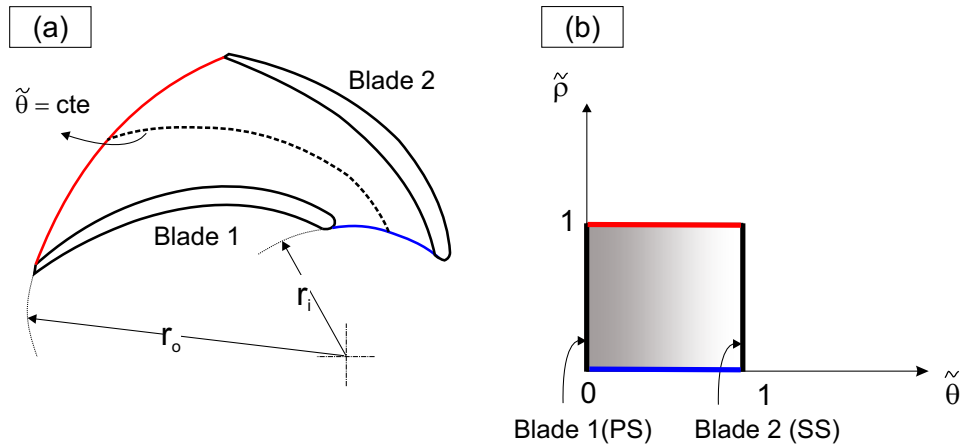


Figure 4.4: Impeller channel: (a) control volume - (b) dimensionless form

Figure 4.5 shows the camber mean-line and the vector $\vec{b}(\theta)$ that links the center of the impeller to the blade. Vector \vec{b} is a parametric curve in function of azimuth θ which describes the blade geometry and it is aligned with \hat{r} . According with logarithmic spiral: $\vec{b}(\theta) = ae^{b\theta}\hat{r}$. The tangent vector $d\vec{b}/d\theta$ is given by:

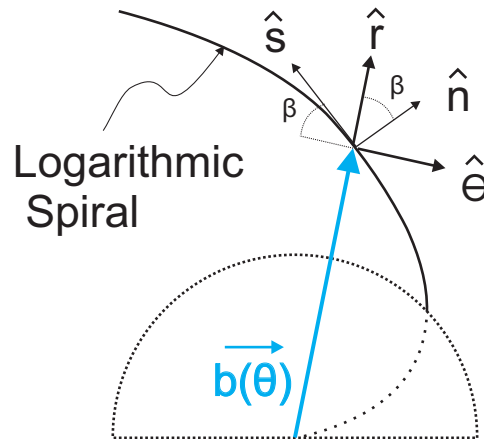


Figure 4.5: Blade coordinates

$$\begin{aligned}
\vec{d}_{sb} &= \frac{d\vec{b}}{d\theta} = \frac{d}{d\theta}(ae^{b\theta})\hat{r} + ae^{b\theta}\frac{d\hat{r}}{d\theta} \\
\vec{d}_{sb} &= ab e^{b\theta}\hat{r} + ae^{b\theta}r\hat{\theta} = br\hat{r} + r\hat{\theta} \\
\|\vec{d}_{sb}\| &= r\sqrt{b^2 + 1}
\end{aligned} \tag{4.9}$$

So, versor \hat{s} is a vector tangent and normalized which follows the blade profile so it can be used as a base for curvilinear coordinate system.

$$\begin{aligned}
\hat{s} &= \frac{\vec{d}_{sb}}{\|\vec{d}_{sb}\|} = \frac{b}{\sqrt{b^2 + 1}}\hat{r} + \frac{1}{\sqrt{b^2 + 1}}\hat{\theta} \\
\hat{s} &= \left\{ \frac{b}{\sqrt{b^2 + 1}}, \frac{1}{\sqrt{b^2 + 1}} \right\}
\end{aligned} \tag{4.10}$$

Normal versor denoted as \hat{n} should be normal in relation to the blades, for this it needs to respect inner product for normal vectors, so:

$$\hat{s} \cdot \hat{n} = 0 \quad \rightarrow \quad (s_r, s_\theta) \cdot (n_r, n_\theta) = 0 \quad \rightarrow \quad s_r n_r = -s_\theta n_\theta \tag{4.11}$$

Equation 4.11 can be solved doing $n_r = -s_\theta$ and $n_\theta = s_r$. So, \hat{n} becomes:

$$\hat{n} = -s_\theta\hat{r} + s_r\hat{\theta} = \{-s_\theta, s_r\} \tag{4.12}$$

Equation 4.12 showed a relation between the components of \hat{s} and \hat{n} . The difference here is the negative component s_θ .

$$\hat{s} \times \hat{n} = \begin{bmatrix} \hat{r} & \hat{\theta} & \hat{z} \\ s_r & s_\theta & 0 \\ -s_\theta & s_r & 0 \end{bmatrix} = (s_r^2 + s_\theta^2) \cdot \hat{z} = \hat{z} \tag{4.13}$$

In the same way, the cross product $\hat{s} \times \hat{n}$ is equal to \hat{z} and also equals to $\hat{r} \times \hat{\theta}$, common for both coordinate system. This was satisfied by Eq. 4.13, where $(s_r^2 + s_\theta^2) = \|s\|^2 = 1$,

as it is a versor. The angle between \hat{s} and \hat{r} indicated in Fig. 4.5 as β is:

$$\frac{\pi}{2} - \beta = \arccos \left(\frac{\vec{s}}{\|\vec{s}\|} \cdot \frac{\vec{r}}{\|\vec{r}\|} \right) \quad \rightarrow \quad \text{where} \quad \begin{cases} \|\vec{s}\| = 1 \\ \|\vec{r}\| = 1 \end{cases}$$

$$\beta = \frac{\pi}{2} - \arccos \left[\left\{ \frac{b}{\sqrt{b^2 + 1}}, \frac{1}{\sqrt{b^2 + 1}} \right\} \cdot \{1, 0\} \right]$$

$$\beta = \frac{\pi}{2} - \arccos \left(\frac{b}{\sqrt{b^2 + 1}} \right) = \frac{\pi}{2} - \arctan \left(\frac{1}{b} \right) = \frac{\pi}{2} - \cot^{-1}(b) \quad (4.14)$$

The trigonometric passage that occurs in Eq. 4.14 is explained using Pythagorean theorem, where $\sqrt{b^2 + 1}$ is the length of the hypotenuse and b and 1 are the other two sides. So, $\arccos (b/(\sqrt{b^2 + 1}))$ is equal to $\arctan (1/b)$. In this case, b is one of the constants used in logarithmic spiral, β is also a constant. It is important to note that considering the camber mean-line the blade profile was not considered. This assumption leads the hypothesis of flow parallel to the blade, which is not real. The blade coordinate system represents a rotation in rigid body of polar coordinate system and may be represented by the follow equations:

$$\begin{aligned} \hat{s} &= \sin \beta \hat{r} - \cos \beta \hat{\theta} \\ \hat{n} &= \cos \beta \hat{r} + \sin \beta \hat{\theta} \end{aligned}$$

$$\begin{bmatrix} \hat{s} \\ \hat{n} \end{bmatrix} = \begin{bmatrix} \sin \beta & -\cos \beta \\ \cos \beta & \sin \beta \end{bmatrix} \begin{bmatrix} \hat{r} \\ \hat{\theta} \end{bmatrix} \quad (4.15)$$

The matrix in Eq. 4.15 rotates points in $r\theta$ -plane counterclockwise through an angle $(\pi/2 - \beta)$ about the origin of the polar coordinate system. This rotation matrix is called \mathbf{R} matrix which is orthogonal and its determinant is equal to 1. This matrix has a property of its inverse matrix is equals to its transpose matrix, in other words $\mathbf{R}^T = \mathbf{R}^{-1}$. So:

$$\begin{bmatrix} \hat{r} \\ \hat{\theta} \end{bmatrix} = \begin{bmatrix} \sin \beta & \cos \beta \\ -\cos \beta & \sin \beta \end{bmatrix} \begin{bmatrix} \hat{s} \\ \hat{n} \end{bmatrix} \quad (4.16)$$

4.1.1 Non-Inertial and Inertial Frames of Reference

A discussion on the equations of motion in fluid mechanics of rotating machinery are often best analyzed in a rotating frame of reference. In this case the continuity equation is unchanged but the momentum equation must be modified. Considering a non-inertial frame of reference xyz in Fig. 4.6 and a inertial frame of reference XYZ .

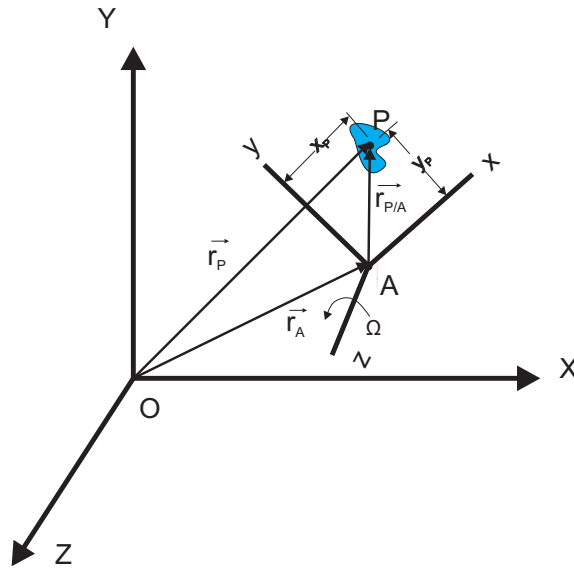


Figure 4.6: Non-inertial (x,y,z) and inertial (X,Y,Z) reference frame

Rotational forces must be considered in centrifugal pump, particularly two fictitious forces must be considered: the Coriolis force and the centrifugal force. They will be discussed later. The position of particle P can be described in relation to non-inertial reference frame, denoted as $\vec{r}_{P/A}$ or it can be described in relation to the inertial reference frame, denoted as \vec{r}_P . This is showed in Fig. 4.6. These distances are simply related by the position vector of a flow particle P as:

$$\vec{r}_P = \vec{r}_A + \vec{r}_{P/A} \quad \rightarrow \quad \text{where} \quad \begin{cases} \vec{r}_P = P \text{ position in } \{X,Y,Z\} \\ \vec{r}_A = A \text{ position in } \{X,Y,Z\} \\ \vec{r}_{P/A} = P \text{ position in } \{x,y,z\} \end{cases} \quad (4.17)$$

The derivative of a vector in a non-inertial reference frame should be used now.

Generally, the representation of a vector in a non-inertial frame neglect its movements, so when the derivative is calculated the translation of system origin must be taken into account besides the impeller rotation. The derivative of a vector is given by:

$$\frac{d(\cdot)_{\{X,Y,Z\}}}{dt} = \frac{d\vec{A}}{dt} + \vec{\Omega} \times (\cdot)_{\{x,y,z\}} + \frac{d(\cdot)_{\{x,y,z\}}}{dt} \quad (4.18)$$

So the time derivative of Eq. 4.17 becomes:

$$\begin{aligned} \frac{d\vec{r}_P}{dt} &= \frac{d\vec{r}_A}{dt} + \vec{\Omega} \times \vec{r}_{P/A} + \frac{d\vec{r}_{P/A}}{dt} \\ \vec{V}_P &= \vec{V}_A + \vec{\Omega} \times \vec{r}_{P/A} + \vec{v}_P \end{aligned} \quad (4.19)$$

where Ω represents the rotation pseudo-vector, V in uppercase letter represents the velocity measured from $\{X, Y, Z\}$ reference and v in lower case is the velocity measured from $\{x, y, z\}$.

Using the same procedure indicated by Eq. 4.18 the velocity expression was derived so the acceleration of P , observed from the $\{X, Y, Z\}$ coordinate system, may be expressed in terms of its motion measured with respect to the rotating system of coordinates by taking the time derivative of Eq. 4.19 (HIBBELER, 2010). The result is:

$$\frac{d\vec{V}_P}{dt} = \frac{d\vec{V}_A}{dt} + \frac{d}{dt}(\vec{\Omega} \times \vec{r}_{P/A}) + \frac{d\vec{v}_P}{dt} + \vec{\Omega} \times \vec{v}_P$$

or:

$$\vec{A}_P = \vec{A}_A + \frac{d}{dt}(\vec{\Omega} \times \vec{r}_{P/A}) + \vec{\Omega} \times \frac{d\vec{r}_A}{dt} + \vec{a}_P + \vec{\Omega} \times \vec{v}_P \quad (4.20)$$

where $d\Omega/dt$ is the acceleration of coordinate system. Substituting $d(\vec{r}_{P/A})/dt$, previously calculated, Eq. 4.20 becomes:

$$\vec{A}_P = \vec{A}_A + \dot{\vec{\Omega}} \times \vec{r}_{P/A} + \vec{\Omega} \times (\vec{\Omega} \times \vec{r}_{P/A} + \vec{v}_P) + \vec{a}_P + \vec{\Omega} \times \vec{v}_P \quad (4.21)$$

This expression can be simplified substituting some terms by \vec{A}_f , fictitious accelerations:

$$\vec{A}_f = \vec{A}_A + \dot{\vec{\Omega}} \times \vec{r}_{P/A} + 2\vec{\Omega} \times \vec{v}_P + \vec{\Omega} \times \vec{\Omega} \times \vec{r}_{P/A} \quad (4.22)$$

$$\text{where } \begin{cases} \dot{\vec{\Omega}} \times \vec{r}_{P/A} = \text{Euler acceleration} \\ 2\vec{\Omega} \times \vec{v}_P = \text{Coriolis acceleration} \\ \vec{\Omega} \times \vec{\Omega} \times \vec{r}_{P/A} = \text{Centripetal acceleration} \end{cases}$$

These three accelerations appear when the vector was derived in a non-inertial reference frame. Those three accelerations does not exists at all, they were derived as a result of a position description of a particle without being connected, in fact, with a force. Moreover, the impeller and the center of reference system coincide, which means that no translation was present and the rotation velocity Ω is constant. So, the fictitious accelerations becomes:

$$\vec{A}_f = 2\vec{\Omega} \times \vec{v}_P + \vec{\Omega} \times \vec{\Omega} \times \vec{r}_{P/A} \quad (4.23)$$

Figure 4.7 shows the rotation $\vec{\Omega}$ and a particle along the impeller's channels. The reference system of this particle was already described in Fig. 4.6. The rotation of the particle is represented by vector Ω which is equal to $\{0, 0, \omega\}$, $\vec{r}_{P/A} = \{r, 0, 0\}$ and $\vec{v}_P = \{v_r, v_\theta, 0\}$ which represents the distance of particle and its velocity, respectively.

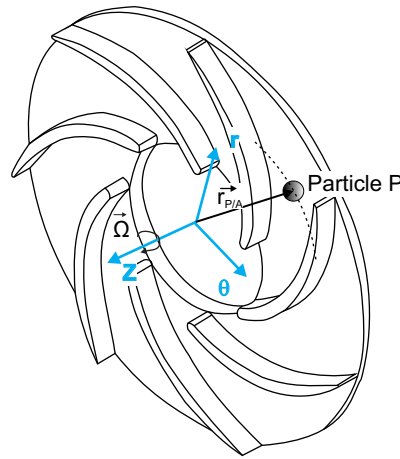


Figure 4.7: Particle P along the impeller

The two terms knowing by Coriolis A_{cor} and centripetal A_{ctp} accelerations in polar

coordinates are showed in Eq. 4.24 and 4.26, respectively.

$$A_{cor} = 2\vec{\Omega} \times (\vec{v}_{P/A})_{xyz} = 2 \begin{bmatrix} \hat{r} & \hat{\theta} & \hat{z} \\ 0 & 0 & \omega \\ v_r & v_\theta & 0 \end{bmatrix}$$

$$\boxed{\vec{A}_{cor} = -2\omega v_\theta \hat{r} + 2\omega v_r \hat{\theta}} \quad (4.24)$$

$$\vec{\Omega} \times \vec{r}_{P/A} = \vec{\Omega} \times \begin{bmatrix} \hat{r} & \hat{\theta} & \hat{z} \\ 0 & 0 & \omega \\ r & 0 & 0 \end{bmatrix} = \omega r \hat{\theta} \quad (4.25)$$

$$A_{ctp} = \vec{\Omega} \times \vec{\Omega} \times \vec{r}_{P/A} = \begin{bmatrix} \hat{r} & \hat{\theta} & \hat{z} \\ 0 & 0 & \omega \\ 0 & \omega r & 0 \end{bmatrix}$$

$$\boxed{\vec{A}_{ctp} = -\omega^2 r \hat{r}} \quad (4.26)$$

4.1.2 Kinematics for Rotor Dynamics

In the previous section the velocity of a point **P** was described, relating it between an inertial {X, Y, Z} and non-inertial {x, y, z} reference frame.

$$\vec{V}_P = \vec{v}_P + \vec{\Omega} \times \vec{r}_{P/A} \quad \text{where it was assumed that: } \vec{V}_A = 0 \quad (4.27)$$

The term $\vec{\Omega} \times \vec{r}_{P/A}$ in this case corresponds to tangential velocity, which is equal to $\omega r \hat{\theta}$ (Eq. 4.25). So:

$$\vec{V}_P = \vec{v}_P + \omega r \hat{\theta} \quad (4.28)$$

Equation 4.28 is represented in a velocity triangle indicated in Fig. 4.8. The Greek letter φ represents the inclination between velocity \vec{v}_P and versor $\hat{\theta}$. In a complex velocity field, as it is in a pump impeller, φ would be a function of r and θ . However, it is common to simplify it for an axisymmetric flow as $\varphi(r)$.

The incidence γ and deviation δ angles are defined in relation to the blade angle.

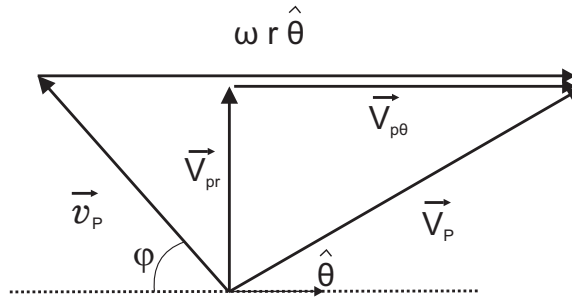


Figure 4.8: Velocity vectors at the discharge

So, they are respectively (BRENNEN, 1994):

$$\gamma = \varphi(r_i) - \beta(r_i) \quad \delta = \varphi(r_o) - \beta(r_o) \quad (4.29)$$

However, for the hypothesis of parallel flow through the blade, both are equal to zero, because $\varphi(r) = \beta(r)$ (BRENNEN, 1994). Considering for a logarithmic spiral $\beta(r) = \beta$, the velocity triangle is rewritten and presented in Fig. 4.9 .

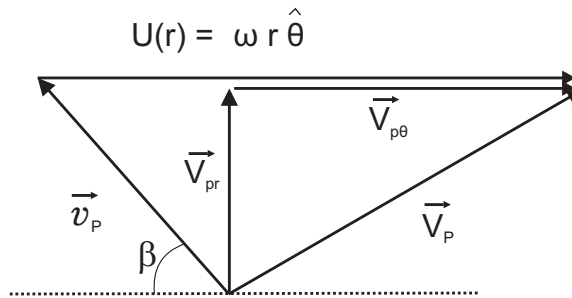


Figure 4.9: Velocity vectors at the discharge

From now, the letter P will be suppressed for simplicity. The velocities are written in function of v_r or V_r , which are equal. This is made because its velocity is related to mass flow rate.

$$v_r = V_r = v \sin \beta \quad \rightarrow \quad \boxed{v = \frac{v_r}{\sin \beta}} \quad (4.30)$$

$$v_\theta = -v \cos \beta = -v_r \frac{\cos \beta}{\sin \beta} \quad \rightarrow \quad \boxed{v_\theta = -v_r \cot \beta} \quad (4.31)$$

$$V_\theta = \omega r + v_\theta = \omega r - v_r \cot \beta \quad \rightarrow \quad \boxed{V_\theta = \omega r - v_r \cot \beta} \quad (4.32)$$

The angle β is equal to $\pi/2 - \cot^{-1}(b)$, so:

$$\cot \beta = \cot \left[\frac{\pi}{2} - \cot^{-1}(b) \right] \quad (4.33)$$

For simplicity, $-\cot^{-1}(b) = B$, so Eq. 4.33 becomes:

$$\cot \left(\frac{\pi}{2} + B \right) = \frac{\cos(\pi/2) \cos B - \sin(\pi/2) \sin B}{\sin(\pi/2) \cos B + \sin B \cos(\pi/2)} = -\frac{\sin B}{\cos B} = -\tan B \quad (4.34)$$

The angle B has its tangent calculated here:

$$B = -\cot^{-1}(b) = -\arctan \left(\frac{1}{b} \right) \quad (4.35)$$

$$\cot \beta = -\tan \left[-\arctan \left(\frac{1}{b} \right) \right] = \tan \left[\arctan \left(\frac{1}{b} \right) \right] = \frac{1}{b}$$

$$\boxed{\cot \beta = \frac{1}{b}} \quad (4.36)$$

The velocity field in non-inertial and inertial reference frame is defined as:

$$\boxed{v_r = V_r} \quad (4.37)$$

$$v_\theta = -v_r \cot \beta = -\frac{v_r}{b} \rightarrow \boxed{v_\theta = -\frac{v_r}{b}} \quad (4.38)$$

$$V_\theta = \omega r + v_\theta = \omega r - v_r \cot \beta = \omega r - \frac{v_r}{b} \rightarrow \boxed{V_\theta = \omega r - \frac{v_r}{b}} \quad (4.39)$$

4.2 Modeling Gas-Liquid Flow - Drift-Flux Model

The development of drift-flux model formulation in this study uses the mass and momentum equations. They are developed considering a specific set of operations of an electric submersible pump (ESP). Considering a two-phase gas-liquid flow where subscript 1 and 2 were used for the gas and water phases, respectively. The letter k was used to represent the phases in the equations. To begin the calculations some hypothesis were assumed:

- Incompressible fluids;
- No mass transfer between the phases;
- Constant local properties (thermal conductivity, specific heat, no fluid thermal expansion);
- Viscosity is function of the temperature only;
- Steady state;
- Neglecting superficial and interfacial tension;
- Assuming no variation in z-direction;
- Neglecting hydrofoil thickness.

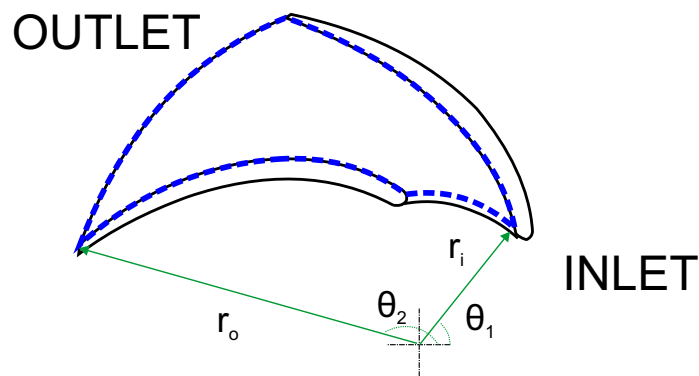


Figure 4.10: Impeller domain

The impeller was modeled using the concept of a radial cascade (BRENNEN, 1994) where the blade profile follows a logarithmic spiral (section 5.1). The real structure has blades whose set forms a hydrofoil distorted whose camber mean line follows a logarithmic spiral. Besides, the domain presented in Fig. 4.10 is axisymmetric and periodic, so the description can be done by just one channel.

The channel is a tube of quadratic section, curved where its area varies in a non-inertial frame of reference. So, beginning with the two-fluid model considering the hypothesis already exposed, the differential equations were written in polar coordinates.

4.2.1 Continuity Equation:

$$\begin{aligned} \frac{1}{r} \frac{\partial}{\partial r} (\alpha_k \rho_k r v_{kr}) + \frac{1}{r} \frac{\partial}{\partial \theta} (\alpha_k \rho_k v_{k\theta}) &= 0 \\ \frac{\partial}{\partial r} (\alpha_k \rho_k r v_{kr}) + \frac{\partial}{\partial \theta} (\alpha_k \rho_k v_{k\theta}) &= 0 \end{aligned} \quad (4.40)$$

The volumetric flux of each phase in mixture, j_k , is given by (ISHII AND HIBIKI, 2010):

$$j_k = \alpha_k v_k \quad (4.41)$$

Equation 4.40 becomes:

$$\frac{\partial}{\partial r} (\rho_k r j_{kr}) + \frac{\partial}{\partial \theta} (\rho_k j_{k\theta}) = 0 \quad (4.42)$$

Using the hypothesis of incompressible flow (Mach $\ll 1$):

$$\rho_k \frac{\partial}{\partial r} (r j_{kr}) = -\rho_k \frac{\partial}{\partial \theta} (j_{k\theta}) \quad (4.43)$$

As we are interesting in variation of velocity through the impeller in r direction Eq. 4.43 is wrote in its weak form for azimuth direction. It is integrated in θ and no-slip condition in the walls is used.

$$\begin{aligned} \frac{\partial}{\partial r} (r j_{kr}) &= -\frac{\partial}{\partial \theta} (j_{k\theta}) \\ \int_{\theta_1(r)}^{\theta_2(r)} \frac{\partial}{\partial r} (r j_{kr}) d\theta &= -\int_{\theta_1(r)}^{\theta_2(r)} \frac{\partial}{\partial \theta} (j_{k\theta}) d\theta \\ \int_{\theta_1(r)}^{\theta_2(r)} \frac{\partial}{\partial r} (r j_{kr}) d\theta &= -j_{k\theta} \Big|_{\theta_1(r)}^{\theta_2(r)} = 0 \end{aligned} \quad (4.44)$$

The term $j_{k\theta}(\theta_1(r))$ and $j_{k\theta}(\theta_2(r))$ where null because the no-slip condition.

$$\boxed{\int_{\theta_1(r)}^{\theta_2(r)} \frac{\partial}{\partial r} (r j_{kr}) d\theta = 0} \quad (4.45)$$

The impeller channel is modeled as a curved duct with variable cross section area.

The interest of the present study is to model the terms in θ as a mean letting the variables in function of radius. The mean in θ is calculated using the Leibniz's rule.

$$\int_{\theta_1(r)}^{\theta_2(r)} \frac{\partial}{\partial r} [r \alpha_k(r, \theta) v_{kr}(r, \theta)] d\theta = \frac{d}{dr} \int_{\theta_1(r)}^{\theta_2(r)} [r \alpha_k(r, \theta) v_{kr}(r, \theta)] d\theta \quad (4.46)$$

$$-r \alpha_k(r, \theta_2) v_{kr}(r, \theta_2(r)) \frac{\partial}{\partial r} \theta_2(r) + r \alpha_k(r, \theta_1) v_{kr}(r, \theta_1(r)) \frac{\partial}{\partial r} \theta_1(r)$$

The two final terms on right hand side, expressed in Eq. 4.47 are equal to zero because of no-slip boundary condition. If this condition was not applied, this will be dependent of parametric curved formed by the logarithm spiral.

$$r \alpha_k(r, \theta_2) v_{kr}(r, \theta_2(r)) \frac{\partial}{\partial r} \theta_2(r) = 0$$

$$r \alpha_k(r, \theta_1) v_{kr}(r, \theta_1(r)) \frac{\partial}{\partial r} \theta_1(r) = 0 \quad (4.47)$$

Equation 4.46 becomes:

$$\boxed{\int_{\theta_1(r)}^{\theta_2(r)} \frac{\partial}{\partial r} [r \alpha_k(r, \theta) v_{kr}(r, \theta)] d\theta = \frac{d}{dr} \int_{\theta_1(r)}^{\theta_2(r)} \alpha_k(r, \theta) v_{kr}(r, \theta) r d\theta} \quad (4.48)$$

The derivative and the integral operator are commutative because of no-slip conditions used for blades (θ_1 and θ_2). So, multiplying Eq. 4.48 for $1/\Delta\theta$, in order to obtain the average operator, where $\Delta\theta = 2\pi/Z_b = \theta_2(r) - \theta_1(r)$:

$$\frac{1}{\Delta\theta} \int_{\theta_1(r)}^{\theta_2(r)} \alpha_k(r, \theta) v_{kr}(r, \theta) r d\theta = C \quad (4.49)$$

The integral above is the volumetric flow rate in the surface of versor \hat{r} between θ_1 and θ_2 for phase k . Defining $(1 - \lambda) = Q_1/Q_m$, and $\lambda = Q_2/Q_m$ and the mixture flow rate as $Q_m + Q_1 + Q_2$ (ISHII AND HIBIKI, 2010), so:

$$\frac{1}{\Delta\theta} \int_{\theta_1(r)}^{\theta_2(r)} \alpha_k(r, \theta) v_{kr}(r, \theta) r d\theta = C = \left(\frac{\lambda_k Q_m}{Z_b h} \right) \left(\frac{Z_b}{2\pi} \right)$$

$$\frac{1}{\Delta\theta} \int_{\theta_1(r)}^{\theta_2(r)} \alpha_k(r, \theta) v_{kr}(r, \theta) r d\theta = \frac{\lambda_k Q_m}{2\pi h} \quad (4.50)$$

As the integral is in θ , Eq. 4.50 becomes:

$$\frac{1}{\Delta\theta} \int_{\theta_1(r)}^{\theta_2(r)} \alpha_k(r,\theta) v_{kr}(r,\theta) d\theta = \frac{\lambda_k Q_m}{2 \pi r h} \quad (4.51)$$

Defining the mean operator as:

$$\frac{1}{\Delta\theta} \int_{\theta_1(r)}^{\theta_2(r)} (\cdot) d\theta = \langle (\cdot) \rangle_\theta \quad (4.52)$$

$$\langle \alpha_k(r,\theta) \rangle_\theta = \overline{\alpha_k(r)} = \frac{1}{\Delta\theta} \int_{\theta_1(r)}^{\theta_2(r)} \alpha_k(r,\theta) d\theta \quad (4.53)$$

$$\langle v_{kr}(r,\theta) \rangle_\theta = \overline{v_{kr}(r)} = \frac{1}{\Delta\theta} \int_{\theta_1(r)}^{\theta_2(r)} v_{kr}(r,\theta) d\theta \quad (4.54)$$

The profile shape factor K is the normalized cross correlation, explained in more details below and is defined as:

$$K(r) = \frac{\langle \alpha_k(r,\theta) v_{kr}(r,\theta) \rangle_\theta}{\langle \alpha_k(r,\theta) \rangle_\theta \langle v_{kr}(r,\theta) \rangle_\theta} \quad (4.55)$$

The volumetric flux or superficial velocity is:

$$j_{kr}(r) = \frac{\lambda_k Q_m}{2 \pi h r} = \frac{Q_k}{A(r)} \quad (4.56)$$

So, Eq. 4.51 becomes:

$$\begin{aligned} \frac{1}{\Delta\theta} \int_{\theta_1(r)}^{\theta_2(r)} \alpha_k(r,\theta) v_{kr}(r,\theta) d\theta &= \frac{\lambda_k Q_m}{2 \pi h r} = j_{kr}(r) \\ \langle \alpha_k(r,\theta) v_{kr}(r,\theta) \rangle_\theta &= \frac{\lambda_k Q_m}{2 \pi h r} = j_{kr}(r) \\ \left(\frac{\langle \alpha_k(r,\theta) v_{kr}(r,\theta) \rangle_\theta}{\langle \alpha_k(r,\theta) \rangle_\theta \langle v_{kr}(r,\theta) \rangle_\theta} \right) \langle \alpha_k(r,\theta) \rangle_\theta \langle v_{kr}(r,\theta) \rangle_\theta &= \frac{\lambda_k Q_m}{2 \pi h r} = j_{kr}(r) \\ \overline{K(r) \alpha_k(r) v_{kr}(r)} &= \frac{\lambda_k Q_m}{2 \pi h r} = j_{kr}(r) \end{aligned} \quad (4.57)$$

In pipeline applications, generally for turbulent flows, the velocity profile across

de duct tends to have a symmetry when their averages were made. The major use of velocity and concentration profiles were applied into a normalized cross correlation, denoted as K (profile shape factor). In order to increase the model accuracy, this factor should be different than unity, as the flow across the impeller is clearly different from ducts. This factor represents the deviance from v and α across the impeller channel, so:

- $K(r) = 1$: Regular profile, the velocities not depends on θ direction.
- $K(r) \neq 1$: The profile across θ is considered.

The mixture volumetric flux is defined as:

$$j_m(r) = Q_m / (2 \pi r h) \quad (4.58)$$

Using this in Eq. 4.57:

$$j_{kr}(r) = \overline{K(r)} \overline{\alpha_k(r)} \overline{v_{kr}(r)} = \frac{\lambda_k Q_m}{2 \pi h r} = \lambda_k j_m(r) \quad (4.59)$$

For simplicity, $K(r)$ is adopted as = 1 and the bar above α and v will be omitted, so:

$$\begin{aligned} j_{kr}(r) &= \alpha_k(r) v_{kr}(r) \\ j_{k\theta}(r) &= \alpha_k(r) v_{k\theta}(r) = -\alpha_k(r) v_{kr} \cot \beta = -j_{kr}(r) \cot \beta \end{aligned} \quad (4.60)$$

Using the velocity triangle in Eq. 4.60, where $v_{k\theta}(r) = -v_{kr} \cot \beta$. The radial and azimuth slip are given by, respectively (ISHII AND HIBIKI, 2010):

$$v_{sr}(r) = v_{2r}(r) - v_{1r}(r) = \frac{j_{2r}}{\alpha_2} - \frac{j_{1r}}{\alpha_1} = j_m(r) \left[\frac{\lambda_2}{\alpha_2(r)} - \frac{\lambda_1}{\alpha_1(r)} \right] \quad (4.61)$$

$$v_{s\theta}(r) = v_{2\theta}(r) - v_{1\theta}(r) = \frac{j_{2\theta}}{\alpha_2} - \frac{j_{1\theta}}{\alpha_1} = -j_m(r) \left[\frac{\lambda_2}{\alpha_2(r)} - \frac{\lambda_1}{\alpha_1(r)} \right] \cot \beta \quad (4.62)$$

Using Eqs. 4.61 and 4.62 a relation between $v_{s\theta}$ and v_{sr} is:

$$\boxed{v_{sr}(r) = j_m(r) \left[\frac{\lambda_2}{\alpha_2(r)} - \frac{\lambda_1}{\alpha_1(r)} \right]} \quad (4.63)$$

$$\boxed{v_{s\theta}(r) = -v_{sr}(r) \cot \beta} \quad (4.64)$$

From Eqs. 4.63 and 4.64 a triangle of velocity indicating the slip can be drawn, as indicated in Fig. 4.11. The term $v_{s\theta}$ is in counterclockwise of the versor $\hat{\theta}$ which means that it is negative. These components indicated that the slip is aligned with blade, as expected.

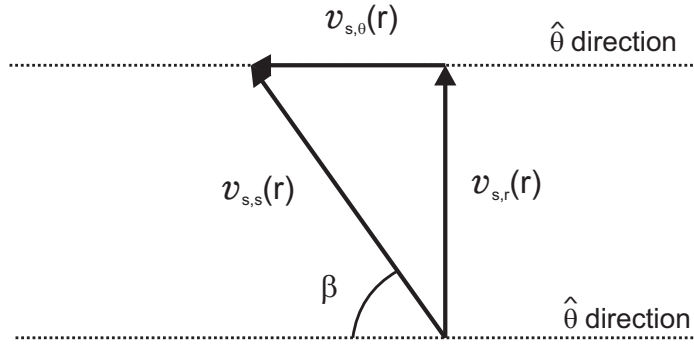


Figure 4.11: Impeller domain

Thus, considering the velocity field premises stated, the slip on normal direction to \hat{s} , represented by \hat{n} is null. The velocity field was simplified with this hypothesis. So:

$$\boxed{v_{s,s}(r) = v_{sr}(r) / \sin \beta} \quad \text{or} \quad \boxed{v_{sr}(r) = v_{s,s} \sin \beta} \quad (4.65)$$

Hence, estimating v_{sr} is possible to find $v_{s,s}$ which is desired. As the channel was treated as a curved duct with variable cross-section area, the interest of calculus is in \hat{s} direction.

The coordinate system change can be done using Eq. 4.15, so the velocities in \hat{s} and \hat{n} become:

$$\vec{v} = \{v_r, v_\theta\} \cdot \begin{Bmatrix} \sin \beta \hat{s} & \cos \beta \hat{n} \\ -\cos \beta \hat{s} & \sin \beta \hat{n} \end{Bmatrix}$$

$$\vec{v} = (v_r \sin \beta - v_\theta \cos \beta) \hat{s} + (v_r \cos \beta + v_\theta \sin \beta) \hat{n} \quad (4.66)$$

The velocity vector is: $\vec{v} = v_s \hat{s} + v_n \hat{n}$. So:

$$\boxed{v_s = v_r \sin \beta - v_\theta \cos \beta} \quad (4.67)$$

$$\boxed{v_n = v_r \cos \beta + v_\theta \sin \beta} \quad (4.68)$$

A similar procedure is done for the slip as the treatment uses the same linear transformation.

$$\vec{v}_s^{\hat{s}\hat{n}} = R \begin{Bmatrix} v_{2r} \\ v_{2\theta} \end{Bmatrix} - R \begin{Bmatrix} v_{1r} \\ v_{1\theta} \end{Bmatrix} = R \vec{v}_s^{\hat{r}\hat{\theta}}$$

$$\boxed{v_{s,s} = v_{sr} \sin \beta - v_{s\theta} \cos \beta} \quad (4.69)$$

$$\boxed{v_{s,n} = v_{sr} \cos \beta + v_{s\theta} \sin \beta} \quad (4.70)$$

Substituting Eq. 4.38 in 4.67 for $v_{s,s}$:

$$\begin{aligned} v_s &= v_r \sin \beta - v_\theta \cos \beta = v_r \sin \beta - (-v_r \cot \beta) \cos \beta \\ v_s &= v_r \left(\frac{\sin^2 \beta + \cos^2 \beta}{\sin \beta} \right) = \frac{v_r}{\sin \beta} \quad \rightarrow \quad \boxed{v_s = \frac{v_r}{\sin \beta}} \end{aligned} \quad (4.71)$$

Substituting Eq. 4.38 in 4.68 for $v_{s,n}$:

$$\begin{aligned} v_n &= v_r \cos \beta + v_\theta \sin \beta = v_r \cos \beta + (-v_r \cot \beta) \sin \beta \\ v_n &= v_r \cos \beta - v_r \frac{\cos \beta}{\sin \beta} \sin \beta = v_r (\cos \beta - \cos \beta) \quad \rightarrow \quad \boxed{v_n = 0} \end{aligned} \quad (4.72)$$

Therefore, as the slip had the same projections and the same components, the result of Eq. 4.71 and 4.72 must be equal for slip, i.e.:

$$\boxed{v_{s,s} = v_{sr} / \sin \beta} \quad (4.73)$$

$$\boxed{v_{s,n} = 0} \quad (4.74)$$

These results are important in the development of this model because with the simplifications already made, these results show that there is only slip in the main direction of the flow, which is in \hat{s} . Besides, the slip in \hat{n} clearly is equal to zero.

The volumetric flux is $j_k = \alpha \vec{v}_k$ (Eq. 4.41) and the same projections of \vec{v} are

applied to \vec{j} , so:

$$v_{s,s} = v_{2s} - v_{1s} = \frac{j_{2s}}{\alpha_2} - \frac{j_{1s}}{\alpha_1} = \frac{(1 - \alpha) j_{2s} - \alpha j_{1s}}{\alpha (1 - \alpha)}$$

$$(1 - \alpha) j_{2s} = \alpha j_{1s} + \alpha (1 - \alpha) v_{s,s}$$

$$j_{2s} - \alpha j_{2s} = \alpha j_{1s} + \alpha (1 - \alpha) v_{s,s}$$

$$j_{2s} = \alpha (j_{1s} + j_{2s}) + \alpha (1 - \alpha) v_{s,s}$$

$$\boxed{v_{2s} = j_{m,s} + (1 - \alpha) v_{s,s}} \quad \text{or} \quad \boxed{v_{2s} = j_{m,s} + v_{2j}} \quad (4.75)$$

where v_s is the relative velocity or slip velocity and v_{2j} is the Drift-flux.

In the literature, based on experimental data a distribution coefficient is required for a better adjust. The explanation of mean operator in Eq. 4.75:

$$j_{2s} = \alpha j_{ms} + \alpha (1 - \alpha) v_{s,s}$$

$$\langle j_{2s} \rangle = \langle \alpha j_{ms} \rangle + \langle \alpha (1 - \alpha) v_{s,s} \rangle$$

where C_0 is the distribution parameter given by:

$$C_0 = \frac{\langle \alpha j_{ms} \rangle}{\langle \alpha \rangle \langle j_{ms} \rangle}$$

$$\langle j_{2s} \rangle = C_0 \langle \alpha \rangle \langle j_{ms} \rangle + \langle \alpha (1 - \alpha) v_{s,s} \rangle \quad (4.76)$$

where v_{2s} is the bubble velocity measured with the image treatment and j_{ms} is acquired from experimental data.

4.2.2 Momentum Equation:

Considering the same hypothesis as the continuity equations, the momentum equation can be written:

• **Radial direction (polar) \hat{r} :**

$$\alpha_k \rho_k \left(v_{kr} \frac{\partial}{\partial r} v_{kr} + \frac{v_{k\theta}}{r} \frac{\partial}{\partial \theta} v_{kr} - \frac{v_{k\theta}^2}{r} \right) = -\alpha_k \frac{\partial}{\partial r} p_k + \alpha_k \rho_k g_r - M_{kr} + S_{kr} + \nabla \cdot \vec{\tau} \quad (4.77)$$

• **Azimuth direction (polar) $\hat{\theta}$:**

$$\alpha_k \rho_k \left(v_{kr} \frac{\partial}{\partial r} v_{k\theta} + \frac{v_{k\theta}}{r} \frac{\partial}{\partial \theta} v_{k\theta} + \frac{v_{kr} v_{k\theta}}{r} \right) = -\alpha_k \frac{1}{r} \frac{\partial}{\partial \theta} p_k + \alpha_k \rho_k g_\theta - M_{k\theta} + S_{k\theta} + \nabla \cdot \vec{\tau} \quad (4.78)$$

where $\nabla \cdot \vec{\tau}$ indicates the viscous stress tensor.

Simplifying comments and premises:

- The velocity field has its dependence only to radius, so any $\partial/\partial\theta$ of any velocity is null.
- The gravity acceleration for this case is neglected ($\vec{g} = g\hat{z}$).
- The momentum received by one phase is equal to the one given by the other, but they have opposite directions, i. e. $\vec{M}_2 = -\vec{M}_1$.
- Fictitious forces are given through fictitious accelerations which already have been calculated. The subscript k is present indicating that they are applied for both phases.
 $S_k = -\alpha_k \rho_k \vec{A}_{kf}$ where $\vec{A}_{kf} = A_{kfr} + A_{kf\theta} = \left(2\vec{\Omega} \times \vec{v}_P + \vec{\Omega} \times \vec{\Omega} \times \vec{r}_{P/A} \right)$.
- They have the same pressure: $p_1 = p_2$.

So Eq. 4.77 and 4.78 in \hat{r} and $\hat{\theta}$ are, respectively:

$$\alpha_k \rho_k \left(v_{kr} \frac{\partial}{\partial r} v_{kr} - \frac{v_{k\theta}^2}{r} \right) = -\alpha_k \frac{\partial p_k}{\partial r} - M_{kr} - \alpha_k \rho_k \vec{A}_{kr} + \nabla \cdot \vec{\tau} \quad (4.79)$$

$$\alpha_k \rho_k \left(v_{kr} \frac{\partial}{\partial r} v_{k\theta} + \frac{v_{kr} v_{k\theta}}{r} \right) = -\alpha_k \frac{1}{r} \frac{\partial p_k}{\partial \theta} - M_{k\theta} - \alpha_k \rho_k \vec{A}_{k\theta} + \nabla \cdot \vec{\tau} \quad (4.80)$$

The pressure gradient and the momentum transfer between the phases need to be estimated using the simplified velocity field assumed. The field pressure ΔP can be obtained integrating in r direction. As already showed the slip occurs only in \hat{s} -direction which can be estimated with momentum transfer rate in \hat{r} direction. So, the momentum equation is analyzed in \hat{r} direction.

Radial pressure gradient: Calculating the radial pressure gradient dp/dr and integrating in r_i and r_o . The momentum equation for phases 1 and 2, described by Eq. 4.79, are added respectively for each phase. As a result, the interfacial momentum transfer are canceled because both have the same module but different directions: $M_{1r} = -M_{2r}$.

$$\begin{aligned} \alpha_1 \rho_1 \left(v_{1r} \frac{\partial}{\partial r} v_{1r} - \frac{v_{1\theta}^2}{r} \right) + \alpha_2 \rho_2 \left(v_{2r} \frac{\partial}{\partial r} v_{2r} - \frac{v_{2\theta}^2}{r} \right) = \\ -(\alpha_1 + \alpha_2) \frac{\partial p}{\partial r} - (\alpha_1 \rho_1 + \alpha_2 \rho_2) A_{kfr} + \nabla \cdot \vec{\tau} \end{aligned} \quad (4.81)$$

The development of Eq. 4.81 is shown in section C.1. The result is Eq. 4.82:

$$\boxed{-\frac{\partial p}{\partial r} = \tilde{\rho}_m \left[\frac{(1 + \cot^2 \beta)}{4 \pi^2 h^2} \right] Q_m^2 \left(\frac{-1}{r^3} \right) + \bar{\rho}_m \left(\frac{\cot \beta}{\pi h} \right) \omega Q_m \left(\frac{1}{r} \right) - \rho_m \omega^2 r - \nabla \cdot \vec{\tau}} \quad (4.82)$$

4.2.3 Viscous Stress Tensor Modeling

The term $\nabla \cdot \vec{\tau}$ is related to surface forces due to the stresses on the sides of the control surface. In polar coordinates considering radial and azimuthal direction, the stress tensor is:

$$\left(\frac{d\mathbf{F}}{dV} \right)_{viscous} = \nabla \cdot \vec{\tau}$$

Applying the Gauss theorem in limited form:

$$\int_{A_k(z,t)} \nabla \cdot \vec{\tau} dA = \frac{\partial}{\partial r} \int_{A_k(r,t)} \vec{\tau} \cdot \vec{n}_r dA + \oint_{\xi(r,t)+\xi_k(r,t)} \vec{n}_k \cdot \vec{\tau} \frac{d\xi}{\vec{n}_k \cdot \vec{n}_{k\xi}} \quad (4.83)$$

where vector \vec{n}_k is normal to interface pointed outside of face k . Unitary vector $\vec{n}_{k\xi}$ is

normal to ξ in the plane A_k . The term ξ_k is the contact of the interface to the wall. ξ is the interface of the fluids. Those variables are represented in Fig. 4.12.

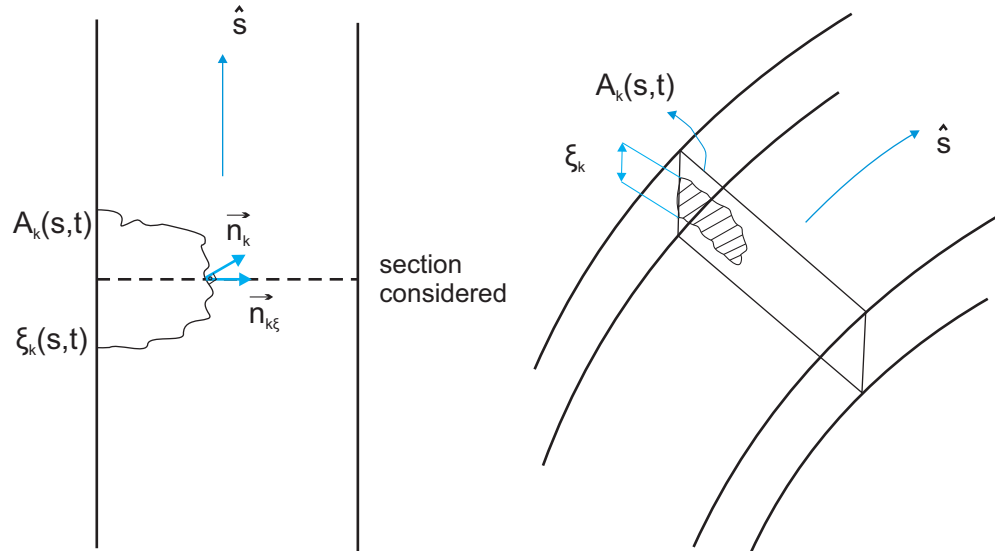


Figure 4.12: Impeller channel approximation

For simplification, the channel of the impeller was considered as a duct and the cross-section area is represented by the hydraulic diameter. The mixture flow is considered homogeneous and the density and viscosity are used for two-phase flow. Figure 4.12 indicates an approximation of the impeller channel as a rectangular duct which has constant cross-section A_k .

$$\text{where } \begin{cases} \text{the wet perimeter : } S_D = 2(2\pi r/Z_b + h) \\ \text{area : } A = 2\pi r h/Z_b \end{cases}$$

Eq. 4.83 is developed in section C.2. The resulting terms in radial direction are used in Eq. 4.82 integrated in r .

Substituting Eqs. C.26 and C.39 into Eq. C.13 and integrating in r .

$$\begin{aligned}
 -\Delta P_r = \int_{r_i}^{r_o} -\frac{\partial p}{\partial r} dr = \tilde{\rho}_m \left[\frac{(1 + \cot^2 \beta)}{4 \pi^2 h^2} \right] Q_m^2 \int_{r_i}^{r_o} \left(\frac{-1}{r^3} \right) dr + \overline{\rho}_m \left(\frac{\cot \beta}{\pi h} \right) \\
 \omega Q_m \int_{r_i}^{r_o} \left(\frac{1}{r} \right) dr - \rho_m \omega^2 \int_{r_i}^{r_o} r dr - \frac{f}{4 \sin \beta} \frac{\rho_m}{2 \pi h} \left(\frac{Q_m}{2 \pi h} \right)^2 \int_{r_i}^{r_o} \left(\frac{1}{h r^2} + \frac{Z_b}{2 \pi r^3} \right) dr \\
 - 4 \mu \frac{\lambda_k}{\alpha_k} \frac{Q_m}{2 \pi h} \int_{r_i}^{r_o} \left(\frac{1}{r^3} \right) dr
 \end{aligned} \tag{4.84}$$

Eq. 4.84 is developed in appendix C, section C.3. Some terms can be grouped in G_1, G_2, G_3 and G_4 . They are all geometric constants, exception to the friction factor, f . So, summarizing:

- Dimensionless group for head two-phase: $C_H = \Delta P / (\overline{\rho}_m \omega^2 r_o^2)$
- Dimensionless group for flow rate two-phase: $C_Q = Q_m / (\omega r_o^3)$
- Specific mass for mixture:
 - "Dukler": $\overline{\rho}_m = \rho_1 \lambda_1 + \rho_2 \lambda_2$
 - Conventional: $\rho_m = \rho_1 \alpha_1 + \rho_2 \alpha_2$
 - $\tilde{\rho}_m = \rho_1 \lambda_1 \frac{\lambda_1}{\alpha_1} + \rho_2 \lambda_2 \frac{\lambda_2}{\alpha_2}$

- Geometric coefficients:

- Factor 1: $r_o/r_i = f_1 \rightarrow > 1$
- Factor 2: $r_o/h = f_2 \rightarrow > 1$
- Factor 3: $\left[\frac{1}{h} \left(\frac{1}{r_i} - \frac{1}{r_o} \right) + \frac{Z_b}{4\pi} \left(\frac{1}{r_i^2} - \frac{1}{r_o^2} \right) \right] = f_3 \rightarrow > 0$ (4.85)

- Geometric constant 1: $G_1 = \left[\frac{(1 + \cot^2 \beta)}{8 \pi^2} \right] f_2^2 (f_1^2 - 1) \rightarrow > 0$
- Geometric constant 2: $G_2 = \left[\left(\frac{\cot \beta}{\pi} \right) f_2 \ln f_1 \right]$ (4.86)

$$+ \frac{\mu}{\rho_m} \frac{\lambda_k}{\alpha_k} \frac{1}{\omega \pi h r_o} \left[\left(\frac{r_o}{r_i} \right)^2 - 1 \right] \rightarrow > 0$$

- Geometric constant 3: $G_3 = \frac{1}{2} \left[1 - \left(\frac{1}{f_1} \right)^2 \right] \rightarrow > 0$

- Geometric constant 4: $G_4 = \frac{r_o^4}{4 \pi^2 h^2} \frac{1}{\sin \beta} f_3 \rightarrow > 0$

Thus the radial pressure term (Eq. C.46) result in:

$$C_H = \frac{1}{2} \left(\frac{\rho_m}{\rho_m} \right) G_3 - G_2 C_Q + \left(\frac{\tilde{\rho}_m}{\rho_m} G_1 - \frac{\rho_m}{\rho_m} \frac{f}{4} G_4 \right) C_Q^2$$
 (4.87)

The drift model is necessary to close the mixture density equations. In order to understand quite better the behavior of density, those terms can be simplified for air and water (or gas/liquid).

- $\frac{\rho_m}{\rho_m} = \frac{\rho_1 \alpha_1 + \rho_2 \alpha_2}{\rho_1 \lambda_1 + \rho_2 \lambda_2} = \frac{\rho_1 \alpha_1 + (\rho_2/\rho_1)\alpha_2}{\rho_1 \lambda_1 + (\rho_2/\rho_1)\lambda_2} \approx \frac{\alpha_1}{\lambda_1}$ if $\rho_2/\rho_1 \ll 1$
- $\frac{\tilde{\rho}_m}{\rho_m} = \frac{\rho_1 \lambda_1 (\lambda_1/\alpha_1) + \rho_2 \lambda_2 (\lambda_2/\alpha_2)}{\rho_1 \lambda_1 + \rho_2 \lambda_2}$
 $= \frac{\rho_1 \lambda_1 (\lambda_1/\alpha_1) + \rho_2/\rho_1 \lambda_2 (\lambda_2/\alpha_2)}{\lambda_1 + (\rho_2/\rho_1) \lambda_2} \approx \frac{\lambda_1}{\alpha_1}$ if $\rho_2/\rho_1 \ll 1$ (4.88)

So for the gas/liquid case:

$$\frac{\rho_m}{\rho_m} \approx \frac{\alpha_1}{\lambda_1} \quad \text{and} \quad \frac{\tilde{\rho}_m}{\rho_m} \approx \frac{\lambda_1}{\alpha_1}$$
 (4.89)

Substituting in Eq. 4.87:

$$C_H = \frac{1}{2} \left(\frac{\alpha_1}{\lambda_1} \right) G_3 - G_2 C_Q + \left(\frac{\lambda_1}{\alpha_1} G_1 - \frac{\alpha_1}{\lambda_1} \frac{f}{4} G_4 \right) C_Q^2 \quad (4.90)$$

Eq. 4.90 becomes:

$$C_H = B_3 G_3 - B_2 C_Q + B_1 C_Q^2 \quad (4.91)$$

where:

- $B_1 = \left(\frac{\lambda_1}{\alpha_1} G_1 - \frac{\alpha_1}{\lambda_1} G_4 \frac{f}{4} \right)$
- $B_2 = G_2$
- $B_3 = \frac{1}{2} \left(\frac{\alpha_1}{\lambda_1} \right)$

Figure 4.13 shown the plot for experimental data of C_H x C_Q . The drift model is necessary in order to calculate the void fraction α_k . The R-squared is equal to 0.95.

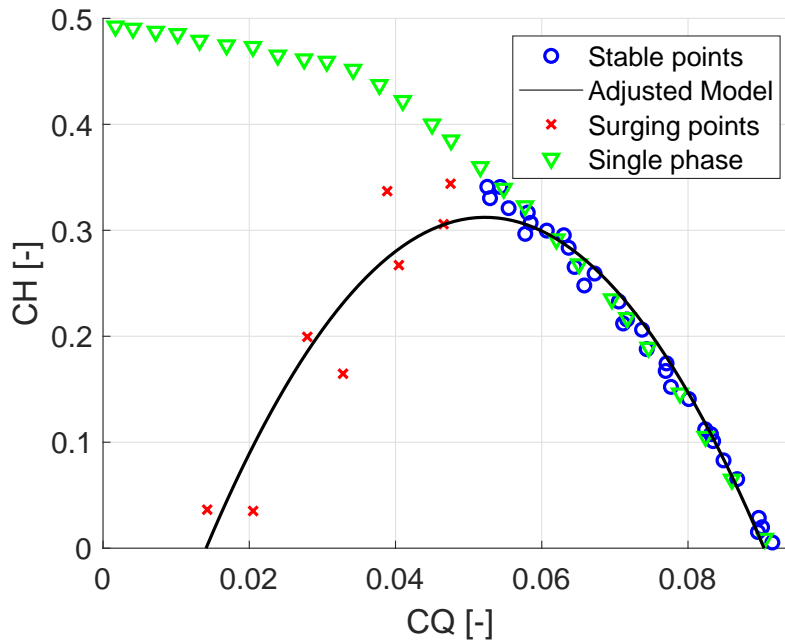


Figure 4.13: C_H x C_Q

The friction factor can be calculated using the data fit present in Fig 4.13. The coefficients are:

$$B_1 = -214.48 \quad B_2 = 22.41 \quad B_3 = -0.27$$

The friction factor calculated by the model f_{model} is compared to the friction factor calculated by the correlations proposed by S.Vieira (2014). The expressions used are showed in appendix E. The coefficients in Eq. E.17 are:

$$f_{r\beta\omega} = 1.2420 \cdot 1.1614 \cdot 1.4619 \cdot 0.0986 \rightarrow f_{r\beta\omega} = 0.2079 \quad (4.92)$$

where $\bar{F}_r = 1.2420$, $\bar{F}_\beta = 1.1614$, $\bar{F}_\omega = 1.4619$ and $\bar{f} = 0.0986$.

The mean value of \bar{f} corresponds to the value a little higher than the expected value using the Moody diagram shown in Fig. 4.14. For the present problem the average flow Reynolds number calculated shown that the friction factor should be in a range between 0.025 to 0.080. More details are presented in the section about the Reynolds number calculation.

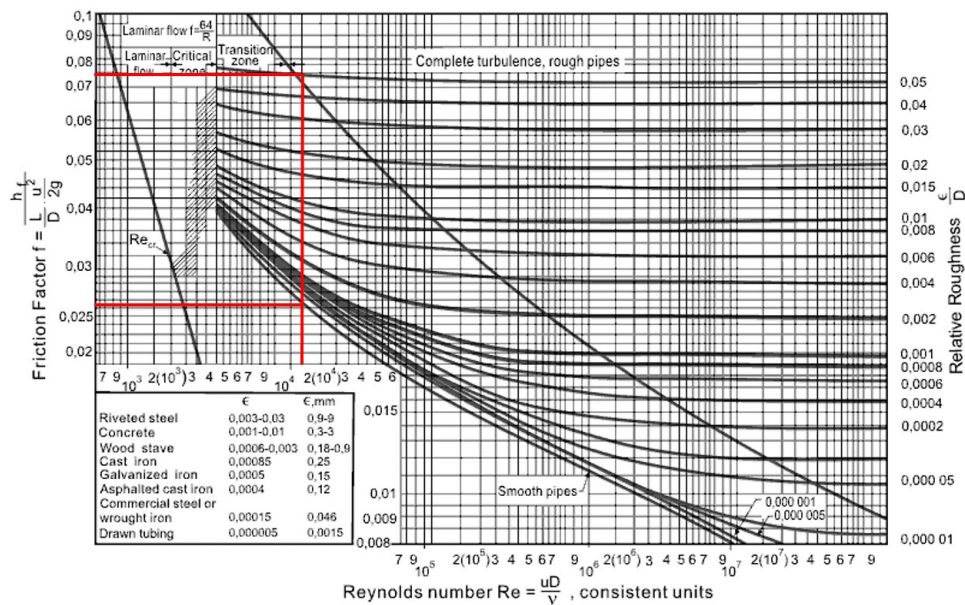


Figure 4.14: Moody diagram.

Considering the corrections made for the centrifugal pump (S.VIEIRA, 2014), the

value of friction factor is $f_{r\beta\omega} = 0.2079$ which represent 210% higher. The friction factor calculated using the model f_{model} is compared with S.Vieira (2014), and it is shown in Fig. 4.15. It is observed that there is no variation of the friction factor calculated by S.VIEIRA, 2014 even with the increase of the flow rate (C_Q). However for values near the BEP the friction factors are of the same magnitude.

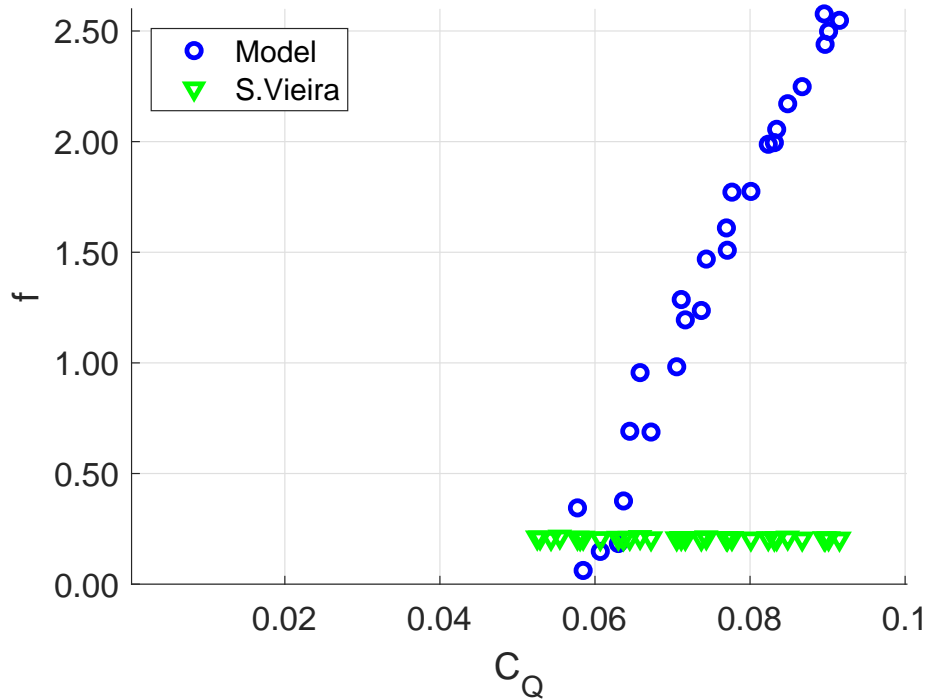


Figure 4.15: Friction factor: model x S.Vieira (2014)

The friction factor calculated using the model tends to reduce as the flow rate C_Q approximates to the BEP, which is in agreement with the literature because the losses reduce. However, the value of f_{model} moving away from the BEP increase so much that reaches values not expected from friction factor, such as 2.44 at $C_Q = 0.089$. This value is overrated because all losses showed in Fig. 2.13 are included in the f_{model} . A deep study of the characteristics of the friction factor in such phenomena is necessary and is left as a recommendation for future work.

4.2.4 Momentum Transfer Between Phases:

When the simplified velocity profile was obtained the slip was estimated. As a result the slip occurs only in \hat{s} direction being null in \hat{n} direction. The versor \hat{s} and \hat{n} indicates the direction in the blade coordinate system using the log spiral cascade. Besides, it was demonstrated that only the radial slip can be estimated to obtain component \hat{s} , which is tangential to the blade. The consequence of the hypothesis that the flow is aligned with the blade results in $v_{s,n} = 0$.

Thus the objective in this section is estimate the rate of momentum transfer per unit volume of liquid phase to the gas phase in radial direction. It will be used to get the radial slip which will be projected in tangential direction of blades. So, different from what was done in the former section, where the pressure gradient was calculated the goal, the next step wants to eliminate this term. In order to achieve this, the equations of momentum for both phases will be subtracted in radial direction and the term M_{2r} will be estimated. The equations in radial direction for phases 1 and 2 are discussed then.

- **Radial direction (polar) \hat{r} :**

$$\alpha_k \rho_k \left(v_{kr} \frac{\partial}{\partial r} v_{kr} + \frac{v_{k\theta}}{r} \frac{\partial}{\partial \theta} v_{kr} - \frac{v_{k\theta}^2}{r} \right) = -\alpha_k \frac{\partial}{\partial r} p_k + \alpha_k \rho_k g_r - M_{kr} + S_{kr} + \nabla \cdot \vec{\tau} \quad (4.93)$$

The pressure are considered equal for both phases ($p_1 = p_2$), the gravity was neglected by hypothesis and the velocity field was simplified, it only depends of the variation on radius, which means that $\partial / \partial \theta = 0$. Considering those simplifications and writing the momentum equation for each phase, dividing by α_k :

$$\rho_1 \left(v_{1r} \frac{\partial v_{1r}}{\partial r} - \frac{v_{1\theta}^2}{r} \right) = -\frac{\partial p}{\partial r} + \frac{S_{1r}}{\alpha_1} - \frac{M_{1r}}{\alpha_1} + \nabla \cdot \vec{\tau} \quad (4.94)$$

$$\rho_2 \left(v_{2r} \frac{\partial v_{2r}}{\partial r} - \frac{v_{2\theta}^2}{r} \right) = -\frac{\partial p}{\partial r} + \frac{S_{2r}}{\alpha_2} - \frac{M_{2r}}{\alpha_2} + \nabla \cdot \vec{\tau} \quad (4.95)$$

The momentum transferred by one phase is received by the other, this means that $M_{1r} = -M_{2r}$. The development of the subtraction between Eq. 4.95 and 4.94 is in section C.4.

The resultant equation is:

$$\frac{M_{2r}}{\alpha_1 \alpha_2} = \widetilde{\Delta\rho} \left[\frac{(1 + \cot^2 \beta)}{4\pi^2 h^2} \right] Q_m^2 \left(\frac{-1}{r^3} \right) + \overline{\Delta\rho} \left(\frac{\cot \beta}{\pi h} \right) \omega Q_m \left(\frac{1}{r} \right) - \Delta\rho \omega^2 r - \langle \nabla \cdot \vec{\tau} \rangle \quad (4.96)$$

The interfacial term is defined using the Zuber model (ZUBER, 1964, ISHII AND HIBIKI, 2010). Thus M_{2r} is given by:

$$M_{2r} = -\frac{\alpha_2}{B_b} \left(\sum \vec{F}_{R \text{ bubbles}} \right) \quad (4.97)$$

where α_2 is the gas void fraction, B_b is the mean volume of a bubble and $\sum \vec{F}_{R \text{ bubbles}}$ is the mean resultant force in one bubble. The mean volume of bubble is given by: $B_b = 4\pi r_b^3/3$ where r_b is the bubble radius.

In the classic models, generally the drag is considered because the relative velocity appears from this term. This force is predominant in stationary and developed flows, such as ducts in steady state without convective terms. This is not the case in this study where the impeller has a strong convective acceleration further the pseudo forces are important and they should all be considered, including Basset and virtual mass force.

$$\sum \vec{F}_{R \text{ bubbles}} = \vec{F}_D + \vec{F}_V + \vec{F}_B \quad (4.98)$$

The drag force is represented by \vec{F}_D , the virtual mass force is \vec{F}_V and Basset force is \vec{F}_B . The forces for a mean bubble diameter in the flow with radius r_b are discussed in section C.4. Grouping the results until now using Eq. 4.97.

$$M_{2r} = M_{2r}^D + M_{2r}^V + M_{2r}^B \quad (4.99)$$

$$M_{2r} = \alpha \rho_1 C_A \sin \beta v_{s,s} \|\vec{v}_s\| - \alpha \rho_1 (C_B + C_V) \left[\left(\frac{\lambda_2}{\alpha_2} \right)^2 - \left(\frac{\lambda_1}{\alpha_1} \right)^2 \right] (1 + \cot^2 \beta) \left(\frac{j_m^2(r)}{r} \right)$$

$$M_{2r} = \alpha \rho_1 C_A \sin \beta v_{s,s} \|\vec{v}_s\| + \alpha \rho_1 (C_B + C_V) \left[\left(\frac{\lambda_2}{\alpha_2} \right)^2 - \left(\frac{\lambda_1}{\alpha_1} \right)^2 \right] \left[\frac{(1 + \cot^2 \beta)}{4\pi^2 h^2} \right] Q_m^2 \left(\frac{-1}{r^3} \right) \quad (4.100)$$

where:

$$\boxed{C_A = \frac{3 C_D}{8 r_b}} \quad \boxed{C_V = \frac{1}{2}} \quad \boxed{C_B = \frac{9}{r_b} \sqrt{\frac{\mu_m t}{\pi \rho_1}}}$$

Finally, putting the equations together of M_{2r} , Eq. 4.100 and 4.96:

$$\begin{aligned} \frac{M_{2r}}{\alpha} &= \rho_1 C_A \sin \beta v_{s,s} \|\vec{v}_s\| + \rho_1 (C_B + C_V) \left[\left(\frac{\lambda_2}{\alpha_2} \right)^2 - \left(\frac{\lambda_1}{\alpha_1} \right)^2 \right] \\ &\quad \left[\frac{(1 + \cot^2 \beta)}{4 \pi^2 h^2} \right] Q_m^2 \left(\frac{-1}{r^3} \right) \\ \frac{M_{2r}}{\alpha} &= \alpha_1 \widetilde{\Delta \rho} \left[\frac{(1 + \cot^2 \beta)}{4 \pi^2 h^2} \right] Q_m^2 \left(\frac{-1}{r^3} \right) + \alpha_1 \overline{\Delta \rho} \left(\frac{\cot \beta}{\pi h} \right) \omega Q_m \left(\frac{1}{r} \right) \\ &\quad - \alpha_1 \Delta \rho \omega^2 r + \alpha_1 \frac{f}{4} \rho_m \left(\frac{Q_m}{2 \pi h} \right)^2 \frac{1}{\sin \beta} \left(\frac{1}{h r^2} + \frac{Z_b}{2 \pi r^3} \right) + 4 \mu \alpha_1 \frac{\lambda_k}{\alpha_k} \frac{Q_m}{2 \pi h} \frac{1}{r^3} \end{aligned}$$

Matching those equations and developing it in section C.4.1. It results in:

$$\begin{aligned} -\overline{v_{s,s}^2} &= - \left\{ \frac{1}{C_A^\infty} \frac{\widetilde{\Delta \rho}}{\rho_1} - \frac{\Delta C^\infty}{C_A^\infty} \left[\left(\frac{\lambda_2}{\alpha_2} \right)^2 - \left(\frac{\lambda_1}{\alpha_1} \right)^2 \right] \right\} \left[\frac{(1 + \cot^2 \beta)}{4 \pi^2 h^2} \right] \frac{1}{\sin \beta} \frac{\bar{r}}{r_o^2 r_i^2} \\ &\quad Q_m^2 + \frac{1}{C_A^\infty} \frac{\overline{\Delta \rho}}{\rho_1} \left(\frac{\cot \beta}{\pi h} \right) \frac{1}{\sin \beta} \frac{\ln(r_o/r_i)}{\Delta r} \omega Q_m - \frac{1}{\sin \beta} \frac{1}{C_A^\infty} \frac{\Delta \rho}{\rho_1} \omega^2 \bar{r} \\ &\quad - \frac{1}{\sin \beta} \frac{1}{C_A^\infty} \frac{\Delta \rho}{\rho_1} \omega^2 \frac{(r_o + r_i)}{2} + \frac{1}{\rho_1} \frac{1}{C_A^\infty} \frac{f}{4} \rho_m \left(\frac{1}{4 \pi^2 h^2} \right) \frac{1}{\sin^2 \beta} \frac{f_3}{\Delta r} Q_m^2 \\ &\quad + 2 \frac{\mu}{\rho_1} \frac{1}{C_A^\infty} \frac{1}{\pi h \sin \beta} \frac{\lambda_k}{\alpha_k} \left(\frac{\bar{r}}{r_o^2 r_i^2} \right) Q_m \end{aligned} \quad (4.101)$$

So, the drift flux model becomes:

$$\begin{aligned} \overline{v_{2s}} &= \left(\frac{\lambda_2}{\alpha_2} \right) \left[\left(\frac{Q_m}{2 \pi h} \right) \frac{\ln(r_o/r_i)}{(r_o - r_i)} \frac{1}{\sin \beta} \right] = C_0 \left(\frac{Q_m}{2 \pi h} \right) \frac{\ln(r_o/r_i)}{(r_o - r_i)} \frac{1}{\sin \beta} \\ &\quad + (1 - \alpha) \overline{v_{s,s}} \end{aligned} \quad (4.102)$$

The format of the model can be now rewritten from Eq. 4.101:

$$-\overline{v_{s,s}^2} = -A_1 Q_m^2 + A_2 \omega Q_m - A_3 \omega^2 \quad (4.103)$$

where $A_{k,k=\{1,2,3\}} = f(\lambda, C_A^\infty, \Delta C^\infty)$

$$\begin{aligned}
\circ A_1 &= \left\{ \frac{\widetilde{\Delta\rho}}{\rho_1} - \Delta C^\infty \left[\left(\frac{\lambda_2}{\alpha_2} \right)^2 - \left(\frac{\lambda_1}{\alpha_1} \right)^2 \right] \right\} \left[\left(\frac{\csc^2 \beta}{\sin \beta} \right) \frac{\bar{r}}{4 C_A^\infty \pi^2 r_i^2 r_o^2 h^2} \right. \\
&\quad \left. - \frac{\rho_m f}{\rho_1 4} \left[\left(\frac{1}{\sin^2 \beta} \right) \frac{f_3}{4 C_A^\infty \pi^2 h^2 \Delta r} \right] \right] \\
\circ A_2 &= \frac{\widetilde{\Delta\rho}}{\rho_1} \left(\frac{\cot \beta}{\sin \beta} \right) \frac{\ln(r_o/r_i)}{C_A^\infty \pi h \Delta r} + 2 \frac{\mu}{\rho_1} \frac{1}{C_A^\infty} \frac{1}{\pi h \sin \beta} \frac{\lambda_k}{\alpha_k} \left(\frac{\bar{r}}{r_o^2 r_i^2} \right) \frac{1}{\omega} \\
\circ A_3 &= \frac{1}{C_A^\infty \sin \beta} \left(\frac{\Delta\rho}{\rho_1} \right) \bar{r} \\
\circ C_A^\infty &= \left(\frac{3 C_D}{8 r_b} \right) \frac{1}{1 - \alpha} \\
\circ \Delta C^\infty &= C_B^\infty + C_V^\infty = \left(\frac{9}{r_b} \sqrt{\frac{\mu_m t}{\pi \rho_1}} + \frac{1}{2} \right) \frac{1}{1 - \alpha}
\end{aligned} \tag{4.104}$$

The term A_1 can be simplified:

$$\begin{aligned}
A_1 &= \left\{ \frac{\widetilde{\Delta\rho}}{\rho_1} - \Delta C^\infty \left[\left(\frac{\lambda_2}{\alpha_2} \right)^2 - \left(\frac{\lambda_1}{\alpha_1} \right)^2 \right] \right\} \left[\left(\frac{\csc^2 \beta}{\sin \beta} \right) \frac{\bar{r}}{4 C_A^\infty \pi^2 r_i^2 r_o^2 h^2} \right. \\
&\quad \left. - \frac{\rho_m f}{\rho_1 4} \left[\left(\frac{1}{\sin^2 \beta} \right) \frac{f_3}{4 C_A^\infty \pi^2 h^2 \Delta r} \right] \right]
\end{aligned}$$

Denoting:

$$Lambdas = \left[\left(\frac{\lambda_2}{\alpha_2} \right)^2 - \left(\frac{\lambda_1}{\alpha_1} \right)^2 \right]$$

So:

$$\begin{aligned}
A_1 &= \frac{1}{4 C_A^\infty \pi^2 h^2} \left\{ \left[\frac{\widetilde{\Delta\rho}}{\rho_1} - \Delta C^\infty Lambdas \right] \left(\frac{\csc^2 \beta}{\sin \beta} \right) \frac{1}{r_i^2 r_o^2} \right. \\
&\quad \left. - \frac{\rho_m f}{\rho_1 4} \left[\left(\frac{1}{\sin^2 \beta} \right) \frac{f_3}{\Delta r} \right] \right\}
\end{aligned} \tag{4.105}$$

The coefficients depend on λ , α , ΔC^∞ and C_A^∞ . In the bubble flow pattern there is a chance that the terms ΔC^∞ and C_A^∞ can be practically constant and $\lambda/\alpha \sim 1$. This means that those coefficients do not depend mostly on $\lambda/\alpha \sim 1$ so do not change so much compared to the others.

The gas locking occurs when the mixture flow rate Q_m decreases. The forces acting on bubbles stabilizes which renders the air unable to move. Thus it promotes the gas locking in the pump.

- **Dimensionless:**

Dividing Eq. 4.101 by $(\Delta\rho/\rho_1)\omega^2 r_o^2$:

$$\begin{aligned} \frac{-\overline{v_{s,s}}^2}{(\Delta\rho/\rho_1)\omega^2 r_o^2} = & -\frac{1}{C_A^\infty} \left\{ \left[\frac{\widetilde{\Delta\rho}}{\rho_1} - \Delta C^\infty \text{Lambdas} \right] \left(\frac{\csc^2 \beta}{\sin \beta} \right) \frac{1}{r_i^2 r_o^2} \right. \\ & \left. - \frac{\rho_m}{\rho_1} \frac{f}{4} \left[\left(\frac{r_o^2}{\sin^2 \beta} \right) \frac{f_3}{\Delta r} \right] \right\} \left[\left(\frac{\rho_1}{\Delta\rho \omega^2 r_o^2} \right) \left(\frac{Q_m}{2\pi r_o h} \right)^2 \right] + \frac{1}{C_A^\infty} \frac{\overline{\Delta\rho}}{\Delta\rho} \left(\frac{\cot \beta}{\pi h} \right) \\ & \frac{1}{\sin \beta} \frac{\ln(r_o/r_i)}{(r_o - r_i)} \frac{Q_m}{\omega r_o^2} - \frac{1}{\sin \beta} \frac{1}{C_A^\infty} \frac{\bar{r}}{r_o^2} \end{aligned} \quad (4.106)$$

Rearranging the terms in Eq. 4.106:

$$\begin{aligned} -\frac{\rho_1 \overline{v_{s,s}}^2}{\Delta\rho \omega^2 r_o^2} = & -\frac{1}{C_A^\infty} \left\{ \left[\frac{\widetilde{\Delta\rho}}{\rho_1} - \Delta C^\infty \text{Lambdas} \right] \left(\frac{\csc^2 \beta}{\sin \beta} \right) \frac{1}{r_i^2 r_o^2} \right. \\ & \left. - \frac{\rho_m}{\rho_1} \frac{f}{4} \left[\left(\frac{r_o^2}{\sin^2 \beta} \right) \frac{f_3}{\Delta r} \right] \right\} \left[\left(\frac{\rho_1}{\Delta\rho \omega^2 r_o^2} \right) \left(\frac{Q_m}{2\pi r_o h} \right)^2 \right] + 2 \left(\frac{\overline{\Delta\rho}}{\sqrt{\Delta\rho} \rho_1} \right) \left(\frac{\cot \beta}{\sin \beta} \right) \\ & \frac{\ln(r_o/r_i)}{C_A^\infty (r_o - r_i)} \left[\sqrt{\frac{\rho_1}{\Delta\rho}} \frac{1}{\omega r_o} \left(\frac{Q_m}{2\pi r_o h} \right) \right] - \frac{\bar{r}}{r_o^2 C_A^\infty \sin \beta} \end{aligned} \quad (4.107)$$

The Froude number for two-phase flow $Fr_{TP,s}$ for the slip under a centrifugal field and the mixture Froude number Fr_m are given by:

$$\boxed{Fr_{TP,s}^2 = \frac{\rho_1 \overline{v_{s,s}}^2}{\Delta\rho \omega^2 r_o^2}}$$

$$\boxed{Fr_m = \sqrt{\frac{\rho_1}{\Delta\rho}} \left(\frac{Q_m}{2\pi r_o h} \right) / \omega r_o}$$

Substituting the Froude number in Eq. 4.107:

$$-Fr_{TP,s}^2 = -\frac{1}{C_A^\infty} \left\{ \left[\frac{\widetilde{\Delta\rho}}{\rho_1} - \Delta C^\infty \text{Lambdas} \right] \left(\frac{\csc^2 \beta}{\sin \beta} \right) \frac{1}{r_i^2 r_o^2} + \frac{\rho_m}{\rho_1} \frac{f}{4} \left[\left(\frac{r_o^2}{\sin^2 \beta} \right) \frac{f_3}{\Delta r} \right] \right\} Fr_m^2 + 2 \left(\frac{\overline{\Delta\rho}}{\sqrt{\Delta\rho \rho_1}} \right) \left(\frac{\cot \beta}{\sin \beta} \right) \frac{\ln(r_o/r_i)}{C_A^\infty (r_o - r_i)} Fr_m - \frac{\bar{r}}{r_o^2 C_A^\infty \sin \beta} \quad (4.108)$$

The dimensionless model format can be now rewritten as in Eq. 4.108:

$$Fr_{TP,s}^2 = A'_1 Fr_m^2 - A'_2 Fr_m + A'_3 \quad (4.109)$$

where $A'_{k,k=\{1,2,3\}} = f(\lambda, C_A^\infty, \Delta C^\infty)$

$$\circ A'_1 = \frac{1}{C_A^\infty} \left\{ \left[\frac{\widetilde{\Delta\rho}}{\rho_1} - \Delta C^\infty \text{Lambdas} \right] \left(\frac{\csc^2 \beta}{\sin \beta} \right) \frac{1}{r_i^2 r_o^2} - \frac{\rho_m}{\rho_1} \frac{f}{4} \left[\left(\frac{r_o^2}{\sin^2 \beta} \right) \frac{f_3}{\Delta r} \right] \right\} \quad (4.110)$$

$$\circ A'_2 = 2 \left(\frac{\overline{\Delta\rho}}{\sqrt{\Delta\rho \rho_1}} \right) \left(\frac{\cot \beta}{\sin \beta} \right) \frac{\ln(r_o/r_i)}{C_A^\infty (r_o - r_i)}$$

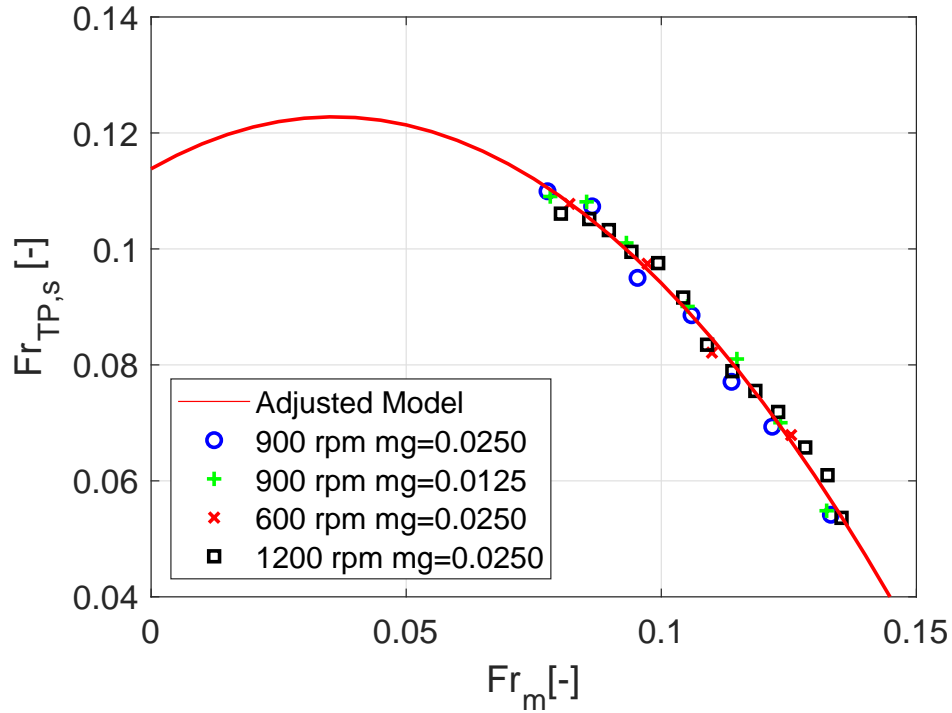
$$\circ A'_3 = \frac{\bar{r}}{r_o^2 C_A^\infty \sin \beta} \quad (4.111)$$

Figure 4.16 shows the result of Eq. 4.109. As expected, the data $Fr_{TP,s}$ tends to decrease as the mixture Froude number increases. When the mixture flow rate Q_m increases it tends to the homogeneous model as $v_s \rightarrow 0$. The coefficients were calculated using the method of non linear least square which provides R^2 equals to 0.99. So, they are:

$$\boxed{A'_1 = 6.971} \quad \boxed{A'_2 = 0.501} \quad \boxed{A'_3 = 0.114}$$

Multiplying Eq. 4.75 by the term $\sqrt{\rho_1/\Delta\rho} \cdot 1/\omega r_o$:

$$\sqrt{\frac{\rho_1}{\Delta\rho}} \cdot \frac{v_{2s}}{\omega r_o} = \sqrt{\frac{\rho_1}{\Delta\rho}} \frac{j_{m,s}}{\omega r_o} + \sqrt{\frac{\rho_1}{\Delta\rho}} \frac{(1 - \alpha) \overline{v_{s,s}}}{\omega r_o} \quad (4.112)$$

Figure 4.16: $Fr_{TP,s} \times Fr_m$

Using Eq. C.75:

$$\sqrt{\frac{\rho_1}{\Delta\rho}} \cdot \frac{v_{2s}}{\omega r_o} = C_0 \left[\frac{r_o \ln(r_o/r_i)}{\sin \beta (r_o - r_i)} \right] \left(\sqrt{\frac{\rho_1}{\Delta\rho}} \frac{1}{\omega r_o} \right) \left(\frac{Q_m}{2\pi r_o h} \right) + (1 - \alpha) \left(\sqrt{\frac{\rho_1}{\Delta\rho}} \frac{v_{s,s}}{\omega r_o} \right) \quad (4.113)$$

where:

$$Fr_{2,s} = \sqrt{\frac{\rho_1}{\Delta\rho}} \cdot \frac{v_{2s}}{\omega r_o}$$

$$C'_0 = C_0 \left[\frac{r_o \ln(r_o/r_i)}{\sin \beta (r_o - r_i)} \right]$$

Substituting the terms $Fr_{2,s}$, C'_0 , $Fr_{TP,s}$ and Fr_m in Eq. 4.113

$$Fr_{2,s} = C'_0 Fr_m + (1 - \alpha) Fr_{TP,s} \quad (4.114)$$

Substituting these terms in Eq. 4.113, using $v_{s,s}$ calculated in Eq. 4.103 and con-

sidering liquid phase faster than gas phase ($v_1 > v_2$), Eq. 4.113 becomes:

$$Fr_{2,s} = C'_0 Fr_m - (1 - \alpha) \sqrt{A'_1 Fr_m^2 - A'_2 Fr_m + A'_3} \quad (4.115)$$

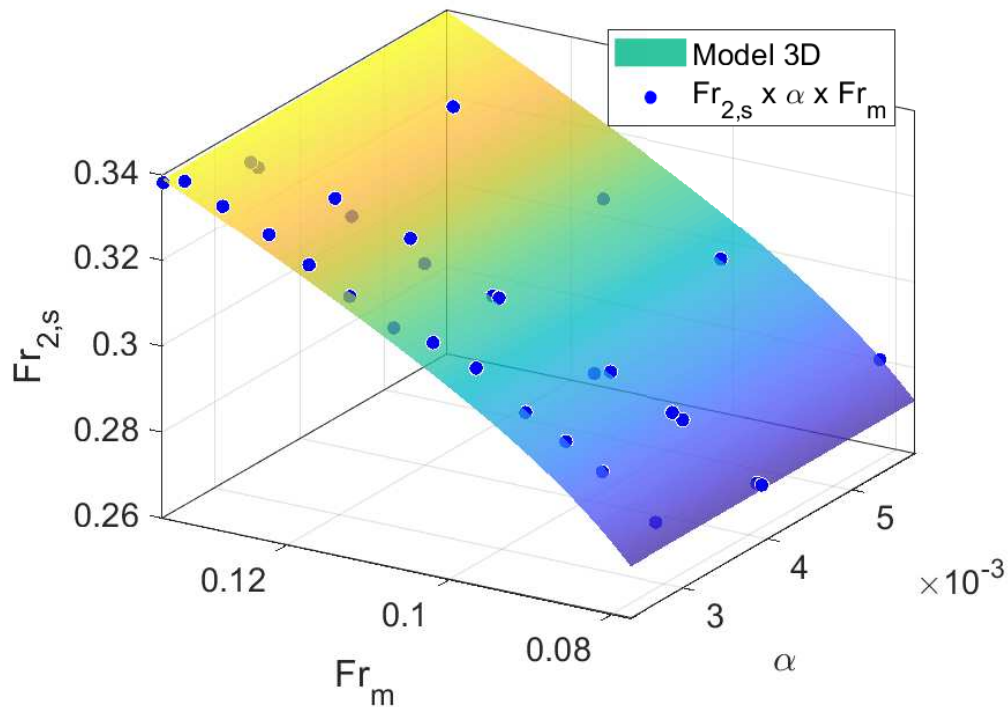


Figure 4.17: $Fr_{TP,s} \times Fr_m \times \alpha$

The coefficients presented in Eq. 4.115 were calculated using the method of non linear least square, which provides R^2 equals to 0.86. The difference from Eq. 4.109 are the distribution coefficient and the terms A'_k . Those terms were under a square root, which means that this expression suffers about the lost of information of signal. By this reason, Eq. 4.115 was modified and the distribution coefficient is equal to 1.23.

Eq. 4.115 was fitted in order to produce the best R^2 . However this equation has a square root, which compared to Eq. 4.109, this is one of the factors that have influence on the value of R^2 , which tends to be lesser. The results will be discussed in chapter 5, section 5.3.

5 RESULTS

This chapter presents the experimental data acquired and their comparison with analytic expression formulated in the chapter 4. The modeling results are discussed and after this, the transition criterion is proposed, and the forces on the bubbles are shown and discussed.

5.1 Experimental Results

The results of the code are shown here and are divided into two sections. First, the probability distribution functions are calculated for the diameters and then, the bubble displacements are shown.

5.1.1 Flow visualization

The experimental data are shown in Fig. 5.1. The points IMs are related to experiments shown in Fig. 5.2. Table 5.1 indicates the flow rate of the points defined as IMs.

Table 5.1: Experimental data flow rate of gas Q_g and water Q_l .

IM	Q/Q_{BEP}	Q_l [m^3/h]	$Q_g 10^{-6}$ [m^3/h]	Reference
1	1.65	5.2843	6.94	5.1(a)
3	1.41	4.5118	6.94	5.1(b)
5	1.18	3.7812	6.94	5.1(c)
7	0.96	3.0814	6.94	5.1(d)
9	0.71	2.2787	6.94	5.1(e)
11	0.26	0.8354	6.94	5.1(f)

As already observed by Monte Verde (2016) from Image IM1 (Fig. 5.1a) to IM 11 (Fig. 5.1e) it is possible to observe the change in flow pattern by changing the liquid flow rate for the same rotational speed (900 *rpm* in this case) and the same gas mass flow rate. The highest liquid flow rate is observed in IM1 (Fig. 5.1a), so, the bubbles are the smallest and the flow pattern is classified as bubbles by Monte Verde (2016). In

the description the authors suggest that in this case the interaction between phases is small and no bubbles agglomeration is observed. The same flow pattern and physics is observed in IM3 condition (Fig. 5.1b). However, due to the decrease in the liquid flow rate the bubbles start to increase. In both cases the void fraction is small.

Next, IM5 (Fig. 5.1c) presents the increase in bubbles population and the start of agglomeration with bubbles of bigger size. This flow pattern was described by Monte Verde (2016) as Agglomerated Bubble flow pattern. IM7 and IM9 can be related to the Gas Pocket flow pattern (MONTE VERDE, 2016). In this case a big bubble is created by the coalescence of small ones, and this bubble occupies a large part of the impeller channel. Due to the characteristics of this flow pattern this is the beginning of unstable pump operation and performance degradation.

Decreasing the flow rate even more, the segregated flow pattern is observed, where a large stationary bubble occupies all the extension of the impeller. As stated by Monte Verde (2016) in this case, due to the small area for liquid flow the pump performance is lost and almost null head is produced. This phenomenon is linked to the gas-locking effect.

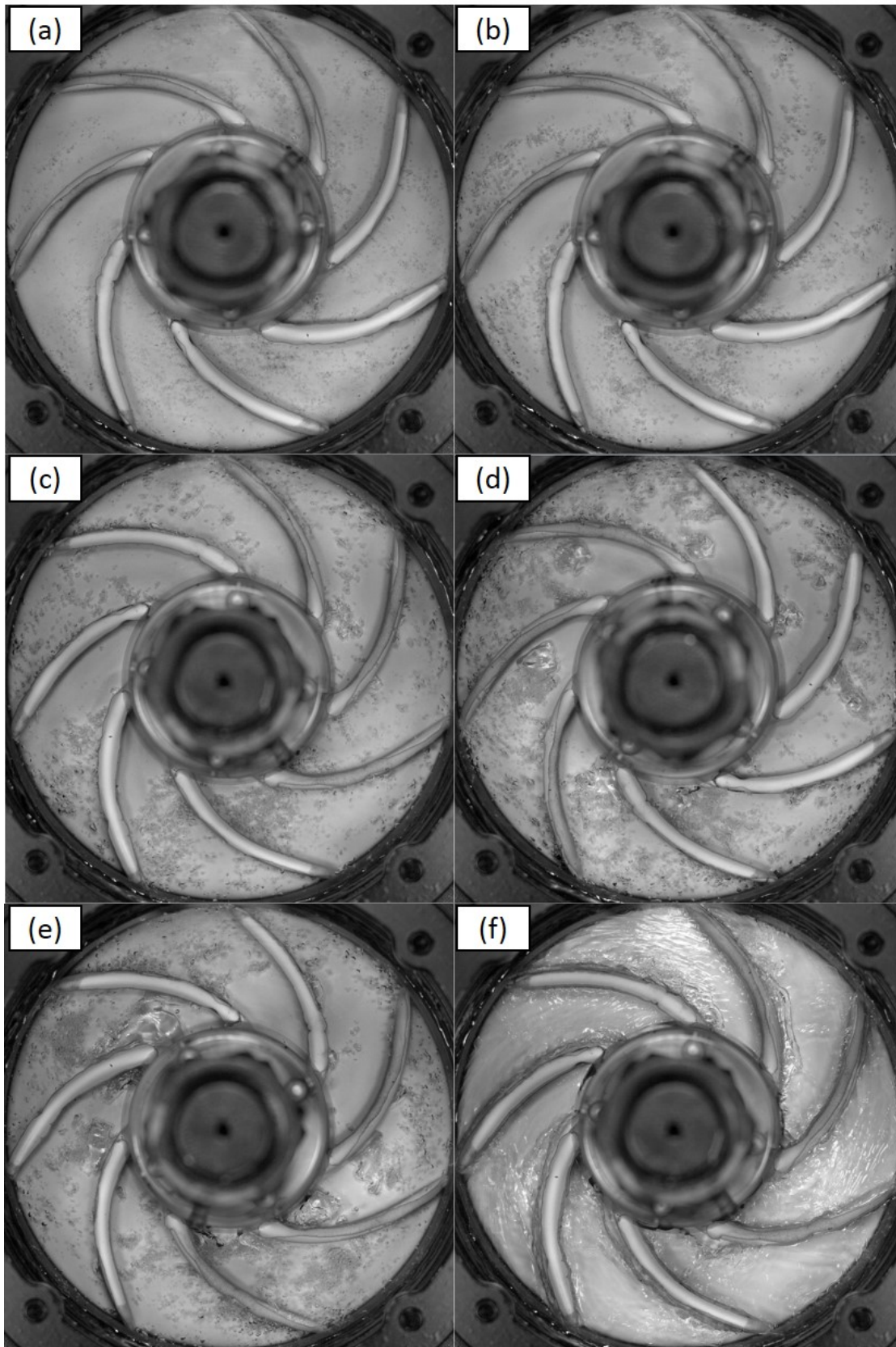


Figure 5.1: Experiment images: (a) IM1 - (b) IM3 - (c) IM5 - (d) IM7 - (e) IM9 - (f) IM11.

Clearly, there is a change of physics due to flow pattern changes by the decrease of liquid flow rate. In some cases it is expected that the homogeneous model would be suitable to characterize the flow inside the impeller. However, due to the change in gas fraction the slip between phases might be important and so a model like drift-flux would be more suitable and will be discussed in chapter 4.

5.1.2 Bubbles Diameter

The code captures the velocities and diameter of the air bubbles. Probability density functions (PDF) of the diameter of the bubbles were made for each condition tested, and are presented in Fig. 5.2. The distribution that fitted the data was a nonparametric representation, and a kernel density estimator was used (for more details about how these PDFs work, please see Hinkelmann and Kempthorne (2005)). Further, Fig. 5.2 presented a chart that shows the pressure increment by the water flow rate, indicating where are the points IM's for reference.

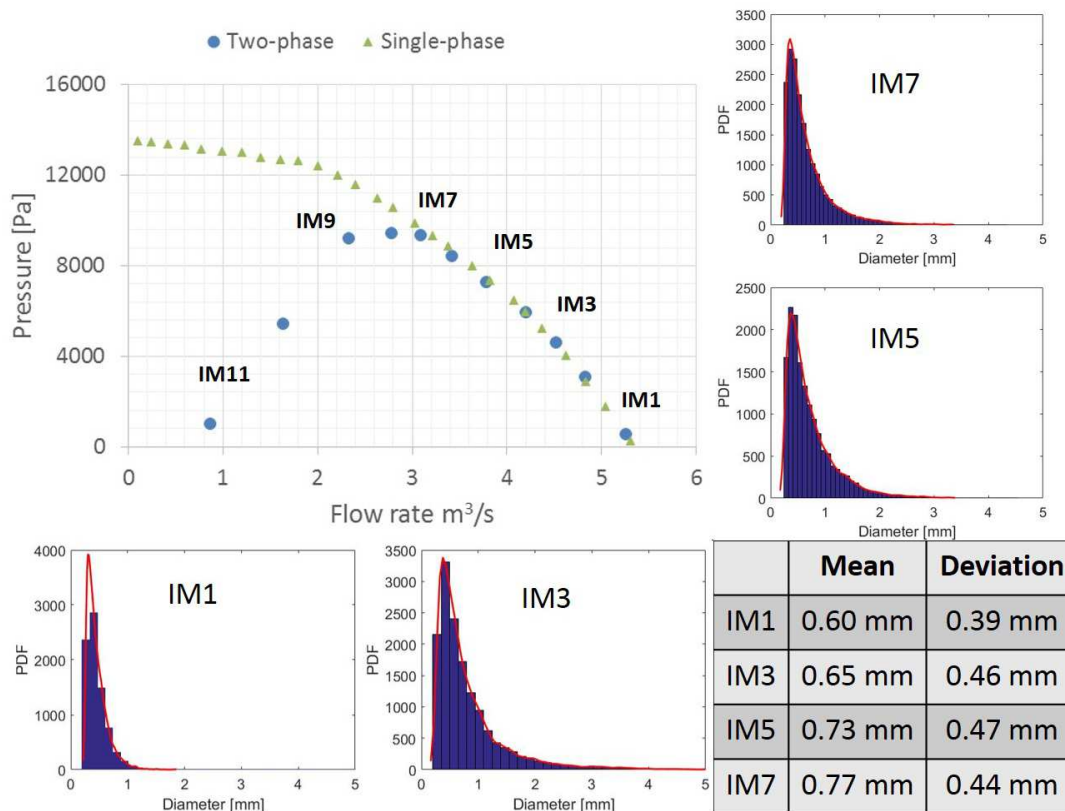


Figure 5.2: Histograms of the experiments - 900 rpm and 0.025 kg/h gas mass flow rate.

Other distributions were tested, such as "Burr" and "Generalized extreme value", which also offers a similar result to fit data, but not better. Besides, the mean diameter and the standard deviation were calculated and are presented in the Figure 5.2.

5.1.3 Bubbles' Trajectories and Velocities

The code needs to be validated, and this is done by following the bubbles manually. The results are shown in Fig. 5.3. The red dots indicated the trajectories of the bubbles while they are crossing the impeller channels. Image by image is analyzed, and the bubble position is recorded. After this, the velocity is acquired. Fig. 5.3 shows the trajectories in the seven channels of the impeller, which are represented by the mask in blue. The axis of the figures is plotted using the pixel scale.

The experiments were calibrated in order to convert the pixel to millimeters. Mil-

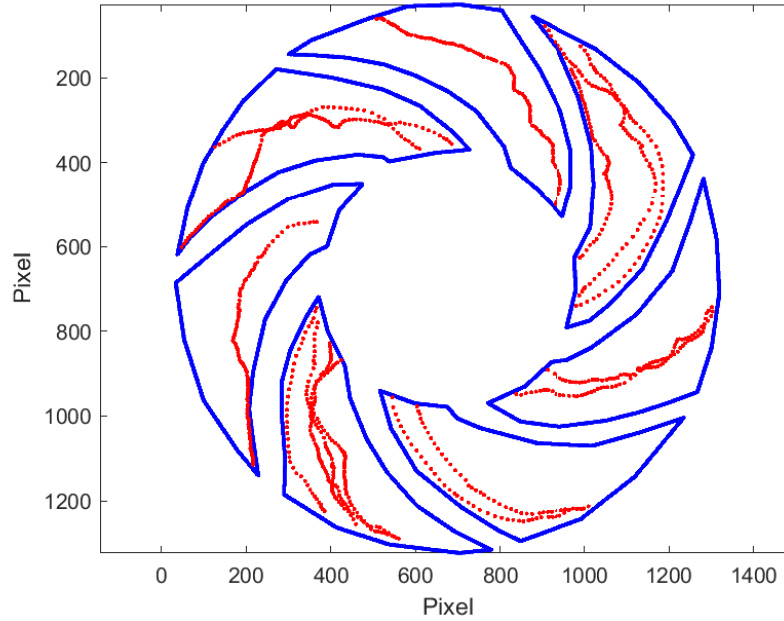


Figure 5.3: Bubble trajectories in the impeller channel.

limeter paper is used, and one millimeter is equivalent to 11.8 pixels, rounded to 12. One pixel may represent a great uncertainty in the velocity calculation. For example, considering a bubble moving with 1.00 m/s or 12 pixels/s between two frames acquired at 1500 fps. With the acquisition of the centroid position, if it changes one pixel, this is enough to change the velocity to 13 pixels/s , consequently to 1.08 m/s . One pixel may represent a difference of 8% in the measurements. This value represents the uncertainty in the velocity measurements.

So the velocity measurement suffers a considerable influence of small changes in the pixel position. In order to reduce this effect a moving average was applied as shown in Fig. 5.4 (PERISSINOTTO *et al.*, 2017). The bubble tracked by the code in the channels of the impeller has oscillations, and both directions suggested this influence. The moving average method (MAM) smooth the curves, using the Eq. 5.1:

$$v_{MAM} = \frac{v_{i-1} + v_i + v_{i+1}}{3} \quad (5.1)$$

where the subscript *MAM* means the moving average method. The fluctuations observed in the velocities curves would be errors acquired in the tracking process. A single pixel

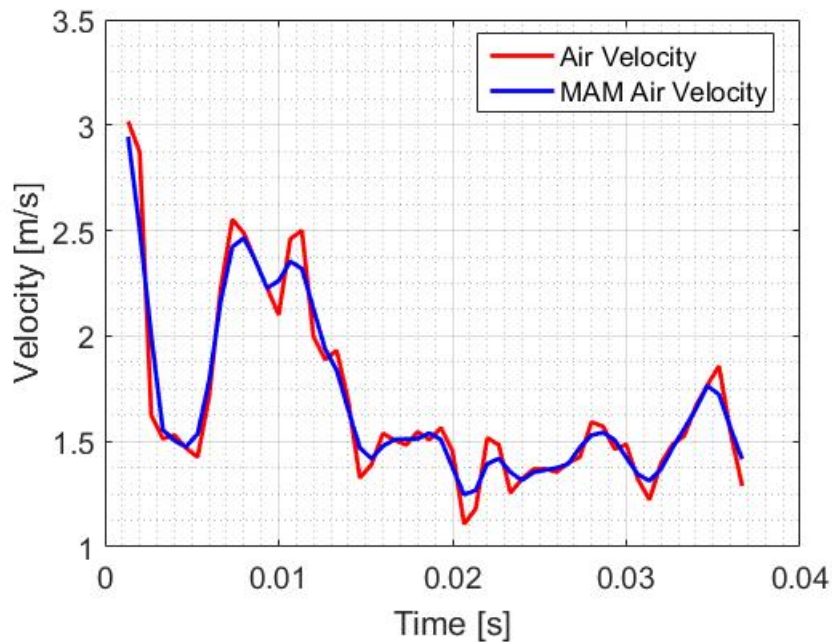


Figure 5.4: Following one bubble with 0.5 mm diameter through the impeller.

error following the bubble from the post-processing can propagate and become larger errors when calculating the velocities and accelerations. Figure 5.3 shows the velocities and the *MAM* applied in the process. Notably, using the *MAM*, the velocities were attenuated.

5.1.4 Gas Void Fraction

The post-processing of the images allows the acquisition of the bubbles' diameter, which sometimes do not correspond to the diameter of a circle, thus the hydraulic diameter is used. The value of void fraction, α , was calculated by dividing the sum of the bubbles' volume by the impeller volume. The bubbles' volume were approximated to a sphere, which is $V = 4/3 \pi r^3$. Figure 5.5 indicates the values of void fraction in the channel by their respective timestep. The mean value of α is equal to 0.0046 for the point IM3 rotating with 900 *rpm* and 0.025 *kg/h*. It is necessary to perform a time average as during the image acquisition bubbles enter and leave the impeller.

Table 5.2 shows the values and standard deviation of radial and circumferential

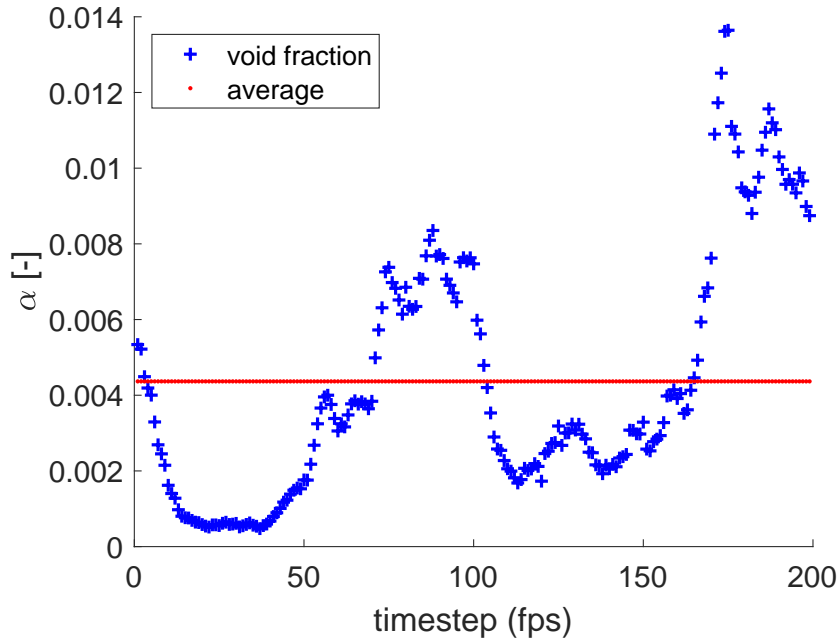


Figure 5.5: Evolution of the measured gas void fraction α in the impeller channel with time.

velocities for each test run. The table presents the rotational velocity ω , mass gas flow rate \dot{m} , bubbles' average diameter d , pressure increment ΔP , bubbles' average radial velocity v_r , bubbles' average circumferential velocity v_θ , standard deviation of radial velocity δv_r , standard deviation of δv_θ and gas void fraction α .

The data acquired are in accordance with the literature (Monte Verde (2016) and Perissinotto *et al.* (2017)). One can observe a decrease in the bubble diameter by increasing the pump rotational speed. Also, the same is observed for the bubble velocities.

The experimental data are used in the next chapters. In appendix A, they are used to compare the velocities acquired by both methods. In chapter 4, the data are used in the two-dimensional drift flux model, in order to validate it.

Table 5.2: Impeller rotation ω , mass gas flow rate \dot{m} , diameter d , pressure increment ΔP , radial velocity v_r , circumferential velocity v_θ , standard deviation of radial velocity δv_r , standard deviation of δv_θ and gas void fraction α

	ω [rpm]	\dot{m} [kg/h]	d [mm]	ΔP [Pa]	v_r [mm/s]	v_θ [mm/s]	δv_r [mm/s]	δv_θ [mm/s]	α_{exp} 10^{-3} [-]
1	600	0.025	1.4	1007	759	876	217	223	4
2			1.4	2280	682	857	242	261	6
3			1.6	3006	606	864	211	240	6
4			1.6	3886	534	821	238	269	7
5	900	0.025	0.6	541	1021	1425	245	298	4
6			0.6	4579	969	1346	257	276	5
7			0.7	7260	868	1283	303	324	5
8			0.8	9318	825	1172	332	350	7
9	900	0.012	0.6	419	980	1447	292	336	2
10			0.6	4168	1028	1342	286	301	2
11			0.7	8078	862	1296	312	388	3
12			0.9	9025	769	1211	271	315	4
13	1200	0.025	0.4	262	1527	1806	318	346	2
14			0.4	5246	1497	1759	341	355	2
15			0.5	11341	1395	1668	319	329	2
16			0.6	16589	1291	1425	295	329	3

5.2 Experimental and Modeling Comparison

In this section, the experimental values calculated using the post-processing of images were showed in Table 5.3. Before that, a summary of what was know is shown. So, summarizing:

- r_i, r_o, β and h are geometric constants measured from the impeller.
- Q_m, λ and Δp are known from the experiments.
- \bar{P} and \bar{T} are the mean pressure and mean temperature, respectively. With them it is possible to calculate ρ_1, ρ_2, μ_1 and μ_2 .

- $\overline{v_{2,s}}$ is measured from the image processing. The in situ velocities of bubbles are a mean on the impeller's space in \hat{s} direction.

The experimental data can be compared with the model following the next steps:

1. As demonstrated before, $\overline{j_{ms}}$ is calculated using Eq. C.75.
2. α is estimated once $v_{2,s}$ was measured from experimental data ($\alpha = \lambda \overline{j_{ms}} / \overline{v_{2,s}}$).
3. With α acquired, it is possible to calculate: $\{\rho_m, \overline{\rho_m}, \tilde{\rho}_m, \Delta\rho, \overline{\Delta\rho}, \tilde{\Delta\rho}\}$.

Table 5.3 shows the mean values for bubbles characteristics in each experiment. Besides, the table presents the rotational velocity ω , mass gas flow rate \dot{m} , pressure increment ΔP , mixture volumetric flux in \hat{s} direction j_{ms} , bubble velocity v_2 and gas void fraction α .

Table 5.3: Impeller rotation ω , mass gas flow rate \dot{m} , pressure increment ΔP , mixture volumetric flux in \hat{s} direction j_{ms} , bubble velocity v_2 and gas void fraction α

	ω [rpm]	\dot{m} [kg/h]	ΔP [Pa]	j_{ms} [mm/s]	v_2 [mm/s]	α 10^{-3} [-]	α_{exp} 10^{-3} [-]
1	600	0.025	1007	922	1159	4	4
2	600	0.025	2280	808	1095	5	6
3	600	0.025	3006	715	1056	5	6
4	600	0.025	3886	603	979	6	7
5	900	0.025	541	1469	1736	3	4
6	900	0.025	4579	1255	1659	4	5
7	900	0.025	7260	1052	1549	4	5
8	900	0.025	9318	857	1433	4	7
9	900	0.012	419	1460	1748	2	2
10	900	0.012	4168	1266	1691	2	2
11	900	0.012	8078	1027	1557	2	3
12	900	0.012	9025	863	1434	2	4
13	1200	0.025	262	1990	2365	2	2
14	1200	0.025	5246	1807	2310	2	2
15	1200	0.025	11341	1534	2174	2	2
16	1200	0.025	16589	1181	1923	3	3

The calculated values of void fraction were compared with the ones given by image processing technique, showing close values. However, as the amount of bubble increases, the difference between them also increases. The highest condition of the amount of gas inside the impeller happens in the point IM11, for segregated flow. Figure 5.6 shows the point IM11. The channel height is very important to predict exactly how much gas the impeller contains. Supposing that in Fig. 5.6 the gas occupied the entire view of the impeller channel. However, the exact height of the gas and water is unknown. Thus, suppose that half of the channel is occupied by the water, so the gas void fraction is 50 %. If the height of the water is three quarters, the gas void fraction is 25 %. In fact, the experiments uncertainty grows with the amount of bubbles.

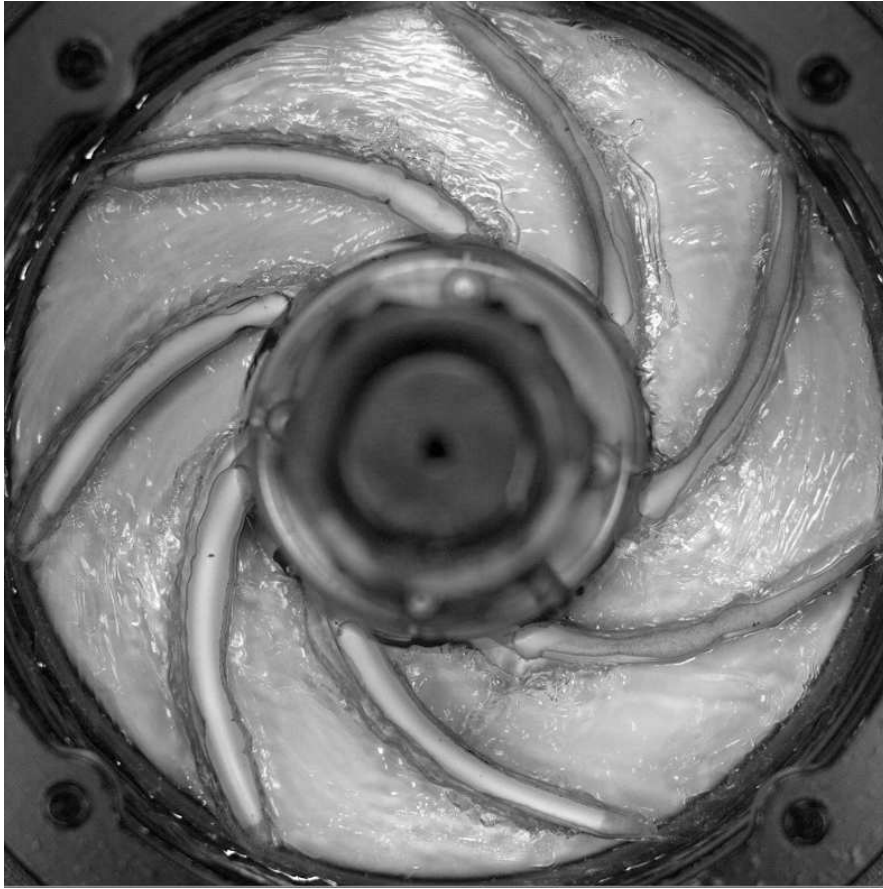


Figure 5.6: Experimental point IM11.

5.3 Modeling Results

The results of the distribution parameter C_0 , the coefficients of Basset and Added Mass and, the bubble shape are discussed in the next sections.

5.3.1 Distribution Parameter - C_0

Wallis (1969) pointed out that for vertical dispersed flow, the distribution parameter lies between 1.0 to 1.5 being more likely 1.2. However, for horizontal and near-horizontal flow, as the bubbles tend to accumulate at the top of the pipe, it is commonly assumed that they move at the average mixture velocity, hence the flow distribution parameter is equal to one.

Clark and Flemmer (1985) performed an experimental work to understand better the upward/downward vertical flows. Their average values for C_0 in upward flow was 1.07 and in downward flow 1.17. The authors proposed a correlation to obtain the distribution parameter as function of void fraction for each direction of the flow, which are:

$$\begin{aligned} C_0 &= 0.934(1 + 1.42\alpha) \quad \rightarrow \quad \text{Upward vertical flow} \\ C_0 &= 1.521(1 - 3.67\alpha) \quad \rightarrow \quad \text{Downward vertical flow} \end{aligned} \quad (5.2)$$

Hibiki and Ishii (2002) proposed one relation using the density of the phases taking into account the effect of the bubble size on the phase distribution, since the presence of the bubbles govern the distribution of the void fraction. Indirectly, the authors relates the Sauter mean diameter, d_{Sm} , with the void fraction. Besides, Eq. 5.3 have its coefficient -22 approximated by the least-square method.

$$C_0 = (1.2 - 0.2\sqrt{\rho_2/\rho_1}) [1 - \exp(-22\langle d_{Sm} \rangle/d)] \quad (5.3)$$

The distribution parameter suggests that the dominant factor to determine itself would be the void fraction. For extreme cases such as concentrated void profile and sharp liquid velocity profiles around the tube center, the distribution parameter may exceed 1.2 as reported by Goda *et al.* (2003).

Biazussi (2014) in his drift model uses different assumptions comparing to the present one. First difference refers to the velocities, which were calculated with the use of correlations proposed by Shoham (2005) instead of measuring them. Besides, the terms related to the acceleration of gravity were substituted by centripetal acceleration.

The present study relates a drift flux using blade coordinate system, taking into account the velocities in \hat{r} and $\hat{\theta}$ direction. On the other hand, Biazussi (2014) used just one direction, so characterizing it as one-dimensional drift-flux model. Another difference relates to the starting point of the formulation for the drift-flux model. The present study used the Navier-Stokes equation which is different from him. The assumptions made by the present work and Biazussi (2014) explains the difference of value found by both authors without implying that one or other model were wrong.

Secondary flows and vortices occur in the impeller and they can be upward or

downward. The phases may behave as co-current or counter-current flow, as presented in the numerical analyses. The operational parameters may influence the flow direction at the impeller inlet which may lead to increase shock losses. These are things that influence the distribution parameter. Therefore the value of C_0 found by Eq. 4.115 is reasonable with the observed ones in turbulent flow in tubes.

5.3.2 Analysis of forces acting on bubbles

The motion of bubbles in laminar or turbulent flows is much more complex than that of rigid solid particles. The interface between bubbles and liquid is not rigid due to the internal flow developing inside the bubbles. This condition implies a relative velocity at the surface. So the drag coefficient is reduced if it was compared with solid particles. The drag coefficient C_D is given as a function of the particle Reynolds number (ISHII AND HIBIKI, 2010):

$$Re_P = \frac{\rho_1 d_b |v_1 - v_2|}{\mu_1} = \frac{\rho_1 d_b |v_s|}{\mu_1} \quad (5.4)$$

The drag coefficient may be altered by numerous physical effects, such as turbulence of the surrounding flow, surface roughness of the particle, particle shape, wall effects, compressibility of the fluids, rarefaction effects and particle concentration effects. All these effects can, in general, only be accounted for by empirical correction factors derived from detailed experiments.

Figure 5.7 shows the drag coefficient as a function of Reynolds number. The chart presented is adapted from Brennen (1994) and the results of the experiments were plotted in red. The drag coefficient is approximately 0.37 for the cases analyzed here.

A generalized graphical correlation in terms of the Eötvös number, E_o , Morton number, M and Reynolds number, Re , was used to compare the shape of bubbles. Figure 5.8 shows those numbers calculated, and the region of wobbling is predominant in the experiments. This shape tends to vary the drag coefficient because for bubbles, it lies below the rigid sphere curve when internal circulation is presented, as reported by Clift *et al.* (2005).

The coefficient ΔC^∞ was calculated with the term A'_1 . This coefficient is studied apart, but it relates Basset and added mass, so the conclusions presented here consider both terms together.

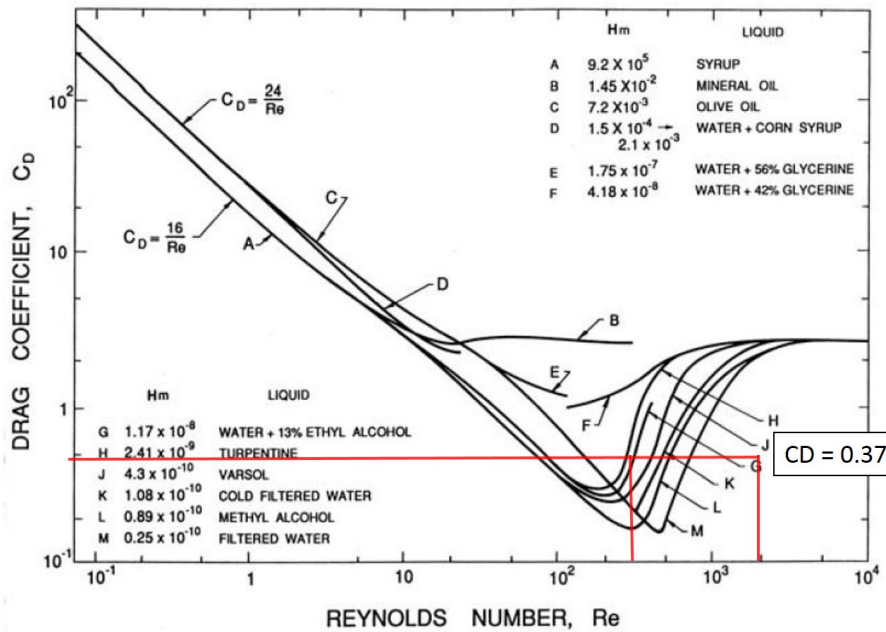


Figure 5.7: Drag Coefficient, C_D x Reynolds Number, Re - Adapted from Haberman and Morton (1953).

It is expected that the added mass coefficient for an individual particle would depend on the void fraction of the surrounding medium. Zuber (1964) first addressed this issue using a cell method and found that the added mass for spherical bubbles increased with volume fraction, α .

Odar and Hamilton (1964) proposed the calculus of coefficients for Basset and added mass as function of acceleration number.

$$C_V = 2.1 - \frac{0.132}{A_c^2 + 0.12}$$

$$C_B = 0.48 + \frac{0.52}{(A_c + 1)^3} \quad (5.5)$$

where: $A_c = \frac{|\vec{v}_1 - \vec{v}_2|^2}{d_B |d| |\vec{v}_1 - \vec{v}_2| / dt}$

For small values of A_c , C_V was found to tend towards the value of 1.05 while the value of 0.5 was recovered for large A_c . However, this value is not so easy to be achieved once other forces are present on bubbles, such as drag, which can influence the calculus if they are not well modeled.

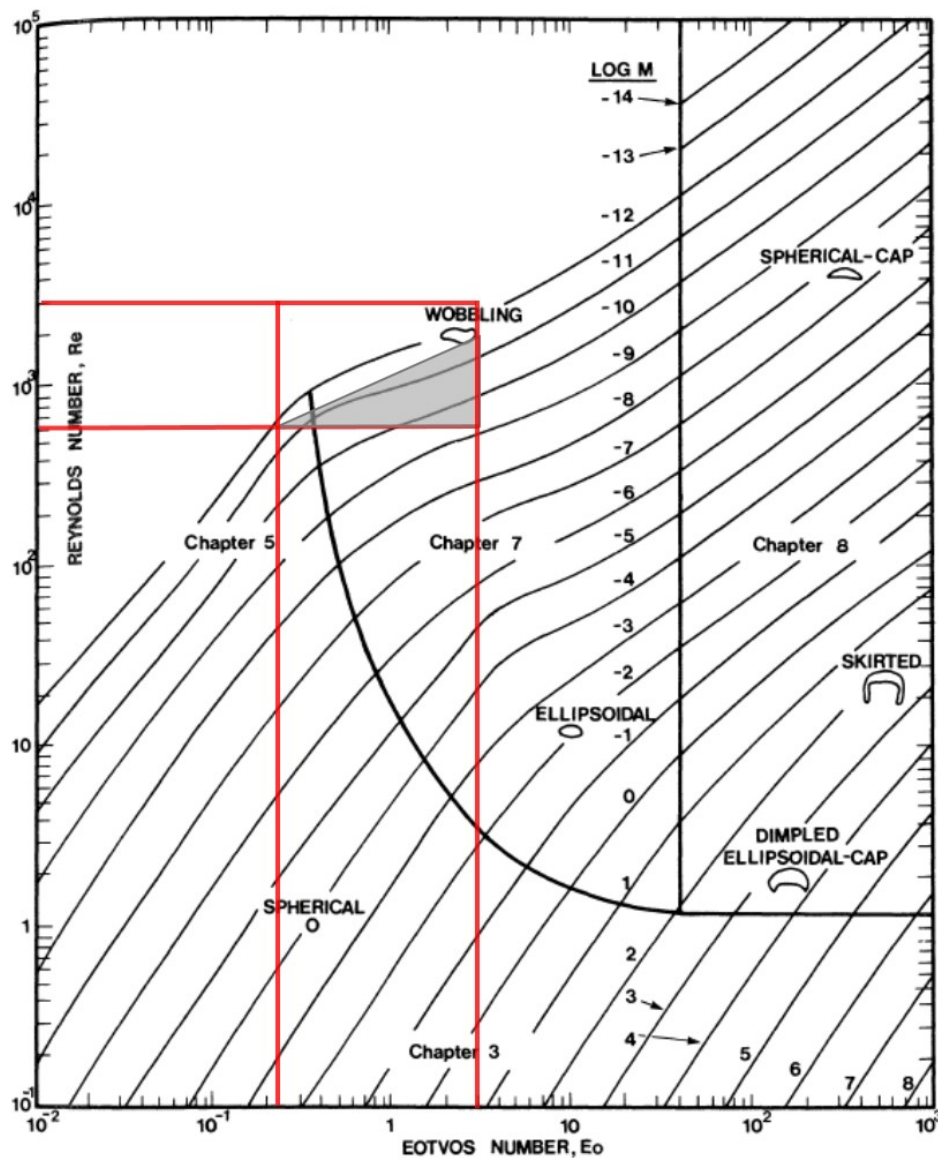


Figure 5.8: Shape regimes for bubbles using: Eötvös Number E_o , Reynolds Number, Re and Morton number M (CLIFT *et al.*, 2005)

Studies of Michaelides and Roig (2011) showed that the added mass coefficient should be constant, equal to 1 and the Basset coefficient should be expressed in dependence of the Strouhal number. The analysis showed that the function of the history term is better correlated with the Reynolds and Strouhal numbers, rather than the acceleration

number which was used originally by Odar and Hamilton (1964).

$$C_B = 2.0 - 1.0533[1 - \exp(-0.14 Re_P Sr^{0.82})^{2.5}] \quad (5.6)$$

The Strouhal number describes the behavior of oscillatory flows. In this context the fluid time scale is the reciprocal value of the characteristic fluid oscillations.

The general expression of Basset force depends on the diffusion process of the vorticity. The well known Basset's expression is found in the limit of unsteady Stokes flow for a rigid sphere. In the case of a bubble, while vorticity comes from no-slip condition at a rigid surface, the bubble tends to vanish the shear stress in its curved surface and vorticity tends to be non-zero. It means that when a particle experiences a sudden change of velocity, a sheet of infinite vorticity is generated at its surface. This effect is even more complicated for bubbles (MAGNAUDET, 1997).

The term ΔC was calculated with the model, taking into account void fraction, which is equal to 1.24. This value calculated using the expression from literature is equal to 1.19, which presents a difference of 4%. Again, this term is related to both forces: added mass and Basset and it is in good agreement with values from literature, once the sum of their results is near 1. The drift-flux model and the slip model developed by Eqs. 4.115 and 4.109 respectively are in good agreement with literature values as they are compared with experiments made in tubes.

The next section will show a proposition of the transition criteria to prevent the surging and gas locking conditions.

5.4 Transition Criteria for Surging and Gas Locking

This section relates the forces on the bubble and they are discussed in in appendix C, in section C.5. Summarizing the forces:

- Drag force:

$$\overline{F_{2s}^D} = \frac{1}{2} A_p C_D \rho_1 \overline{v_{s,s}}^2$$

- Basset and Added Mass force:

$$\overline{F_{2r}^{VB}} = -\rho_1 B_b \Delta C \text{Lambdas} \csc^2 \beta \left[\frac{-\bar{r}}{r_i^2 r_o^2} \right] \left(\frac{Q_m}{2\pi h} \right)^2$$

- Centripetal and Coriolis force:

$$\overline{A_{fr}} = 2\omega \frac{\lambda_2}{\alpha_2} \cot \beta \left(\frac{Q_m}{2\pi h} \right) \frac{\ln(r_o/r_i)}{\Delta r} - \omega^2 \frac{(r_o^2 - r_i^2)}{2\Delta r}$$

$$\overline{A_{f\theta}} = 2\omega \frac{\lambda_2}{\alpha_2} \left(\frac{Q_m}{2\pi h} \right) \frac{\ln(r_o/r_i)}{\Delta r}$$

- Buoyancy force:

$$\overline{F_r^E} = -B_b \left\{ \tilde{\rho}_m \left[\frac{(1 + \cot^2 \beta)}{4\pi^2 h^2} \right] Q_m^2 \frac{1}{\Delta r} \left[\frac{1}{2} \frac{(r_i^2 - r_o^2)}{r_i^2 r_o^2} \right] + \overline{\rho}_m \left(\frac{\cot \beta}{\pi h} \right) \omega \frac{Q_m}{\Delta r} \ln \frac{r_o}{r_i} \right. \\ \left. - \rho_m \omega^2 \frac{(r_o^2 - r_i^2)}{2\Delta r} - \mu \frac{\lambda_k}{\alpha_k} \frac{Q_m}{\pi h} \frac{1}{\Delta r} \left(\frac{r_o^2 - r_i^2}{r_i^2 r_o^2} \right) - \frac{f}{4} \frac{\rho_m}{\sin \beta} \left(\frac{Q_m}{2\pi h} \right)^2 \frac{f_3}{\Delta r} \right\}$$

$$\overline{F_\theta^E} = -B_b \left\{ \tilde{\rho}_m 2 \cot \beta \left(\frac{Q_m}{2\pi h} \right)^2 \left[\left(\frac{\bar{r}}{r_i^2 r_o^2} \right) \right] + 2\overline{\rho}_m \omega \left(\frac{Q_m}{2\pi h} \right) \frac{\ln(r_o/r_i)}{\Delta r} \right. \\ \left. - 2\mu \frac{\lambda_k}{\alpha_k} \frac{Q_m}{\pi h} \cot \beta \left(\frac{\bar{r}}{r_i^2 r_o^2} \right) + \frac{f}{4} \rho_m \frac{\cot \beta}{\sin \beta} \left(\frac{Q_m}{2\pi h} \right)^2 \frac{f_3}{\Delta r} \right\}$$

The subscripts r and θ indicates the forces in polar coordinates. In possess of these forces, the criteria conditions are established in the next sections.

5.4.1 Criteria Conditions

The criteria used here is an extension of those proposed for ducts and applied for centrifugal pumps by some authors (MURAKAMI AND MINEMURA, 1974a, ESTEVAM, 2002, BARRIOS, 2007, among others). Visually the surging occurs when the bubbles start to coalesce. Fig. 5.9 describes the bubble in the impeller channel and its respective blade coordinate system, indicated by \hat{s} and \hat{n} .

From the Transition Criteria it is expected that the bubble can goes to the suction side when the sum of the forces in \hat{n} direction is positive or, it can goes to the pressure side when the opposite happens. This might happen when the resulting force in normal \hat{n} direction begins to be higher than the resulting force in longitudinal direction which is \hat{s} .

It expected that the criterion indicates the region where the surging and gas lock-

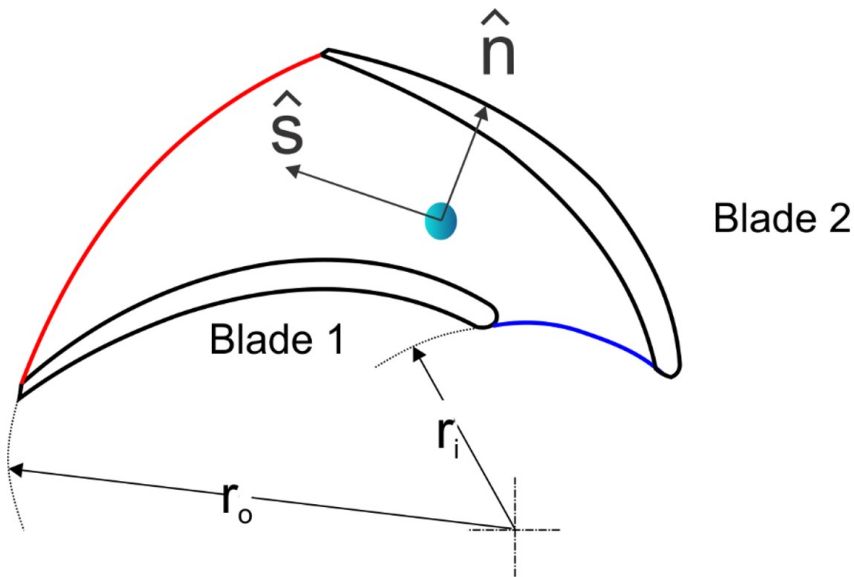


Figure 5.9: Force balance on a bubble inside the impeller channel.

ing begins. These points are showed in Fig. 5.10. As the flow rate of water begins to decrease, the ratio of gas increase, so the bubble swarms appear in the impeller channel, characterizing the pattern of gas pockets. Once the ratio of gas still increase and reach segregated gas, the gas locking will be established, ceasing the pump operation.

$$\sum |\vec{F}_{R \text{ bubbles},s}| = \sum |\vec{F}_{R \text{ bubbles},n}| \quad (5.7)$$

Next, Eq. 5.7 will be developed for Condition 1 and 2.

Condition 1

The first condition tested is the point where the longitudinal force in \hat{s} is equal to the transversal force in \hat{n} . This corresponds to the threshold condition, as the forces are equal in modulus. This condition considers $F_s = F_n$. So, from Eq. 5.7:

$$\overline{\vec{F}}_{2s}^D + \overline{\vec{F}}_{2s}^{VB} + \overline{\vec{F}}_{2s}^E + \overline{\vec{F}}_{2s}^F + \overline{\vec{F}}_{2n}^{VB} + \overline{\vec{F}}_{2n}^E + \overline{\vec{F}}_{2n}^F = 0 \quad (5.8)$$

The development of Eq. 5.8 is presented in section C.6. The result is Eq. 5.9.

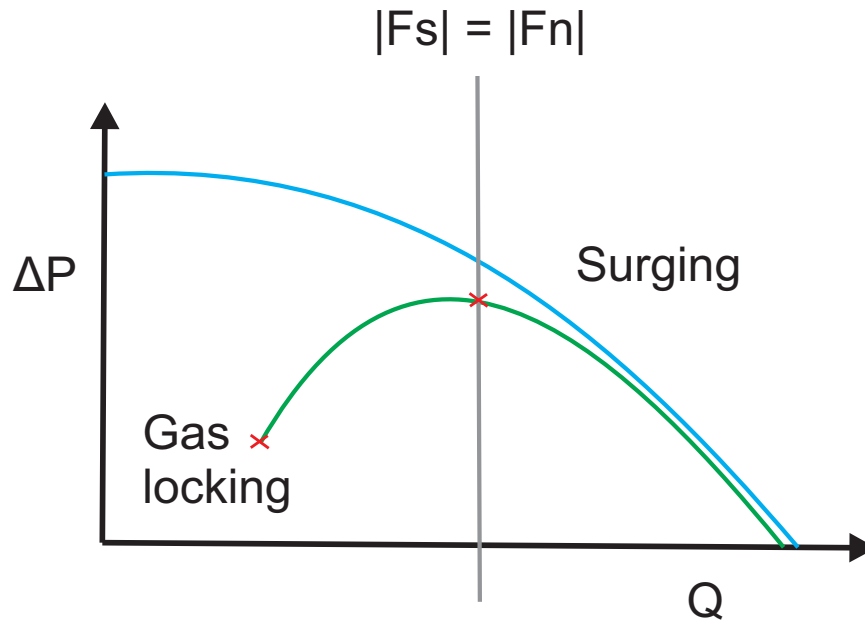


Figure 5.10: Transition criteria

$$C_H = D_1 C_Q^2 + D_2 C_Q + (D_3 F r_{TP,s}^2 + D_4) \quad (5.9)$$

where $D'_{k,k=\{1,2,3,4\}} = f(\lambda, C_D, \Delta C)$

$$\begin{aligned} \circ D_1 &= \frac{\rho_1}{\rho_m} \Delta C \text{Lambdas} G_1 + \frac{\tilde{\rho}_m \cot \beta}{\rho_m 4\pi^2} \left(\frac{r_o}{h}\right)^2 \left[\left(\frac{r_o}{r_i}\right)^2 - 1\right] G_5 \\ &\quad + \frac{f}{4} \frac{\rho_m \cot \beta}{\rho_m \sin \beta} G_5 \left(\frac{r_o^4}{4\pi^2 h^2}\right) f_3 \\ \circ D_2 &= \frac{\rho_2}{\rho_m} \frac{\lambda_2}{\alpha_2} \left(\frac{r_o}{h}\right) \frac{\ln(r_o/r_i)}{\pi} G_5 - \frac{\rho_2}{\rho_m} \frac{\lambda_2}{\alpha_2} \cot \beta \left(\frac{r_o}{h}\right) \frac{\ln(r_o/r_i)}{\pi} \\ &\quad - \left(\frac{r_o}{h}\right) \frac{\ln(r_o/r_i)}{\pi} G_5 + \frac{\mu}{\rho_m} \frac{\lambda_k}{\alpha_k} \frac{\cot \beta}{(\omega \pi h) r_o} \left[\left(\frac{r_o}{r_i}\right)^2 - 1\right] G_5 \\ \circ D_3 &= \frac{1}{2} \left(\frac{A_p}{B_b}\right) \frac{C_D \Delta r}{(\sin \beta + \cos \beta)} \frac{\Delta \rho}{\rho_m} \\ \circ D_4 &= \frac{\rho_2}{\rho_m} \frac{1}{2} \left[1 - \left(\frac{r_i}{r_o}\right)^2\right] \end{aligned} \quad (5.10)$$

Condition 2

The second condition is almost the same as the first. However, as the forces are equal in modulus, here is the point where longitudinal force in \hat{s} is equal to the transversal force in \hat{n} by the other way. This means that $F_s = -F_n$. So, from Eq. 5.7:

$$\overline{F_{2s}^D} + \overline{F_{2s}^{VB}} + \overline{F_{2s}^E} + \overline{F_{2s}^F} - \overline{F_{2n}^{VB}} - \overline{F_{2n}^E} - \overline{F_{2n}^F} = 0 \quad (5.11)$$

The development of Eq. 5.11 is presented in section C.6. The result is Eq. 5.12.

$$\boxed{C_H = E_1 C_Q^2 + E_2 C_Q + \left(E_3 F r_{TP,s}^2 + D_4 \right)} \quad (5.12)$$

where $E'_{k,k=\{1,2,3\}} = f(\lambda, C_D, \Delta C)$

$$\begin{aligned} \circ E_1 &= \frac{\rho_1}{\rho_m} \Delta C \text{Lambdas} G_1 + \frac{\widetilde{\rho_m} \cot \beta}{\rho_m 4\pi^2} \left(\frac{r_o}{h} \right)^2 \left[\left(\frac{r_o}{r_i} \right)^2 - 1 \right] G_6 \\ &\quad + \frac{f}{4} \frac{\rho_m \cot \beta}{\rho_m \sin \beta} G_6 \left(\frac{r_o^4}{4\pi^2 h^2} \right) f_3 \\ \circ E_2 &= \frac{\rho_2}{\rho_m} \frac{\lambda_2}{\alpha_2} \left(\frac{r_o}{h} \right) \frac{\ln(r_o/r_i)}{\pi} G_6 - \frac{\rho_2}{\rho_m} \frac{\lambda_2}{\alpha_2} \cot \beta \left(\frac{r_o}{h} \right) \frac{\ln(r_o/r_i)}{\pi} \\ &\quad - \left(\frac{r_o}{h} \right) \frac{\ln(r_o/r_i)}{\pi} G_6 + \frac{\mu}{\rho_m} \frac{\lambda_k}{\alpha_k} \frac{\cot \beta}{(\omega \pi h)} \frac{1}{r_o} \left[\left(\frac{r_o}{r_i} \right)^2 - 1 \right] G_6 \\ \circ E_3 &= \frac{1}{2} \left(\frac{A_p}{B_b} \right) \frac{C_D \Delta r}{(\sin \beta - \cos \beta)} \frac{\Delta \rho}{\rho_m} \end{aligned} \quad (5.13)$$

Figure 5.11 shows the chart with both conditions plotted. The red curve indicates the condition 1 and the blue curve, condition 2. When the blue curve encounter the experimental curve (the chart only indicates the points) this region is where the surging begins.

The coalescence raises changing the balance on bubble forces resulting in the phenomenon knowing as surging. This is what happens in condition two. As the ratio of gas keep increasing in the impeller channels, the coalescence increases and the bubbles stops its movement, leading into gas-locking condition. This region is shows by the

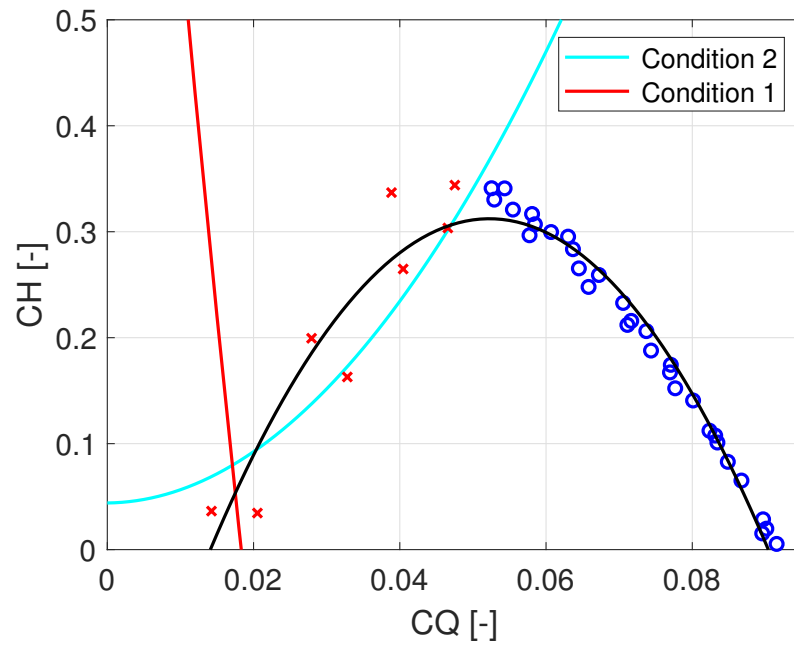


Figure 5.11: Transition criteria - Condition 1 (red line) and Condition 2 (blue line)

encounter of both curves. In this point the resultant of forces are equal to zero.

6 CONCLUSIONS AND RECOMMENDATIONS FOR FUTURE WORK

In this chapter, the first section presents the conclusions about the experimental, numerical and modeling work of gas-liquid flow inside an ESP impeller performed in this work. In the second section, the recommendations for future work on the points still open in this work are covered.

6.1 Conclusions

This work presented an experimental investigation of the two-phase flow, of water and air, inside an electric submersible pump (ESP) impeller. The air was added at the intake of the pump tube entrance. The visualization prototype was designed by Verde *et al.* (2017), and the same experimental apparatus was used. The flow was filmed in several different conditions with a high-speed camera, and the air bubbles were analyzed as they crossed the pump's impeller. The velocities and the diameters were computed from images acquired with numerical scripts written in the course of this work.

The instantaneous fields of gas bubbles velocities were obtained by a sequence of scripts, which for example, have the capability to enhance the edge of the bubbles. The post-processing was able to capture the bubble's centroids in the first part of the code. In the second part, the bubble's velocities were calculated. As the impeller rotated, two kinds of velocities were possible to calculate, the radial and circumferential. The velocities were calculated for 600 *rpm*, 900 *rpm* and 1200 *rpm*. When the tests were performed at 1500 *rpm*, the bubbles were very small, which made their treatment impossible. However, the dimensionless analysis and similarity laws were useful to expand the knowledge obtained by the experimental data collected.

The code developed was verified manually to ensure its functional operation. Its capability to measure a high amount of experimental data allowed the use of statistics for bubble's behavior. The threshold number is an important parameter inside the code that is arbitrarily set by the user.

Also, the code written in the Matlab platform calculates the diameter of the bubbles, which allows the possibility of estimating the gas void (or volume) fraction inside the impeller. Unfortunately, this process is not accurate as the image captured has two

dimensions, so the volume of the bubbles acquired by the code is not reliable. However, considering higher liquid flow rates ($Q > Q_{BEP}$), the volume estimated by the code are near the void fraction predicted by the model, as shown in Table 5.3. The diameters were calculated in the post-processing of the images and mean value of each test were represented in histograms.

The numerical simulation realized for single-phase flow using 600, 900, 1200 and 1500 *rpm* were simulated. The pressure increment of the numerical simulations were compared to experimental data and showed an average value of 4%. The two-phase flow experiments for 900 *rpm* with two different gas mass flow rates were represented in numerical simulations. The water flow varied in a certain range, and the gas mass flow was kept constant at 0.012 *kg/h* and 0.025 *kg/h*. From the numerical results, the total pump pressure was calculated in order to compare with experimental data. The pressure increment showed an average deviation of 9% comparing with experimental data.

The flow streamline in single-phase flow was analyzed and discussed when the ratio Q/Q_{BEP} was higher or less than the value of one. The results show the losses presented in the flow inside the impeller's channels, such as shock losses and flow recirculation. These results are in agreement with Feng *et al.* (2010). The results of two-phase flow simulations, such as velocity and bubble diameter were compared with the experiments. The velocities and bubble diameter values are near as indicated by Table A.19 and A.20. However, the gas void (or volume) fraction calculated numerically was far from the experimental and modeled values. These values are presented in Tables A.18 and 5.3. The gas void fraction analyzed had very low values. The increment pressure of the pump too. Even lower values of gas can lead to operational instabilities in the ESP.

In Chapter 5, a drift-flux model for the two-phase gas-liquid flow inside the impeller was developed. The model was based on blade coordinate system, \hat{s} and \hat{n} correlated with azimuth and radius coordinates, $\hat{\theta}$ and \hat{r} . The concept of radial cascade was used by Brennen (1994). The equations of Mass and Momentum were developed and experimental data provided by the post-processing of images was used to validate the model. The viscous stress tensor was modeled through an analogy with the flow inside a rectangular duct. A closure relationship for the momentum transfer was also used.

The proposed friction factor encompasses all losses expected to happen inside the impeller. The closure of the model showed that the proposed friction factor increases with increasing the pump flow rate as expected, as it goes far from the Best Efficiency

Point. However, for flow rate points near the Q_{BEP} , the friction factor is comparable to the one proposed by S.Vieira (2014).

From the drift-flux model, parameters such as C_0 were discussed in section 5.3.1. Besides, the interphase momentum transfer was analyzed and the forces acting in a bubble were described. The parameters such as drag coefficient, virtual mass and Basset coefficient values showed good agreement with the ones observed in the literature. With these parameters, it was possible to analyze the forces acting on the bubble and propose, based on the literature, transition criteria for surging and gas locking phenomena showing good agreement with the experimental data.

The further improvement of the modeling may lead to better design of geometries for impellers and under gas-liquid flows conditions, for example.

6.2 Recommendations for Future Work

1. The experiments have a gap when the surging condition initiates. The image processing is not able to perform a correct void fraction measure of the impeller channel because the height of it is not considered, as the image has two dimensions the void (or volume) fraction measured is not reliable.
2. The present work studies the impeller in a radial cascade concept (BRENNEN, 1994). In order to improve the knowledge of the flow inside the pump, the idea of composite cascade may be developed so other impellers might be analyzed. Besides, the impeller and diffuser geometries may be improved to deal with multiphase flows.
3. The bubble's recirculation, which generally occurs on the pressure blade side, needs further studies in order to control this phenomenon. The blade profile could be changed to avoid this situation.
4. In aircraft technology there is an idea of active smart blades. Extendable leading edge slats and trailing edges have been regulating the flow conditions on aircraft wings for decades. Integrated leading edge slats were employed experimentally in wind tunnel tests. Measuring instruments recorded the reaction dynamics with respect to the forces acting on the wind tunnel model. This kind of technology could be adapted for uses in centrifugal pumps in order to improve its efficiency.
5. The experiments have two kinds of methodologies, which may deepen the study

in the physics phenomenon that occurs with two-phase flows inside the ESP impellers: Gas variation and constant gas flow rates. Unfortunately, only one was performed in the present study, the constant gas flow rate. The other methodology should be tested.

6. Regarding the CFD simulation, breakup and coalescence models should be further investigated. This could have been realized with the image treatment but was not performed in the course of the present work. This was not an objective but could be done in future works. In order to perform this, the code should be amplified. A first idea to capture this is to set boundaries for the radius because this will occur when $r > r_i$ and $r < r_o$. Further investigations should be done, experiments, and so on. As it is able to be manually followed, the code can be adapted for this.
7. The viscous term was studied, making an analogy with ducts, which is not real. This approximation does not correspond to the impeller channels so that further improvements can be performed for this part.
8. The lift force is not considered in the present analysis because the height is not considered. So, the influence of lift, even giving a small height of the present impeller and the literature and premises indicating that this is not significant, the measurement may be performed to precisely inform that.
9. The commercial code has improvements that should be tested. For example, when the simulations started in April/2018, the breakup model used was the Luo and Svendsen. Now, the ANSYS has other options that may be tested, or even a subroutine may be created for this. For example, the Schmehl Breakup Model and the Taylor Analogy Breakup (TAB) Model (ANSYS, 2017). It was observed that this kind of model could impact the simulation results.
10. Regarding the drift-flux model, a deep analysis on C_0 and v_{2j} parameters for the case of gas-liquid flow inside ESP impeller should be done with an extension of the experimental campaign. Also, further analysis of the proposed transition criteria for other pumps impellers is necessary to discuss its scope under other conditions.
11. It is important to measure the flow velocity field of the continuous phase, with the PIV system, for example, and then analyze the point-to-point velocity of continuous and dispersed phase. In this way a detailed analysis of the C_0 might be performed. Also, the swarm effect of bubbles concentrated in one of the blades

should be carefully analyzed.

12. Studies about breakup and coalescence are needed to close the proposed models. The first guess for the breakup model would be based on Hinze (1955) for the impeller.
13. Some simplifications were performed in the model due to the gas-liquid two-phase flow analysis, however, in its full form it is applicable for other two-phase flows such as liquid-liquid ones. So, a recommendation, as there is data in the literature, is to rewrite the model for liquid-liquid flows and compare with experimental data.
14. The equations developed for the impeller may be used for the diffuser. In this case, the rotation ω is equal to zero.

References

AMARAL, G. D. L. **Modelagem do escoamento monofásico em bomba centrífuga submersa operando com fluidos viscosos**. 2007. Ph.D. Thesis. Ph. D. thesis, Universidade Tecnológica Federal do Paraná.

ANSYS. Cfx-solver theory guide release 17.2. 2017.

ANTAL, S.; LAHEY JR, R. and FLAHERTY, J. Analysis of phase distribution in fully developed laminar bubbly two-phase flow. **International Journal of Multiphase Flow**, v. 17, n. 5, 635–652, 1991.

API, R. 11s2. "recommended practice for electric submersible pump testing". **2nd Edition. American Petroleum Institute**, 1997.

BARRIOS, Lissett J. **Visualization and modeling of multiphase performance inside an electrical submersible pump**. 2007. Ph.D. Thesis. University of Tulsa.

BIAZUSSI, JL. **Modelo de deslizamento para escoamento gás-líquido em bomba centrífuga submersa operando com líquido de baixa viscosidade**. 2014. Ph.D. Thesis. Ph. D. thesis, Universidade Estadual de Campinas.

BRENNEN, C.E. Hydrodynamics of pumps. **Concepts ETI Inc., Oxford Science Publications**, p. 81, 1994.

BURNS, A.D.; FRANK, T.; HAMILL, I.; SHI, J.M. *et al.* The Favre averaged drag model for turbulent dispersion in eulerian multi-phase flows. In **5th international conference on multiphase flow, ICMF**, v. 4, pp. 1–17. ICMF, 2004.

CARIDAD, J. and KENYERY, F. Cfd analysis of electric submersible pumps (esp) handling two-phase mixtures. **J. Energy Resour. Technol.**, v. 126, n. 2, 99–104, 2004.

CHENG, W.J.; SHAO, C.L. and ZHOU, J.F. Unsteady study of molten salt pump conveying mediums with different viscosities. **International Journal of Heat and Mass Transfer**, v. 137, 174–183, 2019.

CHURCHILL, S.W. Friction-factor equation spans all fluid-flow regimes. 1977.

CLARK, N. and FLEMMER, R. Predicting the holdup in two-phase bubble upflow and downflow using the zuber and findlay drift-flux model. **AIChE journal**, v. 31, n. 3, 500–503, 1985.

CLIFT, R.; GRACE, J.R. and WEBER, M.E. **Bubbles, drops, and particles**. Courier Corporation, 2005.

, J. M.OTHERS *et al.* **Estudo experimental do escoamento bifásico ar-água em uma bomba centrífuga radial**. 2017. M.Sc. Dissertation. Universidade Tecnológica Federal do Paraná.

DUKLER, A.; WICKS III, M. and CLEVELAND, R. Frictional pressure drop in two-phase flow: B. an approach through similarity analysis. **AIChE Journal**, v. 10, n. 1, 44–51, 1964.

ESTEVAM, Valdir. **Uma análise fenomenológica da operação de bomba centrífuga com escoamento bifásico**. 2002. Ph.D. Thesis. Ph. D. thesis, Universidade Estadual de Campinas.

FENG, J.; BENRA, F.K. and DOHMEN, H. Application of different turbulence models in unsteady flow simulations of a radial diffuser pump. **Forschung im Ingenieurwesen**,

v. 74, n. 3, 123–133, 2010.

FENG, J.; BENRA, F.K. and DOHMEN, H.J. Unsteady flow visualization at part-load conditions of a radial diffuser pump: by piv and cfd. **Journal of Visualization**, v. 12, n. 1, 65–72, 2009a.

URL: <http://dx.doi.org/10.1007/BF03181944>

FENG, J.; BENRA, F.K. and DOHMEN, H.J. Unsteady flow visualization at part-load conditions of a radial diffuser pump: by piv and cfd. **Journal of Visualization**, v. 12, n. 1, 65–72, 2009b.

FOX, R.W.; MCDONALD, A.T. and PRITCHARD, P.J. **Introduction to fluid mechanics**, v. 5. John Wiley & Sons New York, 1998.

FURUYA, O. An analytical model for prediction of two-phase (noncondensable) flow pump performance. 1985.

GAMBOA, Jose. **Prediction of the transition in two-phase performance of an electrical submersible pump**. 2009. Ph.D. Thesis. University of Tulsa, OK, USA.

GODA, H.; HIBIKI, T.; KIM, S.; ISHII, M. and UHLE, J. Drift-flux model for downward two-phase flow. **International journal of heat and mass transfer**, v. 46, n. 25, 4835–4844, 2003.

GONZALEZ, R.C. and WOODS, R.E. **Digital Image Processing**. Prentice-Hall, Inc, 2008.

GROTJANS, H. and MENTER, F. Wall functions for general application {CFD} codes. **ECCOMAS**, 1998.

GÜLICH, J.F. **Centrifugal pumps**, v. 2. Springer, 2008.

HABERMAN, W.L. and MORTON, R. An experimental investigation of the drag and shape of air bubbles rising in various liquids. Relatório técnico, David Taylor Model Basin Washington DC, 1953.

HIBBELER, R.C. **Engineering Mechanics: Dynamics**. Prentice Hall, 2010.

HIBIKI, T. and ISHII, M. Distribution parameter and drift velocity of drift-flux model in bubbly flow. **International Journal of Heat and Mass Transfer**, v. 45, n. 4, 707–721, 2002.

HINKELMANN, K. and KEMPTHORNE, O. **Design and analysis of experiments: advanced experimental design**, v. 2. Wiley Online Library, 2005.

HINZE, J. Fundamentals of the hydrodynamic mechanism of splitting in dispersion processes. **AIChE Journal**, v. 1, n. 3, 289–295, 1955.

HOU, H.; ZHANG, Y.; LI, Z.; JIANG, T.; ZHANG, J. and XU, C. Numerical analysis of entropy production on a lng cryogenic submerged pump. **Journal of Natural Gas Science and Engineering**, v. 36, 87–96, 2016.

IHME, F.; SCHMIDT-TRAUB, H. and BRAUER, H. Theoretische untersuchung über die umströmung und den stoffübergang an kugeln. **Chemie Ingenieur Technik**, v. 44, n. 5, 306–313, 1972.

ISHII, M. and HIBIKI, T. **Thermo-fluid dynamics of two-phase flow**. Springer Science & Business Media, 2010.

LEGENDRE, D. and MAGNAUDET, J. The lift force on a spherical bubble in a viscous

linear shear flow. **Journal of Fluid Mechanics**, v. 368, 81–126, 1998.

LONGHI, C. **Estudo experimental e Modelagem Do escoamento Bifásico Água e Ar Em Manuseador De Gás Hélico-Axial e Em Bomba Centrífuga**. 2016. M.Sc. Dissertation. University of Campinas.

MAGNAUDET, J.J. The forces acting on bubbles and rigid particles. In **ASME Fluids Engineering Division Summer Meeting, FEDSM**, v. 97, pp. 22–26. 1997.

MENTER, F.R. Two-equation eddy-viscosity turbulence models for engineering applications. **AIAA journal**, v. 32, n. 8, 1598–1605, 1994.

MICHAELIDES, E.E. and ROIG, A. A reinterpretation of the odar and hamilton data on the unsteady equation of motion of particles. **AIChE Journal**, v. 57, n. 11, 2997–3002, 2011.

MIKIELEWICZ, J.; WILSON, D.G.; CHAN, T.C. and GOLDFINCH, A.L. A method for correlating the characteristics of centrifugal pumps in two-phase flow. **Journal of fluids Engineering**, v. 100, n. 4, 395–409, 1978.

MINEMURA, K.; UCHIYAMA, T.; SHODA, S. and EGASHIRA, K. Prediction of air-water two-phase flow performance of a centrifugal pump based on one-dimensional two-fluid model. 1998.

MONTE VERDE, W. **Bombas Centrífugas Submersas: Visualização do escoamento bifásico gás-líquido, operação com fluido viscoso e modelagem de desempenho**. 2016. Ph.D. Thesis. Universidade Estadual de Campinas, UNICAMP, Campinas.

MURAKAMI, M. and MINEMURA, K. Effects of entrained air on the performance of a centrifugal pump: 1st report, performance and flow conditions. **Bulletin of JSME**,

v. 17, n. 110, 1047–1055, 1974a.

MURAKAMI, M. and MINEMURA, K. Effects of entrained air on the performance of a centrifugal pump: 2nd report, effects of number of blades. **Bulletin of JSME**, v. 17, n. 110, 1286–1295, 1974b.

NELIK, L. **Centrifugal & Rotary Pumps: Fundamentals With Applications**. CRC Press, 1999.

ODAR, F. and HAMILTON, W.S. Forces on a sphere accelerating in a viscous fluid. **Journal of Fluid Mechanics**, v. 18, n. 2, 302–314, 1964.

OFUCHI, César Yutaka. **Técnicas avançadas para análise de escoamento bifásico gás-líquido em golfadas**. 2011. M.Sc. Dissertation. Universidade Tecnológica Federal do Paraná.

OFUCHI, E.M.; STEL, H.; SIRINO, T.; VIEIRA, T.S.; PONCE, F.J.; CHIVA, S. and MORALES, R. Numerical investigation of the effect of viscosity in a multistage electric submersible pump. **Engineering Applications of Computational Fluid Mechanics**, v. 11, n. 1, 258–272, 2017.

OPPENHEIM, A.V. and SCHAFER, R.W. **Discrete-time signal processing**. Pearson Education, 2014.

PATANKAR, S. **Numerical heat transfer and fluid flow**. CRC press, 1980.

PATERNOST, G.M. **Estudo experimental sobre bomba centrífuga operando com fluido viscoso e escoamento bifásico gás-líquido**. 2013. M.Sc. Dissertation. University of Campinas.

PATERNOST, G.M.; BANNWART, A.C. and ESTEVAM, V.E.A. Experimental study of a centrifugal pump handling viscous fluid and two-phase flow. **SPE Production & Operations**, v. 30, n. 02, 146–155, 2015.

PENTEADO, M.R.M. and FRANKLIN, E.D.M. Velocity fields of a bed-load layer under a turbulent liquid flow. **Experimental Thermal and Fluid Science**, v. 78, 220–228, 2016.

PERISSINOTTO, R.M.; MONTE VERDE, W.; BIAZUSSI, J.L.; CASTRO, M.S. and BANNWART, A. Oil droplets within an esp impeller: Experimental analysis of velocities and accelerations. In **Experimental Heat Transfer, Fluid Mechanics and Thermodynamics**. Society of Petroleum Engineers, 2017.

SABINO, R. H. G. **Análise da dinâmica de uma bolha de gás em uma bomba centrífuga**. 2015. M.Sc. Dissertation. Universidade Tecnológica Federal do Paraná.

SCHÄFER, T.; BIEBERLE, A.; NEUMANN, M. and HAMPEL, U. Application of gamma-ray computed tomography for the analysis of gas holdup distributions in centrifugal pumps. **Flow Measurement and Instrumentation**, v. 46, 262–267, 2015.

SEGALA, W. Simulação numérica do escoamento monofásico no primeiro estágio de uma bomba centrífuga de duplo estágio. **Universidade Tecnológica Federal do Paraná**, 2010.

SHAH, R. A correlation for laminar hydrodynamic entry length solutions for circular and noncircular ducts. 1978.

SHOHAM, O. **Mechanistic Modeling of Gas/Liquid Two-phase Flow in Pipes**. Spe, 2005.

SIRINO, Thiago. **Estudo numérico da influência da viscosidade no desempenho de uma bomba centrífuga submersa**. 2013. M.Sc. Dissertation. Universidade Tecnológica Federal do Paraná.

SOLANO, Edgar A. **Viscous effects on the performance of electro submersible pumps (ESP's)**. 2009. Ph.D. Thesis. University of Tulsa.

SONKA, M.; HLAVAC, V. and BOYLE, R. **Image processing, analysis, and machine vision**. Cengage Learning, 2014.

STEL, H.; OFUCHI, E.M.; SABINO, R.H.; ANCAJIMA, F.C.; BERTOLDI, D.; MARCELINO NETO, M.A. and MORALES, R.E. Investigation of the motion of bubbles in a centrifugal pump impeller. **Journal of Fluids Engineering**, v. 141, n. 3, 2019.

STEL, H.; SIRINO, T.; PONCE, F.; CHIVA, S. and MORALES, R. Numerical investigation of the flow in a multistage electric submersible pump. **Journal of Petroleum Science and Engineering**, v. 136, 41–54, 2015.

STEPANOFF, A. Flow pumps, design and application. **John Wile & Sons Inc., USA**, 1957.

SUN, D. and PRADO, M. Single-phase model for esp's head performance. In **SPE Production and Operations Symposium**. Society of Petroleum Engineers, 2003.

SUN, D.; PRADO, M.G. *et al.* Single-phase model for electric submersible pump (esp) head performance. **SPE Journal**, v. 11, n. 01, 80–88, 2006.

S.VIEIRA, T. Análise das perdas de carga no escoamento monofásico em rotor de bomba centrífuga submersa utilizada na elevação de petróleo. 2014.

TAKACS, G. Electrical submersible pumps manual: Design. **Operations, and Maintenance: Access online via Elsevier**, 2009.

TOMIYAMA, A. Struggle with computational bubble dynamics. **Multiphase Science and Technology**, v. 10, n. 4, 369–405, 1998.

TREVISAN, Francisco Exaltacao. **Modeling and visualization of air and viscous liquid in Electrical Submersible Pump**. 2009. Ph.D. Thesis. University of Tulsa.

VAN NIEROP, E.A.; LUTHER, S.; BLUEMINK, J.J.; MAGNAUDET, J.; PROSPERETTI, A. and LOHSE, D. Drag and lift forces on bubbles in a rotating flow. **Journal of fluid mechanics**, v. 571, 439–454, 2007.

VERDE, W.M.; BIAZUSSI, J.L.; SASSIM, N.A. and BANNWART, A.C. Experimental study of gas-liquid two-phase flow patterns within centrifugal pumps impellers. **Experimental Thermal and Fluid Science**, v. 85, 37–51, 2017.

WALLIS, G.B. **One-dimensional two-phase flow**. McGraw-Hill, 1969.

WELCH, G.; BISHOP, G. *et al.* An introduction to the kalman filter. 1995.

WELLEK, R.; AGRAWAL, A. and SKELLAND, A. Shape of liquid drops moving in liquid media. **AIChE Journal**, v. 12, n. 5, 854–862, 1966.

WHITE, F.M. Fluid mechanics. 5th. **Boston: McGraw-Hill Book Company**, 2003.

WILCOX, D.C. *et al.* **Turbulence modeling for CFD**, v. 2. DCW industries La Canada, CA, 1998.

WILSON, D.G.; CHAN, T. and MANZANO-RUIZ, J. Analytical models and experimental studies of centrifugal-pump performance in two-phase flow.[pwr]. Relatório técnico, Massachusetts Inst. of Tech., Cambridge (USA). Dept. of Mechanical Engineering, 1979.

ZHOU, D. and SACHDEVA, R. Simple model of electric submersible pump in gassy well. **Journal of Petroleum Science and Engineering**, v. 70, n. 3-4, 204–213, 2010.

ZUBER, N. On the dispersed two-phase flow in the laminar flow regime. **Chemical Engineering Science**, v. 19, n. 11, 897–917, 1964.

APPENDIX A – NUMERICAL SIMULATION

This appendix presents the numerical simulation of single and two-phase flow inside the impeller of an ESP. The commercial software Ansys® was used, specifically CFX® and ICEM CFD™. They were used to process the single and two-phase flow in impellers and to construct the appropriate meshes, respectively. The details of the simulation are presented in this chapter. Also, simulations were performed using the open source code OpenFOAM, however some problems of using the code for this applications were discovered and the results were not interesting. A description of the simulations with OpenFOAM is described in APPENDIX G.

A.1 Computational Procedure

The simulations were performed in two computers, which had two Intel® processors Core i7-4790 CPU 3.60GHz, one with 16GB of memory RAM DDR3 and the other with 8GB. After April/18, the simulations were ran on a workstation with two Intel® processors, Xeon 4116 Silver with 2.1 GHz 33MB, and total memory of 64GB DDR4 2400 ECC RDIMM.

Figure A.1 (a) shows the prototype pump design in CAD, representing the solid part. Figure A.1 (b) represents the fluid domain. The fluid domain was acquired using boolean operations, which consisted of filling the pump with virtual material and then, subtracting the solid components. These operations were performed by the SolidWorks® platform.

The numerical model was composed of 4 different domains, each of them with its own mesh. The components can be identified in Fig. A.1 (b). The first domain is composed of the entrance tube, the second the diffuser entrance, the impeller being the third and, lastly, the diffuser exit. When in possession of these domains, they were meshed using Ansys® ICEM CFD™. The impeller and the diffuser were meshed using Ansys® TurboGrid™. All the meshes were composed of an unstructured grid, employing tetrahedrons. Table A.1 shows the main dimensions of the impeller and diffusers.

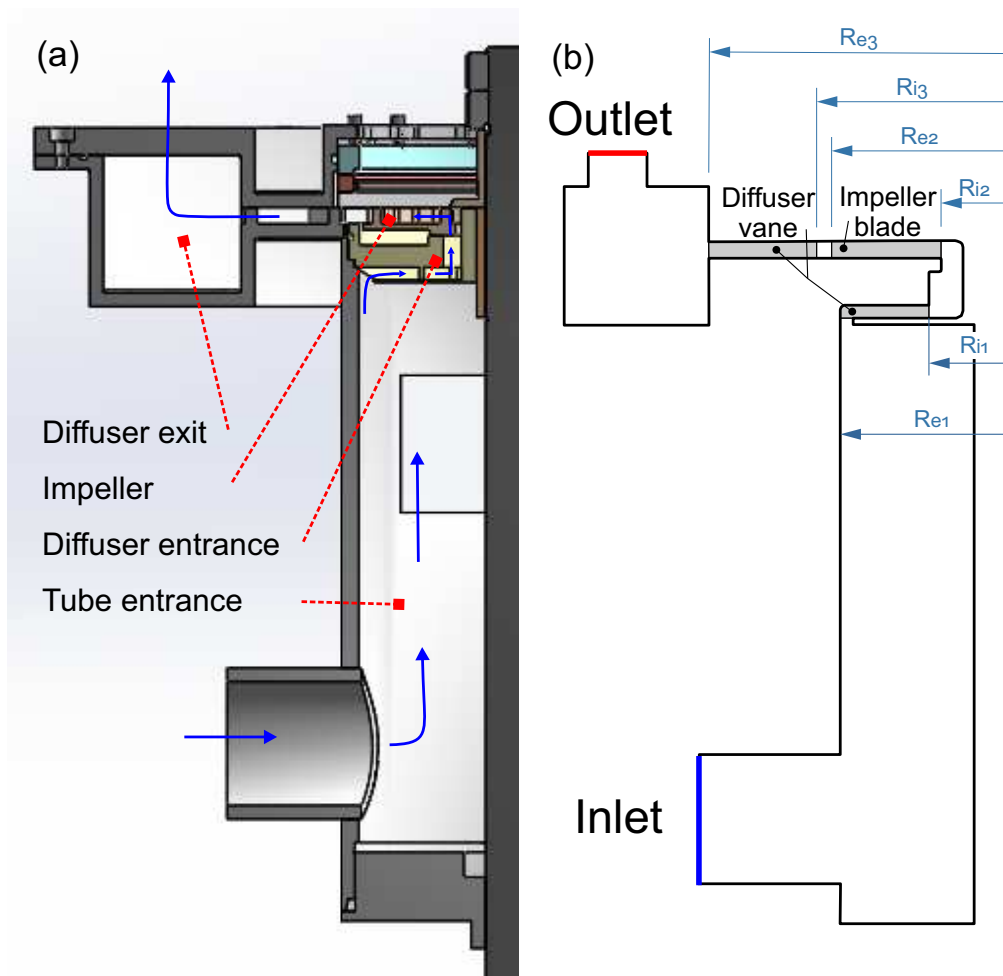


Figure A.1: Prototype Components: (a) Solid components (CAD) (b) Simulation Domains.

A.1.1 Test Matrix - Single-Phase Water Flow

The operational limitations of this prototype were investigated by Monte Verde (2016), who conducted some preliminary tests to define the limits of the experimental setup. The suction pressure and the discharge were limited by the maximum pressure supported by the acrylic window. The pressure limit was 150 kPa. However, the pump rotation was restricted by the seal of the visualization window and unable to operate properly at high rotations, which means above 1500 *rpm*.

The numerical simulations were performed for the single-phase flow at four dif-

Table A.1: Dimensions of Prototype's Impeller and Diffusers

Variable	Diffuser entrance	Impeller	Diffuser exit
Blade/Vane number	6	7	8
Inner diameter [mm]	$Di_1 = 26.9$	$Di_2 = 44.2$	$Di_3 = 125$
Outer diameter [mm]	$De_1 = 58.1$	$De_2 = 111.4$	$De_3 = 200$
Channel height [mm]	7.64	6	6
Entrance blade angle	22.8	19.8	21.8
Exit blade angle [°]	63.0	46.8	30.2

ferent rotational speeds, namely 600, 900, 1200 and 1500 *rpm*. The liquid flow rate was set to the best efficiency point (BEP), 0.8 and 1.2 of the BEP. For the highest rotational speed (1500 rpm) only the BEP flow rate was simulated. Table A.2 shows the cases simulated for single-phase flow.

Table A.2: Numerical Simulation test matrix for single-phase water flow.

Rotation [rpm]	Flow rate [m^3/h]		
	0.8 Q_{BEP}	Q_{BEP}	1.2 Q_{BEP}
600	1.70	2.13	2.56
900	2.56	3.20	3.84
1200	3.41	4.26	5.11
1500	-	5.33	-

The experimental data of maximum efficiency presented in Table A.2 were extracted from Monte Verde (2016) who studied the performance curves of the prototype pump analyzed. The data acquired were used to validate the numerical simulations.

A.1.2 Test Matrix - Two-Phase Air-Water Flow

The two-phase flow simulations were performed with a constant gas flow rate, as described in the experiments in Chapter 3. The tests were performed under two circumstances: 0.025 and 0.012 *kg/h* gas flow rate at 900 *rpm*. For each operational condition,

ten points were simulated. Just one was not simulated because the simulations did not reach convergence due to a higher presence of the gas. Figure A.2 shows the single-phase flow results (blue triangles), which are represented for the reader reference. The results of two-phase experiments are indicated by the red crosses for 0.025 kg/h , and yellow squares for 0.012 kg/h of constant gas mass flow rate. The pump performance

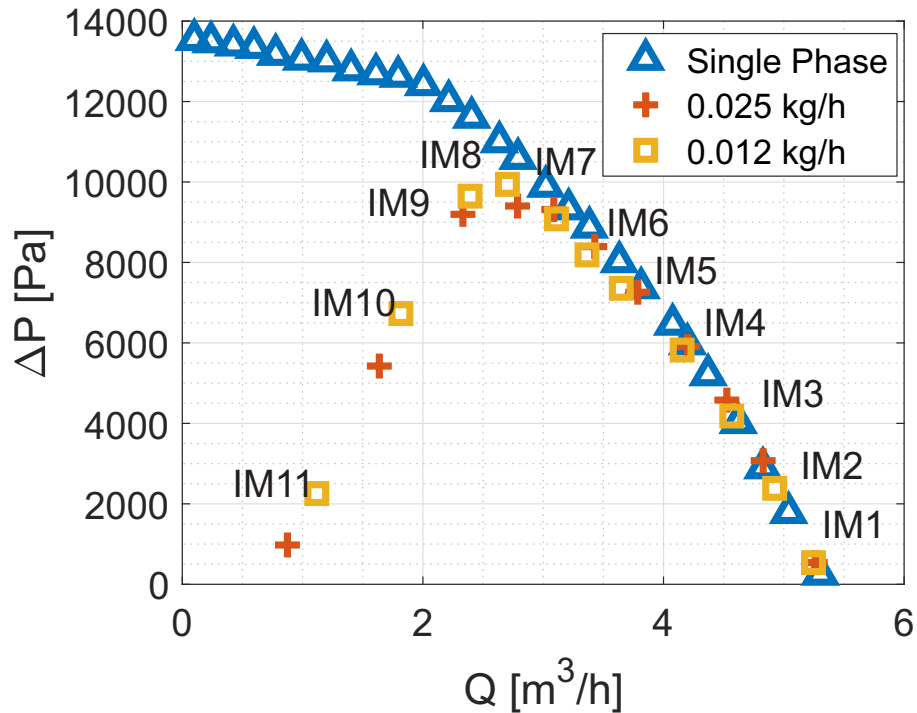


Figure A.2: Two-phase flow experimental data, which will be used to validate numerical simulations.

curve is a reference for ESP, and these are the experimental points (pressure increment) that will be reproduced by numerical simulation. The liquid volumetric flow rates are indicated in Table A.3.

A.2 CFD Simulations

The single-phase and two-phase flow CFD simulations followed the same routine:

1. Generation of the geometry and elaboration of fluid domains.

Table A.3: Numerical simulation test matrix for two-phase air-water flow.

m_g [kg/h]	Liquid flow rate Q [m ³ /h]									
	IM1	IM2	IM3	IM4	IM5	IM6	IM7	IM8	IM9	IM10
0.025	5.260	4.828	4.526	4.201	3.786	3.428	3.088	2.786	2.332	1.637
0.012	5.246	4.923	4.567	4.154	3.649	3.364	3.110	2.702	2.392	1.817

2. Mesh creation.
3. Definition of governing equations adopted.
4. Boundary and initial conditions definition.
5. Simulating the transient and steady state regimes.
6. Comparing the results with the experimental data (pressure).
7. For two-phase flow results, the bubbles' velocities are compared with the image treatment.

Next in this section, details regarding each part of the simulation pre-processing are described.

A.2.1 Creating the mesh

When in possession of the domains, it is possible to generate the mesh which will be used for simulation. The mesh generation of impeller and diffusers were made in the Turbogrid™ and ICEM-CFD™. The remaining components were made in ICEM-CFD™. Basically, the steps for mesh generation are:

1. Define the geometry of the region of interest.
2. Create regions of fluid flow, solid regions and surface boundary names.
3. Set properties for the mesh.

The Ansys Turbogrid™ is a program specialized in the generation of turbomachinery mesh, using geometry to automatically make structured mesh with respect to initial parameters delimited by the user, such as the wall refinement. The first step to create the mesh is the acquisition of the points (between 150 to 300) of the solid regions using

Solidworks™. They are responsible to form the blade profile, hub and shroud. Then, the profile is loaded into Ansys Turbogrid™ and blocks are formed. These blocks are responsible to creating better adjustments of elements which are filled into the geometry.

The geometry is loaded into ICEM-CFD™, in order to use tetrahedral elements to fill the geometry. The user can specify mesh parameters, such as mesh size, type and method. The parameters can be selected to work globally or individually in parts, surfaces, curves or regions. Due to the turbulence model used (described in section A.3.2) the elements near the wall were refined.

The quantity of the elements generated was tested. This process is a mesh sensitivity test and is described in section A.3.3. First, the governing equations and boundary conditions should be discussed. Then, the time step is introduced.

A.2.2 Numerical Discretization

The solutions for real flows, described by the Navier-Stokes equations, should use a numerical approach in order to solve the equations. The numerical approach uses algebraic approximations which are solved using numerical methods, once the analytic solution for N-S equations exists only for very simple flows under ideal conditions in most cases.

The software ANSYS CFX™ uses an element-based finite volume method. This method consists of dividing the region of interest into small sub-regions, called control volumes. The equations are then discretized and solved iteratively for each control volume. The spatial domain discretized by the generated mesh is used to conserve relevant quantities such as mass, momentum, and energy. The values of each variable can be acquired at any specific point of the domain.

For simplicity, a tetrahedral mesh element is illustrated in two dimensions in Fig. A.3, but the mesh is three dimensional. Grouping the elements a full picture of the flow behavior can be determined. All solution variables and fluid properties are stored at the nodes (mesh vertices). A control volume (the shaded area) is constructed around each mesh node using the median-dual scheme (defined by lines joining the centers of the edges and element centers surrounding the node).

The finite volume methodology will not be explained here, but can be found in many books, such as Patankar (1980).

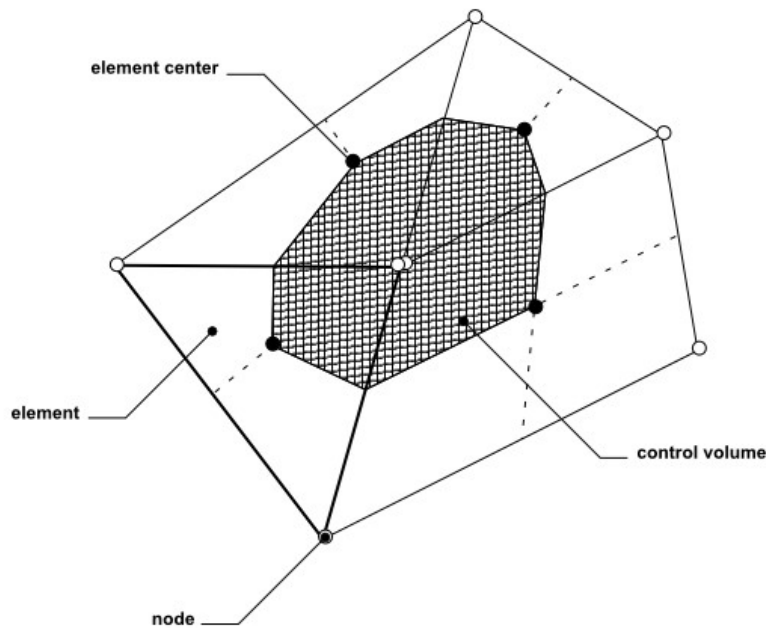


Figure A.3: Control-volume definition. (ANSYS, 2017)

A.2.3 Domains and Interfaces

Basically, the pump was divided in four domains, as described in Fig. A.1: entrance tube, diffuser entrance, impeller and diffuser exit.

- **Entrance tube:** At the entrance of the tube the inlet condition was specified, which is a reference pressure of 0 Pa (gauge). The exit of the entrance tube is a region of other domain which is the beginning of the diffuser entrance.

- **Diffuser entrance:** The diffuser entrance is shown in Fig. A.4. The CAD of the piece is represented with letter (a) while the mesh with (b). This domain is divided in six, as the other channels are the same. So, a cyclic boundary condition was adopted in order to reduce computational efforts.

- **Impeller:** For this region, there are two options of coordinate system: the frozen rotor technique and the transient rotor-stator. The first is a model where the reference coordinate system rotates while the mesh is kept stationary. This method needs appropriate transformations to apply in the governing equations and the computational efforts are lower than the second method. However, this technique does not consider interactions between the impeller blade and diffuser vane leading to no pressure fluctuations.

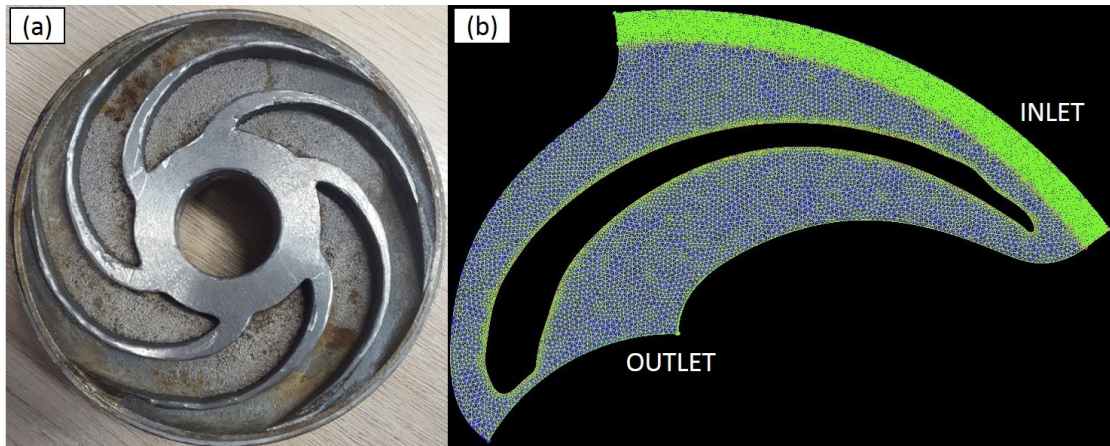


Figure A.4: Diffuser: (a) Diffuser entrance; (b) Diffuser entrance mesh.

This condition was used as an initial condition for the transient simulations.

The transient rotor-stator considers all the interactions between the stationary and rotational domains. The impeller mesh is rotated and the relative movement between the regions needs an important connection between the interfaces, as they do not match. This was performed through the *General Grid Interface (GGI)* connection algorithm (ANSYS, 2017). Consequently, modeling the interaction between rotor-stator demands higher computational efforts although this approach is closest to the real situation. The impeller has seven channels, so as already done for the diffuser entrance, just a part of the domain was simulated.

- **Diffuser exit:** The rotor-stator transient condition is set at the entrance of this region, which is an interface with the impeller. The diffuser has eight vanes, so just one channel was simulated. The passages between diffuser entrance to impeller and impeller to diffuser exit have a change in their area. It means that without an appropriate algorithm the area changes could not be modeled. The turbo-machine reduced model is accomplished with the use of pitch-change methods, such as Profile Transformation, Time Transformation or Fourier Transformation. For the present study, the pitch ratio is 1.16 and 1.14, respectively for the diffuser entrance to impeller and impeller to diffuser exit, both of which are considered small. The model errors grow proportionally with the increase of the pitch ratio value between components. The maximum value recommended of pitch ratio is 1.30 (ANSYS, 2017).

A.2.4 Boundary Conditions

The inlet of the tube entrance domain has a boundary specified as the "opening" which means that flow may enter or leave the boundary. A constant total pressure in the stationary frame and direction are imposed at the inlet. At the outlet, in the diffuser exit domain, the mass flow rate is specified. Cyclic boundary conditions are specified in all domains, obtaining a periodic flow passage. This kind of boundary condition reduces the time of simulation. So, the domains were divided radially and proportionally in 1/6, 1/7 and 1/8 to reduce computational efforts. The interface of these parts should be connected by the GGI algorithm which works with parts that had been overlapped by other interfaces. Interfaces can connect static or rotational meshes, such as the impeller and diffuser. Every surface of the domain related to wall was characterized with no-slip condition and smooth walls were assumed.

The treatment of the interface fluxes is fully implicit and fully conservative in mass, momentum, energy, scalars, and so on. The simulation used water and its properties are density of $\rho = 998 \text{ kg/m}^3$ and dynamic viscosity of $\mu = 1.003 \cdot 10^{-3} \text{ Pa}\cdot\text{s}$ at 20° C .

A.3 Single-phase Water Flow CFD Simulation

This section presents the governing equations, turbulent model, mesh sensitivity test, timestep study and the simulation results for single-phase water flow compared with the experimental data of Monte Verde (2016).

A.3.1 Governing Equations

The governing equations for single-phase flows in ESPs are shown in this section. This work uses unsteady Reynolds Averaged Navier-Stokes (U-RANS). In the U-RANS approach, the fluctuations of the velocity are decomposed into resolved and unresolved parts. In the experiments both fluctuations were considered, so for comparison, the numerical simulation should be transient.

Transient simulations are closest to real cases, but they are computational costly. In order to reduce this, it is common to work with sections of the model. The meshes

were separated through determined planes and new boundary conditions were added, like symmetry. In this study, the model had three sections divided to make the simulations more efficient, which are 1/8, 1/7 and 1/6 as described in the former section. The equations solved by CFD are in their conservative form:

Conservation of mass

$$\frac{\partial \rho}{\partial t} + \nabla \cdot (\rho \vec{v}) = 0 \quad (\text{A.1})$$

where \vec{v} is the velocity vector and ρ is the density.

Conservation of momentum

$$\frac{\partial \rho \vec{v}}{\partial t} + \nabla \cdot (\rho \vec{v} \otimes \vec{v}) = -\nabla P + \nabla \cdot \tau + S_M \quad (\text{A.2})$$

where the stress tensor, τ , is related to the strain rate by:

$$\tau = \mu \left(\nabla \vec{v} + (\nabla \vec{v})^T - \frac{2}{3} \nabla \cdot \vec{v} \right) \quad (\text{A.3})$$

where μ is the viscosity and superscript T stands for the transpose and S_M corresponds to source terms.

Source terms

The source terms corresponds to terms added for flows in a rotating frame of reference with constant angular velocity ω . The pseudo forces are Coriolis force S_{Cor} and the centrifugal force $S_{c.f.g}$, represented in Eq. A.4.

$$S_{M,rot} = S_{Cor} + S_{c.f.g} = -2\rho \vec{\omega} \times \vec{v} - \rho \vec{\omega} \times (\vec{\omega} \times \vec{r}) \quad (\text{A.4})$$

where \vec{v} is the relative frame velocity and \vec{r} is the position vector.

A.3.2 Turbulence Model

Concerning turbulence in single-phase flows, a two equation SST-model (MENTER, 1994) was adopted, since it combines advantages of the $k-\omega$ model near the walls and the $k-\epsilon$ model in the bulk of the flow. The SST model requires near-wall refined treatment to assure the correct use of $k-\omega$ model, which suggests that $y^+(1)$ should be near 1 if the user does not want to use wall functions. Where $y^+(1)$ is the distance of the first off-wall node in viscous length-scales.

Mathematical and experimental analysis has shown that the near-wall region can be subdivided into two layers. In the innermost layer, the so-called viscous sublayer, the flow is almost laminar, and the (molecular) viscosity plays a dominant role in momentum and heat transfer. Further away from the wall, in the logarithmic layer, turbulence dominates the mixing process. Finally, there is a region between the viscous sublayer and the logarithmic layer called the buffer layer, where the effects of molecular viscosity and turbulence are of equal importance. Fig A.5 below illustrates these subdivisions of the near-wall region (ANSYS, 2017).

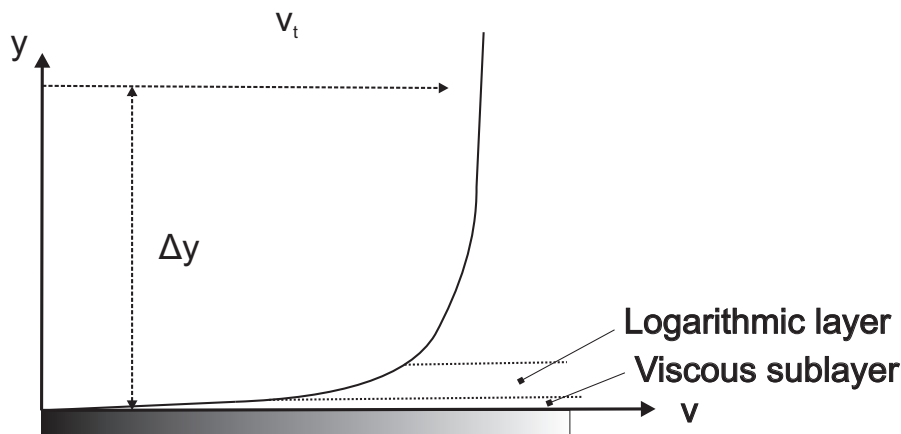


Figure A.5: Subdivisions of the near-wall region (ANSYS, 2017).

Assuming that the logarithmic profile reasonably approximates the velocity distribution near the wall, it provides a means to numerically compute the fluid shear stress as a function of the velocity at a given distance from the wall. This is known as a "wall function" and the logarithmic nature gives rise to the well known "log law of the wall" (WHITE, 2003).

The Low-Reynolds-Number method resolves the details of the boundary layer

profile by using very small mesh length scales in the direction normal to the wall (very thin inflation layers). Turbulence models based on the ω -equation, such as the SST or SMC- ω models, are suitable for a low-Re method. Note that the low-Re method does not refer to the device Reynolds number, but to the turbulent Reynolds number, which is low in the viscous sublayer. This method can therefore be used even in simulations with very high device Reynolds numbers, as long as the viscous sublayer has been resolved.

The low-Re approach requires a very thin mesh in the near-wall zone and correspondingly large number of nodes. Computer-storage and run-time requirements are higher than those of the wall-function approach and care must be taken to ensure good numerical resolution in the near-wall region to capture the rapid variation in variables. To reduce the resolution requirements, CFX uses wall functions. In order to guarantee their functionality, which enables flow solutions independent of the location of the first grid node above the wall, at least ten nodes should be present until outer layer (GROTHJANS AND MENTER, 1998 and ANSYS, 2017).

CFX develops an automatic wall treatment in order to reduce the resolution requirements. This allows a gradual switch between wall functions and low-Reynolds number grids, without a loss in accuracy. For $k - \omega$ based models (including the SST model) this method is applied.

A.3.3 Mesh Sensitivity Test

A mesh sensitivity test was performed considering five levels of mesh refinement, which are presented in Table A.4. The table indicates the pressure increment considering all components, which is indicated by the column "ESP". Impeller nodes and exit diffuser were indicated in the two other columns. The mesh chosen is number three, as it has 1.2% of deviation with experimental data and has one million fewer cells than mesh number two. So approximately three million cells were simulated in the entire pump.

The study of the mesh size was also done for the entrance tube and the diffuser entrance. The pressure increment in both dominions was numerically measured and compared with the reference mesh, presented in the first line of Table A.5.

Considering the data showed in Table A.5, the mesh numbers 3 and 4 for the entrance tube have the same size, it is intentionally tested in order to know how much is the influence of the diffuser entrance mesh. This equipment has helical channels,

Table A.4: Mesh, Number of elements ($Q_{BEP} = 3.2112 m^3/h$)

Mesh	Impeller		Exit Diffuser		ESP	ΔP [Pa]	Deviation [%]
	nodes	y^+	nodes	y^+	nodes		
1	1.190.861	9.1	3.164.352	5.3	6.662.277	7979	[-]
2	788.852	15.5	1.999.387	7.0	4.017.140	8064	1.0
3	788.852	15.5	864.024	10.1	2.970.212	8078	1.2
4	340.865	15.8	864.024	10.5	1.980.816	8220	3.0
5	225.654	19.8	632.606	12.2	1.309.905	8304	4.1

which adds more difficulty in the mesh building. So, more elements are presented in the DE. The difference in % is a little higher because the pressure difference in Pascal is minimal.

Therefore, the mesh of the entrance tube chosen has $\sim 300,000$ elements having a difference of ~ 15 Pa. The diffuser's mesh has $\sim 550,000$ elements having a difference of 110 Pascal. The computational cost to decrease those differences may increase $\sim 650,000$ elements in simulation, if mesh number 2 is chosen. This increase in mesh size was not considered to be reliable in simulations, so mesh number 4 is chosen.

Table A.5: Mesh sensitivity for ET and DE.

Mesh	Entrance tube (ET)			Diffuser entrance (DE)		
	nodes	ΔP [Pa]	Dev. [%]	nodes	ΔP [Pa]	Dev. [%]
1	696.542	-213	[-]	1.610.822	-4363	[-]
2	461.595	-220	3.29	998.317	-4365	0.05
3	326.023	-225	5.63	767.306	-4251	2.56
4	326.023	-229	7.51	555.232	-4223	3.20
5	195.684	-296	38.97	255.961	-4179	4.22

A.3.4 Time step study

Tests setting steps per blade passage were conducted in order to capture the influence in performance pump values. Table A.6 shows the tests from 15 timesteps per blade until 3 timesteps. The average values from static pressure were compared with the solution for the most refined test, which was three degrees per timestep.

Table A.6: Timestep per blade passage

Timestep per blade passage	Degrees per timestep [°]	ΔP [Pa]	Deviation [%]
3	15	9803	4.33
6	7.5	10084	1.59
9	5	10166	0.79
12	3.75	10207	0.39
15	3	10247	[-]

The deviation of 1.59% was considered acceptable for the purposes of this work and it was considered for all cases. So 6 timesteps per blade passage were selected, as it is acceptable and without high computational costly.

A.3.5 Simulation Results for Single-Phase Flow

Figure A.6 shows the curves related to pump performance. It indicates the pressure increment ΔP of 600 rpm, 900 rpm, 1200 rpm and 1500 rpm, where the circles and Xs correspond to experimental and numerical values, respectively. The data of the chart is on Tables A.8 to A.11 showed in the section A.3.6. The difference between the experimental and numerical results correspond to 4%. As the rotation speed increases the difference also increases. The best efficiency points of the rotations are represented with a black dashed line.

The pump head is defined by $H = \Delta P / \rho_l g$, where g is the gravitational acceleration and ρ_l is the density of water. The increment pressure ΔP is measured at the same place as the experiments. Stepanoff (1957) described some of the most common dimensionless numbers, such as specific head, $H^* = gH / \omega^2 d_{pump}^2$, and specific capacity, $Q^* = q / \omega d_{pump}^3$. Figure A.7 shows the dimensionless variable Head H^* versus flow

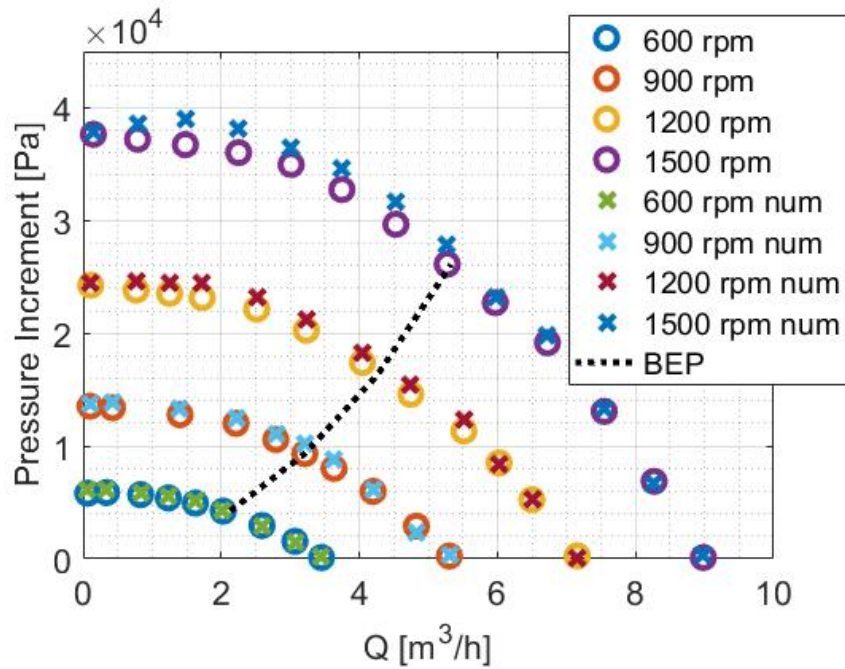


Figure A.6: Comparison between numerical and experimental (MONTE VERDE, 2016) using 600 to 1500 rpm - Pressure increment.

rate Q^* .

Table A.7: Numerical Simulation Results for Single-Phase Water Flow.

Rotation [rpm]	Q_1/Q_{BEP}	Q_1 [m ³ /h]	Mean velocity [m/s]	Reference
600	0.16	0.339	0.680	Fig. A.8(a)
	1.62	3.452	1.545	Fig. A.8(b)
900	0.13	0.424	1.120	Fig. A.8(c)
	1.66	5.303	2.377	Fig. A.8(d)
1200	0.18	0.767	1.439	Fig. A.8(e)
	1.68	7.155	3.207	Fig. A.8(f)
1500	0.70	3.747	2.453	Fig. A.8(g)
	1.26	6.724	3.960	Fig. A.8(h)

The velocity vector for the single-phase flow at 600 to 1500 rpm are shown in Fig. A.8. Table A.7 indicates the liquid flow rate and their respective references in the column "Reference". Besides this, the same table shows the mean velocity of the water

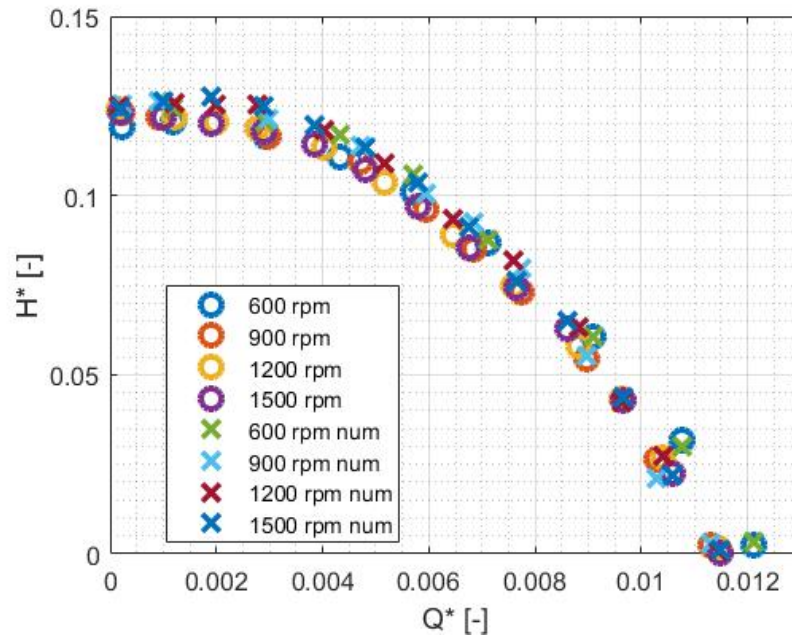


Figure A.7: Comparison between numerical and experimental (MONTE VERDE, 2016) using 600 to 1500 rpm - Head H^* versus flow rate Q^* .

flow in the impeller channels.

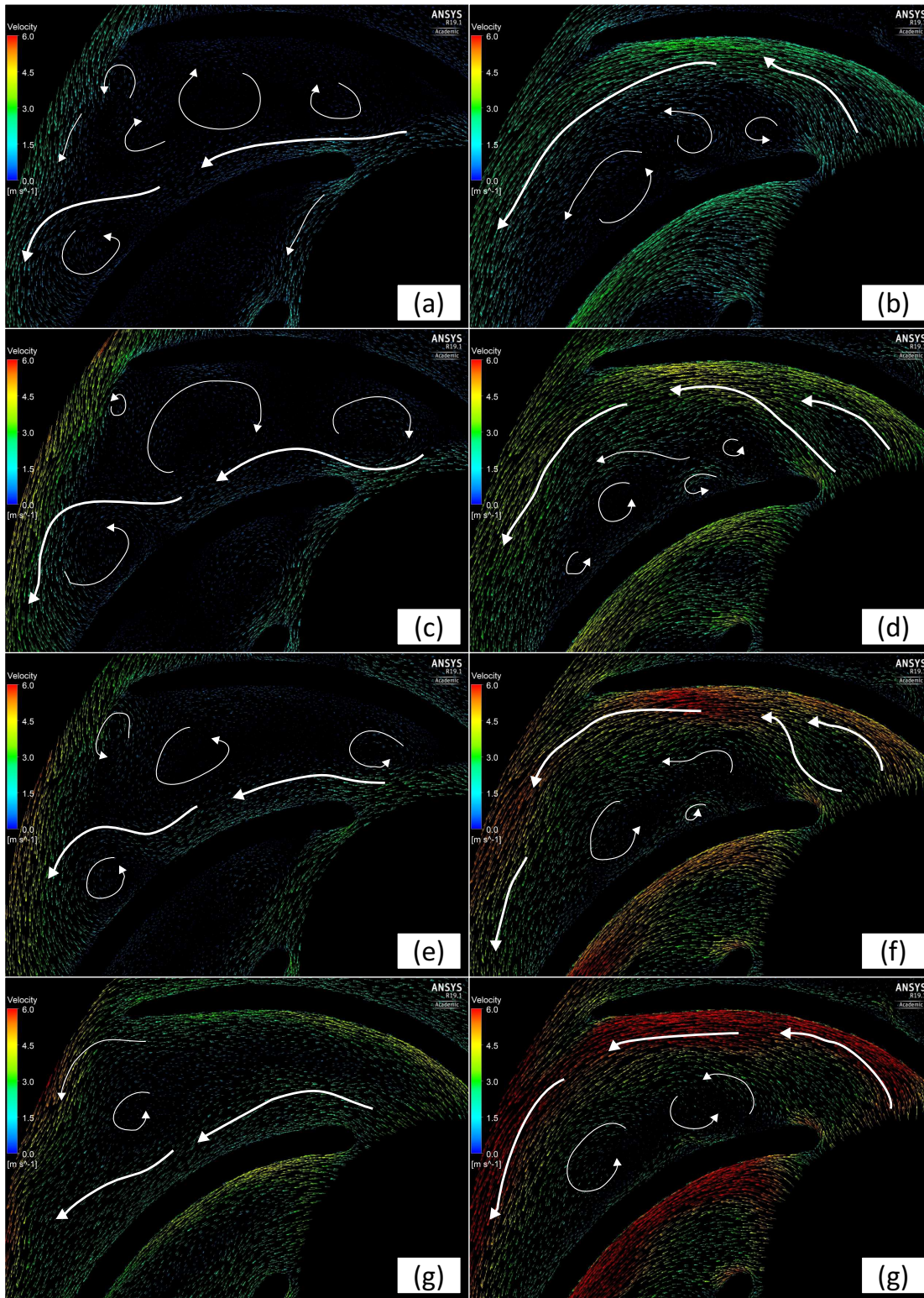


Figure A.8: Part-load condition single-phase simulations: velocity vector

The mean velocity increases with rotational speed, as expected. When the ratio Q_1/Q_{BEP} is higher than one, the flow direction tends to shock with the suction blade side, as presented in the Fig. A.8 on the right. On the other hand, in the left, when the ratio Q_1/Q_{BEP} is lower than one, the flow direction tends to shock with the pressure blade side.

In addition to the shock losses, recirculation losses were observed. For $Q_1/Q_{BEP} > 1$, vortices are present in the pressure blade side, in the counter-clockwise direction. The flow separation starts right on the leading edge, due to the positive incidence angle, hardly influenced by the entrance condition. The opposite occurs for $Q_1/Q_{BEP} < 1$, on the left side of Fig. A.8. The vortices are present on the suction blade side and are much bigger and rotating in a clockwise direction. In this case, the flow separation occurs after the middle of the blade. These observations are in agreement with the ones of Feng *et al.* (2009b).

The next section presents tables of the single-phase numerical simulations data compared with the experimental ones. The data compared is the pressure increment.

A.3.6 Mean results for single-phase flow

This section shows the results of the single-phase water flow simulations. Table A.8, A.9, A.10 and A.11 are related to the single-phase simulations for 600, 900, 1200 and 1500 *rpm*, respectively. The highest value of Q/Q_{BEP} corresponds to simulations in the open-flow condition. The simulations were compared with the experimental data of Monte Verde (2016). The difference between the experimental data and the simulations are high in the first columns of Q/Q_{BEP} due to the low pressure increment. So, for example, as indicated in Table A.8 the difference of 40 Pa is enough to provide a difference of 34.2 %. Considering only the other cases the difference is about 5% in average, considered low for the cases analyzed.

A.4 Two-Phase Flow CFD Simulation

The simulation here used the Euler-Euler method (or two-fluid method). In this approach, both phases are present at the same time and the same place. A key-quantitative

Table A.8: Pressure increment for single phase flow - 600 rpm.

Q/Q_{BEP}	ΔP Exp.[Pa]	ΔP Num.[Pa]	Difference [Pa]	Difference [%]
1.62	118	158	40	34.2
1.44	1553	1467	86	5.5
1.22	2952	2950	2	0.1
0.95	4235	4278	43	1.0
0.76	4946	5172	226	4.6
0.58	5402	5608	206	3.8
0.39	5694	5899	205	3.6
0.16	5882	6093	211	3.6
0.03	58817	6127	310	5.3

Table A.9: Pressure increment for single phase flow - 900 rpm.

Q/Q_{BEP}	ΔP Exp.[Pa]	ΔP Num.[Pa]	Difference [Pa]	Difference [%]
1.66	250	439	189	75.8
1.52	2894	2191	703	24.3
1.31	5976	5592	384	6.4
1.14	8017	8478	461	5.7
1.00	9330	9741	411	4.4
0.87	10585	10998	413	3.9
0.69	12021	12354	333	2.8
0.44	12787	13086	299	2.3
0.13	13403	13819	416	3.1
0.03	13540	14366	826	6.1

is the volume fraction (or void fraction), which determines what the relative amount of a phase is at a given place at a given time. By their very nature, Euler-Euler models provide an averaged description of the multiphase system. An advantage of the formulation is that the interfacial forces are inherently present in the modeling. Besides, the model results in a double set of conservation equations: one set for each phase.

The disadvantage of the two-fluid model is loss of details due to averaging. This

Table A.10: Pressure increment for single phase flow - 1200 rpm.

Q/Q_{BEP}	ΔP Exp.[Pa]	ΔP Num.[Pa]	Difference [Pa]	Difference [%]
1.66	262	94	168	64.2
1.53	5246	5302	56	1.1
1.41	8498	8329	169	2.0
1.29	11341	12324	983	8.7
1.11	14591	15397	806	5.5
0.95	17413	18225	812	4.7
0.76	20280	21261	981	4.8
0.59	22144	23143	998	4.5
0.40	23172	24544	1372	5.9
0.29	23547	24528	981	4.2
0.18	23837	24565	727	3.1
0.03	24264	24423	159	0.7

creates closure problems, similar to those in single phase RANS modeling. For the two-fluid model, not only the turbulence needs to be modelled, but also the averaged form of all types of interactions. Because of the averaging procedure required to derive the two-fluid equations, a DNS (Direct Numerical Simulation) of a laminar flow is not possible. The small-scale fluctuations attached to the velocity difference between the two phases are modeled in an averaged sense: they cannot be resolved, no matter how fine the grid is made.

The two fluid equations, for a system without chemical reactions and phase changes, read in its general form are presented below.

A.4.1 Governing equations - Two-phase air-water flow

The equations presented in this section are similar to the ones showed for single phase flow, except for the interfacial forces between two-phases and the volume fraction α .

Table A.11: Pressure increment for single phase flow - 1500 rpm.

Q/Q_{BEP}	ΔP Exp.[Pa]	ΔP Num.[Pa]	Difference [Pa]	Difference [%]
1.69	114	346	232	203.5
1.55	6873	6742	131	1.9
1.42	13079	13322	243	1.9
1.26	19168	19881	713	3.7
1.12	22725	23255	530	2.3
0.99	26140	27840	1700	6.5
0.85	29675	31621	1946	6.6
0.70	32755	34616	1861	5.7
0.57	34976	36483	1507	4.3
0.42	36030	38121	2091	5.8
0.28	36730	38999	2269	6.2
0.15	37219	38548	1329	3.6
0.03	37649	37920	271	0.7

Conservation of mass

$$\frac{\partial}{\partial t} \alpha_k \rho_k + \nabla \alpha_k \rho_k \vec{v}_k = 0 \quad (\text{A.5})$$

where k represents the phase.

Conservation of momentum

$$\frac{\partial}{\partial t} \alpha_k \rho_k v_k + \nabla \alpha_k \rho_k v_k v_k = -\alpha_k \nabla P - \nabla \alpha_k \tau_k + S_M + M_k + \alpha_k \rho_k g \quad (\text{A.6})$$

where the Interphase momentum transfer is represented by M , and τ_k indicates the stress tensor. The source terms S_M are the same presented in the section for single-phase flow.

Interphase momentum terms

Interphase momentum transfer, M_{21} , occurs due to interfacial forces acting on phase 2, due to interaction with another phase 1, and vice-versa. The total force on phase 2 due to interaction with other phases is denoted by M_2 . The interfacial surface forces present on bubbles can be modeled formulating a linear combination of various known interfacial forces (ISHII AND HIBIKI, 2010):

$$M_2 = \frac{\alpha}{B_p} (F_2^D + F_2^V + F_2^L + F_2^W + F_2^T) \quad (\text{A.7})$$

where B_p , F^D , F^V , F^L , F^W and F^T are: the volume of an example of particle, the standard drag force, the virtual mass force, the lift force, the wall lubrication force and turbulent dispersion force for a single particle, respectively. Note that interfacial forces between two phases are equal and opposite, so the net interfacial forces sum is zero: $M_2 = -M_1$. The bubble volume is $B_p = \pi d_p^3/6$. The interfacial forces explanation is given next.

The significance of the various terms in Eq. A.7 follows. The first term in the right-hand side is the drag force. The second term, virtual mass, is the force required to accelerate the mass surrounding phase when relative velocity changes. The third term is the lift force normal to the velocity distribution change around particles near the wall. The fourth term is the wall lubrication force due to the velocity distribution change around particles near the wall. The fifth term is the turbulent dispersion force due to the concentration gradient. Those forces were modeled using correlations present in Table A.12.

Table A.12: Summary of bubble force correlations

Force	Reference
Interphase Drag	Clift <i>et al.</i> (2005)
Virtual mass	Constant coefficient $C_V = 1/2$
Lift	Tomiyama (1998)
Wall lubrication	Antal <i>et al.</i> (1991)
Interphase turbulent dispersion	Burns <i>et al.</i> (2004)

More details of the forces and the correlations are presented in the Appendix B.

Boundary conditions

The boundary conditions were almost the same as those used for single-phase flow, the exception is that air was specified and bubble diameters needed to have a range of probability, i.e., groups of bubbles diameters were made in order to predict their diameters. The numerical simulations made in ANSYS CFX requires the creation of a group with possible bubble diameters. The bubbles change their size along the impeller channel because they are under coalescence and breakup effects. Thus, adopting a constant diameter in the model can be compromised the results significantly.

These groups of bubbles are modeled by Multiple Size Group (MUSIG), which was developed to handle polydispersed multiphase flows. The dispersed phase has a large variation in size, so polydispersed. The attributes of this method consist of the interaction of different sizes of dispersed phases interacting with each other through the mechanisms of breakup and coalescence. Population balance is a well-established method for calculating the size distribution of a polydispersed phase, including breakup and coalescence effects. MUSIG provides a framework in which the population balance method can be incorporated into three-dimensional CFD calculations. Table A.13 shows the groups of diameters used for simulations.(ANSYS, 2017).

Table A.13: Groups of Diameters used in MUSIG.

Group	1	2	3	4	5	6	7	8	9
Bubble diameter [mm]	0.2	0.5	1.0	1.5	2.0	2.5	3.0	3.5	4.0

The properties of water remained the same of those used in single phase-flow. The properties of air are density of $\rho = 1.2047 \text{ kg}/\text{m}^3$ and dynamic viscosity of $\mu = 1.8205 \cdot 10^{-5} \text{ Pa}\cdot\text{s}$ at 20° C . The boundary conditions and interface assumed to link the rotor and stator domains are described below:

Entrance tube: The pressure is specified to 0 Pa at the inlet of the pipe (gauge). The outlet of the pipe is an interface region with another domain. The rotor is a rotative domain so an interface is used in order to exchange fluxes information which must consider the relative movement. The same interface conditions of Frozen Rotor or Transient

Rotor-Stator, described at single-phase flow section, can be used here.

The Transient Rotor-Stator interface conditions were used to generate the two-phase flow results. Also, the same turbulence models used for single-phase flow were used for both phases in the two-phase flow simulations.

A.4.2 Time step study

Two-phase flow conditions required the time step test per blade passage. The same criterion adopted for single-phase flow is adopted here. Table A.6 shows the tests from 15 timesteps per blade until three timesteps. The average values from static pressure were compared with the experimental data. The point tested is $m_2 = 3.088 \text{ m}^3/h$, which is defined as IM7. It has experimentally $\Delta P = 9318 \text{ Pa}$.

Table A.14: Timestep per blade passage: part-load condition, IM7 - $m_2 = 3.088 \text{ m}^3/h$.

Timestep per blade passage	Degrees per timestep [°]	ΔP [Pa]	Deviation [%]
3	15	11075	18.8
6	7.5	10770	15.5
9	5	10259	10.1
15	3	9676	3.8
45	1	9492	1.8

The deviation is measured in relation to the experimental data, which has $\Delta P = 9318 \text{ Pa}$. The deviation of 3.8% was considered acceptable for the purposes of this work, and it was considered for all cases of two-phase flow. If the option chosen is the deviation of 1.8% , which corresponds to one degree of the impeller rotation, the simulation time will increase at least three times more. So 3 timesteps per blade passage were selected.

A.4.3 Simulation Results for Two-Phase Flow

The simulations results are presented in general comparison with experimental data, then details of velocity and pressure field given by the simulations are presented

and finally a comparison of bubbles displacement and velocity is presented. Figure A.9 shows the curves related to experimental and simulated pump performance. The blue triangles corresponds to water single-phase experimental data. The red Xs and yellow circles are, respectively, the experimental and numerical two-phase flow pump performance. The numerical results for two-phase point in the extreme left in the chart did not converge, so it was not shown in the figure.

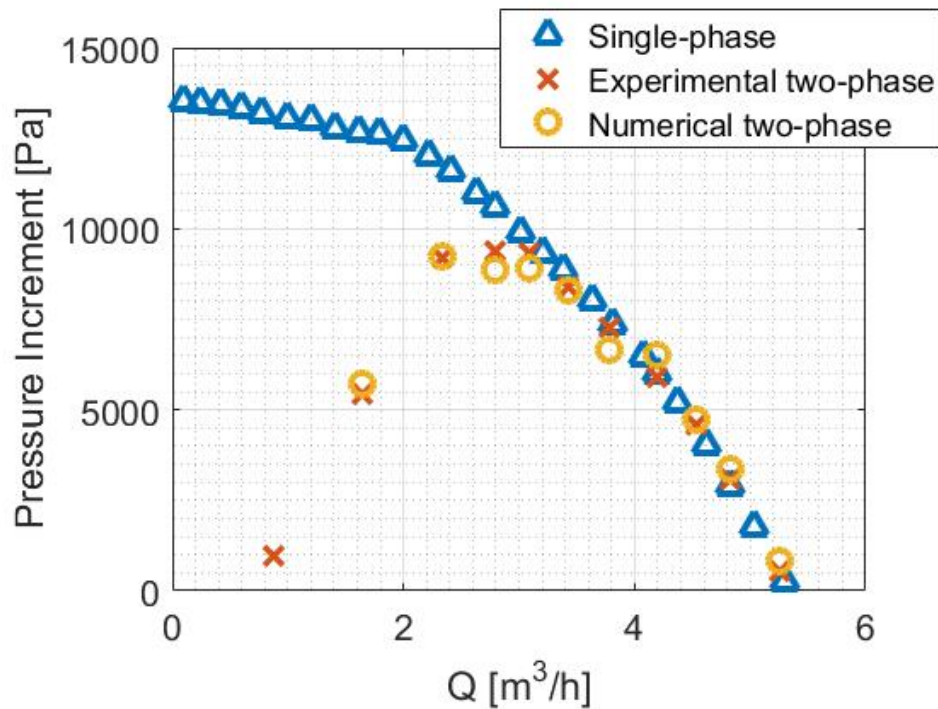


Figure A.9: Comparison of Experimental and simulated Pressure increment for two-phase air-water flow (900 rpm and $m_G = 0.012 \text{ kg/h}$).

Table A.15 shows the numerical results from the two-phase flow simulations. The first column indicates only the number of the test. The second column indicates the mass gas flow rate in kg/h . The third and fourth columns present the experimental and numerical pressure increment, respectively. The fifth column is the pressure difference relative error, which is: $|\Delta P_{exp} - \Delta P_{num}| / \Delta P_{exp}$. The next two columns correspond to circumferential and radial velocities, respectively. Finally, the last column is the ratio between the flow rate and the flow rate at the best efficiency point (BEP).

Figure A.10 shows the pressure and the velocity numerically calculated. The pres-

Table A.15: mass gas flow rate \dot{m} , experimental pressure increment ΔP_{exp} , numerical pressure increment ΔP_{num} , Difference between pressure increment, radial velocity v_r , circumferential velocity v_θ , flow rate ratio Q/Q_{BEP}

	\dot{m} [kg/h]	ΔP_{exp} [Pa]	ΔP_{num} [Pa]	Difference [-]	v_r [mm/s]	v_θ [mm/s]	Q/Q_{BEP} [-]
1	0.025	541	651	20.3%	943	1739	1.65
2	0.025	3073	3351	9.0%	812	1600	1.51
3	0.025	4579	4802	4.9%	729	1483	1.41
4	0.025	5908	6827	15.6%	665	1396	1.31
5	0.025	7260	6562	9.6%	388	1113	1.18
6	0.025	8394	7141	14.9%	344	1101	1.07
7	0.025	9318	9306	0.1%	260	1064	0.96
8	0.025	9403	8743	7.0%	267	1030	0.87
9	0.025	9196	8955	2.6%	90	943	0.71
10	0.025	5425	5639	3.9%	110	762	0.51
11	0.012	419	641	53.0%	957	1746	1.64
12	0.012	2768	3167	14.4%	807	1589	1.53
13	0.012	4168	4589	10.1%	766	1514	1.42
14	0.012	5804	6318	8.9%	659	1369	1.30
15	0.012	8078	8854	9.6%	572	1265	1.15
16	0.012	8110	7962	1.8%	320	1117	1.06
17	0.012	9025	9091	0.7%	311	1108	0.97
18	0.012	8348	7992	4.3%	277	1040	0.85
19	0.012	7284	7415	1.8%	188	1026	0.74
20	0.012	4481	5298	18.2%	54	813	0.60

sure is shown on the left side of the figure. It can be observed in the impeller's inlet that pressure is approximately $-6500 Pa$ (relative pressure), and at the outlet, it is near $3000 Pa$. The difference of $9500 Pa$ between inlet and outlet corresponds to the pressure increment of the impeller. The image on the right side corresponds to the velocity of the water flow. Note that the flow direction tends to be orientated to the middle of the channel, which is without pre-rotation (BIAZUSSI, 2014). Pumps are designed to achieve a no pre-rotation condition close to the best efficiency point since this condition minimizes shock-losses.

The absolute velocity indicated in Fig. A.10 on the right side corresponds to data number six on Table A.15. The column indicated by Q/Q_{BEP} indicated the tendency of the velocity vector. If this number is greater than 1, the flow direction points to the

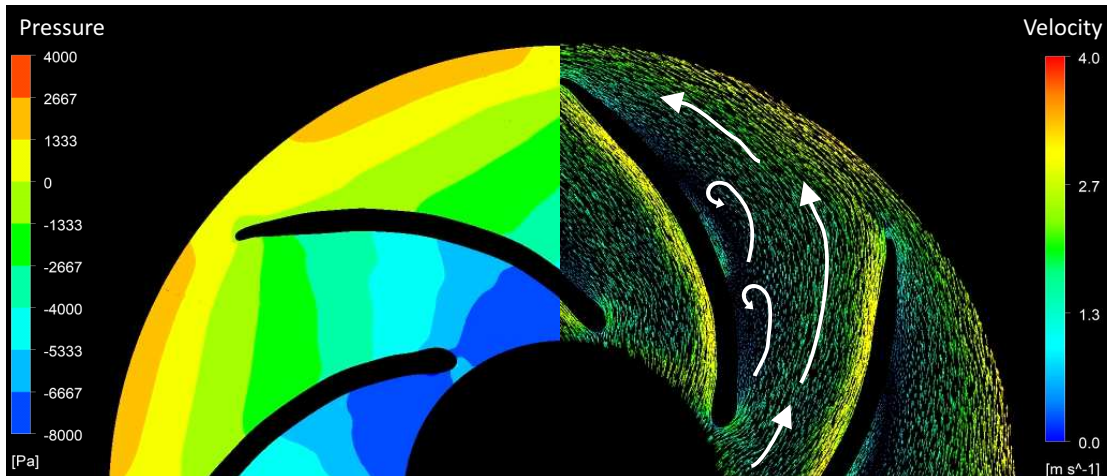


Figure A.10: Pressure and water velocity fields (900 rpm, IM6, $m_L = 3.428 \text{ m}^3/h$ e $m_G = 0.025 \text{ kg/h}$).

pressure side, while reducing this number to less than 1, i.e., the water flow increases, and the flow direction tends to point to the suction side. These configurations are positive and negative pre-rotation, respectively. The flow orientation causes recirculation in the channels, which is characterized as losses.

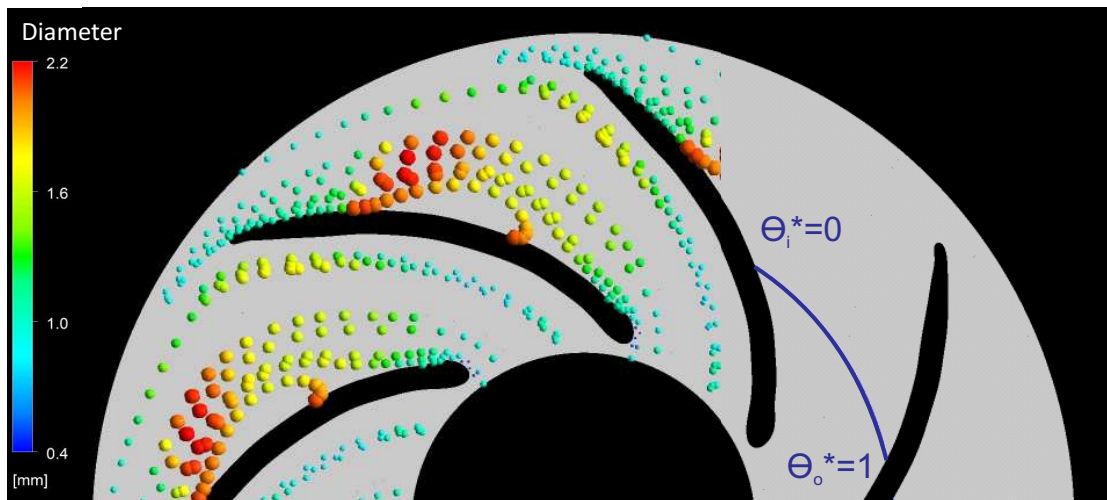


Figure A.11: Bubble size and profile velocity (900 rpm, IM6, $m_L = 3.428 \text{ m}^3/h$ e $m_G = 0.025 \text{ kg/h}$).

The simulation shows gas accumulation in certain regions of the impeller. It can be seen from Figure A.11 that the gas is concentrated in the middle of the pressure

side, which is in agreement with the results of Caridad and Kenyery (2004). The largest bubble's diameters are concentrated in the same place, as reported in Fig. A.11 on the right. The velocity profiles in the azimuth direction are shown in Fig. 4.12. The velocity profiles going from the pressure side are represented by θ_i^* to θ_o^* on the suction side. The values of θ where dimensionless in order to represent one at the suction side and zero at the pressure side. The velocity profile is shown in the middle of the impeller, considering the radius.

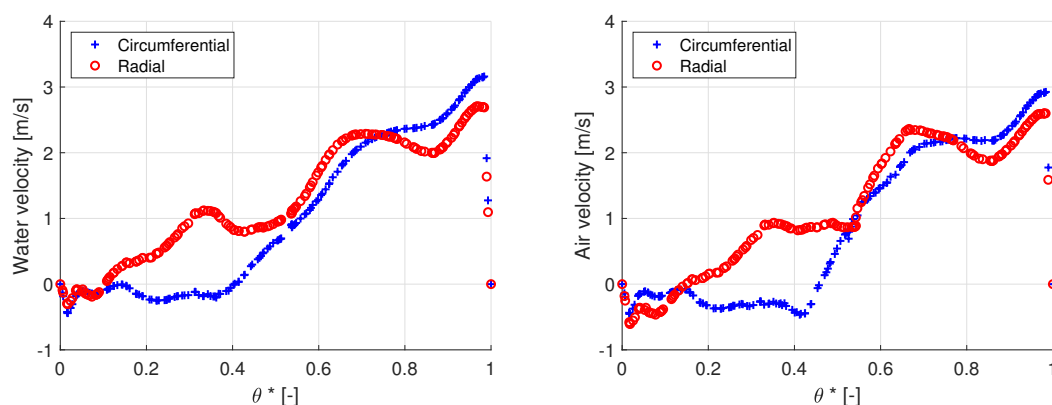


Figure A.12: Numerically data of 900 rpm, indicating circumferential and radial velocity from: (a) Water (b) Air(900 rpm, IM6, $m_L = 3.428 \text{ m}^3/h$ e $m_G = 0.025 \text{ kg/h}$).

The velocities appear contrary to the main flow direction in this region, indicating recirculation, as represented in the chart of Fig. A.12. The profile shown in red is the circumferential velocity, and in blue is the radial velocity. Besides, the rapid increase in velocities near the wall indicates the turbulent flow.

The next section presents tables of the two-phase numerical simulations data compared with the experimental ones.

A.4.4 Mean results for two-phase gas-liquid flow

Table A.16 and A.17 are related to the results of numerical simulations using water and gas with 900 rpm. They shown the values of $m_g = 0.025 \text{ kg/h}$ and $m_g = 0.012 \text{ kg/h}$, respectively. The numerical data is compared with the experimental data acquired by Monte Verde (2016). The highest differences in the results were observed for the lowest pressure increments, as can be observed in $Q/Q_{BEP} = 1.62$, which is

34.2%, representing 40 Pascal. For the other data, the difference is of 6% on average, again considered low for the numerical analysis performed.

Table A.16: Pressure increment for two phase flow - $m_g = 0.025 \text{ kg/h}$.

Q/Q_{BEP}	$\Delta P \text{ Exp. [Pa]}$	$\Delta P \text{ Num. [Pa]}$	Difference [Pa]	Difference [%]
1.65	541	651	110	20.3
1.51	3073	3351	278	9.0
1.41	4579	4802	223	4.9
1.31	5908	6427	519	8.8
1.18	7260	6562	698	9.6
1.07	8394	7841	553	6.6
0.97	9318	9306	12	0.1
0.87	9403	8743	660	7.0
0.73	9196	8955	241	2.6
0.51	5425	5639	214	3.9
0.27	977	-	-	-

Table A.17: Pressure increment for two phase flow - $m_g = 0.0125 \text{ kg/h}$.

Q/Q_{BEP}	$\Delta P \text{ Exp. [Pa]}$	$\Delta P \text{ Num. [Pa]}$	Difference [Pa]	Difference [%]
1.64	419	641	222	53.0
1.53	2768	3067	299	10.8
1.42	4168	4589	145	3.2
1.30	5804	6318	421	10.1
1.15	8078	8854	776	9.6
1.06	8110	7962	148	1.8
0.97	9025	9091	66	0.7
0.85	8348	7992	356	4.3
0.74	7284	7415	131	1.8
0.60	4481	5298	817	18.2
0.38	949	-	-	-

A.4.5 Gas void fraction results

The results of the gas void fraction measured numerically α_{num} are shown in Table A.18. Each phase is assumed to be present in each control volume, and assigned a volume fraction equal to the fraction of the control volume occupied by that phase. So, the gas void fraction is the sum of all these control volumes. The variable α is the gas void fraction measured using the model and it is: $\alpha = \lambda \overline{j_{ms}} / \overline{v_{2,s}}$. This is presented in Chapter 4.

The point IM1 has a higher value of water flow rate, and it decreases until almost zero at point IM11. Considering the values of α_{num} , the point IM11 has the greatest value of the gas void fraction. The α_{num} does not have a linear progression, which it is expected to have. The first numerical data, IM1 to IM3, has small void fractions. However, at point IM4 it abruptly decreases to 0.1%, and rapidly increases to 12.8% in IM5. This does not correspond to what happens in a real situation and should be matter for further studies.

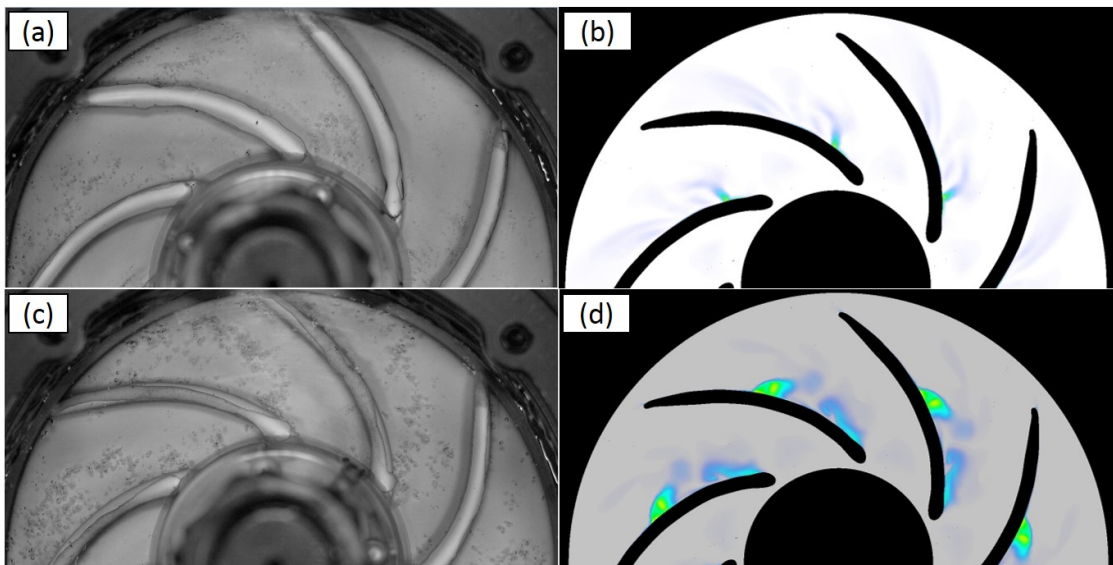


Figure A.13: Experimental and numerical data for IM1 in (a) and (b), and for IM3 in (c) and (d).

The values are compared with the real images in Fig. A.13 and A.14. The real images are shown in the left side, while the numerical images are shown in the right side. Figures A.13(a) and (b) show the data of the point IM1, and Figs. A.13(c) and (d)

Table A.18: Gas void fraction.

IM	Q/Q_{BEP}	Q_t [m^3/h]	Q_g . 10^{-6} [m^3/h]	α_{num} . 10^{-2}	α . 10^{-2}
-	-				
1	1.65	5.2843	6.94	0.2	0.32
2	1.51	4.8284	6.94	0.9	0.33
3	1.41	4.5118	6.94	1.7	0.34
4	1.31	4.2010	6.94	0.1	0.35
5	1.18	3.7812	6.94	12.8	0.36
6	1.07	3.4285	6.94	18.2	0.37
7	0.96	3.0814	6.94	11.7	0.39
8	0.87	2.7865	6.94	18.4	-
9	0.71	2.2787	6.94	27.9	-
10	0.51	1.6378	6.94	39.2	-
11	0.26	0.8354	6.94	-	-
1	1.64	5.2514	3.47	1.6	0.16
2	1.53	4.8920	3.47	0.9	0.16
3	1.42	4.5536	3.47	3.2	0.16
4	1.30	4.1702	3.47	1.0	0.17
5	1.15	3.6947	3.47	0.1	0.18
6	1.06	3.3855	3.47	14.6	0.19
7	0.97	3.1029	3.47	13.3	0.20
8	0.85	2.7304	3.47	25.0	-
9	0.74	2.3723	3.47	29.7	-
10	0.64	1.9244	3.47	47.0	-
11	0.38	1.2036	3.47	-	-

show the data of the point IM3.

Figure A.14(a) and (b) show the data of the point IM5, and Fig. A.14(c) and (d) show the data of the point IM7. If the real figure is compared to the numerical, the results of the void fraction do not match, although the results of pressure increment are almost the same. So, further work on the analysis of void fraction in ESP impellers is

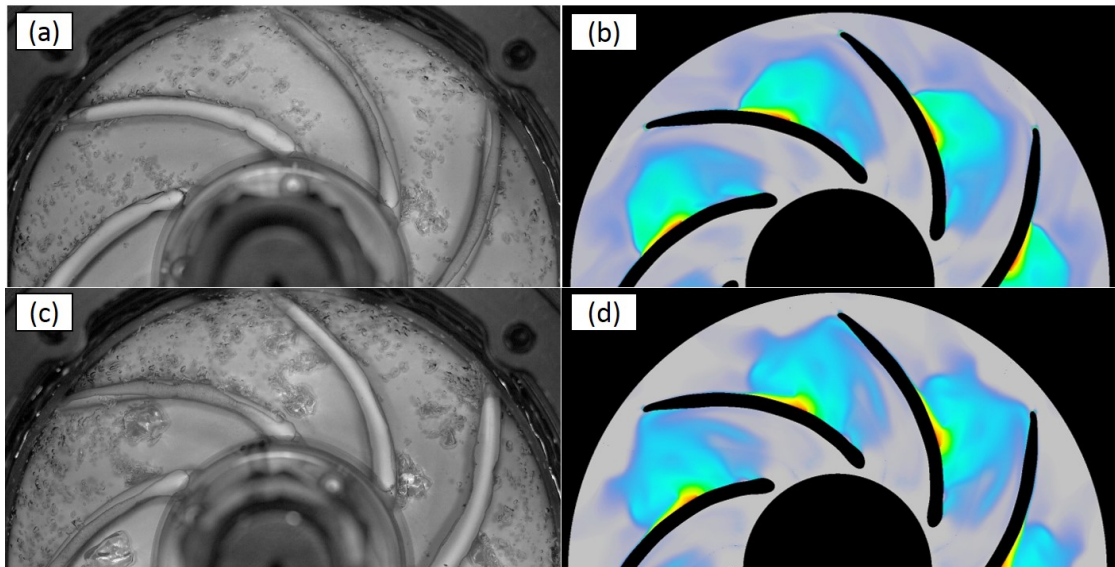


Figure A.14: Experimental and numerical data for IM5 in (a) and (b), and for IM7 in (c) and (d).

needed and will be left as a suggestion for future work.

The experimental and numerical velocities are shown in Table A.19. The average value of Δv_r and Δv_θ are equal to 34.7% and 12.4%, respectively. Consider the experimental standard deviation the values are closer. These values are near for the experimental measurements using the post-processing of images, which may infer that the velocity presented in Fig. A.8 are correct. If so, it is possible to identify the regions where the flow are faster than others, such as in the suction blade side. However, it is necessary further investigations as the gas void fractions did not match with experimental data.

The radial and circumferential velocities are plotted in Fig. A.15. The velocity, and its standard deviation are plotted in blue circle and line. The numerical velocity is plotted with red triangles. The two first points calculated numerically of the radial velocity does not match with experimental data. However, the other numerical points are all inside the standard deviation of velocity calculated by the post-processing of images.

The comparison of the diameter measured experimentally and numerically are shown in Table A.20. The average deviation, which is calculated in the column "*Difference*" and "*Difference in %*" is equal to 0.17 mm and 25.9%, respectively. The value of 0.17 mm are very small considering the size of the impeller channel.

Table A.19: mass gas flow rate \dot{m} , experimental radial velocity $v_{r,exp}$, experimental circumferential velocity $v_{\theta,exp}$, standard deviation of radial velocity δv_r , standard deviation of δv_{θ} , numerical radial velocity $v_{r,num}$, numerical circumferential velocity $v_{\theta,num}$ Deviation v_r , Deviation Δv_{θ}

	\dot{m} [kg/h]	$v_{r,exp}$ [mm/s]	$v_{\theta,exp}$ [mm/s]	δv_r [mm/s]	δv_{θ} [mm/s]	$v_{r,num}$ [mm/s]	$v_{\theta,num}$ [mm/s]	Δv_r [%]	Δv_{θ} [%]	Q/Q_{BEP} [-]
IM1	0.025	1021	1425	245	298	943	1739	7.6	22.0	1.65
IM3	0.025	969	1346	257	276	729	1483	24.8	10.2	1.41
IM5	0.025	868	1283	303	324	388	1113	55.3	13.3	1.18
IM7	0.025	825	1172	332	350	260	1064	68.5	9.2	0.96
IM1	0.012	980	1447	292	336	957	1746	2.3	20.7	1.64
IM3	0.012	1028	1342	286	301	766	1514	25.5	12.8	1.42
IM5	0.012	862	1296	312	388	572	1265	33.6	2.4	1.15
IM7	0.012	769	1211	271	315	311	1108	59.6	8.5	0.97

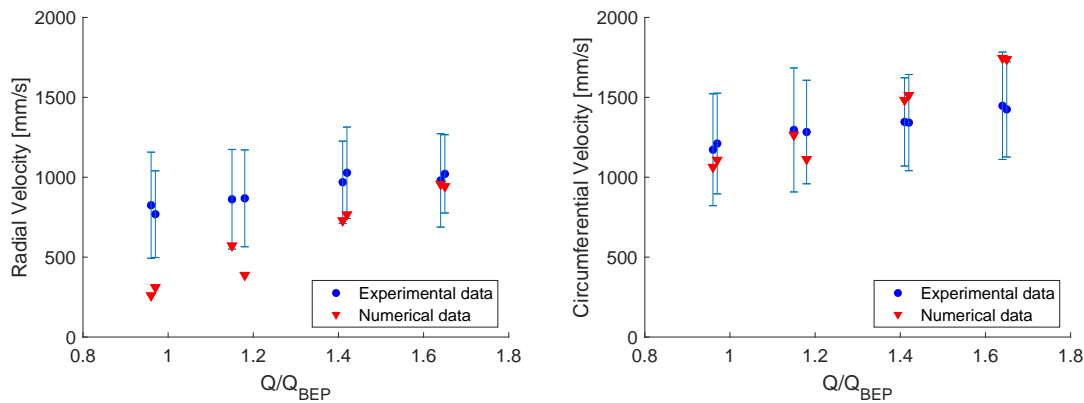


Figure A.15: Numerical x Experimental velocity - (a) Radial (b) Circumferential

Table A.20: Impeller rotation ω , mass gas flow rate \dot{m} , experimental diameter d_{exp} , numerical diameter d_{num} , experimental and numerical difference in value and in %, flow rate ratio Q/Q_{BEP}

	ω [rpm]	\dot{m} [kg/h]	d_{exp} [mm]	d_{num} [mm]	Difference [mm]	Difference in % [%]	Q/Q_{BEP} [-]
IM1	900	0.025	0.6	0.45	0.15	25.0	1.65
IM3	900	0.025	0.6	0.59	0.01	1.7	1.41
IM5	900	0.025	0.7	1.08	0.38	54.3	1.18
IM7	900	0.025	0.8	1.25	0.45	56.3	0.96
IM1	900	0.012	0.6	0.39	0.21	35.0	1.64
IM3	900	0.012	0.6	0.51	0.09	15.0	1.42
IM5	900	0.012	0.7	0.83	0.13	18.6	1.15
IM7	900	0.012	0.9	0.89	0.01	1.1	0.97

APPENDIX B – Bubble force correlations

B.1 Interphase Drag

The total drag force is conveniently expressed in terms of the drag coefficient, which is given by (ANSYS (2017)):

$$C_D = \frac{1}{2} \frac{F_D}{\rho_1 (v_1 - v_2)^2 A} \quad (\text{B.1})$$

where ρ_1 is the water specific mass, F_D is the magnitude of the drag force, $v_1 - v_2$ is the relative speed and A is the projected area of the body in the flow direction.

The area of a single particle projected can be approach by an area of a circle, which is: $A = \pi d_p^2/4$. The bubble mean diameter is represented by d_p . The volume of a single particle is $V_p = \pi d_p^3/6$. The number of particles per unit volume, n_p is given by:

$$n_p = \frac{r_b}{V_p} = \frac{6 r_b}{\pi d_p^3} \quad (\text{B.2})$$

The total drag exerted per unit volume on the continuous phase is:

$$F_D = n_p \frac{1}{2} C_D \rho_1 A_p |v_2 - v_1| (v_2 - v_1) \quad (\text{B.3})$$

The correlation adopted is related to Grace drag model (ANSYS (2017)), formulated for a single bubble. In the distorted particle regime it is given by:

$$C_D(\text{ellipse}) = \frac{4 g d}{3 v_T^2} \frac{\Delta \rho}{\rho_1} \quad (\text{B.4})$$

where v_T is the terminal velocity and is given by:

$$v_T = \frac{\mu_1}{\rho_1 d_p} M^{-0.149} (J - 0.857) \quad (\text{B.5})$$

where M is the Morton number given by:

$$M = \frac{\mu_1^4 g \Delta \rho}{\rho^2 \tau^3} \quad (\text{B.6})$$

where μ_1 is the viscosity of the continuous phase, which is water in the present case, and:

$$J = \begin{cases} 0.94H^{0.757} & 2 < H \leq 59.3 \\ 3.42H^{0.441} & H > 59.3 \end{cases} \quad (\text{B.7})$$

$$H = \frac{4}{3} Eo M^{-0.149} \left(\frac{\mu_1}{\mu_{ref}} \right)^{-0.14} \quad (\text{B.8})$$

where Eo is the Eotvos number. $\mu_{1ref} = 0.0009 \text{ kg m}^{-1} \text{ s}^{-1}$ is the molecular viscosity of water at 25°C and 1 bar. CFX automatically takes into account the spherical particle and spherical cap limits by setting:

$$\begin{aligned} C_D(dist) &= \min(C_D(ellipse), C_D(cap)) \\ C_D &= \max(C_D(sphere), C_D(dist)) \end{aligned} \quad (\text{B.9})$$

B.2 Virtual Mass Force

The virtual mass force is proportional to relative phasic accelerations as follows:

$$F_1^V = F_2^V = r_2 \rho_1 C_V \left(\frac{D_2 v_2}{Dt} - \frac{D_1 v_1}{Dt} \right) \quad (\text{B.10})$$

where the subscript 1 corresponds to the continuous phase and the subscript 2 for the dispersed phase. In a rotating frame of reference with rotation vector Ω , the virtual mass force in terms of v^* is modified by Coriolis theorem, and is given by:

$$F_1^V = -F_2^V = r_2 \rho_1 C_V \left(\frac{D_2 v_2^*}{Dt} - \frac{D_1 v_1^*}{Dt} + 2\Omega \times (v_2^* - v_1^*) \right) \quad (\text{B.11})$$

The non-dimensional virtual mass coefficient $C_V = 0.5$ for inviscid flow around an isolated sphere. In general, $C_V = 0.5$ depends on shape and particle concentration and a constant value of 0.5 was adopted here.

B.3 Lift Force

The non-dimensional lift coefficient C_L can be set as a constant, or an expression. It should be set to 0.5 for inviscid flow around a sphere. For viscous flow, the coefficient varies from 0.01 to 0.5 in a way that is only partially understood. The lift force acts perpendicular to the direction of relative motion of the two phases.

The Tomiyama model used at the simulations is applicable to the lift force on larger-scale deformable bubbles in the ellipsoidal and spherical cap regimes. It depends on Eotvos number, in the same way of Grace model for drag force. Hence, it requires specification of the surface tension between the dispersed and continuous phases. Its main important feature is prediction of the cross-over point in bubble size at which particle distortion causes a reversal of the sign of the lift force to take place. The lift coefficient is given by (TOMIYAMA, 1998):

$$C_L = \begin{cases} \min \left[0.288 \tanh(0.121 Re_p, f(Eo')) \right] & Eo' \leq 4 \\ f(Eo') & 4 < Eo' \leq 10 \\ -0.27 & 10 > Eo' \end{cases} \quad (\text{B.12})$$

where $f(Eo') = 0.00105Eo'^3 - 0.0159Eo'^2 - 0.0204Eo' + 0.474$. Eo' is a modified Eotvos number, based on the long axis d_H , of deformable bubble:

$$\begin{aligned} Eo' &= \frac{g(\rho_1 - \rho_2)d_H^2}{\sigma} & (\text{B.13}) \\ d_H &= d_p(1 + 0.163 Eo^{0.757})^{1/3} \\ Eo &= \frac{g(\rho_1 - \rho_2)d_p^2}{\sigma} \end{aligned}$$

The correlation has been slightly modified from Tomiyama's original form, following Wellek *et al.* (1966), whereby the value of C_L for $Eo' > 10$ has been changed to -0.27 to ensure a continuous dependence on modified Eotvos number.

B.4 Wall Lubrication Force

The dispersed phase (bubbles) in upflow considering a vertical pipe tends to concentrate in a region close to the wall, but not immediately adjacent to the wall. This effect may be modeled by the wall lubrication force, which tends to push the dispersed phase away from the wall. The model adopted was proposed by Antal *et al.* (1991) which computes the wall lubrication force as:

$$F_W = -C_W \alpha_2 \rho_1 |v_1 - v_2|^2 n_W \quad (\text{B.14})$$

where $C_W = \max\{0, C_{W1}/d_b, C_{W2}/y_W\}$. The non-dimensional coefficients $C_{W1} = -0.01$ and $C_{W2} = 0.05$ can be changed. α_2 is the gas volume fraction. ρ_1 is the liquid density. n_W is the unit normal pointing away from the wall. $v_1 - v_2$ is the relative velocity between phases, orthogonal to n_W . d_b is the bubble mean diameter. y_W is the distance to the nearest wall.

This force is only active in a thin layer adjacent to the wall, i.e. only active up to a cut-off distance of:

$$y_W \leq -(C_{W2}/C_{W1})d_b \quad (\text{B.15})$$

where $y_W = 5d_b$ considering the values presented for C_{W1} and C_{W2} .

B.5 Turbulent Dispersion Force

CFX implements a model for turbulent dispersion force, based on the Favre average of the interphase drag force (BURNS *et al.*, 2004):

$$F_1^T = -F_2^T = C_T C_D \frac{\nu_{tc}}{\tau_{tc}} \left(\frac{\nabla r_2}{r_2} - \frac{\nabla r_1}{r_1} \right) \quad (\text{B.16})$$

Here, C_D is the momentum transfer coefficient for the interphase drag force. Hence, the model clearly depends on the details of the drag correlation used τ_{tc} is the turbulent Schmidt number for continuous phase volume fraction, currently taken to be 0.9.

C_T is a value given by the user, by default it is equal to unity. This value is quite good because the simulations were dealing with air bubbles, which specific mass is

much less than the continuous phase (ANSYS, 2017).

APPENDIX C – Math extension

This Appendix presents the extension of math showed in chapter 4.

C.1 Radial Pressure Gradient

In this section the development of radial pressure gradient is shown here:

$$\alpha_1 \rho_1 \left(v_{1r} \frac{\partial}{\partial r} v_{1r} - \frac{v_{1\theta}^2}{r} \right) + \alpha_2 \rho_2 \left(v_{2r} \frac{\partial}{\partial r} v_{2r} - \frac{v_{2\theta}^2}{r} \right) = -(\alpha_1 + \alpha_2) \frac{\partial p}{\partial r} - (\alpha_1 \rho_1 + \alpha_2 \rho_2) A_{kfr} + \nabla \cdot \vec{\tau} \quad (\text{C.1})$$

where $\alpha_1 + \alpha_2 = 1$ and the mixture density ρ_m is equal to $\alpha_1 \rho_1 + \alpha_2 \rho_2$. So Eq. C.1 becomes:

$$\alpha_1 \rho_1 \left(\frac{\partial v_{1r}^2/2}{\partial r} - \frac{v_{1\theta}^2}{r} \right) + \alpha_2 \rho_2 \left(\frac{\partial v_{2r}^2/2}{\partial r} - \frac{v_{2\theta}^2}{r} \right) = -\frac{\partial p}{\partial r} - \rho_m A_{kfr} + \nabla \cdot \vec{\tau}$$

$$\boxed{-\frac{\partial p}{\partial r} = \alpha_1 \rho_1 \left(\frac{\partial v_{1r}^2/2}{\partial r} - \frac{v_{1\theta}^2}{r} \right) + \alpha_2 \rho_2 \left(\frac{\partial v_{2r}^2/2}{\partial r} - \frac{v_{2\theta}^2}{r} \right) + \rho_m A_{kfr} - \nabla \cdot \vec{\tau}} \quad (\text{C.2})$$

The pressure increment ΔP and the pump head H are:

$$\boxed{-\Delta P = \int_{r_i}^{r_o} -\frac{\partial p}{\partial r} dr} \quad \boxed{H = \frac{\Delta P}{\rho_m g}} \quad (\text{C.3})$$

Two dimensionless numbers are shown here, the dimensionless flow rate C_Q and the dimensionless Head C_H (PATERNOST, 2013, BIAZUSSI, 2014, MONTE VERDE, 2016). More details are presented in Appendix D.

$$\boxed{C_Q = \frac{Q_m}{\omega r^3}} \quad \boxed{C_H = \frac{\Delta P}{\rho_m \omega^2 r^2}} \quad (\text{C.4})$$

The velocities in Eq. C.2 can be substituted. For simplicity, $\alpha(r)$ is considered as $\bar{\alpha}$.

$$v_{kr}(r) = \frac{j_{kr}(r)}{\alpha_k} \quad \text{where} \quad j_{kr}(r) = \lambda_k \left[\left(\frac{Q_m}{2\pi h} \right) \frac{1}{r} \right] = \lambda_k j_m(r)$$

$$\boxed{v_{kr}(r) = \left(\frac{\lambda_k}{\alpha_k}\right) j_m(r)} \quad (\text{C.5})$$

$$v_{k\theta}(r) = \frac{j_{k\theta}(r)}{\alpha_k} \quad \text{where} \quad j_{k\theta}(r) = -j_{kr} \cot \beta = -\lambda_k j_m(r) \cot \beta$$

$$\boxed{v_{k\theta}(r) = -\left(\frac{\lambda_k}{\alpha_k}\right) j_m(r) \cot \beta} \quad (\text{C.6})$$

The volumetric flux in r is:

$$\frac{\partial j_m}{\partial r} = \frac{\partial}{\partial r} \left[\left(\frac{Q_m}{2\pi h} \right) \frac{1}{r} \right] = \left(\frac{Q_m}{2\pi h} \right) \left(\frac{-1}{r^2} \right) = -\frac{j_m(r)}{r} \quad (\text{C.7})$$

Substituting the velocities in Eq. C.2:

$$\begin{aligned} & -\frac{\partial p}{\partial r} = \alpha_1 \rho_1 \left[\left(\frac{\lambda_1}{\alpha_1} \right)^2 \frac{\partial}{\partial r} \frac{j_m^2(r)}{2} - \left(\frac{\lambda_1}{\alpha_1} \right)^2 \cot^2 \beta \frac{j_m^2(r)}{r} \right] \\ & + \alpha_2 \rho_2 \left[\left(\frac{\lambda_2}{\alpha_2} \right)^2 \frac{\partial}{\partial r} \frac{j_m^2(r)}{2} - \left(\frac{\lambda_2}{\alpha_2} \right)^2 \cot^2 \beta \frac{j_m^2(r)}{r} \right] + \rho_m A_{kfr} - h_{fr} \\ -\frac{\partial p}{\partial r} & = \left[\alpha_1 \rho_1 \left(\frac{\lambda_1}{\alpha_1} \right)^2 + \alpha_2 \rho_2 \left(\frac{\lambda_2}{\alpha_2} \right)^2 \right] \left(\frac{\partial}{\partial r} \frac{j_m^2(r)}{2} - \cot^2 \beta \frac{j_m^2(r)}{r} \right) + \rho_m A_{kfr} - h_{fr} \\ -\frac{\partial p}{\partial r} & = \left[\rho_1 \lambda_1 \frac{\lambda_1}{\alpha_1} + \rho_2 \lambda_2 \frac{\lambda_2}{\alpha_2} \right] \left(\frac{\partial}{\partial r} \frac{j_m^2(r)}{2} - \cot^2 \beta \frac{j_m^2(r)}{r} \right) + \rho_m A_{kfr} - h_{fr} \\ -\frac{\partial p}{\partial r} & = \left[\rho_1 \lambda_1 \frac{\lambda_1}{\alpha_1} + \rho_2 \lambda_2 \frac{\lambda_2}{\alpha_2} \right] \left[j_m(r) \left(-\frac{j_m(r)}{r} \right) - \cot^2 \beta \frac{j_m^2(r)}{r} \right] + \rho_m A_{kfr} - h_{fr} \\ -\frac{\partial p}{\partial r} & = \left[\rho_1 \lambda_1 \frac{\lambda_1}{\alpha_1} + \rho_2 \lambda_2 \frac{\lambda_2}{\alpha_2} \right] \left[(1 + \cot^2 \beta) \left(-\frac{j_m^2(r)}{r} \right) \right] + \rho_m A_{kfr} - h_{fr} \quad (\text{C.8}) \end{aligned}$$

Substituting $j_m(r)$, showed in Eq. 4.58, in Eq. C.8 it becomes:

$$-\frac{\partial p}{\partial r} = \left[\rho_1 \lambda_1 \frac{\lambda_1}{\alpha_1} + \rho_2 \lambda_2 \frac{\lambda_2}{\alpha_2} \right] \left[(1 + \cot^2 \beta) \left(\frac{Q_m}{2\pi h} \right)^2 \left(\frac{-1}{r^3} \right) \right] + \rho_m A_{kfr} - \nabla \cdot \vec{\tau} \quad (\text{C.9})$$

Using Eqs. 4.24 and 4.26 in order to get the term $\rho_m A_{kfr}$ on the right hand side:

$$\begin{aligned}
\rho_m A_{kfr} &= \alpha_1 \rho_1 A_{1fr} + \alpha_2 \rho_2 A_{2fr} = S_{1r} + S_{2r} \\
&= \alpha_1 \rho_1 \left[- (2 \omega v_{1\theta} + \omega^2 r) \right] + \alpha_2 \rho_2 \left[- (2 \omega v_{2\theta} + \omega^2 r) \right] \\
&= -\alpha_1 \rho_1 \left[2\omega \left(- \left(\frac{\lambda_1}{\alpha_1} \right) j_m(r) \cot \beta \right) + \omega^2 r \right] \\
&\quad - \alpha_2 \rho_2 \left[2\omega \left(- \left(\frac{\lambda_2}{\alpha_2} \right) j_m(r) \cot \beta \right) + \omega^2 r \right] \\
&= -\rho_m \omega^2 r + (\rho_1 \lambda_1 + \rho_2 \lambda_2) \cot \beta 2\omega j_m(r)
\end{aligned}$$

$$\boxed{\rho_m A_{kfr} = -\rho_m \omega^2 r + \overline{\rho_m} \cot \beta 2\omega j_m(r)} \quad (\text{C.10})$$

where $\overline{\rho_m}$ is the mixture density proposed by Dukler *et al.* (1964). Substituting Eq. C.10 in the pressure gradient and summarizing:

$$-\frac{\partial p}{\partial r} = \tilde{\rho}_m (1 + \cot^2 \beta) \left(\frac{-j_m^2(r)}{r} \right) + \overline{\rho_m} \cot \beta 2\omega j_m(r) - \rho_m \omega^2 r - \nabla \cdot \vec{\tau} \quad (\text{C.11})$$

where:

$$\begin{aligned}
\circ \tilde{\rho}_m &= \rho_1 \lambda_1 \left(\frac{\lambda_1}{\alpha_1} \right) + \rho_2 \lambda_2 \left(\frac{\lambda_2}{\alpha_2} \right) \\
\circ \rho_m &= \rho_1 \alpha_1 + \rho_2 \alpha_2 \\
\circ \overline{\rho_m} &= \rho_1 \lambda_1 + \rho_2 \lambda_2
\end{aligned} \quad (\text{C.12})$$

Substituting the volumetric flux of mixture (Eq. 4.58) in Eq. C.11:

$$-\frac{\partial p}{\partial r} = \tilde{\rho}_m (1 + \cot^2 \beta) \left[- \left(\frac{Q_m}{2\pi h} \frac{1}{r} \right)^2 \frac{1}{r} \right] + \overline{\rho_m} \cot \beta 2\omega \left(\frac{Q_m}{2\pi h} \frac{1}{r} \right) - \rho_m \omega^2 r - \nabla \cdot \vec{\tau}$$

$$\boxed{-\frac{\partial p}{\partial r} = \tilde{\rho}_m \left[\frac{(1 + \cot^2 \beta)}{4\pi^2 h^2} \right] Q_m^2 \left(\frac{-1}{r^3} \right) + \overline{\rho_m} \left(\frac{\cot \beta}{\pi h} \right) \omega Q_m \left(\frac{1}{r} \right) - \rho_m \omega^2 r - \nabla \cdot \vec{\tau}} \quad (\text{C.13})$$

C.2 Viscous Stress Tensor Modeling

The term $\nabla \cdot \vec{\tau}$ is related to surface forces due to the stresses on the sides of the control surface. In polar coordinates considering radial and azimuthal direction, the stress tensor is:

$$\left(\frac{d\mathbf{F}}{dV} \right)_{viscous} = \nabla \cdot \vec{\tau}$$

Applying the Gauss theorem in limited form:

$$\int_{A_k(z,t)} \nabla \cdot \vec{\tau} dA = \frac{\partial}{\partial r} \int_{A_k(r,t)} \vec{\tau} \cdot \vec{n}_r dA + \oint_{\xi(r,t)+\xi_k(r,t)} \vec{n}_k \cdot \vec{\tau} \frac{d\xi}{\vec{n}_k \cdot \vec{n}_{k\xi}} \quad (\text{C.14})$$

where vector \vec{n}_k is normal to interface pointed outside of face k . Unitary vector $\vec{n}_{k\xi}$ is normal to ξ in the plane A_k . The term ξ_k is the contact of the interface to the wall. ξ is the interface of the fluids.

The first term on the right hand side in Eq. C.14 is:

$$\frac{\partial}{\partial r} \int_{A_k(r,t)} \vec{\tau} \cdot \vec{n}_r dA = \int_{A_k(r,t)} \frac{\partial}{\partial r} \left(\vec{\tau} \cdot \vec{n}_r \right) dA \quad (\text{C.15})$$

The area is not constant along n_r . The term inside the integration is:

$$\vec{\tau} \cdot \vec{n}_r = \begin{bmatrix} \tau_{rr} & \tau_{r\theta} \\ \tau_{\theta r} & \tau_{\theta\theta} \end{bmatrix} \cdot \begin{bmatrix} 1 \\ 0 \end{bmatrix} = \begin{bmatrix} \tau_{rr} \\ \tau_{\theta r} \end{bmatrix} \quad (\text{C.16})$$

The stress components are (WHITE, 2003):

$$\begin{aligned} \circ \tau_{rr} &= 2\mu \frac{\partial v_{kr}}{\partial r} = 2\mu \frac{\lambda_k}{\alpha_k} \frac{\partial}{\partial r} j_m(r) = -2\mu \frac{\lambda_k}{\alpha_k} \frac{j_m(r)}{r} \\ \circ \tau_{\theta\theta} &= 2\mu \frac{v_{kr}}{r} = 2\mu \frac{\lambda_k}{\alpha_k} \frac{j_m(r)}{r} = -\tau_{rr} \\ \circ \tau_{r\theta} &= \tau_{\theta r} = \mu r \frac{\partial v_{k\theta}}{\partial r} = \mu r \frac{\partial}{\partial r} \left(\frac{1}{r} \right) v_{k\theta} + \mu \frac{r}{r} \frac{\partial v_{k\theta}}{\partial r} = \mu r \left(\frac{-1}{r^2} \right) v_{k\theta} + \mu \frac{\partial v_{k\theta}}{\partial r} \\ &= -\frac{\mu}{r} v_{k\theta} + \mu \frac{\partial v_{k\theta}}{\partial r} = \frac{-\mu}{r} \left(-\frac{\lambda_k}{\alpha_k} \cot \beta j_m(r) \right) + \mu \left(-\frac{\lambda_k}{\alpha_k} \cot \beta \right) \frac{\partial j_m(r)}{\partial r} \\ &= \mu \frac{\lambda_k}{\alpha_k} \cot \beta \frac{j_m(r)}{r} - \mu \frac{\lambda_k}{\alpha_k} \cot \beta \left(-\frac{j_m(r)}{r} \right) = 2\mu \frac{\lambda_k}{\alpha_k} \cot \beta \frac{j_m(r)}{r} \end{aligned}$$

Substituting the stress components in Eq. C.16:

$$\vec{\tau} \cdot \vec{n}_r = \begin{bmatrix} -2\mu \frac{\lambda_k}{\alpha_k} \frac{j_m(r)}{r} \\ 2\mu \frac{\lambda_k}{\alpha_k} \cot \beta \frac{j_m(r)}{r} \end{bmatrix} = 2\mu \frac{\lambda_k}{\alpha_k} \frac{j_m(r)}{r} \begin{bmatrix} -1 \\ \cot \beta \end{bmatrix} \quad (\text{C.17})$$

The derivative of the terms τ_{rr} and $\tau_{r\theta}$ are:

$$\begin{aligned} \frac{\partial}{\partial r} \tau_{rr} &= \frac{\partial}{\partial r} \left(-2\mu \frac{\lambda_k}{\alpha_k} \frac{j_m(r)}{r} \right) = -2\mu \frac{\lambda_k}{\alpha_k} \left[\frac{1}{r} \frac{\partial j_m(r)}{\partial r} + j_m(r) \frac{\partial(1/r)}{\partial r} \right] \\ &= -2\mu \frac{\lambda_k}{\alpha_k} \left[\frac{1}{r} \frac{(-j_m(r))}{r} + j_m(r) \frac{-1}{r^2} \right] = 4\mu \frac{\lambda_k}{\alpha_k} \frac{j_m(r)}{r^2} \end{aligned} \quad (\text{C.18})$$

$$\frac{\partial}{\partial r} \tau_{r\theta} = \frac{\partial}{\partial r} \left(-2\mu \frac{\lambda_k}{\alpha_k} \cot \beta \frac{j_m(r)}{r} \right) = -4\mu \frac{\lambda_k}{\alpha_k} \cot \beta \frac{j_m(r)}{r^2} \quad (\text{C.19})$$

So, the derivative of $\vec{\tau} \cdot \vec{n}_r$ is:

$$\frac{\partial}{\partial r} (\vec{\tau} \cdot \vec{n}_r) = \begin{bmatrix} 4\mu \frac{\lambda_k}{\alpha_k} \frac{j_m(r)}{r^2} \\ -4\mu \frac{\lambda_k}{\alpha_k} \frac{j_m(r)}{r^2} \cot \beta \end{bmatrix} = 4\mu \frac{\lambda_k}{\alpha_k} \frac{j_m(r)}{r^2} \begin{bmatrix} 1 \\ -\cot \beta \end{bmatrix} \quad (\text{C.20})$$

Using Eq. C.20 in C.15:

$$\begin{aligned} \int_{A_k(r,t)} \frac{\partial}{\partial r} (\vec{\tau} \cdot \vec{n}_r) dA &= \int_0^h \int_{\theta_i}^{\theta_o} \frac{\partial}{\partial r} (\vec{\tau} \cdot \vec{n}_r) r dz d\theta \\ &= \frac{\partial}{\partial r} (\vec{\tau} \cdot \vec{n}_r) \frac{2\pi r}{Z_b} h \end{aligned} \quad (\text{C.21})$$

The terms θ_i and θ_o indicates the angle involving the channel and, h is its height. Substituting Eq. C.20 in C.21 and separating in radial and azimuthal direction respectively.

$$\int_{A_k(r,t)} \frac{\partial}{\partial r} (\vec{\tau} \cdot \vec{n}_r) dA \Big|_r = 4\mu \frac{\lambda_k}{\alpha_k} \frac{j_m(r)}{r^2} \frac{2\pi r}{Z_b} h = 4\mu \frac{\lambda_k}{\alpha_k} \frac{j_m(r)}{r} \frac{2\pi h}{Z_b} \quad (\text{C.22})$$

$$\int_{A_k(r,t)} \frac{\partial}{\partial r} (\vec{\tau} \cdot \vec{n}_r) dA \Big|_{\theta} = -4\mu \frac{\lambda_k}{\alpha_k} \frac{j_m(r)}{r^2} \cot \beta \left(\frac{2\pi r}{Z_b} h \right) = -4\mu \frac{\lambda_k}{\alpha_k} \frac{j_m(r)}{r} \cot \beta \frac{2\pi h}{Z_b} \quad (\text{C.23})$$

Dividing Eqs. C.22 and C.23 by the area of the channel.

$$\int_{A_k(r,t)} \frac{\partial}{\partial r} \left(\vec{\tau} \cdot \vec{n}_r \right) dA \Big|_r = 4 \mu \frac{\lambda_k j_m(r)}{\alpha_k r} \frac{2 \pi h}{Z_b} \frac{Z_b}{2 \pi r h} = 4 \mu \frac{\lambda_k j_m(r)}{\alpha_k r^2} \quad (\text{C.24})$$

$$\int_{A_k(r,t)} \frac{\partial}{\partial r} \left(\vec{\tau} \cdot \vec{n}_r \right) dA \Big|_\theta = -4 \mu \frac{\lambda_k j_m(r)}{\alpha_k r} \cot \beta \frac{2 \pi h}{Z_b} \frac{Z_b}{2 \pi r h} = -4 \mu \frac{\lambda_k j_m(r)}{\alpha_k r^2} \cot \beta \quad (\text{C.25})$$

Substituting $j_m(r)$.

$$\int_{A_k(r,t)} \frac{\partial}{\partial r} \left(\vec{\tau} \cdot \vec{n}_r \right) dA \Big|_r = 4 \mu \frac{\lambda_k Q_m}{\alpha_k 2 \pi h r^3} \quad (\text{C.26})$$

$$\int_{A_k(r,t)} \frac{\partial}{\partial r} \left(\vec{\tau} \cdot \vec{n}_r \right) dA \Big|_\theta = -4 \mu \frac{\lambda_k Q_m}{\alpha_k 2 \pi h r^3} \cot \beta \quad (\text{C.27})$$

Integrating Eq. C.26 and C.27.

$$\begin{aligned} \hat{r} &:= 4 \mu \frac{\lambda_k Q_m}{\alpha_k 2 \pi h} \int_{r_i}^{r_o} \frac{1}{r^3} dr = 4 \mu \frac{\lambda_k Q_m}{\alpha_k 2 \pi h} \left[\frac{-1}{2} \left(\frac{1}{r_o^2} - \frac{1}{r_i^2} \right) \right] \\ &= -2 \mu \frac{\lambda_k}{\alpha_k} \left(\frac{Q_m}{2 \pi h} \right) \left(\frac{r_i^2 - r_o^2}{r_i^2 r_o^2} \right) \end{aligned} \quad (\text{C.28})$$

$$\hat{\theta} := -4 \mu \frac{\lambda_k Q_m}{\alpha_k 2 \pi h} \int_{r_i}^{r_o} \frac{1}{r^3} dr = 2 \mu \frac{\lambda_k}{\alpha_k} \left(\frac{Q_m}{2 \pi h} \right) \left(\frac{r_i^2 - r_o^2}{r_i^2 r_o^2} \right) \cot \beta \quad (\text{C.29})$$

So dividing by the term $\overline{\rho_m} \omega^2 r_o^2$.

$$\begin{aligned} \hat{r} &:= -2 \mu \frac{\lambda_k}{\alpha_k} \left(\frac{Q_m}{2 \pi h} \right) \left(\frac{r_i^2 - r_o^2}{r_i^2 r_o^2} \right) \frac{1}{\overline{\rho_m} \omega^2 r_o^2} = -\frac{\mu}{\overline{\rho_m}} \frac{\lambda_k}{\alpha_k} \left(\frac{Q_m}{\omega r_o^3} \right) \frac{1}{\pi h} \frac{1}{\omega} \frac{1}{r_o} \\ &\quad \left(\frac{r_i^2 - r_o^2}{r_i^2} \right) = -\frac{\mu}{\overline{\rho_m}} \frac{\lambda_k}{\alpha_k} \frac{1}{\pi h \omega r_o} \left[1 - \left(\frac{r_o}{r_i} \right)^2 \right] C_Q \end{aligned} \quad (\text{C.30})$$

$$\hat{\theta} := 2 \mu \frac{\lambda_k}{\alpha_k} \left(\frac{Q_m}{2 \pi h} \right) \left(\frac{r_i^2 - r_o^2}{r_i^2 r_o^2} \right) \cot \beta \frac{1}{\overline{\rho_m} \omega^2 r_o^2} = \frac{\mu}{\overline{\rho_m}} \frac{\lambda_k}{\alpha_k} \frac{\cot \beta}{\pi h \omega r_o} \left[1 - \left(\frac{r_o}{r_i} \right)^2 \right] C_Q \quad (\text{C.31})$$

The second term on the right hand side in Eq. C.14 relate to term integrated in

$\xi(r,t)$ is equal to zero as it denotes the interface between fluids (Homogeneous model).

$$\oint_{\xi(r,t)} \vec{n}_k \cdot \vec{\tau} \frac{d\xi}{\vec{n}_k \cdot \vec{n}_{k\xi}} = 0$$

The third term on the right-hand side in Eq. C.14 is:

$$\oint_{\xi_k(r,t)} \vec{n}_k \cdot \vec{\tau} \frac{d\xi}{\vec{n}_k \cdot \vec{n}_{k\xi}} = -\tau_w S_D \quad (\text{C.32})$$

Separating in \hat{r} and $\hat{\theta}$ direction:

$$\begin{aligned} \hat{r} &: = \tau_{ws} \sin \beta \\ \hat{\theta} &: = -\tau_{ws} \cos \beta \end{aligned} \quad (\text{C.33})$$

where:

$$\tau_{ws} = \frac{f}{8} \rho_m j_m s^2 = \frac{f}{8} \rho_m \frac{j_m(r)^2}{\sin^2 \beta} \quad (\text{C.34})$$

wher f is the friction factor.

Using Eq. C.34 in Eq. C.33:

$$\begin{aligned} \hat{r} &: = \frac{f}{8} \rho_m \frac{j_m(r)^2}{\sin \beta} \\ \hat{\theta} &: = -\frac{f}{8} \rho_m \frac{j_m(r)^2}{\sin \beta} \cot \beta \end{aligned} \quad (\text{C.35})$$

Defining the wet perimeter as $S_D = 2(2\pi r/Z_b + h)$:

$$\begin{aligned} \hat{r} : \tau_{wr} S_D &= \frac{f}{8} \rho_m \frac{j_m(r)^2}{\sin \beta} 2 \left(\frac{2\pi r}{Z_b} + h \right) \\ \hat{\theta} : \tau_{w\theta} S_D &= -\frac{f}{8} \rho_m \frac{j_m(r)^2}{\sin \beta} \cot \beta \left[2 \left(\frac{2\pi r}{Z_b} + h \right) \right] \end{aligned} \quad (\text{C.36})$$

Dividing by the channel area Eq. C.36.

$$\begin{aligned}\hat{r} &:= \frac{f}{8} \rho_m \frac{j_m(r)^2}{\sin \beta} 2 \left(\frac{2\pi r}{Z_b} + h \right) \frac{Z_b}{2\pi r h} = \frac{f}{8} \rho_m \frac{j_m(r)^2}{\sin \beta} 2 \left(\frac{1}{h} + \frac{Z_b}{2\pi r} \right) \\ \hat{\theta} &:= -\frac{f}{8} \rho_m \frac{j_m(r)^2}{\sin \beta} \cot \beta \left[2 \left(\frac{2\pi r}{Z_b} + h \right) \right] \frac{Z_b}{2\pi r h} = -\frac{f}{4} \rho_m \frac{j_m(r)^2}{\sin \beta} \cot \beta \left(\frac{1}{h} + \frac{Z_b}{2\pi r} \right)\end{aligned}\quad (\text{C.37})$$

So:

$$\tau_w \frac{S}{A} = \begin{bmatrix} \tau_{wr} S/A \\ \tau_{w\theta} S/A \end{bmatrix} = \frac{f}{4} \rho_m \frac{j_m(r)^2}{\sin \beta} \left(\frac{1}{h} + \frac{Z_b}{2\pi r} \right) \begin{bmatrix} 1 \\ -\cot \beta \end{bmatrix} \quad (\text{C.38})$$

Substituting $j_m(r)$.

$$\tau_w \frac{S}{A} = \frac{f}{4} \rho_m \left(\frac{Q_m}{2\pi h} \right)^2 \frac{1}{\sin \beta} \left(\frac{1}{h r^2} + \frac{Z_b}{2\pi r^3} \right) \begin{bmatrix} 1 \\ -\cot \beta \end{bmatrix} \quad (\text{C.39})$$

Integrating Eq. C.39 in r.

$$\tau_w \frac{S}{A} = \frac{f}{4} \rho_m \left(\frac{Q_m}{2\pi h} \right)^2 \frac{1}{\sin \beta} \begin{bmatrix} 1 \\ -\cot \beta \end{bmatrix} \int_{r_i}^{r_o} \left(\frac{1}{h r^2} + \frac{Z_b}{2\pi r^3} \right) dr \quad (\text{C.40})$$

Solving the integration.

$$\begin{aligned}\int_{r_i}^{r_o} \left(\frac{1}{h r^2} + \frac{Z_b}{2\pi r^3} \right) dr &= \int_{r_i}^{r_o} \frac{1}{h r^2} dr + \int_{r_i}^{r_o} \frac{Z_b}{2\pi r^3} dr = \frac{1}{h} \int_{r_i}^{r_o} \frac{1}{r^2} dr \\ &+ \frac{Z_b}{2\pi} \int_{r_i}^{r_o} \frac{1}{r^3} dr = \frac{1}{h} \left(\frac{1}{r_i} - \frac{1}{r_o} \right) + \frac{Z_b}{4\pi} \left(\frac{1}{r_i^2} - \frac{1}{r_o^2} \right)\end{aligned}\quad (\text{C.41})$$

Using Eqs. C.41 in C.40 and splitting them in radial and azimuth direction.

$$\begin{aligned}\hat{r} &:= \frac{f}{4} \rho_m \left(\frac{Q_m}{2\pi h} \right)^2 \frac{1}{\sin \beta} \left[\frac{1}{h} \left(\frac{1}{r_i} - \frac{1}{r_o} \right) + \frac{Z_b}{4\pi} \left(\frac{1}{r_i^2} - \frac{1}{r_o^2} \right) \right] \\ \hat{\theta} &:= -\frac{f}{4} \rho_m \left(\frac{Q_m}{2\pi h} \right)^2 \frac{\cot \beta}{\sin \beta} \left[\frac{1}{h} \left(\frac{1}{r_i} - \frac{1}{r_o} \right) + \frac{Z_b}{4\pi} \left(\frac{1}{r_i^2} - \frac{1}{r_o^2} \right) \right]\end{aligned}\quad (\text{C.42})$$

So dividing each equation by the term $\overline{\rho_m} \omega^2 r_o^2$.

$$\begin{aligned}\hat{r} &:= \frac{f}{4} \frac{\rho_m}{\overline{\rho_m}} \left(\frac{Q_m^2}{\omega^2 r_o^6} \right) \frac{r_o^4}{4 \pi^2 h^2} \frac{1}{\sin \beta} \left[\frac{1}{h} \left(\frac{1}{r_i} - \frac{1}{r_o} \right) + \frac{Z_b}{4 \pi} \left(\frac{1}{r_i^2} - \frac{1}{r_o^2} \right) \right] \\ &= \frac{f}{4} \frac{\rho_m}{\overline{\rho_m}} \frac{r_o^4}{4 \pi^2 h^2} \frac{1}{\sin \beta} \left[\frac{1}{h} \left(\frac{1}{r_i} - \frac{1}{r_o} \right) + \frac{Z_b}{4 \pi} \left(\frac{1}{r_i^2} - \frac{1}{r_o^2} \right) \right] C_Q\end{aligned}$$

$$\hat{\theta} := -\frac{f}{4} \frac{\rho_m}{\overline{\rho_m}} \frac{r_o^4}{4 \pi^2 h^2} \frac{\cot \beta}{\sin \beta} \left[\frac{1}{h} \left(\frac{1}{r_i} - \frac{1}{r_o} \right) + \frac{Z_b}{4 \pi} \left(\frac{1}{r_i^2} - \frac{1}{r_o^2} \right) \right] C_Q$$

C.3 Radial and viscous term

$$\begin{aligned}-\Delta P_r &= \int_{r_i}^{r_o} -\frac{\partial p}{\partial r} dr = \tilde{\rho}_m \left[\frac{(1 + \cot^2 \beta)}{4 \pi^2 h^2} \right] Q_m^2 \int_{r_i}^{r_o} \left(\frac{-1}{r^3} \right) dr + \overline{\rho_m} \left(\frac{\cot \beta}{\pi h} \right) \\ \omega Q_m \int_{r_i}^{r_o} \left(\frac{1}{r} \right) dr - \rho_m \omega^2 \int_{r_i}^{r_o} r dr - \frac{f}{4} \frac{\rho_m}{\sin \beta} \left(\frac{Q_m}{2 \pi h} \right)^2 \int_{r_i}^{r_o} \left(\frac{1}{h r^2} + \frac{Z_b}{2 \pi r^3} \right) dr \\ &\quad - 4 \mu \frac{\lambda_k}{\alpha_k} \frac{Q_m}{2 \pi h} \int_{r_i}^{r_o} \left(\frac{1}{r^3} \right) dr\end{aligned}$$

$$\begin{aligned}-\Delta P_r &= \tilde{\rho}_m \left[\frac{(1 + \cot^2 \beta)}{4 \pi^2 h^2} \right] Q_m^2 \left(\frac{1}{2} \frac{1}{r^2} \right) \Big|_{r_i}^{r_o} + \overline{\rho_m} \left(\frac{\cot \beta}{\pi h} \right) \omega Q_m \ln r \Big|_{r_i}^{r_o} - \rho_m \omega^2 \frac{r^2}{2} \Big|_{r_i}^{r_o} \\ &\quad - \frac{f}{4} \frac{\rho_m}{\sin \beta} \left(\frac{Q_m}{2 \pi h} \right)^2 \left[\left(\frac{1}{h} \frac{-1}{r} \right) \Big|_{r_i}^{r_o} + \frac{Z_b}{2 \pi} \left(\frac{-1}{2 r^2} \right) \Big|_{r_i}^{r_o} \right] - 4 \mu \frac{\lambda_k}{\alpha_k} \frac{Q_m}{2 \pi h} \left(\frac{1}{2} \frac{-1}{r^2} \right) \Big|_{r_i}^{r_o}\end{aligned}$$

$$\begin{aligned}
-\Delta P_r &= \tilde{\rho}_m \left[\frac{(1 + \cot^2 \beta)}{4 \pi^2 h^2} \right] \frac{Q_m^2}{2} \left(\frac{1}{r_o^2} - \frac{1}{r_i^2} \right) + \overline{\rho}_m \left(\frac{\cot \beta}{\pi h} \right) \omega Q_m (\ln r_o - \ln r_i) \\
&\quad - \rho_m \omega^2 \frac{r_o^2 - r_i^2}{2} - \frac{f}{4} \frac{\rho_m}{\sin \beta} \left(\frac{Q_m}{2 \pi h} \right)^2 \left[\frac{1}{h} \left(\frac{1}{r_i} - \frac{1}{r_o} \right) + \frac{Z_b}{4 \pi} \left(\frac{1}{r_i^2} - \frac{1}{r_o^2} \right) \right] \\
&\quad \quad \quad - 4 \mu \frac{\lambda_k}{\alpha_k} \frac{Q_m}{2 \pi h} \frac{1}{2} \left(\frac{1}{r_i^2} - \frac{1}{r_o^2} \right) \\
-\Delta P_r &= \tilde{\rho}_m \left[\frac{(1 + \cot^2 \beta)}{4 \pi^2 h^2} \right] \frac{Q_m^2}{2} \left(\frac{-(r_o^2 - r_i^2)}{r_i^2 r_o^2} \right) + \overline{\rho}_m \left(\frac{\cot \beta}{\pi h} \right) \omega Q_m \ln \frac{r_o}{r_i} - \rho_m \\
&\quad \omega^2 \left(\frac{r_o^2 - r_i^2}{2} \right) - \frac{f}{4} \frac{\rho_m}{\sin \beta} \left(\frac{Q_m}{2 \pi h} \right)^2 \left[\frac{1}{h} \left(\frac{1}{r_i} - \frac{1}{r_o} \right) + \frac{Z_b}{4 \pi} \left(\frac{1}{r_i^2} - \frac{1}{r_o^2} \right) \right] \\
&\quad \quad \quad - \mu \frac{\lambda_k}{\alpha_k} \frac{Q_m}{\pi h} \left(\frac{r_o^2 - r_i^2}{r_i^2 r_o^2} \right)
\end{aligned} \tag{C.43}$$

The outer radius r_o will be used as characteristic length and $\overline{\rho}_m$ is adopted as a reference density. So dividing by the term $\overline{\rho}_m \omega^2 r_o^2$ Eq. C.43 becomes:

$$\begin{aligned}
-\frac{\Delta P_r}{\overline{\rho}_m \omega^2 r_o^2} &= -\frac{1}{2} \left(\frac{\rho_m}{\overline{\rho}_m} \right) \left(\frac{r_o^2 - r_i^2}{r_o^2} \right) + \left(\frac{\cot \beta}{\pi h} \right) \left(\frac{Q_m}{\omega r_o^2} \right) \ln \frac{r_o}{r_i} \\
- \left(\frac{\tilde{\rho}_m}{\overline{\rho}_m} \right) \left[\frac{(1 + \cot^2 \beta)}{4 \pi^2 h^2} \right] \frac{Q_m^2}{2 \omega^2 r_o^2} \left(\frac{r_o^2 - r_i^2}{r_i^2 r_o^2} \right) &- \frac{f}{4} \frac{\rho_m}{\overline{\rho}_m} \left(\frac{Q_m^2}{\omega^2 r_o^6} \right) \frac{r_o^4}{4 \pi^2 h^2} \frac{1}{\sin \beta} \\
\left[\frac{1}{h} \left(\frac{1}{r_i} - \frac{1}{r_o} \right) + \frac{Z_b}{4 \pi} \left(\frac{1}{r_i^2} - \frac{1}{r_o^2} \right) \right] &- \frac{\mu}{\overline{\rho}_m} \frac{\lambda_k}{\alpha_k} \left(\frac{Q_m}{\omega^2 r_o^2} \right) \frac{1}{\pi h} \left(\frac{r_o^2 - r_i^2}{r_i^2 r_o^2} \right)
\end{aligned} \tag{C.44}$$

Manipulating the previous expression:

$$\begin{aligned}
\frac{\Delta P_r}{\overline{\rho}_m \omega^2 r_o^2} &= \frac{1}{2} \left(\frac{\rho_m}{\overline{\rho}_m} \right) \left[1 - \left(\frac{r_i}{r_o} \right)^2 \right] - \left[\left(\frac{\cot \beta}{\pi} \right) \left(\frac{r_o}{h} \right) \right] \left(\frac{Q_m}{\omega r_o^3} \right) \ln(r_o/r_i) \\
&+ \left(\frac{\tilde{\rho}_m}{\overline{\rho}_m} \right) \left[\frac{(1 + \cot^2 \beta)}{8 \pi^2} \right] \left(\frac{r_o}{h} \right)^2 \frac{Q_m^2}{\omega^2 r_o^6} \left[\left(\frac{r_o}{r_i} \right)^2 - 1 \right] + \frac{f}{4} \frac{\rho_m}{\overline{\rho}_m} \left(\frac{Q_m^2}{\omega^2 r_o^6} \right) \frac{r_o^4}{4 \pi^2 h^2} \\
\frac{1}{\sin \beta} \left[\frac{1}{h} \left(\frac{1}{r_i} - \frac{1}{r_o} \right) + \frac{Z_b}{4 \pi} \left(\frac{1}{r_i^2} - \frac{1}{r_o^2} \right) \right] &+ \frac{\mu}{\overline{\rho}_m} \frac{\lambda_k}{\alpha_k} \left(\frac{Q_m}{\omega r_o^3} \right) \frac{1}{\omega \pi h r_o} \left[\left(\frac{r_o}{r_i} \right)^2 - 1 \right]
\end{aligned} \tag{C.45}$$

Using the dimensionless groups showed in Eq. C.4:

$$\begin{aligned}
C_H = & \frac{1}{2} \left(\frac{\rho_m}{\rho_m} \right) \left[1 - \left(\frac{r_i}{r_o} \right)^2 \right] - \left[\left(\frac{\cot \beta}{\pi} \right) \left(\frac{r_o}{h} \right) \ln \frac{r_o}{r_i} \right] C_Q + \left(\frac{\tilde{\rho}_m}{\rho_m} \right) \\
& \left[\frac{(1 + \cot^2 \beta)}{8 \pi^2} \right] \left(\frac{r_o}{h} \right)^2 \left[\left(\frac{r_o}{r_i} \right)^2 - 1 \right] C_Q^2 - \frac{f}{4} \frac{\rho_m}{\rho_m} \frac{r_o^4}{4 \pi^2 h^2} \frac{1}{\sin \beta} \quad (C.46) \\
& \left[\frac{1}{h} \left(\frac{1}{r_i} - \frac{1}{r_o} \right) + \frac{Z_b}{4\pi} \left(\frac{1}{r_i^2} - \frac{1}{r_o^2} \right) \right] C_Q^2 + \frac{\mu}{\rho_m} \frac{\lambda_k}{\alpha_k} \frac{1}{\omega \pi h r_o} \left[\left(\frac{r_o}{r_i} \right)^2 - 1 \right] C_Q
\end{aligned}$$

C.4 Momentum Transfer Between Phases

The development of the subtraction between Eq. 4.95 and 4.94 is shown in the present section. So:

$$\begin{aligned}
\rho_1 \left(\frac{\partial}{\partial r} \left(\frac{v_{1r}^2}{2} \right) - \frac{v_{1\theta}}{r} \right) - \rho_2 \left(\frac{\partial}{\partial r} \left(\frac{v_{2r}^2}{2} \right) - \frac{v_{2\theta}}{r} \right) = -\rho_1 A_{1fr} + \rho_2 A_{2fr} \\
+ \frac{M_{2r}}{\alpha_1} + \frac{M_{2r}}{\alpha_2} + \nabla \cdot \vec{\tau} \quad (C.47)
\end{aligned}$$

Using Eqs. C.5, C.6, 4.58 and 4.23:

$$\begin{aligned}
\rho_1 \left[\left(\frac{\lambda_1}{\alpha_1} \right)^2 \frac{\partial}{\partial r} \left(\frac{j_m^2(r)}{2} \right) - \left(\frac{\lambda_1}{\alpha_1} \right)^2 \cot^2 \beta \left(\frac{j_m^2(r)}{r} \right) \right] - \rho_2 \left[\left(\frac{\lambda_2}{\alpha_2} \right)^2 \right. \\
\left. \frac{\partial}{\partial r} \left(\frac{j_m^2(r)}{2} \right) - \left(\frac{\lambda_2}{\alpha_2} \right)^2 \cot^2 \beta \left(\frac{j_m^2(r)}{r} \right) \right] = +\rho_1 2\omega v_{1\theta} - \rho_2 2\omega v_{2\theta} \\
+ (\rho_1 - \rho_2) \omega^2 r + M_{2r} \frac{(\alpha_1 + \alpha_2)}{\alpha_1 \alpha_2} + \nabla \cdot \vec{\tau}
\end{aligned}$$

$$\begin{aligned}
\rho_1 \left(\frac{\lambda_1}{\alpha_1} \right)^2 \left[\frac{\partial}{\partial r} \left(\frac{j_m^2(r)}{2} \right) - \cot^2 \beta \left(\frac{j_m^2(r)}{r} \right) \right] - \rho_2 \left(\frac{\lambda_2}{\alpha_2} \right)^2 \left[\frac{\partial}{\partial r} \right. \\
\left. \left(\frac{j_m^2(r)}{2} \right) - \cot^2 \beta \left(\frac{j_m^2(r)}{r} \right) \right] = +2\omega \rho_1 \left[- \left(\frac{\lambda_1}{\alpha_1} \right) \cot \beta j_m(r) \right] \\
- 2\omega \rho_2 \left[- \left(\frac{\lambda_2}{\alpha_2} \right) \cot \beta j_m(r) \right] + (\rho_1 - \rho_2) \omega^2 r + \frac{M_{2r}}{\alpha_1 \alpha_2} + \nabla \cdot \vec{\tau}
\end{aligned}$$

$$\left[\rho_1 \left(\frac{\lambda_1}{\alpha_1} \right)^2 - \rho_2 \left(\frac{\lambda_2}{\alpha_2} \right)^2 \right] \left[\frac{\partial}{\partial r} \left(\frac{j_m^2(r)}{2} \right) - \cot^2 \beta \left(\frac{j_m^2(r)}{r} \right) \right] = \left[-\rho_1 \left(\frac{\lambda_1}{\alpha_1} \right) + \rho_2 \left(\frac{\lambda_2}{\alpha_2} \right) \right] 2\omega \cot \beta j_m(r) + (\rho_1 - \rho_2) \omega^2 r + \frac{M_{2r}}{\alpha_1 \alpha_2} + \nabla \cdot \vec{\tau} \quad (\text{C.48})$$

Integrating the term inside Eq. C.48:

$$\frac{\partial}{\partial r} j_m^2(r) = 2j_m(r) \frac{\partial}{\partial r} j_m(r)$$

Using Eq. C.7:

$$\frac{\partial}{\partial r} j_m^2(r) = 2j_m(r) \left(-\frac{j_m(r)}{r} \right) = -2\frac{j_m^2(r)}{r} \quad (\text{C.49})$$

Substituting Eq. C.49 in C.48 and using Eq. C.24:

$$\frac{M_{2r}}{\alpha_1 \alpha_2} = \left[\rho_1 \left(\frac{\lambda_1}{\alpha_1} \right)^2 - \rho_2 \left(\frac{\lambda_2}{\alpha_2} \right)^2 \right] (1 + \cot^2 \beta) \left(-\frac{j_m^2(r)}{r} \right) + \left[\rho_1 \left(\frac{\lambda_1}{\alpha_1} \right) - \rho_2 \left(\frac{\lambda_2}{\alpha_2} \right) \right] 2\omega \cot \beta j_m(r) - (\rho_1 - \rho_2) \omega^2 r - \langle \nabla \cdot \vec{\tau} \rangle$$

$$\frac{M_{2r}}{\alpha_1 \alpha_2} = \left[\rho_1 \left(\frac{\lambda_1}{\alpha_1} \right)^2 - \rho_2 \left(\frac{\lambda_2}{\alpha_2} \right)^2 \right] (1 + \cot^2 \beta) \left(\frac{Q_m}{2\pi h} \right)^2 \left(\frac{-1}{r^3} \right) + \left[\rho_1 \left(\frac{\lambda_1}{\alpha_1} \right) - \rho_2 \left(\frac{\lambda_2}{\alpha_2} \right) \right] \cot \beta 2\omega \left(\frac{Q_m}{2\pi h} \right) \frac{1}{r} - (\rho_1 - \rho_2) \omega^2 r - \langle \nabla \cdot \vec{\tau} \rangle$$

$$\frac{M_{2r}}{\alpha_1 \alpha_2} = \left[\rho_1 \left(\frac{\lambda_1}{\alpha_1} \right)^2 - \rho_2 \left(\frac{\lambda_2}{\alpha_2} \right)^2 \right] \left[\frac{(1 + \cot^2 \beta)}{4\pi^2 h^2} \right] Q_m^2 \left(\frac{-1}{r^3} \right) + \left[\rho_1 \left(\frac{\lambda_1}{\alpha_1} \right) - \rho_2 \left(\frac{\lambda_2}{\alpha_2} \right) \right] \left(\frac{\cot \beta}{\pi h} \right) \omega Q_m \left(\frac{1}{r} \right) - (\rho_1 - \rho_2) \omega^2 r - \langle \nabla \cdot \vec{\tau} \rangle \quad (\text{C.50})$$

The first term on the right-hand side is the convective buoyancy, the second term is the Coriolis buoyancy, the third one is the centrifugal buoyancy and the last is the viscous term. The net rate of momentum transfer by liquid phase to the gas phase is a result of buoyancy generated by convective acceleration, Coriolis and centrifugal. The

terms involved with density will be simplified:

$$\begin{aligned}
 & \circ \Delta\rho = \rho_1 - \rho_2 \\
 & \circ \overline{\Delta\rho} = \rho_1 \left(\frac{\lambda_1}{\alpha_1} \right) - \rho_2 \left(\frac{\lambda_2}{\alpha_2} \right) \\
 & \circ \widetilde{\Delta\rho} = \rho_1 \left(\frac{\lambda_1}{\alpha_1} \right)^2 - \rho_2 \left(\frac{\lambda_2}{\alpha_2} \right)^2
 \end{aligned}$$

So Eq. C.50 becomes:

$$\frac{M_{2r}}{\alpha_1\alpha_2} = \widetilde{\Delta\rho} \left[\frac{(1 + \cot^2 \beta)}{4\pi^2 h^2} \right] Q_m^2 \left(\frac{-1}{r^3} \right) + \overline{\Delta\rho} \left(\frac{\cot \beta}{\pi h} \right) \omega Q_m \left(\frac{1}{r} \right) - \Delta\rho \omega^2 r - \langle \nabla \cdot \vec{\tau} \rangle \quad (\text{C.51})$$

where:

$$(1 + \cot^2 \beta) = 1 + \frac{\cos^2 \beta}{\sin^2 \beta} = \frac{\sin^2 \beta + \cos^2 \beta}{\sin^2 \beta} = \csc^2 \beta \quad (\text{C.52})$$

The interfacial terms are discussed in the next items.

- **Drag force:**

The drag force acting on the particle can be given in terms of the drag coefficient C_D based on the relative velocity as (ISHII AND HIBIKI, 2010):

$$\vec{M}_2^D = \frac{-\alpha}{B_b} \vec{F}_D \quad (\text{C.53})$$

$$\vec{F}_2^D = -\frac{1}{2} A_p C_D \rho_1 \vec{v}_s \|\vec{v}_s\| \quad (\text{C.54})$$

where A_p is the projected area of typical particle and v_s is the relative velocity given by $\vec{v}_s = \vec{v}_2 - \vec{v}_1$. Then substituting the term \vec{F}_D in Eq. C.53 and replacing $A_p = \pi r_p^2/4$ and $B_p = 4\pi r_p^3/3$:

$$\begin{aligned}
 \vec{M}_2^D &= \frac{-\alpha}{4\pi r_b^3/3} \left(-\frac{1}{2} \pi r_b^2 C_D \rho_1 \vec{v}_s \|\vec{v}_s\| \right) \\
 &= \alpha \rho_1 \left(\frac{3C_D}{8r_b} \right) \vec{v}_s \|\vec{v}_s\| = \alpha \rho_1 C_A \vec{v}_s \|\vec{v}_s\| \quad (\text{C.55})
 \end{aligned}$$

where $C_A = 3C_D/(8r_b)$ and C_D indicates the drag coefficient. The density considered

inside the drag force relates to the continuous phase (ISHII AND HIBIKI, 2010).

Considering this equation in radial direction. It becomes:

$$\boxed{\vec{M}_{2r}^D = \alpha \rho_1 C_A \vec{v}_{sr} \|\vec{v}_s\|} \quad \text{where} \quad \boxed{C_A = \frac{3 C_D}{8 r_b}} \quad (\text{C.56})$$

When the velocity field was estimated in a simplified manner considering the hypothesis adopted, such as the flow aligned with the blade. It has been shown that:

$$\boxed{\|\vec{v}_s\| = v_{s,s}} \quad \text{and} \quad \boxed{v_{sr} = v_{s,s} \sin \beta}$$

Substituting in Eq. C.56:

$$\boxed{\vec{M}_2^D = \alpha \rho_1 C_A \sin \beta v_{s,s} \|\vec{v}_s\|} \quad (\text{C.57})$$

The drag coefficient C_D can be calculated in many ways. It is related to flow pattern as suggested by Ishii and Hibiki (2010).

- **Virtual or added mass force:**

This force is caused by the fact that the particle has to accelerate some of the surrounding fluid, leading to an additional drag. Zuber (1964) studied the effect of the concentration on the virtual mass force \vec{F}_V which is (ISHII AND HIBIKI, 2010):

$$\vec{F}_V = -\rho_1 \frac{B_b}{2} \frac{D(\vec{v}_s)}{Dt} \quad (\text{C.58})$$

Substituting the virtual mass force in the interfacial term:

$$\vec{M}_2^V = \frac{-\alpha}{B_b} \vec{F}_V = \frac{-\alpha}{B_b} \left[-\rho_1 \frac{B_b}{2} \frac{D(\vec{v}_s)}{Dt} \right]$$

$$\vec{M}_2^V = \alpha \rho_1 \frac{1}{2} \frac{D(\vec{v}_s)}{Dt} \quad \text{or} \quad \boxed{\vec{M}_2^V = \alpha \rho_1 C_V \frac{D(\vec{v}_s)}{Dt}} \quad (\text{C.59})$$

where C_V is the virtual mass coefficient and it is approximate to 1/2. Considering steady state, the derivatives relative with time are equal to zero.

$$\begin{aligned}\vec{M}_2^V &= \alpha \rho_1 C_V \left(\frac{Dv_2}{Dt} - \frac{Dv_1}{Dt} \right) \\ \vec{M}_2^V &= \alpha \rho_1 C_V \left(\frac{\overset{=0}{\partial v_2}}{\partial t} + v_2 \cdot \nabla v_2 - \frac{\overset{=0}{\partial v_1}}{\partial t} - v_1 \cdot \nabla v_1 \right) \\ \boxed{M_2^V} &= \alpha \rho_1 C_V (v_2 \cdot \nabla v_2 - v_1 \cdot \nabla v_1)\end{aligned}\quad (\text{C.60})$$

- **Basset force:**

The Basset force term describes the force due to the lagging boundary layer development with changing relative velocity (acceleration) of bodies moving through a fluid. The Basset term accounts for viscous effects and addresses the temporal delay in boundary layer development as the relative velocity changes with time. It is also known as the "history" term. The Basset force is given by (ISHII AND HIBIKI, 2010):

$$F_2^B = -6r_b^2 \sqrt{\pi \rho_1 \mu_m} \int_t^D \frac{D}{D\xi} (v_2 - v_1) \frac{d\xi}{\sqrt{t - \xi}}$$

where μ_m is the mixture viscosity and ξ is an integration variable related with time. So, expanding the time derivative:

$$\begin{aligned}F_2^B &= -6r_b^2 \sqrt{\pi \rho_1 \mu_m} \int_0^t \left(\frac{D v_2}{D\xi} - \frac{D v_1}{D\xi} \right) \frac{d\xi}{\sqrt{t - \xi}} \\ F_2^B &= -6r_b^2 \sqrt{\pi \rho_1 \mu_m} \int_0^t \left(\frac{\overset{=0}{\partial v_2}}{\partial \xi} + v_2 \cdot \nabla v_2 - \frac{\overset{=0}{\partial v_1}}{\partial \xi} - v_1 \cdot \nabla v_1 \right) \frac{d\xi}{\sqrt{t - \xi}}\end{aligned}\quad (\text{C.61})$$

Considering steady state, the derivatives relative with time are equal to zero. Convective terms do not depend on time, so they can be placed out of integration.

$$\begin{aligned}F_2^B &= -6r_b^2 \sqrt{\pi \rho_1 \mu_m} (\vec{v}_2 \cdot \nabla \vec{v}_2 - \vec{v}_1 \cdot \nabla \vec{v}_1) \int_0^t \frac{d\xi}{\sqrt{t - \xi}} \\ F_2^B &= -6r_b^2 \sqrt{\pi \rho_1 \mu_m} (\vec{v}_2 \cdot \nabla \vec{v}_2 - \vec{v}_1 \cdot \nabla \vec{v}_1) (-2\sqrt{t - \xi}) \Big|_0^t \\ F_2^B &= -12r_b^2 \sqrt{\pi \rho_1 \mu_m} (\vec{v}_2 \cdot \nabla \vec{v}_2 - \vec{v}_1 \cdot \nabla \vec{v}_1) \sqrt{t}\end{aligned}\quad (\text{C.62})$$

So from the Zuber (1964) model:

$$\vec{M}_2^B = \frac{-\alpha}{B_b} \vec{F}_B = \frac{-\alpha}{B_b} \left[-12r_b^2 \sqrt{\pi \rho_1 \mu_m} (\vec{v}_2 \cdot \nabla \vec{v}_2 - \vec{v}_1 \cdot \nabla \vec{v}_1) \sqrt{t} \right]$$

$$\vec{M}_2^B = \frac{9\alpha}{\pi r_b} \sqrt{\pi \rho_1 \mu_m} t (\vec{v}_2 \cdot \nabla \vec{v}_2 - \vec{v}_1 \cdot \nabla \vec{v}_1)$$

$$\vec{M}_2^B = \alpha \rho_1 \frac{9}{r_b} \sqrt{\frac{\mu_m t}{\pi \rho_1}} (\vec{v}_2 \cdot \nabla \vec{v}_2 - \vec{v}_1 \cdot \nabla \vec{v}_1)$$

$$\boxed{\vec{M}_2^B = \alpha \rho_1 C_B (\vec{v}_2 \cdot \nabla \vec{v}_2 - \vec{v}_1 \cdot \nabla \vec{v}_1)} \quad \text{and} \quad \boxed{C_B = \frac{9}{r_b} \sqrt{\frac{\mu_m t}{\pi \rho_1}}} \quad (\text{C.63})$$

where t is the time scale of the Basset force, which may be estimated from the momentum penetration depth as (ISHII AND HIBIKI, 2010):

$$\sqrt{\pi \nu t} \simeq r_p \quad \rightarrow \quad \boxed{\sqrt{t} = \frac{r_p}{\sqrt{\pi \nu}}} \quad (\text{C.64})$$

where $\nu = \mu/\rho$.

The Basset and Added mass can be combined as:

$$\vec{M}_2^{B+V} = \alpha \rho_1 (C_B + C_V) (\vec{v}_2 \cdot \nabla \vec{v}_2 - \vec{v}_1 \cdot \nabla \vec{v}_1) \quad (\text{C.65})$$

Considering the radial direction for those forces, the convective acceleration becomes:

$$\begin{aligned} \left(\vec{v}_2 \cdot \nabla \vec{v}_2 - \vec{v}_1 \cdot \nabla \vec{v}_1 \right)_{\hat{r}} &= v_{2r} \frac{\partial v_{2r}}{\partial r} - \frac{v_{2\theta}^2}{r} - v_{1r} \frac{\partial v_{1r}}{\partial r} - \frac{v_{1\theta}^2}{r} \\ &= \frac{\partial}{\partial r} \left(\frac{v_{2r}^2}{2} \right) - \frac{\partial}{\partial r} \left(\frac{v_{1r}^2}{2} \right) - \left(\frac{v_{2\theta}^2 - v_{1\theta}^2}{r} \right) \end{aligned}$$

$$\boxed{\left(\vec{v}_2 \cdot \nabla \vec{v}_2 - \vec{v}_1 \cdot \nabla \vec{v}_1 \right)_{\hat{r}} = \frac{\partial}{\partial r} \left(\frac{v_{2r}^2 - v_{1r}^2}{2} \right) - \left(\frac{v_{2\theta}^2 - v_{1\theta}^2}{r} \right)} \quad (\text{C.66})$$

Substituting Eq. C.5, C.6 and 4.58:

$$\begin{aligned} \left(\vec{v}_2 \cdot \nabla \vec{v}_2 - \vec{v}_1 \cdot \nabla \vec{v}_1 \right)_{\hat{r}} &= \left[\left(\frac{\lambda_2}{\alpha_2} \right)^2 - \left(\frac{\lambda_1}{\alpha_1} \right)^2 \right] \frac{\partial}{\partial r} \left(\frac{j_m^2(r)}{2} \right) - \left[\left(\frac{\lambda_2}{\alpha_2} \right)^2 \right. \\ &\quad \left. - \left(\frac{\lambda_1}{\alpha_1} \right)^2 \right] \cot^2 \beta \frac{j_m^2(r)}{r} \\ \left(\vec{v}_2 \cdot \nabla \vec{v}_2 - \vec{v}_1 \cdot \nabla \vec{v}_1 \right)_{\hat{r}} &= \left[\left(\frac{\lambda_2}{\alpha_2} \right)^2 - \left(\frac{\lambda_1}{\alpha_1} \right)^2 \right] \frac{1}{2} \left(\frac{-2 j_m^2(r)}{r} \right) - \left[\left(\frac{\lambda_2}{\alpha_2} \right)^2 \right. \\ &\quad \left. - \left(\frac{\lambda_1}{\alpha_1} \right)^2 \right] \cot^2 \beta \frac{j_m^2(r)}{r} \\ \left(\vec{v}_2 \cdot \nabla \vec{v}_2 - \vec{v}_1 \cdot \nabla \vec{v}_1 \right)_{\hat{r}} &= - \left[\left(\frac{\lambda_2}{\alpha_2} \right)^2 - \left(\frac{\lambda_1}{\alpha_1} \right)^2 \right] \frac{j_m^2(r)}{r} - \left[\left(\frac{\lambda_2}{\alpha_2} \right)^2 \right. \\ &\quad \left. - \left(\frac{\lambda_1}{\alpha_1} \right)^2 \right] \cot^2 \beta \frac{j_m^2(r)}{r} \\ \boxed{\left(\vec{v}_2 \cdot \nabla \vec{v}_2 - \vec{v}_1 \cdot \nabla \vec{v}_1 \right)_{\hat{r}} = - \left[\left(\frac{\lambda_2}{\alpha_2} \right)^2 - \left(\frac{\lambda_1}{\alpha_1} \right)^2 \right] (1 + \cot^2 \beta) \left(\frac{j_m^2(r)}{r} \right)} & \quad (\text{C.67}) \end{aligned}$$

So Eq. C.65 becomes:

$$\vec{M}_{2r}^{B+V} = -\alpha \rho_1 (C_B + C_V) \left[\left(\frac{\lambda_2}{\alpha_2} \right)^2 - \left(\frac{\lambda_1}{\alpha_1} \right)^2 \right] (1 + \cot^2 \beta) \left(\frac{j_m^2(r)}{r} \right) \quad (\text{C.68})$$

C.4.1 Development of Interfacial Terms

The development of term M_{2r} is shown in the next steps.

$$\begin{aligned} \frac{M_{2r}}{\alpha} &= \rho_1 C_A \sin \beta v_{s,s} \|\vec{v}_s\| + \rho_1 (C_B + C_V) \left[\left(\frac{\lambda_2}{\alpha_2} \right)^2 - \left(\frac{\lambda_1}{\alpha_1} \right)^2 \right] \\ &\quad \left[\frac{(1 + \cot^2 \beta)}{4 \pi^2 h^2} \right] Q_m^2 \left(\frac{-1}{r^3} \right) \end{aligned}$$

$$\begin{aligned} \frac{M_{2r}}{\alpha} &= \alpha_1 \widetilde{\Delta\rho} \left[\frac{(1 + \cot^2 \beta)}{4\pi^2 h^2} \right] Q_m^2 \left(\frac{-1}{r^3} \right) + \alpha_1 \overline{\Delta\rho} \left(\frac{\cot \beta}{\pi h} \right) \omega Q_m \left(\frac{1}{r} \right) \\ &- \alpha_1 \Delta\rho \omega^2 r + \alpha_1 \frac{f}{4} \rho_m \left(\frac{Q_m}{2\pi h} \right)^2 \frac{1}{\sin \beta} \left(\frac{1}{h r^2} + \frac{Z_b}{2\pi r^3} \right) + 4\mu \alpha_1 \frac{\lambda_k}{\alpha_k} \frac{Q_m}{2\pi h} \frac{1}{r^3} \end{aligned}$$

Matching those equations.

$$\begin{aligned} \rho_1 C_A \sin \beta v_{s,s} \|\vec{v}_s\| + \rho_1 (C_B + C_V) \left[\left(\frac{\lambda_2}{\alpha_2} \right)^2 - \left(\frac{\lambda_1}{\alpha_1} \right)^2 \right] \left[\frac{(1 + \cot^2 \beta)}{4\pi^2 h^2} \right] Q_m^2 \\ \left(\frac{-1}{r^3} \right) &= \alpha_1 \widetilde{\Delta\rho} \left[\frac{(1 + \cot^2 \beta)}{4\pi^2 h^2} \right] Q_m^2 \left(\frac{-1}{r^3} \right) + \alpha_1 \overline{\Delta\rho} \left(\frac{\cot \beta}{\pi h} \right) \omega Q_m \left(\frac{1}{r} \right) \\ &- \alpha_1 \Delta\rho \omega^2 r + \alpha_1 \frac{f}{4} \rho_m \left(\frac{Q_m}{2\pi h} \right)^2 \frac{1}{\sin \beta} \left(\frac{1}{h r^2} + \frac{Z_b}{2\pi r^3} \right) + 4\mu \alpha_1 \frac{\lambda_k}{\alpha_k} \frac{Q_m}{2\pi h} \frac{1}{r^3} \end{aligned}$$

$$\begin{aligned} \rho_1 C_A \sin \beta v_{s,s} \|\vec{v}_s\| &= \left\{ \alpha_1 \widetilde{\Delta\rho} - \rho_1 (C_B + C_V) \left[\left(\frac{\lambda_2}{\alpha_2} \right)^2 - \left(\frac{\lambda_1}{\alpha_1} \right)^2 \right] \right\} \\ &\left[\frac{(1 + \cot^2 \beta)}{4\pi^2 h^2} \right] Q_m^2 \left(\frac{-1}{r^3} \right) + \alpha_1 \overline{\Delta\rho} \left(\frac{\cot \beta}{\pi h} \right) \omega Q_m \left(\frac{1}{r} \right) - \alpha_1 \Delta\rho \omega^2 r \\ &+ \alpha_1 \frac{f}{4} \rho_m \left(\frac{Q_m}{2\pi h} \right)^2 \frac{1}{\sin \beta} \left(\frac{1}{h r^2} + \frac{Z_b}{2\pi r^3} \right) + 4\mu \alpha_1 \frac{\lambda_k}{\alpha_k} \frac{Q_m}{2\pi h} \frac{1}{r^3} \end{aligned}$$

Adopting $\|\vec{v}_s\| = v_{s,s}$:

$$\begin{aligned} -v_{s,s}^2 &= \frac{1}{\sin \beta} \left\{ \frac{\alpha_1 \widetilde{\Delta\rho}}{\rho_1 C_A} - \frac{(C_B + C_V)}{C_A} \left[\left(\frac{\lambda_2}{\alpha_2} \right)^2 - \left(\frac{\lambda_1}{\alpha_1} \right)^2 \right] \right\} \left[\frac{(1 + \cot^2 \beta)}{4\pi^2 h^2} \right] \\ &Q_m^2 \left(\frac{-1}{r^3} \right) + \frac{\alpha_1 \overline{\Delta\rho}}{\rho_1 C_A} \frac{1}{\sin \beta} \left(\frac{\cot \beta}{\pi h} \right) \omega Q_m \left(\frac{1}{r} \right) - \frac{1}{\sin \beta} \frac{\alpha_1 \Delta\rho}{\rho_1 C_A} \omega^2 r \\ &+ \frac{\alpha_1}{\rho_1} \frac{1}{C_A} \frac{f}{4} \rho_m \left(\frac{Q_m}{2\pi h} \right)^2 \frac{1}{\sin^2 \beta} \left(\frac{1}{h r^2} + \frac{Z_b}{2\pi r^3} \right) + 4 \frac{\alpha_1}{\rho_1} \frac{1}{C_A} \frac{\mu}{\sin \beta} \frac{\lambda_k}{\alpha_k} \frac{Q_m}{2\pi h} \left(\frac{1}{r^3} \right) \end{aligned} \tag{C.69}$$

The square term $v_{s,s}$ in Eq. C.69 lost the information of signal but using physic interpretation it is knowing that this term is negative. Generally in pump the liquid flow accelerates more than gas as a result of the centrifugal field ($\rho_1 \gg \rho_2$). If the liquid

phase is faster than the gas phase, clearly the slip velocity is negative ($v_1 > v_2 \rightarrow v_2 - v_1 < 0 \rightarrow \overline{v_{s,s}} < 0$). So: $v_{s,s} = -\sqrt{v_{s,s}^2}$.

The coefficients for an isolate bubble:

$$\boxed{C_A^\infty = \frac{C_A}{1 - \alpha}} \quad \boxed{\Delta C^\infty = \frac{C_B + C_V}{1 - \alpha}} \quad (\text{C.70})$$

where:

$$\boxed{C_B^\infty = \frac{C_B}{1 - \alpha}} \quad \boxed{C_V^\infty = \frac{C_V}{1 - \alpha}} \quad \boxed{\Delta C^\infty = C_B^\infty + C_V^\infty}$$

Substituting the terms presented in Eqs. C.70 and C.69 and applying the mean operator for the slip, which is:

$$-\overline{v_{s,s}^2} = \frac{1}{(r_o - r_i)} \int_{r_i}^{r_o} -v_{s,s}^2 \, dr \quad (\text{C.71})$$

So:

$$\begin{aligned} -\overline{v_{s,s}^2} &= \frac{1}{(r_o - r_i)} \int_{r_i}^{r_o} v_{s,s}^2 \, dr = \frac{1}{\sin \beta} \left\{ \frac{1}{C_A^\infty} \frac{\widetilde{\Delta \rho}}{\rho_1} - \frac{\Delta C^\infty}{C_A^\infty} \left[\left(\frac{\lambda_2}{\alpha_2} \right)^2 - \left(\frac{\lambda_1}{\alpha_1} \right)^2 \right] \right\} \\ &\quad \left[\frac{(1 + \cot^2 \beta)}{4 \pi^2 h^2} \right] Q_m^2 \frac{1}{(r_o - r_i)} \int_{r_i}^{r_o} \left(\frac{-1}{r^3} \right) \, dr + \frac{1}{C_A^\infty} \frac{\overline{\Delta \rho}}{\rho_1} \frac{1}{\sin \beta} \left(\frac{\cot \beta}{\pi h} \right) \omega Q_m \\ &\quad \frac{1}{(r_o - r_i)} \int_{r_i}^{r_o} \left(\frac{1}{r} \right) \, dr - \frac{1}{\sin \beta} \frac{1}{C_A^\infty} \frac{\Delta \rho}{\rho_1} \omega^2 \frac{1}{(r_o - r_i)} \int_{r_i}^{r_o} r \, dr + \frac{1}{\rho_1} \frac{1}{C_A^\infty} \frac{f}{4} \\ &\quad \rho_m \left(\frac{Q_m}{2 \pi h} \right)^2 \frac{1}{\sin^2 \beta} \frac{1}{(r_o - r_i)} \int_{r_i}^{r_o} \left(\frac{1}{h r^2} + \frac{Z_b}{2 \pi r^3} \right) \, dr + 4 \frac{1}{\rho_1} \frac{1}{C_A^\infty} \frac{\mu}{\sin \beta} \frac{\lambda_k}{\alpha_k} \\ &\quad \frac{Q_m}{2 \pi h} \frac{1}{(r_o - r_i)} \int_{r_i}^{r_o} \left(\frac{1}{r^3} \right) \, dr \end{aligned}$$

$$\begin{aligned}
-\overline{v_{s,s}}^2 &= \frac{1}{\sin \beta} \left\{ \frac{1}{C_A^\infty} \frac{\widetilde{\Delta \rho}}{\rho_1} - \frac{\Delta C^\infty}{C_A^\infty} \left[\left(\frac{\lambda_2}{\alpha_2} \right)^2 - \left(\frac{\lambda_1}{\alpha_1} \right)^2 \right] \right\} \left[\frac{(1 + \cot^2 \beta)}{4 \pi^2 h^2} \right] \frac{Q_m^2}{(r_o - r_i)} \\
&\left(\frac{1}{2} \frac{1}{r^2} \right) \Big|_{r_i}^{r_o} + \frac{1}{C_A^\infty} \frac{\widetilde{\Delta \rho}}{\rho_1} \frac{1}{\sin \beta} \left(\frac{\cot \beta}{\pi h} \right) \omega \frac{Q_m}{(r_o - r_i)} \ln(r) \Big|_{r_i}^{r_o} - \frac{1}{\sin \beta} \frac{1}{C_A^\infty} \frac{\Delta \rho}{\rho_1} \omega^2 \frac{1}{(r_o - r_i)} \\
&\frac{r^2}{2} \Big|_{r_i}^{r_o} + \frac{1}{\rho_1} \frac{1}{C_A^\infty} \frac{f}{4} \rho_m \left(\frac{Q_m}{2 \pi h} \right)^2 \frac{1}{\sin^2 \beta} \frac{1}{(r_o - r_i)} \left[\left(\frac{1}{h} \frac{-1}{r} \right) \Big|_{r_i}^{r_o} + \frac{Z_b}{2 \pi} \left(\frac{-1}{2 r^2} \right) \Big|_{r_i}^{r_o} \right] \\
&+ 4 \frac{1}{\rho_1} \frac{1}{C_A^\infty} \frac{\mu}{\sin \beta} \frac{\lambda_k}{\alpha_k} \frac{Q_m}{2 \pi h} \frac{1}{(r_o - r_i)} \left(\frac{-1}{2} \frac{1}{r^2} \right) \Big|_{r_i}^{r_o}
\end{aligned}$$

Using Eq. 4.85:

$$\begin{aligned}
-\overline{v_{s,s}}^2 &= \frac{1}{\sin \beta} \left\{ \frac{1}{C_A^\infty} \frac{\widetilde{\Delta \rho}}{\rho_1} - \frac{\Delta C^\infty}{C_A^\infty} \left[\left(\frac{\lambda_2}{\alpha_2} \right)^2 - \left(\frac{\lambda_1}{\alpha_1} \right)^2 \right] \right\} \left[\frac{(1 + \cot^2 \beta)}{4 \pi^2 h^2} \right] \frac{Q_m^2}{2(r_o - r_i)} \\
&\left(\frac{1}{r_o^2} - \frac{1}{r_i^2} \right) + \frac{1}{C_A^\infty} \frac{\widetilde{\Delta \rho}}{\rho_1} \frac{1}{\sin \beta} \left(\frac{\cot \beta}{\pi h} \right) \omega \frac{Q_m}{(r_o - r_i)} \left(\ln(r_o) - \ln(r_i) \right) - \frac{1}{\sin \beta} \frac{1}{C_A^\infty} \\
&\frac{\Delta \rho}{\rho_1} \omega^2 \frac{1}{(r_o - r_i)} \frac{(r_o^2 - r_i^2)}{2} + \frac{1}{\rho_1} \frac{1}{C_A^\infty} \frac{f}{4} \rho_m \left(\frac{Q_m}{2 \pi h} \right)^2 \frac{1}{\sin^2 \beta} \frac{f_3}{(r_o - r_i)} \\
&- 4 \frac{1}{\rho_1} \frac{1}{C_A^\infty} \frac{\mu}{\sin \beta} \frac{\lambda_k}{\alpha_k} \frac{Q_m}{2 \pi h} \frac{1}{(r_o - r_i)} \frac{1}{2} \left(\frac{1}{r_o^2} - \frac{1}{r_i^2} \right)
\end{aligned} \tag{C.72}$$

Simplifying the terms:

- $\bar{r} = \frac{r_i + r_o}{2}$
- $\Delta r = r_o - r_i$
- $\frac{1}{r_o - r_i} (r_o^2 - r_i^2) = (r_o + r_i) = 2\bar{r}$
- $\frac{1}{r_o - r_i} \left(\frac{1}{r_o^2} - \frac{1}{r_i^2} \right) = \frac{1}{r_o - r_i} \frac{r_i^2 - r_o^2}{r_o^2 r_i^2} = \frac{-(r_o^2 - r_i^2)}{\Delta r} \frac{1}{r_o^2 r_i^2} = \frac{-2\bar{r}}{r_o^2 r_i^2}$
- $\frac{\ln(r_o) - \ln(r_i)}{\Delta r} = \frac{1}{\Delta r} \ln \left(\frac{r_o}{r_i} \right) = \ln \left(\frac{r_o}{r_i} \right)^{1/\Delta r}$ (C.73)

Using Eq. C.73 in Eq. C.72:

$$\begin{aligned}
-\overline{v_{s,s}}^2 &= \frac{1}{\sin \beta} \left\{ \frac{1}{C_A^\infty} \frac{\widetilde{\Delta \rho}}{\rho_1} - \frac{\Delta C^\infty}{C_A^\infty} \left[\left(\frac{\lambda_2}{\alpha_2} \right)^2 - \left(\frac{\lambda_1}{\alpha_1} \right)^2 \right] \right\} \left[\frac{(1 + \cot^2 \beta)}{4 \pi^2 h^2} \right] \\
Q_m^2 \left(-\frac{(r_o + r_i)}{2} \right) &\frac{1}{r_o^2 r_i^2} + \frac{1}{C_A^\infty} \frac{\overline{\Delta \rho}}{\rho_1} \frac{1}{\sin \beta} \left(\frac{\cot \beta}{\pi h} \right) \omega Q_m \left[\ln \left(\frac{r_o}{r_i} \right) \frac{1}{(r_o - r_i)} \right] \\
&- \frac{1}{\sin \beta} \frac{1}{C_A^\infty} \frac{\Delta \rho}{\rho_1} \omega^2 \frac{(r_o + r_i)}{2} + \frac{1}{\rho_1} \frac{1}{C_A^\infty} \frac{f}{4} \rho_m \left(\frac{Q_m}{2 \pi h} \right)^2 \frac{1}{\sin^2 \beta} \frac{f_3}{\Delta r} \\
&+ 4 \frac{1}{\rho_1} \frac{1}{C_A^\infty} \frac{\mu}{\sin \beta} \frac{\lambda_k}{\alpha_k} \frac{Q_m}{2 \pi h} \left(\frac{\bar{r}}{r_o^2 r_i^2} \right) \\
-\overline{v_{s,s}}^2 &= - \left\{ \frac{1}{C_A^\infty} \frac{\widetilde{\Delta \rho}}{\rho_1} - \frac{\Delta C^\infty}{C_A^\infty} \left[\left(\frac{\lambda_2}{\alpha_2} \right)^2 - \left(\frac{\lambda_1}{\alpha_1} \right)^2 \right] \right\} \left[\frac{(1 + \cot^2 \beta)}{4 \pi^2 h^2} \right] \frac{1}{\sin \beta} \frac{\bar{r}}{r_o^2 r_i^2} \\
&Q_m^2 + \frac{1}{C_A^\infty} \frac{\overline{\Delta \rho}}{\rho_1} \left(\frac{\cot \beta}{\pi h} \right) \frac{1}{\sin \beta} \frac{\ln(r_o/r_i)}{\Delta r} \omega Q_m - \frac{1}{\sin \beta} \frac{1}{C_A^\infty} \frac{\Delta \rho}{\rho_1} \omega^2 \bar{r} \\
&- \frac{1}{\sin \beta} \frac{1}{C_A^\infty} \frac{\Delta \rho}{\rho_1} \omega^2 \frac{(r_o + r_i)}{2} + \frac{1}{\rho_1} \frac{1}{C_A^\infty} \frac{f}{4} \rho_m \left(\frac{1}{4 \pi^2 h^2} \right) \frac{1}{\sin^2 \beta} \frac{f_3}{\Delta r} Q_m^2 \\
&+ 2 \frac{\mu}{\rho_1} \frac{1}{C_A^\infty} \frac{1}{\pi h} \frac{1}{\sin \beta} \frac{\lambda_k}{\alpha_k} \left(\frac{\bar{r}}{r_o^2 r_i^2} \right) Q_m
\end{aligned} \tag{C.74}$$

Some terms were obtained before, which are:

$$\begin{aligned}
\bullet \quad v_{2s} &= C_0 j_{ms} + v_{2j} & \bullet \quad v_{2s} &= j_{2s}/\alpha \\
\bullet \quad v_{2j} &= (1 - \alpha)v_s & \bullet \quad j_{mr} &= \frac{Q_m}{2 \pi h r} \\
\bullet \quad j_{ms} &= j_{mr}/\sin \beta
\end{aligned}$$

The flow is not developed (it has convective acceleration) and those terms vary with radius. However, this study is interested in the mean effect of the variables on the impeller. So applying the average operator in the drift-flux model:

$$v_{2s} = C_0 j_{m,s} + (1 - \alpha)v_{s,s} \quad \rightarrow \quad \overline{v_{2s}} = C_0 \overline{j_{m,s}} + (1 - \alpha)\overline{v_{s,s}}$$

$$\begin{aligned}
\overline{j_{mr}} &= \frac{1}{(r_o - r_i)} \int_{r_i}^{r_o} j_{mr} \, dr = \frac{1}{(r_o - r_i)} \int_{r_i}^{r_o} \left[\left(\frac{Q_m}{2\pi h} \right) \left(\frac{1}{r} \right) \right] dr \\
&= \left(\frac{Q_m}{2\pi h} \right) \frac{1}{(r_o - r_i)} \int_{r_i}^{r_o} \left(\frac{1}{r} \right) dr = \left(\frac{Q_m}{2\pi h} \right) \frac{1}{(r_o - r_i)} \ln(r) \Big|_{r_i}^{r_o} \\
\boxed{\overline{j_{mr}} = \left(\frac{Q_m}{2\pi h} \right) \frac{\ln(r_o/r_i)}{(r_o - r_i)}} &\quad \rightarrow \quad \boxed{\overline{j_{ms}} = \overline{j_{mr}} \frac{1}{\sin \beta}} \quad (C.75)
\end{aligned}$$

So:

$$\boxed{\overline{v_{2s}} = \frac{\overline{j_{2s}}}{\alpha} = C_0 \left(\frac{Q_m}{2\pi h} \right) \frac{\ln(r_o/r_i)}{(r_o - r_i)} \frac{1}{\sin \beta} + (1 - \alpha)\overline{v_{s,s}}} \quad (C.76)$$

Using Eq. 4.58, 4.71 and applying the average operator for the slip (Eq. C.71), Eq. C.76 becomes:

$$\begin{aligned}
\overline{v_{2s}} &= \left(\frac{\lambda_2}{\alpha_2} \right) \left[\left(\frac{Q_m}{2\pi h} \right) \frac{\ln(r_o/r_i)}{(r_o - r_i)} \frac{1}{\sin \beta} \right] = C_0 \left(\frac{Q_m}{2\pi h} \right) \frac{\ln(r_o/r_i)}{(r_o - r_i)} \frac{1}{\sin \beta} \\
&\quad + (1 - \alpha)\overline{v_{s,s}} \quad (C.77)
\end{aligned}$$

C.5 Development of Bubble Forces

The next sections treat the forces on the bubble, which are: Drag, Basset, Virtual Mass, Pseudo forces and Buoyancy. These forces were used in the development of the Transition Criteria in section 5.4.

C.5.1 Drag force

Equation C.54 refers to the drag force (SHOHAM, 2005). Describing it in \hat{r} and $\hat{\theta}$ direction:

So the drag force in \hat{s} and \hat{n} are:

$$\begin{aligned}
\vec{F}_{2r}^D &= -\frac{1}{2} A_p C_D \rho_1 v_{s,s}^{\vec{}} |v_{s,s}^{\vec{}}| \sin \beta \\
\vec{F}_{2\theta}^D &= -\frac{1}{2} A_p C_D \rho_1 v_{s,s}^{\vec{}} |v_{s,s}^{\vec{}}| \cos \beta \quad (C.78)
\end{aligned}$$

The term A_p corresponds to the area of the circle which is an approximation for a

bubble. Figure 5.8 indicates that this assumption does not correspond to what is happening in the impeller because the bubble is in the wobbling region. As explained before, the component $v_{s,n}$ is equal to zero in \hat{n} direction (Eq. 4.74). So the drag force in \hat{s} direction is:

$$\vec{F}_{2s}^D = -\frac{1}{2} A_p C_D \rho_1 v_{s,s} \vec{v}_{s,s} |v_{s,s}| \quad (\text{C.79})$$

As explained before, adopting $v_{s,s} \vec{v}_{s,s} |v_{s,s}| = -v_{s,s}^2$:

$$F_{2s}^D = \frac{1}{2} A_p C_D \rho_1 v_{s,s}^2 \quad (\text{C.80})$$

Applying the mean operator (Eq. C.71):

$$\boxed{\overline{F_{2s}^D} = \frac{1}{2} A_p C_D \rho_1 \overline{v_{s,s}^2}} \quad (\text{C.81})$$

C.5.2 Basset and Virtual/Added Mass Force

The virtual mass force from Eq. C.58 is:

$$\vec{F}_2^V = -\rho_1 \frac{B_b D(\vec{v}_s)}{2 Dt} = -\rho_1 \frac{B_b}{2} \left(\frac{D\vec{v}_2}{Dt} - \frac{D\vec{v}_1}{Dt} \right)$$

$$\vec{F}_2^V = -\rho_1 \frac{B_b}{2} (\vec{v}_2 \cdot \nabla \vec{v}_2 - \vec{v}_1 \cdot \nabla \vec{v}_1) = -\rho_1 C_V B_b (\vec{v}_2 \cdot \nabla \vec{v}_2 - \vec{v}_1 \cdot \nabla \vec{v}_1)$$

The Basset force from Eq. C.62 is:

$$\vec{F}_2^B = -12r_b^2 \sqrt{\pi \rho_1 \mu_m} (\vec{v}_2 \cdot \nabla \vec{v}_2 - \vec{v}_1 \cdot \nabla \vec{v}_1) \sqrt{t}$$

$$\vec{F}_2^B = -\frac{4}{3} r_b^3 \rho_1 \pi \left(\frac{9}{r_b} \sqrt{\frac{\mu_m t}{\rho_1 \pi}} \right) (\vec{v}_2 \cdot \nabla \vec{v}_2 - \vec{v}_1 \cdot \nabla \vec{v}_1)$$

$$\vec{F}_2^B = -\frac{4}{3} r_b^3 \rho_1 \pi C_B (\vec{v}_2 \cdot \nabla \vec{v}_2 - \vec{v}_1 \cdot \nabla \vec{v}_1)$$

Adding the virtual mass force and Basset force:

$$\vec{F}_2^V + \vec{F}_2^B = -\rho_1 C_V B_b (\vec{v}_2 \cdot \nabla \vec{v}_2 - \vec{v}_1 \cdot \nabla \vec{v}_1) - \left(\frac{4}{3} r_b^3 \pi \right) \rho_1 C_B (\vec{v}_2 \cdot \nabla \vec{v}_2 - \vec{v}_1 \cdot \nabla \vec{v}_1)$$

$$\begin{aligned}\vec{F}_2^{VB} &= -\rho_1 (C_V + C_B) B_b (\vec{v}_2 \cdot \nabla \vec{v}_2 - \vec{v}_1 \cdot \nabla \vec{v}_1) \\ \vec{F}_2^{VB} &= -\rho_1 \Delta C B_b (\vec{v}_2 \cdot \nabla \vec{v}_2 - \vec{v}_1 \cdot \nabla \vec{v}_1)\end{aligned}\quad (\text{C.82})$$

The convective term in radial direction was showed in Eq. C.67. In $\hat{\theta}$ direction it becomes:

$$\left(\vec{v}_2 \cdot \nabla \vec{v}_2 - \vec{v}_1 \cdot \nabla \vec{v}_1 \right)_{\hat{\theta}} = v_{2r} \frac{\partial v_{2\theta}}{\partial r} + \frac{v_{2\theta} v_{2r}}{r} - v_{1r} \frac{\partial v_{1\theta}}{\partial r} - \frac{v_{1\theta} v_{1r}}{r}$$

Substituting Eq. C.5, C.6:

$$\begin{aligned}\left(\vec{v}_2 \cdot \nabla \vec{v}_2 - \vec{v}_1 \cdot \nabla \vec{v}_1 \right)_{\hat{\theta}} &= \frac{\lambda_2}{\alpha_2} j_m(r) \frac{\partial}{\partial r} \left(-\frac{\lambda_2}{\alpha_2} j_m(r) \cot \beta \right) + \left(-\frac{\lambda_2}{\alpha_2} j_m(r) \cot \beta \frac{\lambda_2}{\alpha_2} j_m(r) \right) / r \\ &\quad - \frac{\lambda_1}{\alpha_1} j_m(r) \frac{\partial}{\partial r} \left(-\frac{\lambda_1}{\alpha_1} j_m(r) \cot \beta \right) - \left(-\frac{\lambda_1}{\alpha_1} j_m(r) \cot \beta \frac{\lambda_1}{\alpha_1} j_m(r) \right) / r \\ &= -\left(\frac{\lambda_2}{\alpha_2} \right)^2 \cot \beta j_m(r) \frac{\partial}{\partial r} j_m(r) - \left(\frac{\lambda_2}{\alpha_2} \right)^2 \cot \beta \frac{j_m^2(r)}{r} \\ &\quad + \left(\frac{\lambda_1}{\alpha_1} \right)^2 \cot \beta j_m(r) \frac{\partial}{\partial r} j_m(r) + \left(\frac{\lambda_1}{\alpha_1} \right)^2 \cot \beta \frac{j_m^2(r)}{r} \\ &= \left[\left(\frac{\lambda_1}{\alpha_1} \right)^2 - \left(\frac{\lambda_2}{\alpha_2} \right)^2 \right] \cot \beta j_m(r) \frac{\partial j_m(r)}{\partial r} + \left[\left(\frac{\lambda_1}{\alpha_1} \right)^2 - \left(\frac{\lambda_2}{\alpha_2} \right)^2 \right] \cot \beta \frac{j_m^2(r)}{r} \\ &= \left[\left(\frac{\lambda_1}{\alpha_1} \right)^2 - \left(\frac{\lambda_2}{\alpha_2} \right)^2 \right] \cot \beta \left(j_m(r) \frac{\partial j_m(r)}{\partial r} + \frac{j_m^2(r)}{r} \right) \\ &= \left[\left(\frac{\lambda_1}{\alpha_1} \right)^2 - \left(\frac{\lambda_2}{\alpha_2} \right)^2 \right] \cot \beta \left[j_m(r) \left(-\frac{j_m(r)}{r} \right) + \frac{j_m^2(r)}{r} \right]\end{aligned}$$

So:

$$\boxed{\left(\vec{v}_2 \cdot \nabla \vec{v}_2 - \vec{v}_1 \cdot \nabla \vec{v}_1 \right)_{\hat{\theta}} = 0} \quad (\text{C.83})$$

The convective term in $\hat{\theta}$ direction is equal to zero. On the other hand, the convective term in \hat{r} is already know by Eq. C.67. Thus Basset and added mass does not have

component in $\hat{\theta}$ direction, so in \hat{r} direction:

$$\boxed{\vec{F}_{2r}^{VB} = -\rho_1 B_b \Delta C \left[\left(\frac{\lambda_2}{\alpha_2} \right)^2 - \left(\frac{\lambda_1}{\alpha_1} \right)^2 \right] \csc^2 \beta \left(\frac{Q_m}{2\pi h} \right)^2 \left(\frac{-1}{r^3} \right)} \quad (\text{C.84})$$

Applying the mean operator in \vec{F}_{2r}^{VB} :

$$\frac{1}{\Delta r} \int_{r_i}^{r_o} F_{2r}^{VB} dr = -\rho_1 B_b \Delta C \left[\left(\frac{\lambda_2}{\alpha_2} \right)^2 - \left(\frac{\lambda_1}{\alpha_1} \right)^2 \right] \csc^2 \beta \left(\frac{Q_m}{2\pi h} \right)^2 \frac{1}{\Delta r} \int_{r_i}^{r_o} \left(\frac{-1}{r^3} \right) dr$$

$$\overline{F_{2r}^{VB}} = -\rho_1 B_b \Delta C \left[\left(\frac{\lambda_2}{\alpha_2} \right)^2 - \left(\frac{\lambda_1}{\alpha_1} \right)^2 \right] \csc^2 \beta \left(\frac{Q_m}{2\pi h} \right)^2 \frac{1}{\Delta r} \left[\frac{1}{2} \left(\frac{r_i^2 - r_o^2}{r_i^2 r_o^2} \right) \right]$$

$$\overline{F_{2r}^{VB}} = -\rho_1 B_b \Delta C \text{Lambdas} \csc^2 \beta \left[\frac{-(r_o + r_i)/2}{r_i^2 r_o^2} \right] \left(\frac{Q_m}{2\pi h} \right)^2$$

$$\boxed{\overline{F_{2r}^{VB}} = -\rho_1 B_b \Delta C \text{Lambdas} \csc^2 \beta \left[\frac{-\bar{r}}{r_i^2 r_o^2} \right] \left(\frac{Q_m}{2\pi h} \right)^2}$$

Projecting \vec{F}_{2r}^{VB} in \hat{s} and in \hat{n} direction:

$$\begin{aligned} \vec{F}_{2s}^{VB} &= \vec{F}_{2r}^{VB} \sin \beta - \cancel{\vec{F}_{2\theta}^{VB}} \cos \beta = 0 \\ \vec{F}_{2n}^{VB} &= \vec{F}_{2r}^{VB} \cos \beta + \cancel{\vec{F}_{2\theta}^{VB}} \sin \beta = 0 \end{aligned} \quad (\text{C.85})$$

C.5.3 Centripetal and Coriolis Forces

From Eq. 4.24 and 4.26

$$A_f = A_{cor} + A_{ctp} = \left(-2\omega v_{k\theta} - \omega^2 r \right) \hat{r} + \left(2\omega v_{kr} \right) \hat{\theta}$$

The fictitious forces are:

$$\vec{F}_2^F = -m A_f = -\rho_2 B_b A_f \quad (\text{C.86})$$

In \hat{r} direction:

$$A_{fr} = -2\omega v_{k\theta} - \omega^2 r = -2\omega \left(-\frac{\lambda_2}{\alpha_2} \right) j_m(r) \cot \beta - \omega^2 r$$

$$\boxed{A_{fr} = 2\omega \frac{\lambda_2}{\alpha_2} \left(\frac{Q_m}{2\pi h} \right) \frac{1}{r} \cot \beta - \omega^2 r} \quad (\text{C.87})$$

Applying the mean operator:

$$\overline{A_{fr}} = \frac{1}{\Delta r} \int_{r_i}^{r_o} A_{fr} dr = 2\omega \frac{\lambda_2}{\alpha_2} \left(\frac{Q_m}{2\pi h} \right) \cot \beta \frac{1}{\Delta r} \int_{r_i}^{r_o} \frac{1}{r} dr - \omega^2 \frac{1}{\Delta r} \int_{r_i}^{r_o} r dr$$

$$\boxed{\overline{A_{fr}} = 2\omega \frac{\lambda_2}{\alpha_2} \cot \beta \left(\frac{Q_m}{2\pi h} \right) \frac{\ln(r_o/r_i)}{\Delta r} - \omega^2 \frac{(r_o^2 - r_i^2)}{2\Delta r}} \quad (\text{C.88})$$

In $\hat{\theta}$ direction:

$$A_{f\theta} = 2\omega v_{kr} = 2\omega \frac{\lambda_2}{\alpha_2} j_m(r)$$

$$\boxed{A_{f\theta} = 2\omega \frac{\lambda_2}{\alpha_2} \left(\frac{Q_m}{2\pi h} \right) \frac{1}{r}} \quad (\text{C.89})$$

Applying the mean operator:

$$\overline{A_{f\theta}} = \frac{1}{\Delta r} \int_{r_i}^{r_o} A_{f\theta} dr = 2\omega \frac{\lambda_2}{\alpha_2} \left(\frac{Q_m}{2\pi h} \right) \frac{1}{\Delta r} \int_{r_i}^{r_o} \frac{1}{r} dr$$

$$\boxed{\overline{A_{f\theta}} = 2\omega \frac{\lambda_2}{\alpha_2} \left(\frac{Q_m}{2\pi h} \right) \frac{\ln(r_o/r_i)}{\Delta r}} \quad (\text{C.90})$$

Projecting in \hat{s} and in \hat{n} direction:

$$\begin{aligned} \vec{F}_{2s}^F &= \vec{F}_{2r}^F \sin \beta - \vec{F}_{2\theta}^F \cos \beta \\ \vec{F}_{2n}^F &= \vec{F}_{2r}^F \cos \beta + \vec{F}_{2\theta}^F \sin \beta \end{aligned} \quad (\text{C.91})$$

C.5.4 Buoyancy Force

The buoyancy term was already considered in momentum equations. However, in order to use this term for a single bubble the buoyancy in \hat{r} and $\hat{\theta}$ are:

$$\begin{aligned} F_r^E &= -B_b \frac{\partial P}{\partial r} \\ F_\theta^E &= -B_b \frac{1}{r} \frac{\partial P}{\partial \theta} \end{aligned} \quad (\text{C.92})$$

Applying the mean operator:

$$\begin{aligned} \overline{F_r^E} &= -B_b \frac{1}{\Delta r} \int_{r_i}^{r_o} \frac{\partial P}{\partial r} dr = -B_b \frac{\Delta P_r}{\Delta r} \\ \overline{F_\theta^E} &= -B_b \frac{1}{\Delta r} \int_{r_i}^{r_o} \frac{1}{r} \frac{\partial P}{\partial \theta} dr = -B_b \frac{\ln(r_o/r_i)}{\Delta r} \Delta P_\theta \end{aligned} \quad (\text{C.93})$$

The pressure gradient is given by Eq. C.13:

$$\begin{aligned} -\frac{\partial p}{\partial r} &= \tilde{\rho}_m \left[\frac{(1 + \cot^2 \beta)}{4 \pi^2 h^2} \right] Q_m^2 \left(\frac{-1}{r^3} \right) + \overline{\rho}_m \left(\frac{\cot \beta}{\pi h} \right) \omega Q_m \left(\frac{1}{r} \right) - \rho_m \omega^2 r \\ &\quad - 4 \mu \frac{\lambda_k}{\alpha_k} \frac{Q_m}{2 \pi h} \frac{1}{r^3} - \frac{f}{4} \rho_m \left(\frac{Q_m}{2 \pi h} \right)^2 \frac{1}{\sin \beta} \left(\frac{1}{h r^2} + \frac{Z_b}{2 \pi r^3} \right) \end{aligned}$$

Applying the mean operator:

$$\begin{aligned} \frac{1}{\Delta r} \int_{r_i}^{r_o} -\frac{\partial p}{\partial r} dr &= \tilde{\rho}_m \left[\frac{(1 + \cot^2 \beta)}{4 \pi^2 h^2} \right] Q_m^2 \frac{1}{\Delta r} \int_{r_i}^{r_o} \left(\frac{-1}{r^3} \right) dr + \overline{\rho}_m \left(\frac{\cot \beta}{\pi h} \right) \omega Q_m \\ &\quad \frac{1}{\Delta r} \int_{r_i}^{r_o} \left(\frac{1}{r} \right) dr - \rho_m \omega^2 \frac{1}{\Delta r} \int_{r_i}^{r_o} r dr - 4 \mu \frac{\lambda_k}{\alpha_k} \frac{Q_m}{2 \pi h} \frac{1}{\Delta r} \int_{r_i}^{r_o} \frac{1}{r^3} dr \\ &\quad - \frac{f}{4} \rho_m \left(\frac{Q_m}{2 \pi h} \right)^2 \frac{1}{\sin \beta} \frac{1}{\Delta r} \int_{r_i}^{r_o} \left(\frac{1}{h r^2} + \frac{Z_b}{2 \pi r^3} \right) dr \end{aligned}$$

$$\begin{aligned}
-\frac{\Delta P}{\Delta r} &= \tilde{\rho}_m \left[\frac{(1 + \cot^2 \beta)}{4 \pi^2 h^2} \right] Q_m^2 \frac{1}{\Delta r} \left[\frac{1}{2} \frac{(r_i^2 - r_o^2)}{r_i^2 r_o^2} \right] + \bar{\rho}_m \left(\frac{\cot \beta}{\pi h} \right) \omega Q_m \frac{\ln(r_o/r_i)}{\Delta r} \\
&\quad - \rho_m \omega^2 \frac{(r_o^2 - r_i^2)}{2 \Delta r} - 4 \mu \frac{\lambda_k}{\alpha_k} \frac{Q_m}{2 \pi h} \frac{1}{\Delta r} \left(\frac{1}{2} \frac{-1}{r^2} \right) \Bigg|_{r_i}^{r_o} - \frac{f}{4} \frac{\rho_m}{\sin \beta} \left(\frac{Q_m}{2 \pi h} \right)^2 \frac{1}{\Delta r} \\
&\quad \left[\left(\frac{1}{h} \frac{-1}{r} \right) \Bigg|_{r_i}^{r_o} + \frac{Z_b}{2 \pi} \left(\frac{-1}{2 r^2} \right) \Bigg|_{r_i}^{r_o} \right] \\
-\frac{\Delta P}{\Delta r} &= \tilde{\rho}_m \left[\frac{(1 + \cot^2 \beta)}{4 \pi^2 h^2} \right] Q_m^2 \frac{1}{\Delta r} \left[\frac{1}{2} \frac{(r_i^2 - r_o^2)}{r_i^2 r_o^2} \right] + \bar{\rho}_m \left(\frac{\cot \beta}{\pi h} \right) \omega Q_m \frac{\ln(r_o/r_i)}{\Delta r} \\
&\quad - \rho_m \omega^2 \frac{(r_o^2 - r_i^2)}{2 \Delta r} - 4 \mu \frac{\lambda_k}{\alpha_k} \frac{Q_m}{2 \pi h} \frac{1}{2} \frac{1}{\Delta r} \left(\frac{1}{r_i^2} - \frac{1}{r_o^2} \right) - \frac{f}{4} \frac{\rho_m}{\sin \beta} \left(\frac{Q_m}{2 \pi h} \right)^2 \frac{1}{\Delta r} \\
&\quad \left[\frac{1}{h} \left(\frac{1}{r_i} - \frac{1}{r_o} \right) + \frac{Z_b}{4 \pi} \left(\frac{1}{r_i^2} - \frac{1}{r_o^2} \right) \right]
\end{aligned} \tag{C.94}$$

Substituting Eq. C.94 in the buoyancy force in \hat{r} direction and using Eq. 4.85:

$$\begin{aligned}
\overline{F_r^E} &= -B_b \left\{ \tilde{\rho}_m \left[\frac{(1 + \cot^2 \beta)}{4 \pi^2 h^2} \right] Q_m^2 \frac{1}{\Delta r} \left[\frac{1}{2} \frac{(r_i^2 - r_o^2)}{r_i^2 r_o^2} \right] + \bar{\rho}_m \left(\frac{\cot \beta}{\pi h} \right) \omega \frac{Q_m}{\Delta r} \ln \frac{r_o}{r_i} \right. \\
&\quad \left. - \rho_m \omega^2 \frac{(r_o^2 - r_i^2)}{2 \Delta r} - \mu \frac{\lambda_k}{\alpha_k} \frac{Q_m}{\pi h} \frac{1}{\Delta r} \left(\frac{r_o^2 - r_i^2}{r_i^2 r_o^2} \right) - \frac{f}{4} \frac{\rho_m}{\sin \beta} \left(\frac{Q_m}{2 \pi h} \right)^2 \frac{f_3}{\Delta r} \right\}
\end{aligned} \tag{C.95}$$

For $\hat{\theta}$ direction, the momentum equations in Eq. 4.80 for phases 1 and 2 are:

$$\begin{aligned}
\alpha_1 \rho_1 \left(v_{1r} \frac{\partial}{\partial r} v_{1\theta} - \frac{v_{1r} v_{1\theta}}{r} \right) &= -\alpha_1 \frac{1}{r} \frac{\partial p_1}{\partial \theta} - M_{1\theta} - \alpha_1 \rho_1 \vec{A}_{1\theta} + \nabla \cdot \vec{\tau} \\
\alpha_2 \rho_2 \left(v_{2r} \frac{\partial}{\partial r} v_{2\theta} - \frac{v_{2r} v_{2\theta}}{r} \right) &= -\alpha_2 \frac{1}{r} \frac{\partial p_2}{\partial \theta} - M_{2\theta} - \alpha_2 \rho_2 \vec{A}_{2\theta} + \nabla \cdot \vec{\tau}
\end{aligned}$$

The pressure gradient need to be estimated in $\hat{\theta}$ direction. So the momentum equation are summed in order to get the pressure term, once the momentum have the same

value but opposite direction, which means $M_{1\theta} = -M_{2\theta}$.

$$\alpha_1 \rho_1 \left(v_{1r} \frac{\partial}{\partial r} v_{1\theta} - \frac{v_{1r} v_{1\theta}}{r} \right) + \alpha_2 \rho_2 \left(v_{2r} \frac{\partial}{\partial r} v_{2\theta} - \frac{v_{2r} v_{2\theta}}{r} \right) = -(\alpha_1 + \alpha_2) \frac{1}{r} \frac{\partial p}{\partial \theta} - (\alpha_1 \rho_1 + \alpha_2 \rho_2) \vec{A}_{kf\theta} + \nabla \cdot \vec{\tau}$$

$$-\frac{1}{r} \frac{\partial p}{\partial \theta} = \alpha_1 \rho_1 \left(v_{1r} \frac{\partial}{\partial r} v_{1\theta} - \frac{v_{1r} v_{1\theta}}{r} \right) + \alpha_2 \rho_2 \left(v_{2r} \frac{\partial}{\partial r} v_{2\theta} - \frac{v_{2r} v_{2\theta}}{r} \right) + \rho_m \vec{A}_{kf\theta} - \nabla \cdot \vec{\tau} \quad (\text{C.96})$$

Substituting Eq. C.5 and C.6 in C.96:

$$-\frac{1}{r} \frac{\partial p}{\partial \theta} = \alpha_1 \rho_1 \left[- \left(\frac{\lambda_1}{\alpha_1} \right)^2 \cot \beta \left(\frac{\partial j_m(r)^2 / 2}{\partial r} \right) + \left(\frac{\lambda_1}{\alpha_1} \right)^2 \cot \beta \left(\frac{j_m(r)^2}{r} \right) \right] + \alpha_2 \rho_2 \left[- \left(\frac{\lambda_2}{\alpha_2} \right)^2 \cot \beta \left(\frac{\partial j_m(r)^2 / 2}{\partial r} \right) + \left(\frac{\lambda_2}{\alpha_2} \right)^2 \cot \beta \left(\frac{j_m(r)^2}{r} \right) \right] + \rho_m \vec{A}_{kf\theta} - \langle \nabla \cdot \vec{\tau} \rangle_\theta$$

$$-\frac{1}{r} \frac{\partial p}{\partial \theta} = \left[\alpha_1 \rho_1 \left(\frac{\lambda_1}{\alpha_1} \right)^2 \cot \beta + \alpha_2 \rho_2 \left(\frac{\lambda_2}{\alpha_2} \right)^2 \cot \beta \right] \left(\frac{j_m(r)^2}{r} - \frac{\partial j_m(r)^2 / 2}{\partial r} \right) + \rho_m \vec{A}_{kf\theta} - \langle \nabla \cdot \vec{\tau} \rangle_\theta$$

$$-\frac{1}{r} \frac{\partial p}{\partial \theta} = \left[\rho_1 \lambda_1 \left(\frac{\lambda_1}{\alpha_1} \right) \cot \beta + \rho_2 \lambda_2 \left(\frac{\lambda_2}{\alpha_2} \right) \cot \beta \right] \left(\frac{j_m(r)^2}{r} - \frac{2 j_m(r)}{2} \frac{\partial j_m(r)}{\partial r} \right) + \rho_m \vec{A}_{kf\theta} - \langle \nabla \cdot \vec{\tau} \rangle_\theta \quad (\text{C.97})$$

Substituting Eq. C.7:

$$-\frac{1}{r} \frac{\partial p}{\partial \theta} = \left[\rho_1 \lambda_1 \left(\frac{\lambda_1}{\alpha_1} \right) \cot \beta + \rho_2 \lambda_2 \left(\frac{\lambda_2}{\alpha_2} \right) \cot \beta \right] \left(\frac{2 j_m(r)^2}{r} \right) + \rho_m \vec{A}_{kf\theta} - \langle \nabla \cdot \vec{\tau} \rangle_\theta$$

$$-\frac{1}{r} \frac{\partial p}{\partial \theta} = \left[\rho_1 \frac{\lambda_1^2}{\alpha_1} \cot \beta + \rho_2 \frac{\lambda_2^2}{\alpha_2} \cot \beta \right] 2 \left(\frac{Q_m}{2\pi h} \right)^2 \frac{1}{r^3} + \rho_m \vec{A}_{kf\theta} - \langle \nabla \cdot \vec{\tau} \rangle_\theta \quad (\text{C.98})$$

The term $\vec{A}_{kf\theta}$ is:

$$\begin{aligned}
 \rho_m \vec{A}_{kf\theta} &= \alpha_1 \rho_1 A_{1f\theta} + \alpha_2 \rho_2 A_{2f\theta} = (S_{1\theta} + S_{2\theta}) \\
 &= 2 \alpha_1 \rho_1 \omega v_{1r} + 2 \alpha_2 \rho_2 \omega v_{2r} \\
 &= 2 \alpha_1 \rho_1 \omega \frac{\lambda_1}{\alpha_1} j_m(r) + 2 \alpha_2 \rho_2 \omega \frac{\lambda_2}{\alpha_2} j_m(r) \\
 &= 2 \rho_1 \omega \lambda_1 j_m(r) + 2 \rho_2 \omega \lambda_2 j_m(r) = 2 \omega j_m(r) (\rho_1 \lambda_1 + \rho_2 \lambda_2) \\
 &= 2 \omega j_m(r) \overline{\rho_m}
 \end{aligned}$$

$$\boxed{\rho_m \vec{A}_{kf\theta} = 2 \omega j_m(r) \overline{\rho_m}} \quad (\text{C.99})$$

Substituting Eq. C.99 in the pressure gradient:

$$-\frac{1}{r} \frac{\partial p}{\partial \theta} = \left[\rho_1 \frac{\lambda_1^2}{\alpha_1} \cot \beta + \rho_2 \frac{\lambda_2^2}{\alpha_2} \cot \beta \right] 2 \left(\frac{Q_m}{2\pi h} \right)^2 \frac{1}{r^3} + 2 \overline{\rho_m} \omega j_m(r) - \langle \nabla \cdot \vec{\tau} \rangle_\theta \quad (\text{C.100})$$

Substituting the volumetric flux of mixture in Eq. C.100:

$$-\frac{1}{r} \frac{\partial p}{\partial \theta} = \tilde{\rho}_m 2 \cot \beta \left(\frac{Q_m}{2\pi h} \right)^2 \left(\frac{1}{r^3} \right) + 2 \overline{\rho_m} \omega \left(\frac{Q_m}{2\pi h} \right) \left(\frac{1}{r} \right) - \langle \nabla \cdot \vec{\tau} \rangle_\theta \quad (\text{C.101})$$

Using Eq. C.27 and C.39 in order to substitute the term $\langle \nabla \cdot \vec{\tau} \rangle_\theta$:

$$\begin{aligned}
 -\frac{1}{r} \frac{\partial p}{\partial \theta} &= \tilde{\rho}_m 2 \cot \beta \left(\frac{Q_m}{2\pi h} \right)^2 \left(\frac{1}{r^3} \right) + 2 \overline{\rho_m} \omega \left(\frac{Q_m}{2\pi h} \right) \left(\frac{1}{r} \right) - 4 \mu \frac{\lambda_k}{\alpha_k} \frac{Q_m}{2\pi h} \frac{1}{r^3} \cot \beta \\
 &\quad - \frac{f}{4} \rho_m \left(\frac{Q_m}{2\pi h} \right)^2 \frac{1}{\sin \beta} \left(\frac{1}{h r^2} + \frac{Z_b}{2\pi r^3} \right) (-\cot \beta)
 \end{aligned}$$

Applying the mean operator:

$$\begin{aligned} \frac{1}{\Delta r} \int_{r_i}^{r_o} -\frac{1}{r} \frac{\partial p}{\partial \theta} dr &= \tilde{\rho}_m 2 \cot \beta \left(\frac{Q_m}{2\pi h} \right)^2 \frac{1}{\Delta r} \int_{r_i}^{r_o} \left(\frac{1}{r^3} \right) dr - 2\bar{\rho}_m \omega \left(\frac{Q_m}{2\pi h} \right) \frac{1}{\Delta r} \\ &\int_{r_i}^{r_o} \left(\frac{1}{r} \right) dr - 4\mu \frac{\lambda_k}{\alpha_k} \frac{Q_m}{2\pi h} \frac{\cot \beta}{\Delta r} \int_{r_i}^{r_o} \frac{1}{r^3} dr - \frac{f}{4} \rho_m \left(\frac{Q_m}{2\pi h} \right)^2 \frac{1}{\sin \beta} \frac{(-\cot \beta)}{\Delta r} \\ &\int_{r_i}^{r_o} \left(\frac{1}{h r^2} + \frac{Z_b}{2\pi r^3} \right) dr \end{aligned}$$

$$\begin{aligned} \frac{\ln(r_o/r_i)}{\Delta r} \Delta P_\theta &= \tilde{\rho}_m 2 \cot \beta \left(\frac{Q_m}{2\pi h} \right)^2 \frac{1}{\Delta r} \left[\frac{-1}{2} \left(\frac{r_i^2 - r_o^2}{r_i^2 r_o^2} \right) \right] + 2\bar{\rho}_m \omega \left(\frac{Q_m}{2\pi h} \right) \frac{\ln(r_o/r_i)}{\Delta r} \\ &- \mu \frac{\lambda_k}{\alpha_k} \frac{Q_m}{\pi h} \frac{\cot \beta}{\Delta r} \left(\frac{r_o^2 - r_i^2}{r_i^2 r_o^2} \right) + \frac{f}{4} \rho_m \frac{\cot \beta}{\sin \beta} \left(\frac{Q_m}{2\pi h} \right)^2 \frac{f_3}{\Delta r} \end{aligned} \quad (\text{C.102})$$

Substituting Eq. C.102 in C.93:

$$\begin{aligned} \overline{F_\theta^E} &= -B_b \left\{ \tilde{\rho}_m 2 \cot \beta \left(\frac{Q_m}{2\pi h} \right)^2 \left[\left(\frac{\bar{r}}{r_i^2 r_o^2} \right) \right] + 2\bar{\rho}_m \omega \left(\frac{Q_m}{2\pi h} \right) \frac{\ln(r_o/r_i)}{\Delta r} \right. \\ &\left. - 2\mu \frac{\lambda_k}{\alpha_k} \frac{Q_m}{\pi h} \cot \beta \left(\frac{\bar{r}}{r_i^2 r_o^2} \right) + \frac{f}{4} \rho_m \frac{\cot \beta}{\sin \beta} \left(\frac{Q_m}{2\pi h} \right)^2 \frac{f_3}{\Delta r} \right\} \end{aligned} \quad (\text{C.103})$$

Projecting buoyancy forces in blade coordinate system:

$$\begin{aligned} \vec{F}_{2s}^E &= \vec{F}_{2r}^E \sin \beta - \vec{F}_{2\theta}^E \cos \beta \\ \vec{F}_{2n}^E &= \vec{F}_{2r}^E \cos \beta + \vec{F}_{2\theta}^E \sin \beta \end{aligned} \quad (\text{C.104})$$

C.6 Development of Transition Criteria

The next sections describes the two conditions of the Transition Criteria. These conditions were explained in chapter 4, section 5.4.1.

C.6.1 Condition 1

$$\overline{\vec{F}}_{2s}^D + \overline{\vec{F}}_{2s}^{VB} + \overline{\vec{F}}_{2s}^E + \overline{\vec{F}}_{2s}^F + \overline{\vec{F}}_{2n}^{VB} + \overline{\vec{F}}_{2n}^E + \overline{\vec{F}}_{2n}^F = 0$$

$$\begin{aligned} \overline{\vec{F}}_{2s}^D + \overline{\vec{F}}_{2r}^{VB} \sin \beta + \left[\overline{\vec{F}}_{2r}^E \sin \beta - \overline{\vec{F}}_{2\theta}^E \cos \beta \right] + \left[\overline{\vec{F}}_{2r}^F \sin \beta - \overline{\vec{F}}_{2\theta}^F \cos \beta \right] + \overline{\vec{F}}_{2r}^{VB} \cos \beta \\ + \left[\overline{\vec{F}}_{2r}^E \cos \beta + \overline{\vec{F}}_{2\theta}^E \sin \beta \right] + \left[\overline{\vec{F}}_{2r}^F \cos \beta + \overline{\vec{F}}_{2\theta}^F \sin \beta \right] = 0 \end{aligned}$$

$$\begin{aligned} \overline{\vec{F}}_{2s}^D + \overline{\vec{F}}_{2r}^{VB} (\sin \beta + \cos \beta) + \overline{\vec{F}}_{2r}^F (\sin \beta + \cos \beta) - \overline{\vec{F}}_{2\theta}^F (\cos \beta - \sin \beta) \\ - \overline{\vec{F}}_{2\theta}^E (\cos \beta - \sin \beta) = -\overline{\vec{F}}_{2r}^E (\sin \beta + \cos \beta) \\ - \overline{\vec{F}}_{2r}^E = \frac{\overline{\vec{F}}_{2s}^D}{\sin \beta + \cos \beta} + \overline{\vec{F}}_{2r}^{VB} + \overline{\vec{F}}_{2r}^F - \overline{\vec{F}}_{2\theta}^F \frac{\cos \beta - \sin \beta}{\sin \beta + \cos \beta} - \overline{\vec{F}}_{2\theta}^E \frac{\cos \beta - \sin \beta}{\sin \beta + \cos \beta} \end{aligned} \quad (\text{C.105})$$

Where:

$$G_5 = \frac{\cos \beta - \sin \beta}{\sin \beta + \cos \beta} \quad (\text{C.106})$$

Substituting Eq. C.106 in C.105:

$$-\overline{\vec{F}}_{2r}^E = \frac{\overline{\vec{F}}_{2s}^D}{\sin \beta + \cos \beta} + \overline{\vec{F}}_{2r}^{VB} + \overline{\vec{F}}_{2r}^F - \overline{\vec{F}}_{2\theta}^F G_5 - \overline{\vec{F}}_{2\theta}^E G_5 \quad (\text{C.107})$$

Substituting the forces:

$$\begin{aligned} B_b \frac{\Delta P_r}{\Delta r} = \frac{1}{2} \frac{A_p C_D \rho_1 \overline{v}_{s,s}^2}{(\sin \beta + \cos \beta)} - \rho_1 B_b \Delta C \text{ Lambdas } \csc^2 \beta \left(\frac{Q_m}{2\pi h} \right)^2 \left(\frac{-\bar{r}}{r_i^2 r_o^2} \right) \\ - \rho_2 B_b \left[2\omega \frac{\lambda_2}{\alpha_2} \cot \beta \left(\frac{Q_m}{2\pi h} \right) \frac{\ln(r_o/r_i)}{\Delta r} - \omega^2 r \right] + \rho_2 B_b \left[2\omega \frac{\lambda_2}{\alpha_2} \left(\frac{Q_m}{2\pi h} \right) \frac{\ln(r_o/r_i)}{\Delta r} \right] G_5 \\ - B_b \left[\widetilde{\rho}_m \cot \beta 2 \left(\frac{Q_m}{2\pi h} \right)^2 \left(\frac{\bar{r}}{r_i^2 r_o^2} \right) + \overline{\rho}_m 2\omega \left(\frac{Q_m}{2\pi h} \right) \frac{\ln(r_o/r_i)}{\Delta r} - 2\mu \frac{\lambda_k}{\alpha_k} \frac{Q_m}{\pi h} \right. \\ \left. \cot \beta \left(\frac{\bar{r}}{r_i^2 r_o^2} \right) + \frac{f}{4} \rho_m \frac{\cot \beta}{\sin \beta} \left(\frac{Q_m}{2\pi h} \right)^2 \frac{f_3}{\Delta r} \right] G_5 \end{aligned}$$

$$\begin{aligned}
\Delta P_r &= \frac{1}{2} \frac{A_p}{B_b} \frac{C_D \rho_1 \bar{v}_{s,s}^2 \Delta r}{(\sin \beta + \cos \beta)} - \rho_1 \Delta C \text{Lambdas} \csc^2 \beta \left(\frac{Q_m}{2\pi h} \right)^2 \left(\frac{-\bar{r} \Delta r}{r_i^2 r_o^2} \right) \\
&- 2\omega \rho_2 \frac{\lambda_2}{\alpha_2} \cot \beta \left(\frac{Q_m}{2\pi h} \right) \ln(r_o/r_i) + \omega^2 r \Delta r \rho_2 + 2\omega \rho_2 \frac{\lambda_2}{\alpha_2} \left(\frac{Q_m}{2\pi h} \right) \ln(r_o/r_i) G_5 \\
&- \widetilde{\rho}_m \cot \beta 2 \left(\frac{Q_m}{2\pi h} \right)^2 G_5 \left(\frac{\bar{r} \Delta r}{r_i^2 r_o^2} \right) - \overline{\rho}_m 2\omega \left(\frac{Q_m}{2\pi h} \right) \ln(r_o/r_i) G_5 \\
&- 2\mu \frac{\lambda_k}{\alpha_k} \frac{Q_m}{\pi h} \cot \beta \left(\frac{\bar{r} \Delta r}{r_i^2 r_o^2} \right) G_5 + \frac{f}{4} \rho_m \frac{\cot \beta}{\sin \beta} G_5 \left(\frac{Q_m}{2\pi h} \right)^2 f_3
\end{aligned} \tag{C.108}$$

Where:

$$\circ \quad \frac{\bar{r} \Delta r}{r_i^2 r_o^2} = \frac{-(r_o + r_i)(r_o - r_i)/2}{r_i^2 r_o^2} = \frac{(-r_o^2 - r_i^2)/2}{r_i^2 r_o^2} = -\frac{1}{2} \frac{1}{r_o^2} \left[\left(\frac{r_o}{r_i} \right)^2 - 1 \right]$$

Dividing Eq. C.108 by $\overline{\rho}_m \omega^2 r_o^2$:

$$\begin{aligned}
\frac{\Delta P_r}{\overline{\rho}_m \omega^2 r_o^2} &= \frac{1}{2} \frac{A_p}{B_b} \frac{C_D \Delta r}{(\sin \beta + \cos \beta)} \left[\frac{\rho_1 \bar{v}_{s,s}^2}{\Delta \rho \omega^2 r_o^2} \right] \frac{\Delta \rho}{\overline{\rho}_m} - \frac{\rho_1}{\overline{\rho}_m} \Delta C \text{Lambdas} \frac{\csc^2 \beta}{4\pi^2} \\
&\left(\frac{Q_m^2}{\omega^2 r_o^6} \right) \left(\frac{r_o}{h} \right)^2 \left\{ \frac{1}{2} \left[\left(\frac{r_o}{r_i} \right)^2 - 1 \right] \right\} - \frac{\rho_2}{\overline{\rho}_m} \frac{\lambda_2}{\alpha_2} \frac{\cot \beta}{\pi} \left(\frac{Q_m}{\omega r_o^3} \right) \left(\frac{r_o}{h} \right) \ln(r_o/r_i) + \frac{\rho_2}{\overline{\rho}_m} \\
&\frac{\bar{r} \Delta r}{r_o^2} + \frac{\rho_2}{\overline{\rho}_m} \frac{\lambda_2}{\alpha_2} \left(\frac{Q_m}{\omega r_o^3} \right) \left(\frac{r_o}{h} \right) \frac{\ln(r_o/r_i)}{\pi} G_5 - \frac{\widetilde{\rho}_m \cot \beta}{\overline{\rho}_m} \frac{2}{4\pi^2} \left(\frac{Q_m^2}{\omega^2 r_o^6} \right)^2 \left(\frac{r_o}{h} \right)^2 G_5 \\
&\left\{ -\frac{1}{2} \left[\left(\frac{r_o}{r_i} \right)^2 - 1 \right] \right\} - \frac{r_o}{h} \left(\frac{Q_m}{\omega r_o^3} \right) \frac{\ln(r_o/r_i)}{\pi} G_5 - 2 \frac{\mu}{\overline{\rho}_m} \frac{\lambda_k}{\alpha_k} \left(\frac{Q_m}{\omega r_o^3} \right) \frac{\cot \beta}{(\omega \pi h)} \\
&\left\{ -\frac{1}{2} \frac{1}{r_o} \left[\left(\frac{r_o}{r_i} \right)^2 - 1 \right] \right\} G_5 + \frac{f}{4} \frac{\rho_m}{\overline{\rho}_m} \frac{\cot \beta}{\sin \beta} G_5 \left(\frac{Q_m^2}{\omega^2 r_o^6} \right) \frac{r_o^4}{4\pi^2 h^2} f_3
\end{aligned}$$

$$\begin{aligned}
C_H = & \frac{1}{2} \frac{A_p}{B_b} \frac{C_D \Delta r}{(\sin \beta + \cos \beta)} \frac{\Delta \rho}{\rho_m} F r_{TP,s}^2 + \frac{\rho_1}{\rho_m} \Delta C \text{Lambdas} G_1 C_Q^2 - \frac{\rho_2}{\rho_m} \frac{\lambda_2}{\alpha_2} \cot \beta \\
& \left(\frac{r_o}{h} \right) \frac{\ln(r_o/r_i)}{\pi} C_Q + \frac{\rho_2}{\rho_m} \left(\frac{r_o^2 - r_i^2}{2 r_o^2} \right) + \frac{\rho_2}{\rho_m} \frac{\lambda_2}{\alpha_2} \left(\frac{r_o}{h} \right) \frac{\ln(r_o/r_i)}{\pi} G_5 C_Q + \frac{\widetilde{\rho_m} \cot \beta}{\rho_m 4\pi^2} \\
& \left(\frac{r_o}{h} \right)^2 \left[\left(\frac{r_o}{r_i} \right)^2 - 1 \right] G_5 C_Q^2 - \left(\frac{r_o}{h} \right) \frac{\ln(r_o/r_i)}{\pi} G_5 C_Q + \frac{\mu}{\rho_m} \frac{\lambda_k}{\alpha_k} \frac{\cot \beta}{(\omega \pi h)} \\
& \frac{1}{r_o} \left[\left(\frac{r_o}{r_i} \right)^2 - 1 \right] G_5 C_Q + \frac{f}{4} \frac{\rho_m}{\rho_m} \frac{\cot \beta}{\sin \beta} G_5 \left(\frac{r_o^4}{4 \pi^2 h^2} \right) f_3 C_Q^2
\end{aligned} \tag{C.109}$$

Coupling the terms:

$$\begin{aligned}
C_H = & \left\{ \frac{\rho_1}{\rho_m} \Delta C \text{Lambdas} G_1 + \frac{\widetilde{\rho_m} \cot \beta}{\rho_m 4\pi^2} \left(\frac{r_o}{h} \right)^2 \left[\left(\frac{r_o}{r_i} \right)^2 - 1 \right] G_5 + \frac{f}{4} \frac{\rho_m}{\rho_m} \frac{\cot \beta}{\sin \beta} G_5 \right. \\
& \left. \left(\frac{r_o^4}{4 \pi^2 h^2} \right) f_3 \right\} C_Q^2 + \left\{ \frac{\rho_2}{\rho_m} \frac{\lambda_2}{\alpha_2} \left(\frac{r_o}{h} \right) \frac{\ln(r_o/r_i)}{\pi} G_5 - \frac{\rho_2}{\rho_m} \frac{\lambda_2}{\alpha_2} \cot \beta \left(\frac{r_o}{h} \right) \frac{\ln(r_o/r_i)}{\pi} \right. \\
& \left. - \left(\frac{r_o}{h} \right) \frac{\ln(r_o/r_i)}{\pi} G_5 + \frac{\mu}{\rho_m} \frac{\lambda_k}{\alpha_k} \frac{\cot \beta}{(\omega \pi h)} \frac{1}{r_o} \left[\left(\frac{r_o}{r_i} \right)^2 - 1 \right] G_5 \right\} C_Q + \frac{1}{2} \left(\frac{A_p}{B_b} \right) \\
& \frac{C_D \Delta r}{(\sin \beta + \cos \beta)} \frac{\Delta \rho}{\rho_m} F r_{TP,s}^2 + \frac{\rho_2}{\rho_m} \frac{1}{2} \left[1 - \left(\frac{r_i}{r_o} \right)^2 \right]
\end{aligned} \tag{C.110}$$

$$\boxed{C_H = D_1 C_Q^2 + D_2 C_Q + \left(D_3 F r_{TP,s}^2 + D_4 \right)} \tag{C.111}$$

where $D'_{k,k=\{1,2,3,4\}} = f(\lambda, C_D, \Delta C)$

$$\begin{aligned}
\circ D_1 &= \frac{\rho_1}{\rho_m} \Delta C \text{Lambdas} G_1 + \frac{\widetilde{\rho}_m \cot \beta}{\rho_m 4\pi^2} \left(\frac{r_o}{h}\right)^2 \left[\left(\frac{r_o}{r_i}\right)^2 - 1\right] G_5 \\
&\quad + \frac{f}{4} \frac{\rho_m \cot \beta}{\rho_m \sin \beta} G_5 \left(\frac{r_o^4}{4\pi^2 h^2}\right) f_3 \\
\circ D_2 &= \frac{\rho_2}{\rho_m} \frac{\lambda_2}{\alpha_2} \left(\frac{r_o}{h}\right) \frac{\ln(r_o/r_i)}{\pi} G_5 - \frac{\rho_2}{\rho_m} \frac{\lambda_2}{\alpha_2} \cot \beta \left(\frac{r_o}{h}\right) \frac{\ln(r_o/r_i)}{\pi} \\
&\quad - \left(\frac{r_o}{h}\right) \frac{\ln(r_o/r_i)}{\pi} G_5 + \frac{\mu}{\rho_m} \frac{\lambda_k}{\alpha_k} \frac{\cot \beta}{(\omega \pi h)} \frac{1}{r_o} \left[\left(\frac{r_o}{r_i}\right)^2 - 1\right] G_5 \\
\circ D_3 &= \frac{1}{2} \left(\frac{A_p}{B_b}\right) \frac{C_D \Delta r}{(\sin \beta + \cos \beta)} \frac{\Delta \rho}{\rho_m} \\
\circ D_4 &= \frac{\rho_2}{\rho_m} \frac{1}{2} \left[1 - \left(\frac{r_i}{r_o}\right)^2\right]
\end{aligned} \tag{C.112}$$

C.6.2 Condition 2

$$\overrightarrow{F}_{2s}^D + \overrightarrow{F}_{2s}^{VB} + \overrightarrow{F}_{2s}^E + \overrightarrow{F}_{2s}^F - \overrightarrow{F}_{2n}^{VB} - \overrightarrow{F}_{2n}^E - \overrightarrow{F}_{2n}^F = 0$$

$$\begin{aligned}
\overrightarrow{F}_{2s}^D + \overrightarrow{F}_{2r}^{VB} \sin \beta + \left[\overrightarrow{F}_{2r}^E \sin \beta - \overrightarrow{F}_{2\theta}^E \cos \beta\right] + \left[\overrightarrow{F}_{2r}^F \sin \beta - \overrightarrow{F}_{2\theta}^F \cos \beta\right] - \overrightarrow{F}_{2r}^{VB} \cos \beta \\
- \left[\overrightarrow{F}_{2r}^E \cos \beta + \overrightarrow{F}_{2\theta}^E \sin \beta\right] - \left[\overrightarrow{F}_{2r}^F \cos \beta + \overrightarrow{F}_{2\theta}^F \sin \beta\right] = 0
\end{aligned}$$

$$\begin{aligned}
\overrightarrow{F}_{2s}^D + \overrightarrow{F}_{2r}^{VB} (\sin \beta - \cos \beta) + \overrightarrow{F}_{2r}^F (\sin \beta - \cos \beta) - \overrightarrow{F}_{2\theta}^F (\cos \beta + \sin \beta) \\
- \overrightarrow{F}_{2\theta}^E (\cos \beta + \sin \beta) = -\overrightarrow{F}_{2r}^E (\sin \beta - \cos \beta)
\end{aligned}$$

$$-\overrightarrow{F}_{2r}^E = \frac{\overrightarrow{F}_{2s}^D}{\sin \beta - \cos \beta} + \overrightarrow{F}_{2r}^{VB} + \overrightarrow{F}_{2r}^F - \overrightarrow{F}_{2\theta}^F \frac{\cos \beta + \sin \beta}{\sin \beta - \cos \beta} - \overrightarrow{F}_{2\theta}^E \frac{\cos \beta + \sin \beta}{\sin \beta - \cos \beta} \tag{C.113}$$

Where:

$$G_6 = \frac{\cos \beta + \sin \beta}{\sin \beta - \cos \beta} \tag{C.114}$$

Substituting Eq. C.113 in C.114:

$$-\overline{\vec{F}}_{2r}^E = \frac{\overline{\vec{F}}_{2s}^D}{\sin \beta - \cos \beta} + \overline{\vec{F}}_{2r}^{VB} + \overline{\vec{F}}_{2r}^F - \overline{\vec{F}}_{2\theta}^F G_6 - \overline{\vec{F}}_{2\theta}^E G_6 \quad (\text{C.115})$$

Eq. C.107 and C.115 are almost the same with exception of the terms G_5 , G_6 and the drag force which has his dividend been $(\sin \beta - \cos \beta)$. So, the final expression is:

$$\begin{aligned} C_H = & \left\{ \frac{\rho_1}{\rho_m} \Delta C \text{Lambdas} G_1 + \frac{\widetilde{\rho}_m \cot \beta}{\rho_m 4\pi^2} \left(\frac{r_o}{h} \right)^2 \left[\left(\frac{r_o}{r_i} \right)^2 - 1 \right] G_6 + \frac{f \rho_m \cot \beta}{4 \rho_m \sin \beta} G_6 \right. \\ & \left. \left(\frac{r_o^4}{4 \pi^2 h^2} \right) f_3 \right\} C_Q^2 + \left\{ \frac{\rho_2 \lambda_2}{\rho_m \alpha_2} \left(\frac{r_o}{h} \right) \frac{\ln(r_o/r_i)}{\pi} G_6 - \frac{\rho_2 \lambda_2}{\rho_m \alpha_2} \cot \beta \left(\frac{r_o}{h} \right) \frac{\ln(r_o/r_i)}{\pi} \right. \\ & \left. - \left(\frac{r_o}{h} \right) \frac{\ln(r_o/r_i)}{\pi} G_6 + \frac{\mu \lambda_k}{\rho_m \alpha_k} \frac{\cot \beta}{(\omega \pi h) r_o} \left[\left(\frac{r_o}{r_i} \right)^2 - 1 \right] G_6 \right\} C_Q + \frac{1}{2} \left(\frac{A_p}{B_b} \right) \\ & \frac{C_D \Delta r}{(\sin \beta + \cos \beta)} \frac{\Delta \rho}{\rho_m} F r_{TP,s}^2 + \frac{\rho_2}{\rho_m} \frac{1}{2} \left[1 - \left(\frac{r_i}{r_o} \right)^2 \right] \end{aligned} \quad (\text{C.116})$$

$$\boxed{C_H = E_1 C_Q^2 + E_2 C_Q + (E_3 F r_{TP,s}^2 + D_4)} \quad (\text{C.117})$$

where $E'_{k,k=\{1,2,3\}} = f(\lambda, C_D, \Delta C)$

$$\begin{aligned} \circ E_1 &= \frac{\rho_1}{\rho_m} \Delta C \text{Lambdas} G_1 + \frac{\widetilde{\rho}_m \cot \beta}{\rho_m 4\pi^2} \left(\frac{r_o}{h} \right)^2 \left[\left(\frac{r_o}{r_i} \right)^2 - 1 \right] G_6 \\ &+ \frac{f \rho_m \cot \beta}{4 \rho_m \sin \beta} G_6 \left(\frac{r_o^4}{4 \pi^2 h^2} \right) f_3 \\ \circ E_2 &= \frac{\rho_2 \lambda_2}{\rho_m \alpha_2} \left(\frac{r_o}{h} \right) \frac{\ln(r_o/r_i)}{\pi} G_6 - \frac{\rho_2 \lambda_2}{\rho_m \alpha_2} \cot \beta \left(\frac{r_o}{h} \right) \frac{\ln(r_o/r_i)}{\pi} \\ &- \left(\frac{r_o}{h} \right) \frac{\ln(r_o/r_i)}{\pi} G_6 + \frac{\mu \lambda_k}{\rho_m \alpha_k} \frac{\cot \beta}{(\omega \pi h) r_o} \left[\left(\frac{r_o}{r_i} \right)^2 - 1 \right] G_6 \\ \circ E_3 &= \frac{1}{2} \left(\frac{A_p}{B_b} \right) \frac{C_D \Delta r}{(\sin \beta - \cos \beta)} \frac{\Delta \rho}{\rho_m} \end{aligned} \quad (\text{C.118})$$

- Geometric coefficients:

- Geometric constant 5: $\frac{\cos \beta - \sin \beta}{\sin \beta + \cos \beta} \rightarrow = -0.031$

- Geometric constant 6: $\frac{\cos \beta + \sin \beta}{\sin \beta - \cos \beta} \rightarrow = 31.82$

APPENDIX D – Dimensionless Groups and Diffuser Pressure Gradient Analysis

D.1 Dimensionless Groups

In this section the most used dimensionless variables during the development of this work are explained.

- Eötvös number: It measures the relation between gravitational forces and surface tension forces. It is correlated to bubbles and fluids interface shape.

$$Eo = \frac{g(\rho_1 - \rho_2)D_b^2}{\sigma_{21}} \quad (D.1)$$

where σ is the interfacial or surface tension.

- Morton number: It is used together with the Eötvös number to characterized the shape of bubbles. However, it does not use bubble diameter as one of the variables.

$$M = g \mu_1^4 \Delta\rho / \rho_1^2 \sigma_{21}^3 \quad (D.2)$$

- Strouhal number: It describes oscillating flow mechanisms.

$$Sr = \frac{1}{2\pi f \tau_{diff,B}} = \frac{\rho_2}{8\pi\rho_1} \frac{1}{St} \quad \text{where:} \quad \tau_{diff,B} = \frac{\rho_1 d_B^2}{18\mu_1} \quad (D.3)$$

- Reynolds number: This number is defined as the ratio between inertia and viscous forces. This number is used to measure the turbulence of the flow.

$$Re_\omega = \frac{\rho_f L_\infty^2}{t_\infty \mu_\infty} \quad (D.4)$$

- Froude number: It is defined as the ratio between inertial and field forces (such as gravitational and/or rotational), being important in segregated flow.

$$Fr = \frac{L_\infty}{t_\infty^2 |g|} \quad (D.5)$$

D.1.1 Scaling

The choice of reference variables is arbitrary. For this problem, the length scale chose is the radius of the particle in the cases where the flow of the particle is important. In the case of the Reynolds number associated with the flow rate the variable for length scale chosen is the hydraulic diameter or the pump diameter/radius. Also, the time scale might be the rotational speed or th time itself.

$$L_\infty = r_p \quad ;or \quad t_\infty = \omega^{-1} \text{ or } t_\infty \quad (\text{D.6})$$

The dimensionless groups become:

- Reynolds number:

$$Re_\omega = \frac{\rho_f \omega r_p^2}{\mu_f} \quad (\text{D.7})$$

This Reynolds number Re_ω is related to the rotation of the pump and it is usually used for single-phase flow. The Reynolds number can be related to the mixture which is known as two-phase mixture Reynolds:

$$Re = \frac{\rho_k v_k L_\infty}{\mu_k} \quad \rightarrow \quad Re = \frac{\rho_m \dot{j}_{ms} D_H}{\mu_m} \quad (\text{D.8})$$

The subscript k is related to the phase. In this work, the hydraulic diameter D_H is used as characteristic length. The literature indicates that the Reynolds number written from mixture properties is more representative, for example, the calculus of pressure gradient might be a function of the friction factor, which is a function of mixture Reynolds number (SHOHAM, 2005 , WALLIS, 1969). The particle Reynolds number is given in function of relative velocity:

$$Re_P = \frac{\rho_1 d_b |v_s|}{\mu_1} \quad (\text{D.9})$$

Table D.1 shows the three Reynolds number calculated for the two-phase flow experiments.

Table D.1: Impeller rotation ω , mass gas flow rate \dot{m} , rotational Reynolds Re_ω , two-phase mixture Reynolds Re , particle Reynolds Re_P

	ω [rpm]	\dot{m} [kg/h]	Re_ω [-]10 ⁸	Re [-]10 ⁴	Re_P [-]10 ³
1	600	0.025	1.191	0.984	0.652
2	600	0.025	1.352	0.862	0.840
3	600	0.025	1.642	0.763	1.099
4	600	0.025	1.766	0.643	1.261
5	900	0.025	0.337	1.568	0.339
6	900	0.025	0.460	1.338	0.563
7	900	0.025	0.938	1.122	0.992
8	900	0.025	1.351	0.914	1.378
9	900	0.012	0.337	1.558	0.343
10	900	0.012	0.460	1.351	0.592
11	900	0.012	0.938	1.096	1.055
12	900	0.012	1.351	0.920	1.367
13	1200	0.025	0.210	2.123	0.306
14	1200	0.025	0.253	1.928	0.450
15	1200	0.025	0.406	1.636	0.727
16	1200	0.025	0.562	1.260	0.990

The table shows that a turbulent behavior is expected in every case analyzed.

- Froude number: As done with Reynolds numbers, the hydraulic diameter and mixture properties are used. This number was written for the mixture and was used as a coordinate in the flow pattern map of Beggs and Brill's model (SHOHAM, 2005 ; WALLIS, 1969).

$$Fr = \frac{v_k^2}{|g| L_\infty} \quad (\text{D.10})$$

The Reynolds and Froude numbers are the most important to describe properly the flow because they are connected to the turbulence and fluid segregation. The Froude number can be related to the mixture velocity in the context of the Boussinesq approximation. In the present work, the two-phase Froude number $Fr_{TP,s}$ and mixture Froude number Fr_m are used, which are:

$$Fr_{TP,s}^2 = \frac{\rho_1 \overline{v_{s,s}}^2}{\Delta\rho \omega^2 r_o^2}$$

$$Fr_m = \sqrt{\frac{\rho_1}{\Delta\rho} \left(\frac{Q_m}{2\pi r_o h} \right)} / \omega r_o$$

The two-phase Froude number $Fr_{TP,s}$ is related with slip velocity $v_{s,s}$ and the mixture Froude number Fr_m with the mixture velocity $j_m(r)$.

D.2 Diffuser Pressure Gradient

When the rotational speed is equal to zero, the pressure term in Eq. C.13 can be used for the diffuser which is:

$$\boxed{-\frac{\partial p}{\partial r} = \tilde{\rho}_m \left[\frac{(1 + \cot^2 \beta)}{4\pi^2 h^2} \right] Q_m^2 \left(\frac{-1}{r^3} \right) + \nabla \cdot \vec{\tau}} \quad (\text{D.11})$$

Table D.2 shows the increment of pressure for pump, diffuser, and impeller. Comparing the values, it can be observed that the increment pressure in the diffuser is much smaller than the ones in the impeller. This fact is in agreement of the findings explained by Amaral (2007) found in his experiments.

The equation of Navier-Stokes was applied directly in the impeller, so it was necessary to do the pressure correction.

Table D.2: Pressure increment

IM	ω	\dot{m}	ΔP_{pump}	ΔP_{dif}	ΔP_{imp}
1	600	0.025	1007	86	921
2	600	0.025	2280	66	2215
3	600	0.025	3006	52	2954
4	600	0.025	3886	36	3850
5	900	0.025	541	221	320
6	900	0.025	4579	160	4419
7	900	0.025	7260	112	7148
8	900	0.025	9318	74	9244
9	900	0.012	418	217	201
10	900	0.012	4168	163	4005
11	900	0.012	8078	107	7971
12	900	0.012	9025	75	8950
13	1200	0.025	262	405	-143
14	1200	0.025	5246	334	4912
15	1200	0.025	11341	240	11101
16	1200	0.025	16589	142	16447

APPENDIX E – Friction Factor Comparison

This appendix shows the procedure to calculate the friction factor in a centrifugal pump realized by S.Vieira (2014), which adopted procedures from the literature. The flow through an impeller happens basically in a duct of rectangular section, curvilinear and under rotation. Thus, it is necessary to apply corrections for the impeller friction factor. The hydraulic diameter needs to be defined referring to the cross-section of the impeller channel, which is approximately the shape of a rectangle with an average width of a and an average height of b . Figure E.1 shows the shape of the rectangle in the impeller channel.

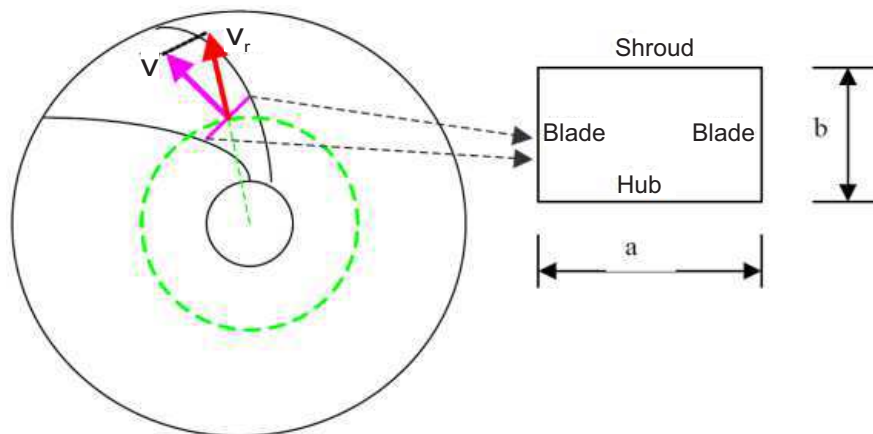


Figure E.1: Rectangle shape of the impeller channel.

Equation E.1 shows the relationship that defines the average width of the impeller channel:

$$a = \frac{2\pi r}{N_a} \sin \beta \quad (\text{E.1})$$

where r is the average radius, N_a is the number of blades and β is the angle between the relative velocity and the tangential direction, measured in the opposite direction to the impeller rotation. The hydraulic diameter is given by Eq.E.2 :

$$D_H = \frac{2ab}{a+b} \quad (\text{E.2})$$

E.1 Reynolds number

The friction factor is related to the type of flow regime that is occurring in the impeller channel, if it is laminar or turbulent. This determination depends on the Reynolds number Re , which is related to the relative velocity v along the impeller channel.

$$Re = \frac{\rho v D_H}{\mu} \quad (\text{E.3})$$

where ρ is the density, μ is the viscosity and D_H is the hydraulic diameter.

E.2 Friction factor for circular, straight and stationary tubes

The friction factor correlation used in this study was given by CHURCHILL, 1977, for turbulent flow:

$$f = 8 \left\{ 2.457 \ln \left[1 / \left(\left(\frac{7}{Re} \right)^{0.9} + 0.27 \left(\frac{\epsilon}{D_H} \right) \right) \right] \right\}^{-2} \quad (\text{E.4})$$

where ϵ is the absolute surface roughness of the impeller channel, which for our case this value is approximated to 0.09 from Moody diagram in Fig. 4.14.

E.3 Effects in friction factor

The friction factor showed before can not be applied directly in the ESP impeller channel, whose the cross-section is rectangular, the channel is curved and rotates at angular velocity ω . These problems were studied independently from each other by many authors. Next, these factors are showed separately.

E.3.1 Friction factor due to rectangular cross-section

The effect of rectangular cross-section on the friction factor in a duct was studied by Shah (1978), which uses the concept of laminar hydraulic diameter D_{eq} , defined by:

$$D_{eq} = \left(\frac{2}{3} + \frac{11}{24} l(2-l) \right) D_H \quad (\text{E.5})$$

where l is the aspect ratio of the rectangular cross-section for the liquid, defined as:

$$l = \frac{\min(a,b)}{\max(a,b)} \quad (\text{E.6})$$

The equivalent Reynolds number Re_{eq} is:

$$Re_{eq} = \frac{\rho v D_{eq}}{\mu} \quad (\text{E.7})$$

The friction factor corrector F_r for turbulent flow is:

$$F_r = \frac{f_r}{f} = 1 / \left[\frac{2}{3} + \frac{11}{24} l (2 - l) \right]^{0.25} \quad (\text{E.8})$$

E.3.2 Friction factor due to channel curvature

The ratio between R_c and r_H is measured in this section, where R_c is the channel curvature and r_H is the hydraulic radius. Two conditions exist for the calculus of a critic Reynolds, which is this ratio be higher than 860 or lesser. In our experiments, R_c/r_H is lesser, so:

$$\frac{R_c}{r_H} < 880 \quad \text{so:} \quad Re_{crit_\beta} = 2.10^4 \left(\frac{r_H}{R_c} \right)^{0.32} \quad (\text{E.9})$$

The friction factor due to curvature is (S.VIEIRA, 2014):

$$f_\beta = 1.5 \left[Re \left(\frac{r_H}{R_c} \right)^{0.5} / 53 \right]^{-0.611} \quad (\text{E.10})$$

The friction factor for the turbulent flow depends on the Reynolds number Re and the ratio between the radius curvature R_c and the hydraulic radius of the channel r_H where:

$$\text{If: } 300 > Re \left(\frac{r_H}{R_c} \right)^2 > 0.034 \quad \text{so:} \quad F_\beta = \frac{f_\beta}{f} = 0.092 \left[Re \left(\frac{r_H}{R_c} \right)^2 \right]^{0.25} + 0.962 \quad (\text{E.11})$$

where R_c and r_H are:

$$R_c = \frac{1}{2} \frac{r_o^2 - r_i^2}{r_o \cos \beta_o - r_i \cos \beta_i} \quad ; \quad r_H = \frac{D_H}{4} \quad (\text{E.12})$$

E.3.3 Friction factor due to pump rotation

The rotational Reynolds number is important here, defined as:

$$Re_\omega = \frac{\rho \omega D_H^2}{\mu} \quad (\text{E.13})$$

This number needs to be higher than 28 (S.VIEIRA, 2014) in order to consider rotational parameters. So:

$$\text{If: } Re_\omega \geq 28 \quad \text{so: } Re_{crit_\omega} = 1070 Re_\omega^{0.23} \quad (\text{E.14})$$

The dimensionless parameter K_{turb} is defined as:

$$K_{turb} = \frac{Re_\omega^2}{Re} \quad (\text{E.15})$$

So:

$$\text{If: } K_{turb} > 15 \quad \text{so: } F_\omega = \frac{f_\omega}{f} = 0.942 K_{turb}^{0.05} \quad (\text{E.16})$$

E.4 Friction factor for the ESP impeller channel

The friction factors' overlap was adopted by Estevam (2002), Sun *et al.* (2006), Amaral (2007), S.Vieira (2014) and also in the present work. It is assumed that the individual effects of each correction factor F_r , F_β and F_ω multiply the friction factor for round pipe in the same condition, so, the one for ESP is found, which is $f_{r\beta\omega}$.

$$f_{r\beta\omega} = F_r F_\beta F_\omega f \quad (\text{E.17})$$

APPENDIX F – Spreading Illumination Efficiently

Exist an efficient way to distribute point over a disc/plate, in our case it helps to distribute light source points to prevent the formation of small portions of shadows over a surface. One way to formulate a solution is to rely on a particle system. Each point is a particle, particles are repulsing each other with a $1/r^2$ force. A way to find this best efficient distribution is to put the particles on the disc, at random location, then shake vigorously, add some small drag force, let the particles reach a steady stare, shake again, rinse, repeat. It is not as easy as sounds. The setup of the forces, the distribution over the disk, the integrator to use to compute the particle's motion are topics that until now are discussed. For more than a few hundred particles, this process will be terribly slow. A way to distribute the points is presented in Fig. F.1, given by Vogel's method which will be discussed in the next paragraphs.

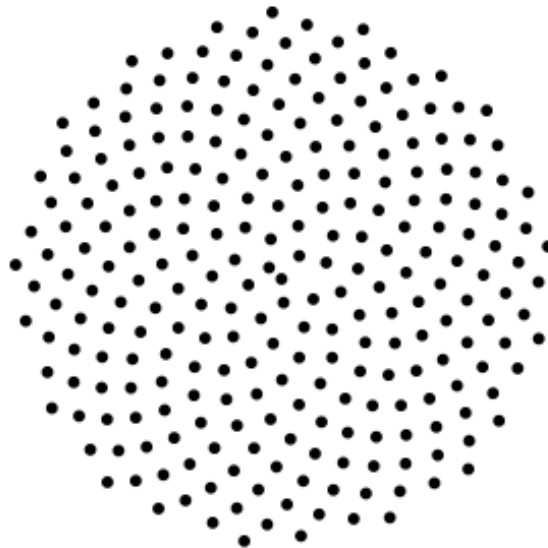


Figure F.1: 256 points with Vogel's method.

There are much simpler and leaner algorithms to evenly distribute N points over a disc. A good approximation is the spiral. Imagine a spiral of dots starting from the

center of the disc. In polar coordinates, the N points are produced by the sequence:

$$\begin{aligned} \rho_i &= \theta_i \\ \tau_i &= \sqrt{\frac{i}{N}} \end{aligned} \tag{F.1}$$

where ρ_i and τ_i are respectively the angle in radian and the radius of the i -th point. Why $\tau_i = \sqrt{i/N}$? Suppose that a unit disc was cut in one disc and one ring of equal areas, thus $\pi r_1^2 = \pi r_2^2$. Thus $r_1 = \sqrt{1/2}$. Next, a unit disc, as before, was cut in one disc and two concentric rings, all of equal areas. A slightly more complex calculation would tell us that the disc should be cut at radius $r_1 = \sqrt{1/3}$ and $r_2 = \sqrt{2/3}$. The calculation is a bit more complex when cutting the unit disc in N equal areas rings, but as did for one and two cut, it becomes: $r_1 = \sqrt{1/N}$, $r_2 = \sqrt{2/N}$, \dots , $r_i = \sqrt{i/N}$. Figure F.2 presents discs cut in equal thickness and equal area concentric rings, showing the difference between them.

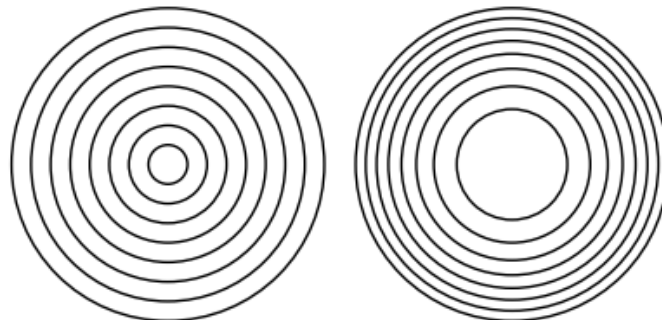


Figure F.2: Equal thickness versus equal areas concentric rings.

The ideal angle θ should be the golden angle, which is: $\pi(3 - \sqrt{5})$. It is roughly equal to 137.508° , or about 2.39996 radians; The golden angle is the "most irrational" angle, defined as $2\pi(1 - 1/\theta)$ with θ being the golden ratio. If θ is a rational number, we would obtain clusters of points aligned with the center of the disk. Thus θ have to be irrational. As is turns out, the golden angle ratio is the irrational number the hardest approximate with a continued fraction. Written as a continued fraction, the golden ratio is the irrational number with the slowest convergence of all the irrational numbers. The

golden angle gives the best possible spread for the ρ_i angles. This method to spread points over a disc is called *Vogel's method*, and it is shown in Fig. F.1.

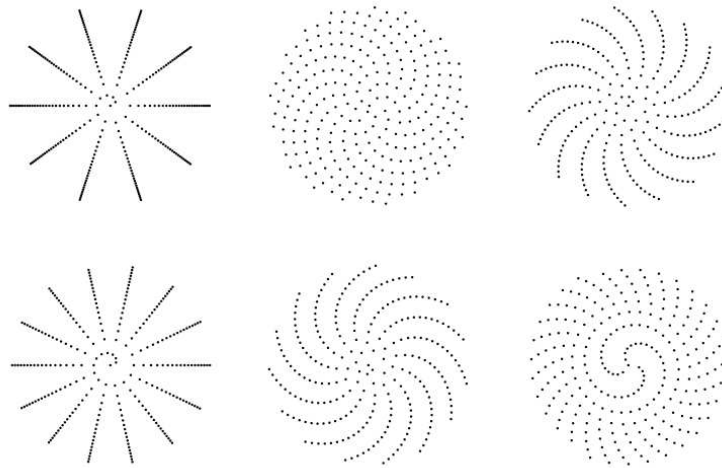


Figure F.3: Effect of the angle step parameter, on 256 points.

Figure F.3 shows the effect of the angle step parameter. The two leftmost points layouts are for rational values of the angle step. The top center one is for square root of 2, the 3 others are for others irrational values. This method was implemented in Matlab with results presented in Fig. F.4. The circle in red is where the camera was positioned, while the marks in blue are for the lamps.

The lamps used are LEDs (Light Emitting Diode) of 10 Watts capable of delivering 1000 lumens. Three Atx computer's source provides a continuous current of 9000 mA and the source voltage of 12 V . Each Atx source provided electricity to ten LEDs in parallel, a total of 30 LEDs. Figure F.5 shows the equipment constructed, frontal and rear view. Each LED works with a resistor of 1.2 ohms, so delivering 800 lumens each, so the total 24.000 lumens.

This illumination was tested with the high-speed camera model I-Speed 3, manufactured by Olympus. However, during the work, a new camera was purchased PHANTON VEO 630, which was able to capture more details without the necessity of the illumination described in this Appendix.

The objective of this equipment is the reduction of shadows generated by the old setup. As the new setup reduce the shadows, the illumination constructed was not

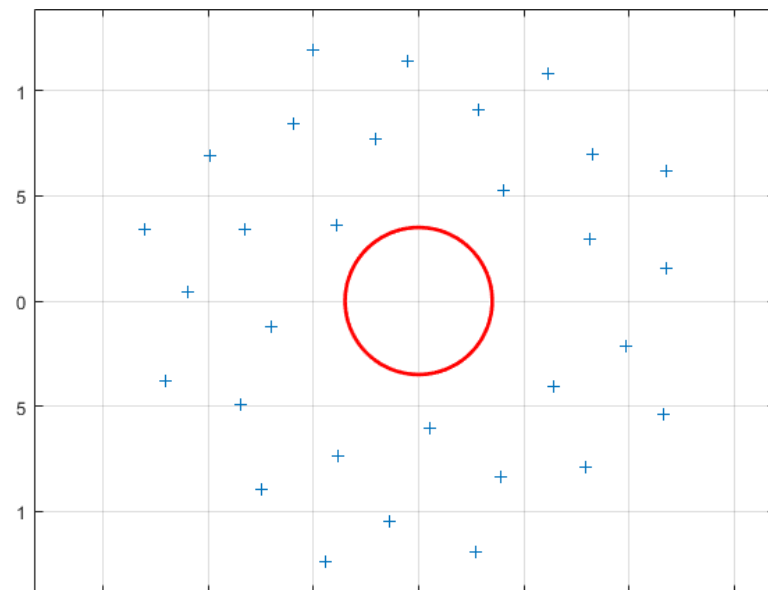


Figure F.4: Matlab code projection for LED's



Figure F.5: (a) Front view - (b) Rear view

necessary, so it was not used. This appendix was written because the light source is much cheaper, costing no more than R\$30.00, and the distribution of the light can be used in other applications.

APPENDIX G – OpenFOAM Numerical Simulations

At the beginning of this work, only the impeller was simulated. It means that the entrance of the flow in the impeller channels was set up as a boundary condition. The other components were not simulated. The flow was assumed to enter normal to the entrance of the impeller in the simulations. This condition reduces losses that naturally occur in the ESP. First, the mesh was built in the BlockMesh utility, supplied with OpenFOAM. Figure G.1 shows the mesh generated.

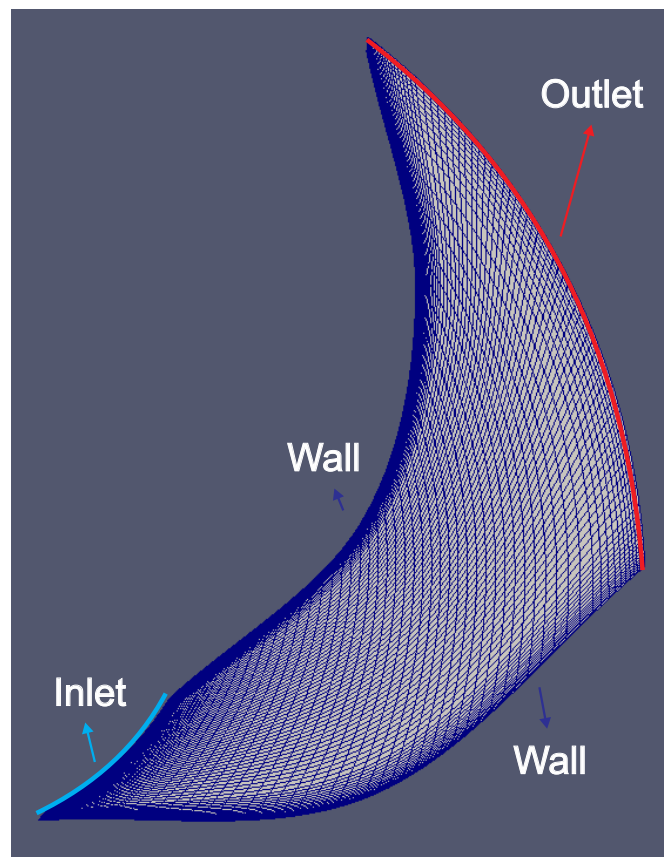


Figure G.1: Impeller mesh.

Figure G.2 shows the results of the simulations performed. However, the simulations at points far from the BEP do not show good results. This stems from the fact that they are not well computed, since, for example, shocks are minimized when the direction of the flow was adopted normally entering at the entrance surface. Figure G.2 shows the results of the simulation in comparison with the experimental data (Monte Verde (2016))

for single-phase flow. The green line corresponds to the maximum pressure increment the pump can add to the fluid, where no losses are considered, it is Euler's correlation (WHITE, 2003). The blue line corresponds to the experiments, and the red line is the simulations. The triangle in black is where the best efficiency point is located.

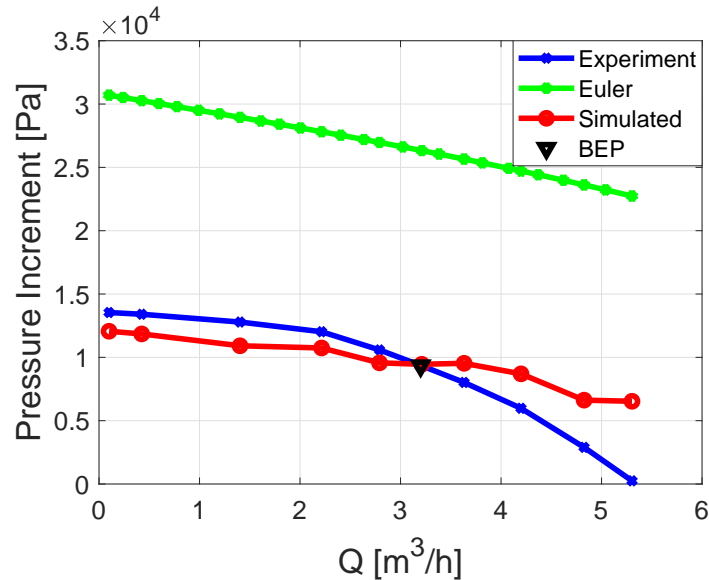


Figure G.2: Pressure increment x flow rate.

This simulations were not carried out. After the diffuser entrance was measured, it was possible to simulate the pump with entire components. However, a different kind of interface algorithm is now required, which is the GGI (General Grid Interface). This is an intersection algorithm that is a class of grid connections where the grid on either side of the two connected surfaces does not match. In general, GGI connections allow non-matching of node location, element type, surface extent, surface shape and even non-matching of the flow physics across the connection (ANSYS, 2017).

The fluid domain, as explained in Fig. A.1 and complemented in section A.2.4 were simulated considering cyclic conditions. This condition is shown in Fig. G.3, where in (a) it is possible to visually observe the domain and in (b) the file to configure each cyclic condition. Besides this configuration, the overlap regions needs to be configured.

This is the moment where the package present in any OpenFOAM version, until the moment, does not be able to connect our case. GGI is an exception to have in some

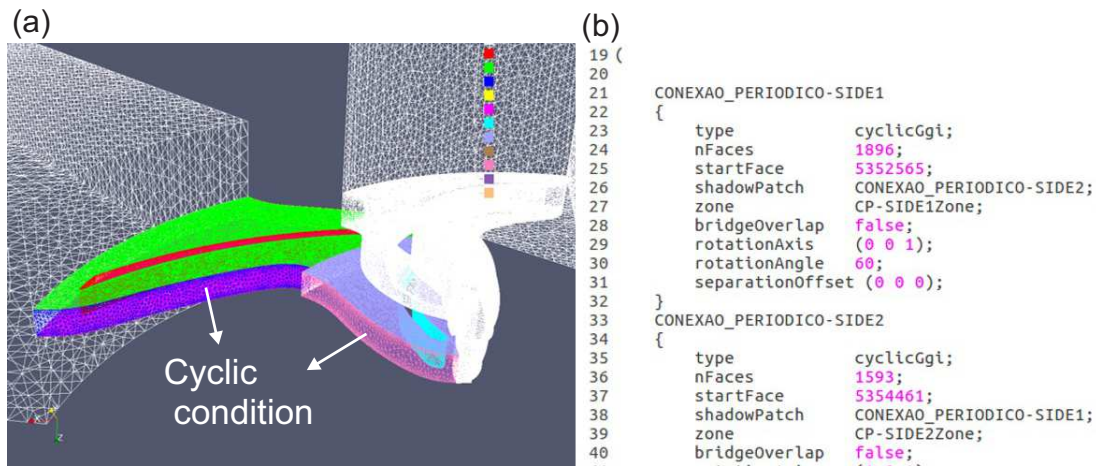


Figure G.3: (a) Domain view - (b) Configuration of cyclic boundary condition with GGI.

versions, but a GGI capable of connecting different size of areas is not present at now. Figure G.4 shows an example of the region where the overlapGgi was implemented. However, the difference in the number of blades and vanes, leads to a difference in areas between the impeller and the diffuser domain, resulting in a problem. A face on one side should get more than one flux at the same time. It would be necessary to add some Fourier decomposition and time lagging to make it work.

The objective of the present work does not evolve the resolution of this problem. The software Ansys already has this implemented, so the platform OpenFOAM was not used after the upgrade done in the fluid domain.

